Freie Universität Berlin

Large-scale distribution of fluids in the subduction zone of Northern Chile - constraints from magnetotelluric monitoring

Dissertation

zur Erlangung des akademischen Grades
doctor rerum naturalium (Dr. rer. nat.)
im Fachbereich Geowissenschaften
der Freien Universität Berlin

vorgelegt von

Jaime Andrés Araya Vargas

Berlin 2016

Gutachter:

Prof. Dr. Oliver Ritter (1. Gutachter)
Freie Universität Berlin, Deutsches GeoForschungsZentrum Potsdam

Prof. Dr. Serge A. Shapiro (2. Gutachter)
Freie Universität Berlin

Tag der Disputation: 14.07.2016

Abstract

Fluids play a critical role in tectonic processes which generate earthquakes. To determine the interplay between deformation processes and the associated fluid systems can provide insights into the key factors which control the occurrence of earthquakes. This thesis presents studies which address the regional-scale distribution of fluids during the seismic cycle in the subduction zone of Northern Chile. This area is an exceptional natural laboratory, because it experienced large earthquakes during the studied interval and it has still a high probability of generating a large earthquake in the near future. To infer the distribution of fluids, this work investigated the regional-scale electrical resistivity structure of the subduction zone. The resistivity structure was imaged and monitored using the magnetotelluric (MT) geophysical method. The analysed MT data were collected at nine permanent sites of the Integrated Plate Boundary Observatory Chile (IPOC) located along the forearc region in northern Chile (21°S-23.5°S, 69°W-70°W).

The regional-scale resistivity structure was derived by modelling long-period MT data using 3-D inversion approach. This model exhibits a complex resistivity structure, suggesting significant spatial variability in the fluid content at different regions of the subduction zone. The model shows that the continental South American plate within the forearc region is mainly characterized by high resistivities ($>$1000 Ωm) between the coast and 69°W. The model shows additionally a number of regional low resistivity zones (LRZs, $<$10 Ωm) within the continental crust. Long-active fault zones and clusters of seismicity are observed within these LRZs, suggesting that these resistivity anomalies are relatively weak and permeable regions of the continental crust, where deformation processes and circulation of fluids have been focused over geologic time. Some of these LRZs reach the continental lower crust above the intraplate seismogenic zone, coinciding spatially with boundaries of the rupture area of large earthquakes and regional NW-SE structural lineaments. In the forearc mantle wedge the model exhibits a 150 km-long trench-parallel LRZ above the intermediate-depth seismogenic zone, suggesting significant along-strike variability in the amount of fluids released from the oceanic Nazca plate.

The temporal evolution of the regional-scale resistivity structure was monitored by analysing the variability of the IPOC MT data from 2007 to 2014. This analysis reveals anomalous temporal variations of the vertical magnetic transfer function (VTF) at one IPOC site during two intervals. These anomalous variations were reproduced by modelling a decrease in resistivity within a seismically active region of the continental crust located above the interplate seismogenic zone. The spatiotemporal distribution of seismicity suggests that the inferred changes in resistivity were associated with episodes of upward migration of fluids generated at the plate interface.

The sensitivity of MT data to changes in the deep resistivity structure and in the geomagnetic activity was evaluated. Possible regional-scale resistivity changes above the interplate seismogenic zone were simulated, obtaining that they can generate measurable variations in MT responses (TFs) recorded at the IPOC sites. However, the modelled variations in IPOC TFs can be masked by unwanted effects correlated with changes in magnetic fields generated in the atmosphere (source effects). The analysis of 18 years of geomagnetic data recorded at mid-latitude sites reveals that globally the VTF exhibits patterns related to source effects. Main patterns identified were periodical seasonal variations and a long-term trend correlated with the 11-year solar cycle. Such source effects can be identified as patterns observed synchronously in temporal variations of VTFs recorded at neighbouring sites, and which additionally show significant correlation with fluctuations of the geomagnetic activity. These results highlight the importance of understanding the contribution of source effects to variations in TFs, in order to interpret correctly results from MT monitoring studies.

Kurzfassung

In der vorliegenden Dissertation untersuche ich die großräumige Verteilung von geologischen Fluiden in der Subduktionszone im Norden Chiles sowie deren räumliche und zeitliche Variation und Verbindung zu tektonischen Prozessen. Dazu wird eine Analyse langperiodischer magnetotellurischer (MT) Daten durchgeführt und zur Abbildung und zum Monitoring der elektrischen Widerstandsstrukturen genutzt. Die MT-Daten wurden an neun permanenten Stationen des Intergrated Plate Boundary Observatory Chile Array (IPOC) vermessen, das sich im Forearc-Bereich (21°S-23.5°S, 69°W-70°W) befindet.

Ein dreidimensionales Modell des elektrischen Widerstands der Subduktionszone wurde durch Inversion von MT-Daten gewonnen. Dieses Modell zeigt, dass die kontinentale südamerikanische Platte unter dem Forearc-Bereich zwischen der Küste und 69°W im Wesentlichen aus Gesteinen mit hohem Widerstand ($>$1000 Ωm) besteht. In der kontinentalen Kruste wurden elektrische Leiter ($<$10 Ωm) abgebildet. In Gebieten wo Sedimentbecken, seismische Aktivität, große orogenparallele Störungssysteme und regionale NW-SE-streichenden Lineamente sich finden, erreichen einige dieser Leiter die kontinentale untere Kruste. Deshalb interpretiere ich diese Leiter als Orte anomal schwacher und permeabler kontinentaler Erdkruste, wo über geologische Zeiträume Deformationprozesse und Fluidtransport stattgefunden haben. Im Mantelkeil zeigt das Modell einen 150 km langen N-S-verlaufenden Leiter, welcher signifikante Unterschiede bei den freigesetzten Fluidmengen in der ozeanischen Nazca-Platte entlang des Streichens der Subduktionsstruktur anzeigen.

Zum Monitoring des elektrischen Widerstands der Subduktionszone wurden zeitliche Variationen der MT-Daten von 2007 bis 2014 analysiert. Anomale Variationen der vertikalen magnetischen Übertragungsfunktion (VTF) wurden an einer Station im nordwestlichen Teil des Arrays beobachtet. Um diese Anomalien anzupassen, wurden Änderungen der elektrischen Widerstandstruktur im Modell mittels 3D-Vortwärtsmodellierung simuliert. Diese Modellstudie zeigt, dass eine Verminderung des Widerstands in 5-25 km Tiefe unter dem Salar Grande die Anomalie erklären kann. Die räumliche und zeitliche Verteilung der seismischen Aktivität in diesem Gebiet stützt die These, dass die Änderung der elektrischen Widerstandsverteilung von Fluiden verursacht wird, welche von der Plattengrenzfläche entlang der Störungszonen durch die kontinentale Erdkruste wandern.

Mit Hilfe der Sensitivitätsstudien wurde getestet, wie sich Änderungen der elektrischen Widerstandsverteilung auf die magnetotellurischen Übertragungsfunktionen auswirken. So konnte mittels 3D-Vorwärtsmodellierung gezeigt werden, dass Widerstandsänderungen oberhalb der seismischen Zone an der Plattengrenzfläche einen messbaren Effekt auf die MT Übertragungsfunktionen haben. Die gemessene Amplitudenänderung hatte allerdings die gleiche Größenordnung wie Amplitudenänderungen aufgrund geomagnetischer Aktivität (Quelleffekte). Um die Quelleffekte besser zu verstehen, wurden daher geomagnetische Daten von 18 Jahren analysiert, die weltweit an Stationen mittlerer Breitengrade aufgenommen worden sind. Dabei konnten bei allen Stationen Quelleffekte in den VTF beobachtet werden, insbesondere die jahreszeitliche Variationen und ein Trend, der mit dem 11-jährigen Sonnenfleckenzyklus korreliert. Diese Quelleffekte kann man durch Vergleich der Daten von benachbarten Stationen erkennen. Variationen in den VTF, die gleichzeitig an benachbarten Stationen beobachten werden und mit der magnetischen Aktivität korrelieren, sind wahrscheinlich Quelleffekte. Dieses Ergebnis zeigt, dass für das Monitoring des elektrischen Widerstands im Untergrund der Beitrag der Quelleffekte zu den Übertragungsfunktionen berücksichtigt werden muss, der andernfalls zu falschen Interpretationen der MT-Daten führen kann.

Resumen

Los fluidos juegan un rol fundamental en los procesos que generan terremotos. Determinar como la ocurrencia de terremotos interactúa con la distribución de fluidos puede ser clave para entender los mecanismos que controlan la generación de grandes terremotos. Sin embargo, la distribución de fluidos en profundidad y su evolución durante el ciclo sísmico es un tema pobremente conocido. Esta tesis presenta estudios sobre la distribución de fluidos durante el ciclo sísmico en la zona de subducción en el norte de Chile. El norte de Chile constituye un laboratorio natural excepcional, ya que dos grandes terremotos ocurrieron durante el período estudiado y hay todavía altas probabilidades de que pueda ocurrir un gran terremoto dentro de los próximos años. En esta investigación se infirió la distribución a gran escala de fluidos en la zona de subducción mediante el estudio de la variabilidad espacial y temporal de las propiedades eléctricas en las placas tectónicas. Para estimar y monitorear la estructura de resistividad eléctrica de la zona de subducción se aplicó el método geofísico magnetotelúrico (MT). Los datos MT analizados fueron adquiridos en nueve estaciones permanentes de la red IPOC (Integrated Plate Boundary Observatory Chile), las cuales cubren la región del antearco del norte de Chile (21-23.5°S, 69-70°W).

Se obtuvo un modelo tridimensional (3D) de la estructura de resistividad eléctrica de la zona de subducción mediante la modelación de datos MT de período largo (10-10.000 segundos) utilizando el programa de inversión 3D ModEM. Este modelo muestra una estructura de resistividad eléctrica compleja, lo cual sugiere importantes variaciones espaciales en la distribución de fluidos en el antearco de la zona de subducción. La placa Sudamericana se caracteriza principalmente por altas resistividades eléctricas ($>$1.000 Ωm) entre la costa y la Precordillera (69°W). El modelo muestra una serie de zonas eléctricamente conductoras ($<$10 Ωm) dentro de la corteza continental. Algunas de estas zonas conductoras se extienden hasta la corteza inferior, en áreas donde convergen sistemas de fallas paralelos a la fosa (rumbo N-S) y lineamientos estructurales regionales de rumbo NW-SE, y donde además se registran clusters de sismicidad cortical. La correlación espacial de estos rasgos sugiere que estas zonas conductoras son regiones excepcionalmente permeables y mecánicamente débiles dentro de la corteza continental, en las cuáles se han concentrado procesos de deformación y acumulación/circulación de fluidos en escala de tiempo geológico. En la cuña del manto el modelo muestra una zona conductora de rumbo N-S y 150 km de largo, la cual se extiende en profundidad hasta la zona sismogénica intraplaca. La acotada extensión N-S de este rasgo sugiere importantes variaciones espaciales en la cantidad de fluidos que son liberados por la placa de Nazca a lo largo del antearco de la zona de subducción.

La evolución temporal de la estructura de resistividad se monitoreó mediante el análisis de las variaciones temporales de los parámetros MT entre los años 2007 y 2014. Se detectaron variaciones anómalas del parámetro VTF (función de transferencia magnética vertical) durante dos intervalos de tiempo en una estación ubicada en la parte noroccidental de la red. Para identificar el origen de estas anomalías, se simularon cambios en el modelo de resistividad utilizando modelación directa. El resultado de estas simulaciones muestra que las anomalías pueden ser explicadas por una disminución de la resistividad eléctrica en una zona sismológicamente activa de la corteza media-superior bajo el sector de Salar Grande. La distribución espacial y temporal de la sismicidad en esta zona sugiere que el cambio en resistividad que se interpretó pudo haber sido generado por alteraciones en las propiedades hidráulicas de la corteza en este sector, como consecuencia de eventos de migración de fluidos desde la zona de contacto interplacas hacia la corteza continental.

Para obtener una metodología de monitoreo, se estudió la sensibilidad que tienen los parámetros MT a cambios en la estructura de resistividad y a variaciones en la actividad magnética natural de la Tierra. Se simularon escenar-

ios posibles de cambios de resistividad sobre el área de ruptura de terremotos interplacas, obteniendo que dichos cambios pueden producir variaciones detectables en los parámetros MT medidos en las estaciones IPOC. Sin embargo, estas variaciones pueden ser ocultadas por variaciones correlacionadas con efectos de fuente, es decir, con cambios en las propiedades de campos magnéticos generados en la Atmósfera. El análisis de 18 años de datos magnéticos, medidos en estaciones distribuidas en diferentes continentes a latitudes medias, muestra que efectos de fuente se pueden observar globalmente en variaciones temporales de la VTF. Los principales efectos de fuente reconocidos son variaciones estacionales y un patrón correlacionado con el ciclo solar de 11 años. Estos efectos de fuente pueden ser identificados como aquellos patrones en las variaciones temporales de VTFs que se observan en varias estaciones al mismo tiempo, y que adicionalmente muestran significativa correlación con variaciones en la actividad magnética terrestre. Estos resultados relevan la importancia de identificar y descontar efectos de fuente en estudios de monitoreo MT, ya que pueden inducir interpretaciones erróneas acerca de la evolución temporal de las propiedades eléctricas del subsuelo.

Acknowledgements

Many people and institutions have contributed in different aspects of my doctoral work. I want to especially thank:

Prof. Dr. Oliver Ritter for giving me the opportunity to work under his supervision, for supporting my application to my doctoral scholarship, for providing all necessary resources to develop this research project, for keeping me focused when necessary, for discussing my results and for correcting my texts.

The Deutscher Akademischer Austauschdienst (DAAD) for financial support during these years in Germany. The GeoForschungsZentrum Potsdam (GFZ) for providing necessary resources to develop this research project. Institutions and people that support the Integrated Plate Boundary Observatory Chile (IPOC) and the INTERMAGNET magnetic observatories networks.

Researchers and students that have been part of the Geo-Electromagnetic and Magnetotelluric groups of the GFZ during these years. This group of people has represented for me a very stimulating scientific environment, in which I have additionally experienced several nice moments. In this group, special thanks to Dr. Naser Meqbel for his key help in several aspects regarding the data modelling, Reinhard Klose for improvements in processing codes which facilitated my analyses of data, Dr. Dirk Brändlein for his introduction to practical aspects of the IPOC data and stations, Dr. Kristina Tietze and Dr. Sintia Niasari for many advises related to modelling, the use of programs and hints concerning practical aspects of the doctorate. I am also very grateful for help and discussions in many aspects provided by (in alphabetical order): Dr. Filipe Adão, Roxana Barth, Dr. Mangal Bhatt, Dr. Xiaoming Chen, Dr. Alexander Grayver, Dr. Gerhard Kapinos, Walja Korolevski, Dr. Sissy Kütter, Dr. Gerard Muñoz, Cedric Patzer, Anna Platz, Stefan Rettig, Dr. Paul Sass, Stephan Schennen, Manfred Schüler, Dr. habil. Ute Weckmann and Gregor Willkommen. Many thanks to Thomas Beka, Jade Greve, Reinhard Klose, Walja Korolevski, Dr. Gerard Muñoz, Cedric Patzer, Anna Platz and Dr. Kristina Tietze for reviewing chapters of this thesis.

Dr. Henri Brasse for feedback about my work, for discussions about the Andes, and for supporting my scholarship extensions.

Dr. habil. Günter Asch for explaining me several aspects of the IPOC sites and for logistical help related to the maintenance of the MT stations. I would also like to thank Günter and Amerika Manzanares for helping me in issues related to the IPOC MT data available in the server.

I participated in two field campaigns to maintain the IPOC MT stations and to install new sites. I would like to thank Prof. Dr. Oliver Ritter, Manfred Schüler, Reinhard Klose and Dr. Kristina Tietze for taking part in these field trips. I am also indebted to Prof. Gabriel González, Prof. Guillermo Chong, Prof. Pablo Salazar, Raúl Ortiz, Martin Haxter, Dr. Jens Bribach and Dr. Ben Heit for logistical support in these fieldworks.

Dr. habil. Günter Asch, Dr. Bernd Schurr, Dr. Ben Heit and Dr. Mauro Palo for answering seismic and seismological questions. Anke Lerch and Matthias Wanjek, for helping me in solving administrative and computational issues.

Gary Egbert and Anne Kelbert for providing ModEM, Naser Meqbel for 3d Grid, and developers of Qgis.

Prof. Gonzalo Yáñez for encouraging me to pursue my PhD and to follow a research career.

Friends at these latitudes, for sharing good moments after-office, which were necessary for having productive in-office intervals: Dr. Pablo Araya, Juan Camilo Moreno, Eduardo Gallardo, Eduardo Martínez.

My family for their love and encouragement, specially my parents Jaime and Loreto, siblings and parents-in-law.

Finally, but first in my heart and in my thoughts, I want to thank my wife, Ana María, for all of her love, patience, emotional support and practical help during these happy years. This thesis is dedicated to you.

To Ana María

In memory of my friend and colleague Antonio Ormeño.

Alle, welche dich suchen, versuchen dich.
Und die, so dich finden, binden dich
an Bild und Gebärde.

Ich aber will dich begreifen
wie dich die Erde begreift;
mit meinem Reifen
reift
dein Reich.

Rainer Maria Rilke

Alguien se preguntará entonces para qué el viento,
para qué el hombre, para qué la vida,
y quién podría responder sino la tierra?

Mario Bahamonde

Contents

List of Figures

List of Tables

Introduction

Research motivation and goals

The subduction of the oceanic Nazca Plate beneath the continental South American Plate controls the intensive seismic activity that is observed along the Chilean margin. This natural phenomenon has had catastrophic consequences on the population, and the geodynamic processes that explain them are far from being fully understood. An exceptional region to study the geological processes that occur before, during and after large subduction earthquakes is northern Chile between latitudes 19°S and 22°S. This region is considered to be in a terminal stage of a seismic cycle (e.g. Comte and Pardo, 1991), and therefore has a high probability of generating a large earthquake in the near future. Since 2006, a permanent array of geophysical and geodetic stations is monitoring the dynamic behaviour of the active subduction zone along this region of northern Chile. This array of stations, known as the Integrated Plate Boundary Observatory Chile (IPOC) network, aids in better understanding of the physical mechanisms underlying earthquake and deformation processes.

Increasing evidence shows that deformation and deep hydrogeological processes are interconnected at subduction zones during the seismic cycle. For example, studies have suggested that the rupture areas of large thrust earthquakes are controlled by the fluid distribution along the plate interface (e.g. Audet et al., 2009; Audet and Schwartz, 2013; Moreno et al., 2014). It has been also suggested that deep large scale relocation of fluids can be triggered by large earthquakes (e.g. Magee and Zoback, 1993; Husen and Kissling, 2001). However, the association between hydrogeological and tectonic processes has not been quantified. To improve the knowledge about these apparently coupled processes, it is fundamental to determine the spatiotemporal variability in the distribution of fluids during the seismic cycle. Both the spatial and temporal variability in the distribution of fluids can cause significant changes in the associated deep electrical resistivity structure, as the electrical resistivity of rocks is highly sensitive to the presence of interconnected conductive fluids. For instance, previous studies in subduction zones have shown that changes in the coupling between tectonic plates correlate with spatial variations in the electrical resistivity structure above the plate interface (Heise et al., 2013; Wannamaker et al., 2014). In order to monitor the electrical resistivity structure of the subduction zone in northern Chile, magnetotelluric (MT) data are collected at eleven IPOC stations. MT is a geophysical method to image Earth's subsurface electrical resistivity distribution, which is estimated from measurements of naturally occurring electric and magnetic field variations at surface.

The main aim of this doctoral work was to determine the spatial and temporal variability of the electrical resistivity structure in northern Chile in order to infer the large-scale distribution of fluids in the subduction zone. The electrical resistivity structure was examined and monitored by analyzing the IPOC MT data. To achieve the main purpose of this study, specific objectives were: (1) to obtain a model of the regional-scale resistivity structure of the forearc in northern Chile; (2) to evaluate the sensitivity of the IPOC MT data to resolve and detect variations in the deep resistivity structure of the subduction zone; (3) to develop a monitoring methodology for interpreting the temporal variations of MT responses as proxies for deep resistivity changes; and (4) to identify variations in the MT responses that can indicate changes in the resistivity structure and to locate such resistivity changes. The spatiotemporal variability in the resistivity structure was compared with the distribution of seismicity during the observation period in order to test possible correlation between fluid and deformation processes.

Thesis outline

This thesis is organized into 7 chapters:

- Chapter 1 summarizes connections between major deformation processes and fluid distribution that have been interpreted in subduction zones, introduces the regional tectonic setting of Northern Chile, and presents the geology of the study area.
- Chapter 2 summarizes the fundamental concepts of the MT method which are relevant for the analyses carried out in this study.
- Chapter 3 describes the main characteristics of the IPOC MT array and MT data. The data quality is analysed and the data processing scheme is explained. Major characteristics observed in MT responses are described and compared with previous studies. Finally, a characterisation of the temporal variations of MT responses is presented.
- Chapter 4 presents a three dimensional (3-D) model of the regional-scale resistivity structure of the forearc region in northern Chile. This model is obtained by inverting data measured at the IPOC MT array using the ModEM program (Egbert and Kelbert, 2012), parallelized with the scheme of Meqbel (2009). The geological implications of the preferred inversion model are discussed. This model suggests that the regional-scale distribution of fluids along the forearc is controlled by discrete and along-strike constrained heterogeneities of the continental and oceanic lithosphere. Some parts of this chapter are contained in a manuscript submitted to *Journal of Geophysical Research*.
- Chapter 5 contains an analysis of the temporal variability of geomagnetic data acquired at various mid-latitudes stations. Data from worldwide distributed magnetic observatories are analysed to test whether systematic source effects observed in the IPOC MT data are present in other regions. This analysis reveals that the presence of source effects in the temporal variations of MT responses is a global effect. These results have relevant implications concerning how to interpret the variability

of MT data for monitoring changes in the resistivity structure. Some parts of this chapter have been published in Araya Vargas and Ritter (2016).

- Chapter 6 contains the analysis of the temporal variability of MT data collected at the IPOC array from May 2007 to December 2014. The aim of this analysis was to investigate the temporal evolution of the resistivity structure in northern Chile. The MT data are analysed following the monitoring concept derived in chapter 5. Forward and inversion modelling tests are performed in order to locate resistivity changes that can explain the observed anomalous variations in MT responses. In addition, the sensitivity of IPOC MT responses to regional-scale changes in the resistivity structure is assessed, by simulating resistivity changes above the interplate seismogenic zone and computing their responses at IPOC sites. The implications of these results for the temporal variability in the fluid distribution and deformation processes are discussed.
- Chapter 7 contains the conclusions of this study and suggested future work.

Thesis contributions

The regional-scale resistivity structure of northern Chile forearc has been studied by a number of authors (e.g. Schwarz et al., 1994; Echternacht et al., 1997; Schilling et al., 1997; Lezaeta, 2001; Brasse et al., 2002; Schwalenberg et al., 2002; Soyer, 2002; Lezaeta and Haak, 2003; Brasse and Eydam, 2008; Díaz et al., 2012; Brändlein, 2013; Kühn et al., 2014). In most of these studies, the main aim was to image spatial variations in the resistivity structure along the trench-normal direction. Consequently, in such works the data were acquired along roughly east-west profiles and/or interpreted using 2-D modelling approach, i.e. assuming invariance in the resistivity distribution approximately in the north-south direction. However, recent studies on other subduction zones have shown that major resistivity features can significantly vary along-strike in convergent margins, and that these spatial changes correlate with first-order segmentation observed in deformation and fluid processes (e.g. Heise et al., 2013; Wannamaker et al., 2014; Hata et al., 2015). Only few studies have presented 3-D resistivity models covering the forearc in northern Chile (e.g. Lezaeta, 2001; Brändlein, 2013; Kühn et al., 2014). From these studies, a larger segment of the forearc region is covered by the model of Brändlein (2013), which was derived from analysis of data collected at the IPOC array. The resistivity model obtained in this thesis (chapter 4) contributes to the understanding of the regional structure of the subduction zone by (i) expanding the area covered by the model of Brändlein (2013) towards south, and (ii) by examining in detail the along-strike variations in the deep resistivity structure and their correlations with geological processes. The obtained model suggests that the subduction zone in the study area presents significant along-strike structural variations, which seem to control the large-scale distribution of fluids and deformation processes both in the continental and oceanic plates.

The analysis of the IPOC MT data (chapter 3) shows that temporal variations of MT responses exhibit patterns which are correlated with fluctuations in the geomagnetic activity. The most prominent pattern correlates with seasonal variations that Brändlein (2013) interpreted as source field effects, i.e. effects due to changes in the properties of magnetic fields generated in the atmosphere. To better understand the

influence of source effects on the temporal variability of MT responses, geomagnetic data collected at various mid-latitudes observatories were analysed (chapter 5). This analysis reveals that MT responses at mid-latitudes exhibit systematic patterns which are correlated with source field effects, violating an assumption commonly accepted by MT practitioners. Furthermore, this thesis shows that the amplitude of these source effects can obscure variations in MT parameters related to changes in the underground resistivity structure, suggesting that the determination of these effects is fundamental for applying the MT method to monitor transient processes in the subsurface. Therefore, a conceptual method to identify and remove source effects is proposed in chapter 5. These methodology is further applied to the analysis of the temporal variability of the IPOC data in chapter 6.

Up to date, the only attempt to systematically investigate the temporal evolution of the resistivity structure in subduction zones is presented by Brändlein (2013). Brändlein (2013) interpreted resistivity variations related to the 2007 M7.7 Tocopilla earthquake, after analysing the IPOC MT data collected in the interval between 2007 and 2011. This thesis complements the study of Brändlein (2013) by: (i) providing an assessment of the resistivity changes that can be detected and resolved by the IPOC MT array (chapter 6), (ii) identifying source effects on MT data that have not been considered before (e.g. influence of the 11-year solar cycle), and (iii) extending the analysis of MT data to the interval between 2011 and 2015, which includes the seismic sequence related to the 2014 M8.1 Iquique earthquake. The analysis of the temporal evolution of the MT data presented in chapter 6 reveals clear anomalous variations in MT parameters at one site, which is located close to the southern boundary of the seismotectonic segment broken by the 2014 M8.1 Iquique earthquake. Forward modelling tests presented in chapter 6 show that the observed anomalies can be explained by resistivity changes within a seismically active region of the continental crust. Comparison with spatiotemporal distribution of seismicity suggests that the interpreted resistivity changes may be related to episodic migration of fluids from the interplate seismogenic zone into the continental crust.

Related publications

Peer-reviewed papers:

Araya Vargas, J., Ritter, O. (2016). Source effects in mid-latitude geomagnetic transfer functions. *Geophysical Journal International*, 204 (1): 606-630, doi:10.1093/gji/ggv474.

Araya Vargas, J., Ritter, O., Meqbel, N. M., Weckmann, U. Along-strike segmentation of subduction processes in the central Andes forearc - constraints from the deep electrical resistivity structure. (Submitted to *Journal of Geophysical Research*).

Conference contributions:

Araya Vargas, J., Ritter, O. (2015). Monitoring deep resistivity changes with geomagnetic transfer functions: Expected variability range and removal of source effects. 26. Schmucker-Weidelt-Kolloquium für Elektromagnetische Tiefenforschung (Dassel, Germany).

Araya, J., Ritter, O. (2014). Detection of deep fluid flow in subduction zones with magnetotelluric monitoring. AGU 2014 Fall Meeting (San Francisco, United States of America).

Araya, J., Ritter, O. (2014). The active subduction zone in northern Chile monitored with magnetotellurics. 22nd Electromagnetic Induction Workshop 2014 (Weimar, Germany).

Araya, J., Ritter, O., Brändlein, D. (2013). Long-term variations of magnetotelluric transfer functions in northern Chile. 25. Schmucker-Weidelt-Kolloquium für Elektromagnetische Tiefenforschung (Kirchhundem-Rahrbach, Germany).

Ritter, O., Brändlein, D., Araya, J., Weckmann, U. (2013). A modern magnetometer array to monitor the electrical conductivity structure of the South American subduction system in Northern Chile. 12th Scientific Assembly of the IAGA (Mérida, Mexico).

Chapter 1

Geodynamic background

This chapter presents an introduction to the geodynamic processes and problems which motivate this study. Section 1.1 contains a brief review of evidences that suggest the presence of fluids at depth in subduction zones, and the interconnections between deep fluid distribution and deformation processes. The tectonic setting and local geology of the study area are described in sections 1.2 and 1.3, respectively.

1.1 The link between fluid distribution and deformation processes in subduction zones

1.1.1 Fluid distribution in subduction zones

The current knowledge about the deep fluid distribution in active subduction zones is based on indirect observations (e.g. geophysical and geochemical data), and additionally inferred from studies of outcropping rocks that were formed at old subduction zones. The presence of fluids at depth has been generally interpreted by inferring the subsurface distribution of two petrophysical properties that are especially sensitive to the amount of fluid phases within rocks (see e.g. Unsworth and Rondenay, 2013): (i) the electrical resistivity, because the abundance of interconnected fluids of low resistivity tends to significantly decrease the bulk resistivity of rocks; and (ii) the seismic velocity, especially parameters like the ratio between the seismic P and S wave velocities (Vp/Vs ratio) and the seismic attenuation. The physical and chemical processes that control the generation, movement and trapping of fluids are usually explained using numerical models with petrological constraints (see e.g. Peacock, 1990; Saffer and Tobin, 2011).

Large-scale regions enriched in fluids above the plate interface have been consistently inferred by several studies at different subduction zones. Figure 1.1 summarizes the major fluid-enriched regions that have normally been interpreted in the forearc of subduction margins, and the suggested processes which would explain the connections between these regions and deformation processes. The origin of these large-scale fluid reservoirs are normally interpreted as being a consequence of fluid-releasing metamor-

phic reactions that take place in the subducting slab (e.g. Peacock, 1990). Therefore, the amount and distribution of fluids in subduction zones would be determined by factors which control these metamorphic reactions (e.g. mineralogical composition of the slab, thermal and pressure conditions), and by factors which control the permeability of the subduction's hydrological system (e.g. porosity distribution and interconnectivity) (see e.g. Peacock, 1990; Ingebritsen and Manning, 2010; Saffer and Tobin, 2011). It is important to remark that the distribution of fluids can also vary parallel to the axis of the subduction margin (i.e. perpendicular to the section shown in Figure 1.1), for example due to along strike fluid flow controlled by temperature gradients in the oceanic crust (Spinelli and Saffer, 2007, see Figure 1.2).

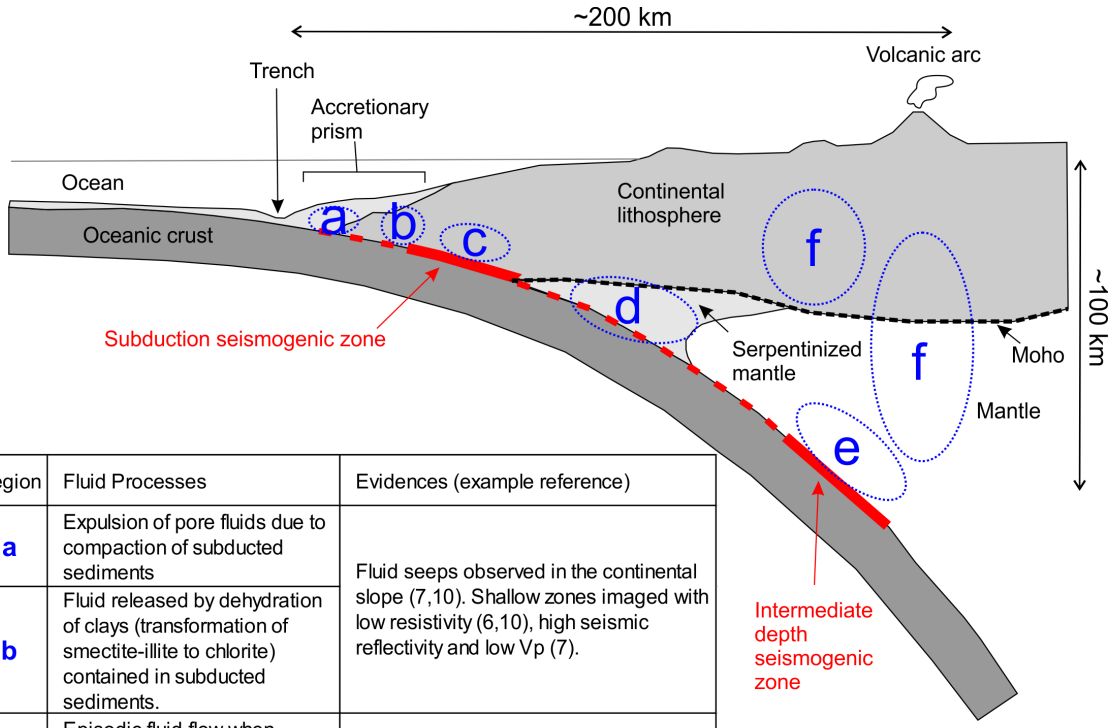

Region	Fluid Processes	Evidences (example reference)
a	Expulsion of pore fluids due to compaction of subducted sediments	Fluid seeps observed in the continental slope (7,10). Shallow zones imaged with low resistivity (6,10), high seismic reflectivity and low Vp (7).
b	Fluid released by dehydration of clays (transformation of smectite-illite to chlorite) contained in subducted sediments.	
c	Episodic fluid-flow when subduction earthquakes break low-permeability region along subduction thrust.	Temporal variations in Vp/Vs ratio (5) and in seismicity distribution (9) after large subduction earthquakes.
d	Fluids released by porosity collapse and mineral dehydration of the oceanic lithosphere.	Low resistivity (6) and low seismic velocity (1) zones in forearc mantle wedge. Alteration of mantle rocks (serpentinisation).
e		Intermediate-depth seismogenic zone (3).
f	Migration path of partial melts which feed volcanic arc	Low resistivity (2), low seismic velocity (1) and high seismic reflectivity (11) zones in the continental crust. High seismic attenuation (8) and low resistivity (4) zones of large vertical extent connecting the top of the slab with

Figure 1.1: Schematic section of a subduction zone illustrating the major fluid-enriched regions that are interpreted in the forearc of subduction margins (blue ellipses), and the spatially related patterns in slip modes (red lines). The suggested physical and chemical processes that would explain these fluid-rich zones are indicated in the table. Reference indicated in the table are: (1) ANCORP Working Group (2003), (2) Brasse et al. (2002), (3) Hacker et al. (2003), (4) Hata et al. (2015), (5) Husen and Kissling (2001), (6) Kapinos et al. (2016), (7) Saffer and Tobin (2011), (8) Schurr et al. (2003), (9) Shapiro et al. (2003), (10) Worzewski et al. (2011), (11) Yoon et al. (2009). Section adapted from Hyndman et al. (1997).

1.1.2 Spatial correlation between fluids and deformation mechanisms at subduction zones

Several studies on subduction zones have described spatial correlation between the occurrence of deformation processes (mainly interpreted from seismological and geodetic observations) and the inferred presence of fluids in depth (see Figure 1.1). This spatial correlation can be explained by different phenomena. On one hand, laboratory experiments show that the the presence of fluids play a key role in the frictional strength of faults, because the pore pressure partly controls the shear stress necessary to slip (e.g. Scholz, 1998). For example, rupture events that define the intermediate-depth seismogenic zone in subduction systems would be favoured by fluids released by dehydration reactions related to eclogitization (e.g. Hacker et al., 2003) (see region E in Figure 1.1). In addition, frictional properties of fault rocks depend on their mineralogy, which can be modified by mineral reactions that normally release or consume fluids (and therefore alter the amount of free-fluids available).

The updip limit of the interplate seismogenic zone appears spatially correlated with fluid-rich regions at subduction zones. The stable slip observed in the shallowest part of the subduction thrusts would be explained by the presence of H_2O-rich clay minerals, which are characterized by weak frictional strength. The dehydration of these clay minerals would determine the transition to unstable slip and would explain the accumulation of fluids which has been imaged above the updip limit of the subduction earthquakes (e.g. Hyndman et al., 1997) (see region B in Figure 1.1). In convergent margins where a cold oceanic plate is subducted, the downdip limit of interplate earthquakes normally coincides where the oceanic slab reaches the forearc mantle wedge (e.g. Hyndman et al., 1997). Stable slip observed downdip of this point would be explained by the presence in the forearc mantle of minerals with weak mechanical properties (e.g. serpentine minerals, talc). The generation of these minerals is related to the hydration of mantle rocks (which results in serpentinite rocks), a process which is favoured by the large amounts of fluids released by the dehydrating oceanic slab at this region (e.g. Hyndman and Peacock, 2003). The abundance of fluids can explain low resistivity zones observed in this region (Reynard et al., 2011), while the mineralogy of serpentinite rocks can explain anomalously low seismic velocity and high magnetization observed at the forearc mantle wedge (e.g. Hyndman and Peacock, 2003) (see region D in Figure 1.1).

It has been proposed that the fluid distribution also controls the along strike extent of the rupture plane of large subduction thrust earthquakes. For instance, a spatial correlation between the amount of fluids and the along strike segmentation of slip patterns at the subduction plate interface was documented in Costa Rica (Audet and Schwartz, 2013) and Southern Chile (Moreno et al., 2014). In these studies, the amount of fluids is inferred by modeling the Vp/Vs ratio. These works show that low Vp/Vs ratio (interpreted as indicator of regions with low pore fluid pressure) are correlated with zones in which the plate interface is locked and large earthquakes can be produced, while areas with high Vp/Vs ratio (high pore fluid pressure) are characterized by low degree of plate coupling and slow slip events (see scheme in Figure 1.2). In both studies it is suggested that differences in the amount of fluids at the plate interface are related to variations in the amount of fluids produced and/or carried by the oceanic plate into the subduction zone. Along-strike variations in the distribution of deformation mechanism has been also related to complex variations in the frictional properties of the plate interface, which can be controlled

by the amount of subducted sediments (Pritchard and Simons, 2006).

Although several lines of evidence suggest a relevant role of fluids in the spatiotemporal distribution of deformation during the seismic cycle, the underlying mechanisms that would explain their interrelation have not been quantified. Moreover, it is not evident if the distribution of fluids and deformation processes along the plate interface are temporally coupled. For example, while factors which may control the budget of fluids in the plate interface act over geological time scales (e.g. age and thermal state of the oceanic plate, mineral reactions which consume/generate fluids), historical records show that each segment of the Chilean margin is broken by large interplate earthquakes with a recurrence interval in the order of hundreds of years (e.g. Lomnitz, 2004). To start addressing these questions, one basic aspect is to gain more information about the temporal distribution of fluids in the subduction zone during the seismic cycle, which constitutes the main aim of this thesis. In addition, but beyond the scope of this work, it is necessary to detect manifestations of different deformation mechanisms that release the energy accumulated due to plate convergence (e.g. slow slip events), in order to explore possible correlation between activity in the fluid system and deformation processes.

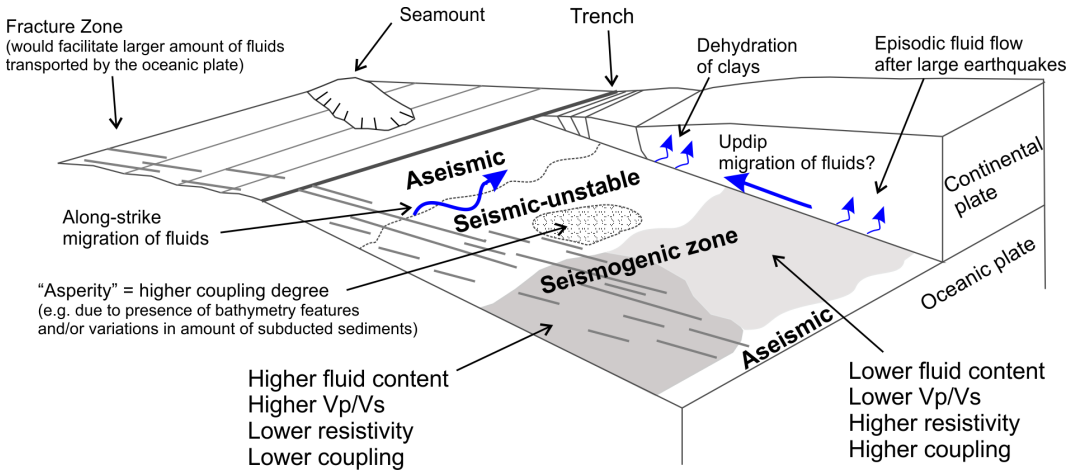

Figure 1.2: Scheme illustrating along-strike variations in the distribution of fluids and deformation mechanisms that have been interpreted along the plate interface at subduction zones (see examples described in the text). Grey areas indicate the seismogenic zone. Diagram modified after Bilek and Lay (2002) and Moreno et al. (2014).

1.2 Tectonic setting of Central Andes

The Andes are the result of geological processes primarily controlled by the subduction zone along the western margin of South America. Geological records suggest that this subduction system has been active since the Jurassic at least (e.g. Coira et al., 1982). Currently, the oceanic Nazca Plate subducts the continental South American Plate between ∼7°N and 46°S, with a convergence rate of 6.6 cm/yr and an azimuth of 078° (Angermann et al., 1999). South of the subduction of the Chile Rise (∼46°S), the Antartic Plate subducts under South America.

The Andes exhibit first order segmentation along their 8000 km of length. This segmentation is observed as significant along-strike variations in several aspects, notably in: width and topography of the mountain range; distribution and characteristics of active volcanism (e.g. Stern, 2004); distribution of seismicity (e.g. Bilek, 2010); current geodetic velocity fields (e.g. Nocquet et al., 2014); structural architecture and style of deformation (e.g. Kley et al., 1999); distribution of basins (e.g. Jacques, 2003); density structure (e.g. Tassara et al., 2006); patterns of paleomagnetic rotations (e.g. Taylor et al., 2005); and geologic evolution (e.g. Mpodozis and Ramos, 1989). The main topographic and geological segments of the Andes spatially coincide with first-order variations in properties of the Nazca Plate at the subduction zone (e.g. subduction angle, geometry, structure and age), which several authors have explained as evidence of the causal control on the Andean segmentation (e.g. Barazangi and Isacks, 1976; Jordan et al., 1983; Isacks, 1988; Cahill and Isacks, 1992; Yáñez and Cembrano, 2004). However, it has been suggested that heterogeneities in the continental plate may also significantly control the segmented deformation pattern observed along the Andean orogen (e.g. Kley et al., 1999; Oncken et al., 2006; Mamani et al., 2008).

The Central Andes between 15° and 28°S exhibit three outstanding features: the Altiplano-Puna Plateau, a first-order curvature observed in the direction of the Andean chain at ∼20°S (known as Bolivian Orocline), and active volcanism (the Central Volcanic Zone, see Figure 1.3). The Altiplano-Puna Plateau is a global topographic anomaly (∼2000 km length and maximum 400 km wide with an average elevation of 3700 m), which origin has been explained by significant horizontal shortening and crustal thickening during the Cenozoic (e.g. Allmendinger et al., 1997). It has been proposed that along-strike variations in the Andean horizontal shortening could explain the deformation processes that resulted in the origin of the Bolivian Orocline (e.g. Arriagada et al., 2008). The Central Volcanic Zone comprises 44 active stratovolcanoes and large ignimbrite eruptions, mainly of andesitic, dacitic and rhyolitic composition. The geochemical signature of these volcanic products implies important crustal contamination, which suggests the presence of a very thick crust (Stern, 2004). Seismic studies have estimated that the crustal thickness in this region is >50 km, reaching a maximum of ∼75 km below the Altiplano (e.g. Yuan et al., 2000).

Along the Central Andean margin the subducted Nazca plate is characterized by subduction angles between 25° and 30° (e.g. Barazangi and Isacks, 1976). With such subduction angles, at ∼100 km depth the Nazca plate reaches some physical conditions which allow the development of petrological processes responsible for the observed active volcanism (Stern, 2004). According to the isochrons of the ocean floor (Müller et al., 1997), the oldest age segment of the Nazca's crust at the trench of the western margin

of South America is observed along the Central Andes subduction zone (see Figure 1.3). Two major structures observed in the ocean floor are subducted along the Central Andes margin: the Nazca and the Iquique ridge (see Figure 1.3). It has been suggested that the presence of these oceanic features may control deformation processes at the subduction zone (e.g. rupture area of large earthquakes and seismic coupling observed in northern Chile, Contreras-Reyes and Carrizo, 2011).

By the end of the 19th century two great tsunami earthquakes affected the region which currently comprises southern Peru (in 1868, approximately between latitudes 16° and 19°S) and northern Chile (in 1868, 19°-23°S) (see left panel in Figure 1.3). Historical records show that the southern Peru segment was previously broken by great earthquakes in 1604 and 1784, suggesting a recurrence interval of approximately 100 years for the occurrence of large events. Therefore, taking into account the absence of significant earthquakes during the 20th century, the southern Peru - northern Chile region was considered as a seismic gap which was in the terminal stage of its seismic cycle (e.g. Comte and Pardo, 1991). While two earthquakes (Mw 8.4 and 7.5) in 2001 broke almost two thirds of the southern Peru segment (Bilek, 2010), the northern Chile segment was partly broken by the 2007 M7.7 Tocopilla and 2014 M8.1 Iquique events (see left panel in Figure 1.3). However, these two earthquakes broke only the central part and southern border of the 1877 event's rupture area, leaving significant unbroken segments with high potential of generating M$\sim$8 earthquakes (e.g. Schurr et al., 2014). The limits of the rupture length of the 1868 southern Peru and 1877 northern Chile earthquakes exhibit spatial correlation with three major morphological features: the Nazca ridge (northern limit of the 1868 event), the change in the direction of the coastline (which separates the southern Peru from the northern Chile segment, e.g. Comte and Pardo, 1991), and the Mejillones Peninsula (southern limit of the 1877 and 2007 earthquakes, e.g. Schurr et al., 2012).

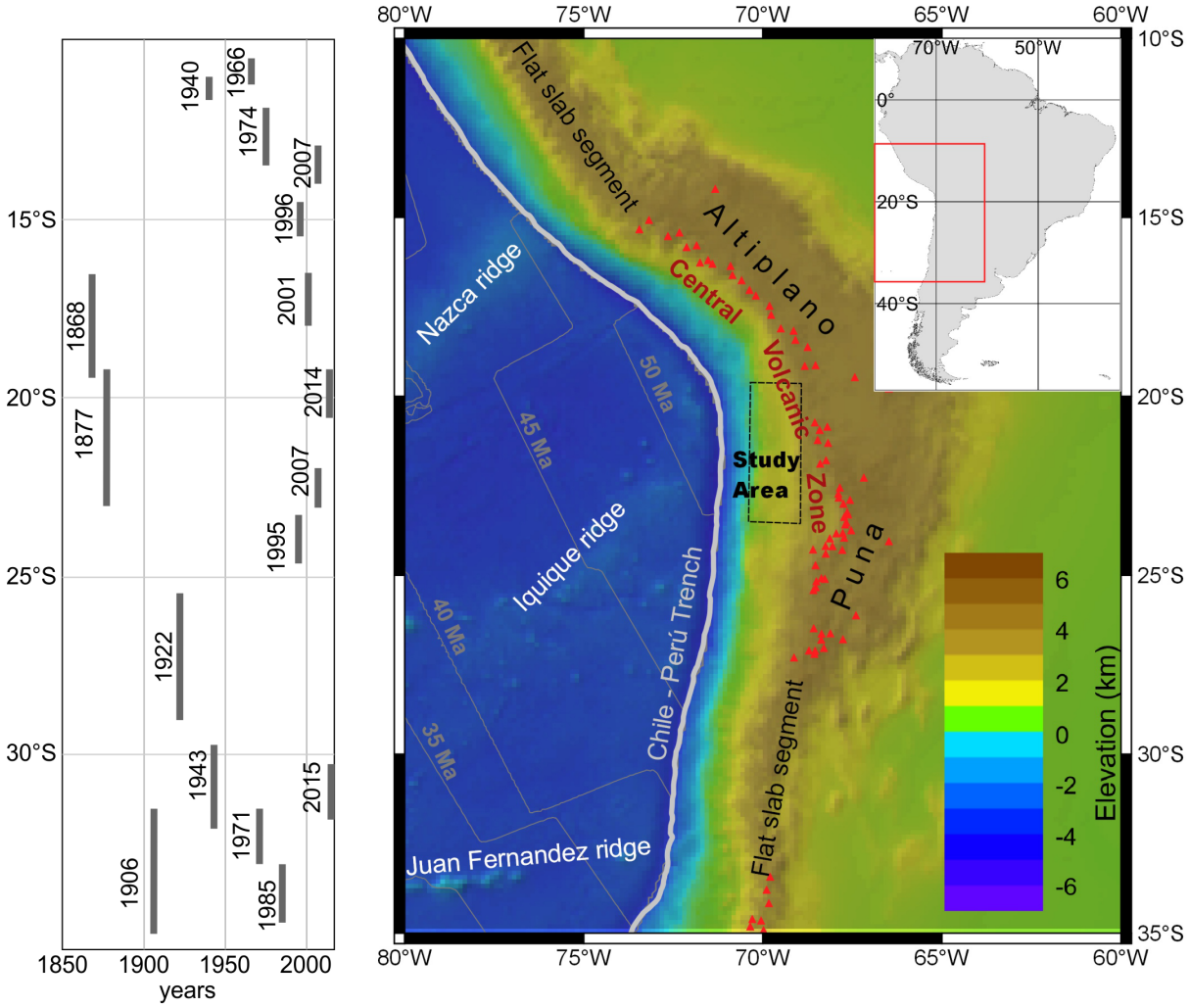

Figure 1.3: Tectonic setting of Central Andes. (Left) Rupture length of large subduction earthquakes (M ∼8) since 1850 (compiled from: Barrientos, 2007; Bilek, 2010; Tilmann et al., 2016). (Right) Elevation map obtained from NOAA (http://www.ngdc.noaa.gov/mgg/topo/topo.html). Red triangles are active volcanoes, obtained from The Smithsonian Institution's Global Volcanism Program (http://volcano.si.edu). Light grey lines are isochrons of the Nazca plate (Müller et al., 1997). Major morphological features are labelled. The polygon with black borders shows the location of the study area and map shown in Figure 1.4.

1.3 Geology of the study area

Figure 1.4 shows the simplified geology of the study area. The IPOC array is located in the forearc domain of the Central Andes, in a region in which three main longitudinal morphological units can be recognized from west to east: the Coastal Cordillera, the Longitudinal Valley and the Chilean Precordillera. The position of the active volcanic arc is located east of the Chilean Precordillera, in a morphological unit known as Western Cordillera.

The Coastal Cordillera is a 1-2 km high and 20-50 km wide mountain range, whose geology is dominated by outcrops of volcanic, plutonic and sedimentary rocks of Jurassic to Early Cretaceous age (e.g. La Negra Formation), partly covered by Cenozoic unconsolidated continental sediments. Metamorphic, plutonic and volcanic rocks of Paleozoic or Triassic age are locally observed (e.g. at Mejillones Peninsula). The main structural feature in the Coastal Cordillera is the north-south trending Atacama Fault System (AFS), which is observed for more than 1000 km along northern Chile, and cuts Mesozoic rocks and Cenozoic sediments (e.g. Arabasz, 1971). Kinematic studies of the AFS suggest predominantly left strike-slip and normal movements during Jurassic to Early Cretaceous, and reactivation of faults with normal and reverse displacements during the Cenozoic (e.g. Scheuber and González, 1999; Allmendinger and González, 2010). Another large scale structural feature in the Coastal Cordillera is a $\sim$1 km height topographic scarp observed for more than 500 km along the coast, which has been interpreted as a major west-dipping fault (e.g. Armijo and Thiele, 1990).

The Longitudinal Valley (also called Central Depression) is a relatively flat basin, mainly filled by Cenozoic continental sediments and ignimbrites. Based on stratigraphic studies and interpretation of seismic sections, previous works have estimated up to 1.7 km thickness for Cenozoic deposits between 20° and 21°30 S (e.g. Nester, 2008). The flat topography of the Central Depression is interrupted by isolated hills, where predominantly Cretaceous volcanic, sedimentary and plutonic rocks are exposed. A system of north-south trending west-vergent faults have been described at the eastern limit of the Longitudinal Valley at least between 18 and 22° S, whose reverse movements during the Neogene could have accommodated the uplift of the Altiplano (e.g. Muñoz and Charrier, 1996; Victor et al., 2004; Farías et al., 2005).

The Precordillera is a 2-4 km high mountain range, in which outcrops of Paleozoic, Mesozoic and Cenozoic rocks are observed. Especially north of 21° S, these units are covered by Miocene ignimbrites. The main structural feature along the Precordillera is the north-south trending Precordilleran (or Domeyko) Fault System (PFS), which is described between 19 and 27° S (Maksaev and Zentilli, 1999). Dextral and sinistral strike slip displacements, and also reverse movements, have been documented for the PFS (e.g. Reutter et al., 1996; Amilibia et al., 2008).

The following summary of the geological evolution is based on the reviews of Mpodozis and Ramos (1989) and Charrier et al. (2007). The geology of Northern Chile forearc represents records of geological process that are normally divided in three major tectonic cycles: formation of Gondwanan continent (Late Proterozoic to Late Palaeozoic), pre-Andean (Permian and Triassic) and Andean (Jurassic to Present). Currently outcropping Paleozoic rocks in the northern Chilean forearc were formed in a subduction

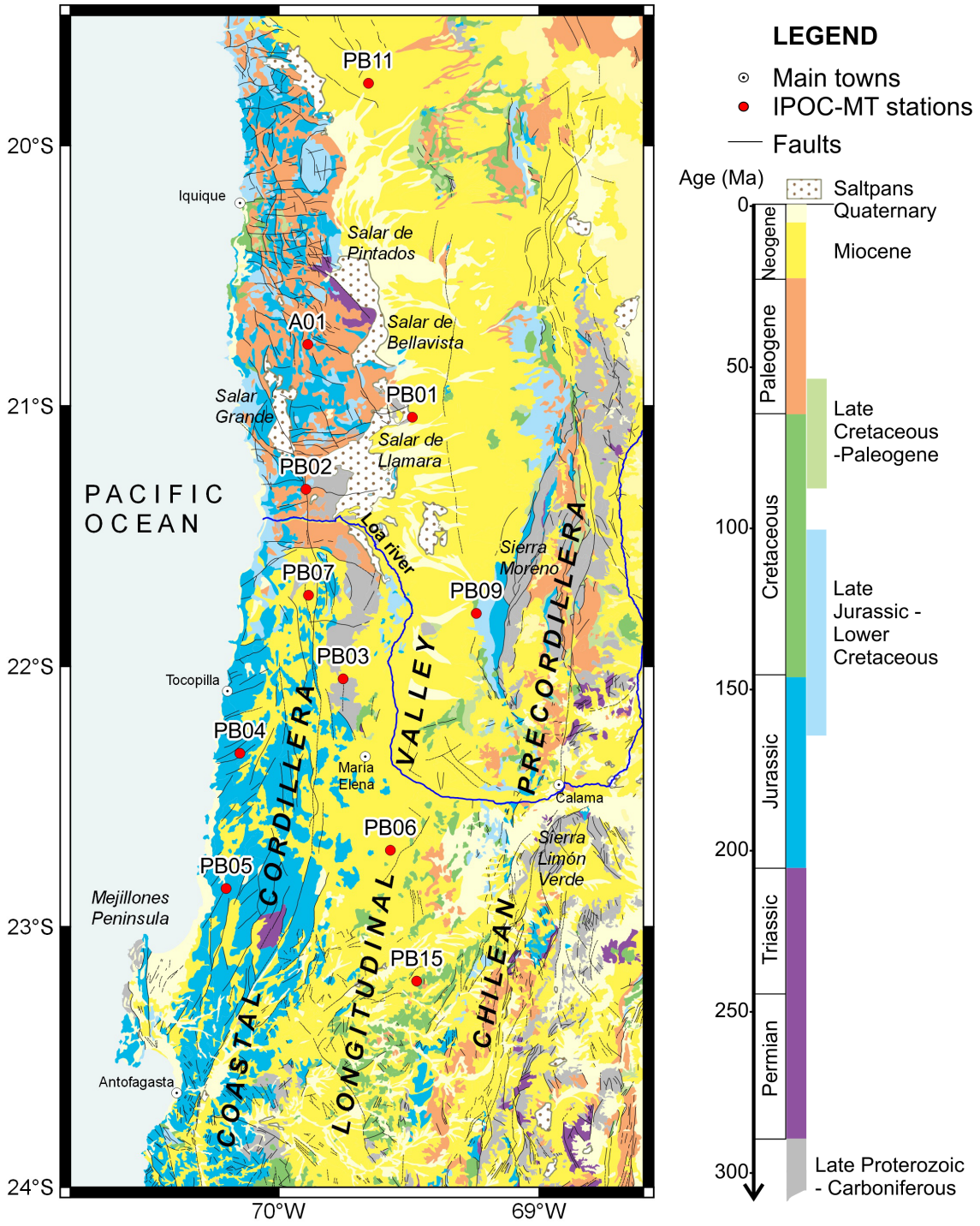

Figure 1.4: Simplified geological map of the forearc region in Northern Chile (19.5-24°S), modified from Sernageomin (2003). Locations of the IPOC MT stations are shown.

zone located at the western margin of Gondwana, in which terrane accretion caused westward migration of the arc and lateral growth of the Gondwana continent. During the pre-Andean tectonic cycle the convergence activity decreased, the paleographic configuration was dominated by NNW-SSE oriented basins (oblique to the Gondwana margin), and large volumes of silicic magmas were produced mainly by crustal melting. The Andean cycle is characterized by the development of a subduction system with a progressive eastward migration of the magmatic arc, which is interpreted to be a result of subduction tectonic erosion of the continent. The episodes in which the arc migrated to the east during the Andean cycle have been related to major deformational phases controlled by changes in the re-arrangement in geometry and convergence rate of plates.

The Jurassic to Early Cretaceous paleographic configuration is interpreted as a margin-parallel volcanic arc (currently exposed along the Coastal Cordillera) with a back-arc basin to its eastern side (partly filled with marine deposits). The AFS acted as intra-arc fault system, partly controlling the emplacement of plutons. The dominant sinistral strike slip movements recorded during Jurassic to Early Cretaceous in the AFS are interpreted as a consequence of oblique towards south-east convergence of the oceanic Phoenix (or Aluk) plate during this stage. The closing of the back-arc basin took place during middle to Late Cretaceous, which has been mainly related to the westward movement of the South American plate due to the opening of the Atlantic. During this tectonic phase the arc migrated to the east, as is suggested by the presence of the late Cretaceous to Oligocene magmatic rocks in the present Precordillera. Here, the PFS controlled the emplacement of magmatism and related processes (e.g. genesis of big porphyry copper deposits). Kinematic records during late Cretaceous to Oligocene in the PFS are interpreted as evidence of oblique towards north-east convergence of the oceanic Farallon plate. A change to almost orthogonal convergence is interpreted at 25 Ma, accompanied by a high increment in the convergence rate until $\sim$10 Ma. This major tectonic re-arrangement has been interpreted as a key factor for explaining the uplift of the Precordillera and Altiplano region, whose erosion could explain the deposition of sediments that currently fill the Longitudinal Valley. Following this tectonic phase, the magmatic arc formed in its current position at the Western Cordillera.

Chapter 2

Methods

2.1 Electrical resistivity of earth's materials

The electrical resistivity (ρ, which has units of [Ωm]) is a physical property that quantifies the ability of materials to oppose the flow of electric currents. The reciprocal of the resistivity is the electrical conductivity (σ, [S/m]). Laboratory measurements show that resistivity of minerals varies within a wide range (0.01 to $>$10,000 Ωm, e.g. Carmichael, 1989). The resistivity of minerals depends on factors like chemical composition, crystallographic structure, temperature and pressure. The resistivity of rocks depends on the resistivity and amount of their components (minerals, interstitial fluids), and how they are interconnected. Laboratory measurements show that the resistivity of rocks is a frequency dependent property, however, it is assumed that this dependence is not significant for the frequencies of electromagnetic fields measured in magnetotelluric studies ($<$10 kHz, see e.g. Pommier, 2014b).

Considering that most abundant silicates in the crust are characterized by high resistivities ($>$100 Ωm), comparatively lower bulk resistivities in crustal environments are normally interpreted as evidence of rocks containing conductive minerals (e.g. clays, metallic minerals, graphite) and/or interstitial fluids, or alternatively the presence of partial melts. The resistivity of fluids under typical crustal conditions ranges between 0.01 and 10 Ωm, and is primarily controlled by the fluid composition (e.g. dissolved ions like NaCl and KCl decrease resistivity), temperature and density (Nesbitt, 1993). Laboratory measurements of partial melts simulating crustal conditions have obtained resistivities $<$10 Ωm, which decrease with increasing temperature or increasing water content (e.g. Pommier et al., 2008).

Different models have been proposed to calculate the bulk resistivity of multi-phase materials (like rocks), by considering the resistivity of their components, for example:

- Archie (1942) proposed an empirical formula for the resistivity of sediments containing electrolyte, after studying the resistivity of sands in which all pores were filled with low resistivity brines. Archie's law (eq. (2.1)) establishes that the resistivity of a rock containing an interstitial fluid depends on the resistivity of the fluid phase (ρ_f), the porosity of the rock (θ), and on an empirical factor (m, sometimes called the cementation exponent, see e.g. Glover et al., 2000). The cemen-

tation exponent m is related to the pore geometry: the better connected are the pores within the rock, the smaller is the value of m. It is important to note that Archie's law is valid for rocks in which the resistivity of the fluid is significantly lower than the resistivity of the matrix.

$$\rho_{archie} = \rho_f \theta^{-m} \tag{2.1}$$

- Hermance (1979) proposed a modification of Archie's law (eq. (2.2)), in order to account for the influence of the resistivity of the matrix (ρ_m), which is especially relevant in rocks with low porosity and/or with matrix with low resistivity.

$$\frac{1}{\rho_{hermance}} = \frac{1}{\rho_m} + (\frac{1}{\rho_f} - \frac{1}{\rho_m})\theta^2 \tag{2.2}$$

- Hashin and Shtrikman (1962) derived a mathematical expression for calculating the minimum and maximum bounds of the effective magnetic permeability of a macroscopically isotropic and homogeneous material composed of two phases. The authors proposed that this relationship is also valid for other physical properties, e.g. for electrical conductivity. Therefore, the bulk conductivity of a two-phase medium ($\sigma_{\text{effective}}$) can be constrained by the Hashin-Shtrikmann lower and upper bounds (2.3), in which σ_{max} and ϕ are the conductivity and volume fraction of the more conductive material, and σ_{min} is the conductivity of the material with lower conductivity (e.g. Simpson and Bahr, 2005)

$$\sigma_{min} + \frac{\phi}{\frac{1}{\sigma_{max}-\sigma_{min}} + \frac{1-\phi}{3\sigma_{min}}} < \sigma_{effective} < \sigma_{max} + \frac{1-\phi}{\frac{1}{\sigma_{min}-\sigma_{max}} + \frac{\phi}{3\sigma_{max}}} \tag{2.3}$$

2.2 Geoelectromagnetic induction methods with natural sources

At the IPOC array, time variations of natural electric and magnetic fields are recorded. These measurements allow to apply two methods that probe the underground electrical resistivity structure: the magnetotelluric method (MT), which uses time variations of horizontal electric and magnetic fields, and the geomagnetic deep sounding method (GDS, also known as magnetovariation method), which employs time variations of only magnetic fields (horizontal and vertical components). Both methods are based on the phenomenon of electromagnetic induction in the earth. More details about the MT method can be found in the books of Simpson and Bahr (2005), Berdichevsky and Dmitriev (2008), and Chave and Jones (2012). Among these books, Berdichevsky and Dmitriev (2008) give a more profound treatment about theoretical aspects involved in the GDS method. The following concise introduction is mostly based on these books.

2.2.1 Electromagnetic induction in the earth

In the MT and GDS methods, it is assumed that electromagnetic fields variations observed at surface are a sum of: (i) natural external (inducing) magnetic fields generated by processes that take place above the surface of the earth (see subsection 2.2.2), (ii) natural internal electromagnetic fields induced in the earth's subsurface by the external fields, and (iii) electromagnetic noise generated by artificial sources (e.g. cultural activity). The phenomenon of electromagnetic induction which relates the observed natural fields can be described using Maxwell's equations :

$$\nabla \times \mathbf{E} = -\frac{\partial \mathbf{B}}{\partial t} \tag{2.4}$$

$$\nabla \times \mathbf{H} = \mathbf{J} + \frac{\partial \mathbf{D}}{\partial t} \tag{2.5}$$

$$\nabla \cdot \mathbf{B} = 0 \tag{2.6}$$

$$\nabla \cdot \mathbf{D} = Q_V \tag{2.7}$$

where $\mathbf{E}$ is the electric field [V/m], $\mathbf{B}$ is the magnetic induction [nT], $\mathbf{H}$ is the magnetic intensity [A/m], $\mathbf{J}$ is the electric current density [A/m^2], $\mathbf{D}$ is the electric displacement [C/m^2], and Q_V is the electric charge density [C/m^3].

Following Faraday's law of induction (eq. 2.4), time-varying external magnetic fields induce an electric field within the earth's subsurface. This induced electric field drives electric currents, which will have an associated magnetic field according to Ampère's law (2.5). Applying Ohm's law (eq. 2.8)

$$\mathbf{J} = \sigma \mathbf{E} \tag{2.8}$$

the Ampère's law shows that the magnitude of the induced magnetic field will be proportional to the electrical conductivity (σ) of the medium in which the induced currents flow (eq. 2.9). Therefore, the amplitude of the induced fields is dependent on the properties of the external fields and on the conductivity of underground materials.

$$\nabla \times \mathbf{H} = \sigma \mathbf{E} + \frac{\partial \mathbf{D}}{\partial t} \tag{2.9}$$

2.2.2 Natural external magnetic source fields

For the EM fields variations studied in this thesis (period range of 10 - 10,000 s), the natural external magnetic source fields observed at surface are generated by a variety of phenomena that take place in the

ionosphere and the magnetosphere. The magnitude of these fields generally represent a small fraction of the amplitude of the Earth's magnetic main field. Four main mechanisms are thought to be responsible of the external magnetic fields observed in the studied period range (see for example Kaufman and Keller, 1981; Viljanen, 2012):

- **Geomagnetic pulsations:** For the period band between 1 - 1000 s, the natural sources are oscillations in the earth's magnetic field called geomagnetic pulsations or Ultra Low Frequency (ULF) waves. Pulsations observed at surface are waves produced by complex magnetohydrodinamic processes resulting from interactions between the solar wind, different regions of the magnetosphere and the ionosphere (e.g. McPherron, 2005). Pulsations are classified based on their character (continuous or with quasi-periodic waveform, and irregular) and on their period range.

- **Electrojets:** Electrojets are current systems that flow in the ionosphere. The equatorial electrojet (EEJ) is an eastward current system located in the day-side equatorial ionospheric region (approximately at altitudes between 90 and 130 km). The EEJ would explain abnormally large daily variations observed in the north magnetic component at low geomagnetic latitudes (e.g. Forbes, 1981). For regions located $\pm$1000 km around the geomagnetic dip Equator (like northern Chile), magnetic variations in a period range of 10 s to 3 hours ($\sim$10,000 s) can be influenced by the equatorial electrojet (EEJ) (Stoerzel, 1996). Friedel (1997) suggested that the EEJ does not affect MT measurements in northern Chile at $\sim$20°S (i.e. northern part of the IPOC array), after analysing MT data collected at four stations located at this latitude in the Precordillera. Friedel (1997) observed that MT responses calculated from data collected during night (when the EEJ is not active) do not differ from MT responses obtained from daytime intervals (which could possibly be affected by the influence of the EEJ), at least for a period range of 10-1000 s. However, Brändlein et al. (2012) described that some MT responses at IPOC sites show significant variations between daytime and night data for a period range of 100-1000 s, but they suggested that such variations where caused by the interplanetary electric field.

- **Magnetospheric ring current:** the ring current system flows westward in the magnetosphere, roughly around the magnetic equator at an altitude of 10,000 to 60,000 km. This current system is generated by movement of electrons and ions along the Earth's magnetic field. These particles are injected from the solar wind into the magnetosphere. An enhancement in the ejection of solar particles, therefore, causes an increment in the amount of electrons and ions which is injected into the magnetosphere, resulting in an enhancement in the ring current. As the ring current generates a magnetic field which opposes the predominant component of the Earth's main magnetic field observed at equatorial regions, an enhancement in the ring current results in a decrease in the intensity of the magnetic field. This mechanism would explain the sudden decrease in the intensity of the magnetic field which is observed during the initial phase of magnetic storms (e.g. Daglis et al., 1999). Magnetic storms generate magnetic variations in a period range of $\sim$10 seconds to several hours (Constable, 2016).

- **Daily variations:** For periods between 3 hours and 24 hours ($\sim$10,000 - 100,000 s), dominant EM variations during days of low geomagnetic activity are caused by the Solar quiet (Sq) current

system located in the ionosphere (approximately 100-140 km above the earth surface). This current system is generated by movements of the ionospheric plasma and variations in the ionospheric conductivity as a consequence of thermal gradients. Such thermal gradients in the ionosphere are caused by differential exposition to the solar heating (e.g. Viljanen, 2012). The Sq current system can be modelled as two current vortices in the dayside hemisphere, centred at latitudes $\sim$30° N and $\sim$35° S (e.g. Matsushita and Maeda, 1965). Takeda (1997) suggested that Sq magnetic fields variations can also affect MT responses at a period of $\sim$2000 s.

2.2.3 Assumptions of the MT and GDS methods

The following assumptions are considered for the MT and GDS methods:

1. The constitutive relationships for linear, isotropic and homogeneous materials: $\mathbf{D} = \epsilon\mathbf{E}$ and $\mathbf{B} = \mu\mathbf{H}$, where ϵ is the electrical permittivity [F/m], and μ is the magnetic permeability [H/m].
2. The electrical permittivity and magnetic permeability are approximated by vacuum's values (ϵ_0 = 8.85 x 10^{-12} F/m and μ_0 = 1.2566 x 10^{-6} H/m, respectively).
3. For the sounding periods employed in these methods, displacement currents are neglible compared to conduction currents (i.e. $\frac{\partial \mathbf{D}}{\partial t} \rightarrow 0$ in (2.9)).
4. Free charges are not accumulated (i.e. $\nabla \cdot \mathbf{D} = 0$ in (2.7)).
5. External electromagnetic fields propagate as a homogeneous and normal incident plane wave over the induction region (the *plane wave assumption*). Generally, practitioners assume that the plane wave assumption is valid at mid-latitude regions for periods shorter than 10,000 s (e.g. Simpson and Bahr, 2005; Shimizu et al., 2011).
6. There are no electromagnetic sources inside the earth.
7. Electromagnetic waves have harmonic time dependence (i.e. $exp^{i\omega t}$, where $\omega = 2\pi/\tau$, and $\tau \equiv$ period of the wave [s])

By applying assumptions 1-3, equation (2.9) can be written as:

$$\nabla \times \mathbf{B} = \mu\sigma\mathbf{E} \tag{2.10}$$

For a resistivity distribution that varies only in the vertical direction (1-D case), considering the assumption 4 and using the vectorial identity $\nabla \times (\nabla \times \mathbf{F}) = (\nabla \cdot \nabla \cdot \mathbf{F}) - \nabla^2\mathbf{F}$, it can be derived from (2.4) and (2.10) that the time-varying electric fields satisfy a diffusion equation of the form:

$$\nabla^2\mathbf{F} = \mu_0\sigma\frac{\partial \mathbf{F}}{\partial t} \tag{2.11}$$

Taking into account assumptions 5-7, eq. (2.11) can be solved by the function:

$$\mathbf{F} = F_0 exp^{(i\omega t)-kz} \tag{2.12}$$

Where $\mathbf{F} = \mathbf{E}$ or $\mathbf{B}$, and $k = \sqrt{i\omega\mu_0\sigma}$ is the complex wave number.

2.2.4 Induction in a homogeneous half space

Two important concepts in electromagnetic induction methods can be illustrated by considering the case of a homogeneous half space of resistivity ρ_h (= $1/\sigma_h$):

- The *skin depth* (δ [m]) or penetration depth of an electromagnetic wave with period τ is defined as the inverse of the real part of the complex wave number (2.13). It represents the depth at which the amplitude of the wave is $1/e$ of the amplitude observed at the surface.

$$\delta(\tau) = \sqrt{\frac{\rho_h \tau}{\pi\mu_0}} \tag{2.13}$$

  where τ is the period of the wave [seconds]. The skin depth in a homogeneous half space can be approximated by $\delta(\tau) \sim \frac{1}{2}\sqrt{\rho_h \tau}$ [km].

- By considering ratios between measured electromagnetic fields at surface, it is possible to gain information about the subsurface resistivity structure, independently of the intensity of the external fields. For example, the resistivity of the half space can be calculated from the ratio between orthogonal horizontal electric and magnetic fields, and their period:

$$(2.4) \Leftrightarrow \frac{\partial E_x}{\partial z} = -\frac{\partial B_y}{\partial t}$$

$$(2.12) \Rightarrow -kE_x = -\frac{i2\pi}{\tau} B_y$$

$$\Rightarrow \frac{E_x}{B_y} = \frac{i2\pi}{k\tau} = \sqrt{\frac{i2\pi\rho_h}{\mu_0\tau}}$$

2.2.5 Electromagnetic transfer functions

Maxwell equations show that, in the frequency domain, input (inducing fields) and output (induced fields) signals are linked by linear relationships (see e.g. Weidelt and Chave, 2012). In EM methods, such linear relationships are described by the electromagnetic transfer functions (TFs).

Magnetotelluric transfer function

The magnetotelluric transfer function ($\underline{\mathbf{Z}}$) is a complex 2 x 2 tensor that relates the horizontal components of magnetic and electric fields observed at one site (2.14). This linear relationship is valid if the horizontal

components of the primary field vary slowly over the induction region (Wait, 1954; Price, 1962).

$$\begin{pmatrix} E_x(\tau) \\ E_y(\tau) \end{pmatrix} = \begin{pmatrix} Z_{xx}(\tau) & Z_{xy}(\tau) \\ Z_{yx}(\tau) & Z_{yy}(\tau) \end{pmatrix} \begin{pmatrix} B_x(\tau) \\ B_y(\tau) \end{pmatrix} \tag{2.14}$$

Where x and y are normally the north-south and east-west geomagnetic directions, respectively; E_i and B_j (i,j=x, y) are the orthogonal components of horizontal electric and magnetic field variations respectively; and Z_{ij} [km/s] are the components of the $\underline{\mathbf{Z}}$ tensor. Note that some authors calculate the $\underline{\mathbf{Z}}$ tensor using $\mathbf{H}$ instead of $\mathbf{B}$, which results in Z components with units of impedance [Ω]. Usually MT results are displayed as apparent resistivity (ρ_a [Ωm], (2.15)) and impedance phase (ϕ [degrees], (2.16)), which are functions of $\underline{\mathbf{Z}}$ components.

$$\rho_{a,ij}(\tau) = \frac{\tau}{\mu_0} \| Z_{ij}(\tau) \|^2 \tag{2.15}$$

$$\phi_{ij}(\tau) = \arctan\left(\frac{Im\{Z_{ij}(\tau)\}}{Re\{Z_{ij}(\tau)\}} \right) \tag{2.16}$$

For a half-space with homogeneous and isotropic resistivity, the apparent resistivity is equal to the actual resistivity of the medium.

Components of $\underline{\mathbf{Z}}$ and apparent resistivity can be affected by a phenomenon called *galvanic distortion*. This effect is relevant when measured electric fields include significant contributions of non-inductive secondary fields, which are generated by accumulation of charges at high resistivity contrasts located very close to the point of measurement (e.g. Jiracek, 1990). Another alternative representation of $\underline{\mathbf{Z}}$ components is the non-dimensional phase tensor ($\underline{\mathbf{\Phi}}$, (2.17)). Unlike $\underline{\mathbf{Z}}$ and apparent resistivity, the phase tensor is not affected by galvanic distortion (Caldwell et al., 2004).

$$\underline{\mathbf{\Phi}}(\tau) = \begin{pmatrix} \Phi_{xx}(\tau) & \Phi_{xy}(\tau) \\ \Phi_{yx}(\tau) & \Phi_{yy}(\tau) \end{pmatrix} = [Real(\underline{\mathbf{Z}})]^{-1}[Imag(\underline{\mathbf{Z}})] \tag{2.17}$$

In addition, the phase tensor is characterized by rotational invariants, whose properties can give information about the dimensionality of the resistivity structure (Caldwell et al., 2004). For example, the phase tensor skew angle β (2.18) is zero in 1-D and 2-D environments.

$$\beta(\tau) = \frac{1}{2} \arctan\left(\frac{\Phi_{xy}(\tau) - \Phi_{yx}(\tau)}{\Phi_{xx}(\tau) + \Phi_{yy}(\tau)} \right) \tag{2.18}$$

Vertical magnetic transfer function

The vertical magnetic transfer function (VTF, sometimes called "tipper") is a non-dimensional complex 2 x 1 vector that relates the horizontal and vertical magnetic field components observed at one site (2.19). If the plane wave assumption is fulfilled, the relationship between horizontal and vertical components of magnetic field variations can be obtained at a point of observation by (e.g. Everett and Hyndman, 1967):

$$B_z(\tau) = \begin{pmatrix} T_x(\tau) & T_y(\tau) \end{pmatrix} \begin{pmatrix} B_x(\tau) \\ B_y(\tau) \end{pmatrix} \tag{2.19}$$

Where B_x, B_y, B_z are the orthogonal components of magnetic field variations, and $\mathbf{T} = (T_x\, T_y)$ is the Vertical Magnetic TF. When the plane wave assumption is fulfilled, non-zero time-varying vertical magnetic fields can only be observed at surface if the underground's resistivity exhibits spatial variations within the induction volume. Therefore, VTF are diagnostic of lateral contrasts in resistivity, and commonly are represented as *induction vectors* (2.20). In map view, the length and direction of the induction vectors depend on the size and geometry of resistivity contrasts. In the convention employed in this thesis (the Wiese convention, Wiese, 1962), the real induction vectors point away from the low resistive side of a resistivity contrast.

$$\text{Real Induction vector} = Real(T_x)\hat{x} + Real(T_y)\hat{y} \tag{2.20}$$

Horizontal magnetic transfer function

The horizontal magnetic TF (HTF, sometimes called "inter-station transfer function") is a non-dimensional complex 2 x 2 tensor that relates the horizontal magnetic field variations measured at two different sites (2.21):

$$\begin{pmatrix} B_x^{site1}(\tau) \\ B_y^{site1}(\tau) \end{pmatrix} = \begin{pmatrix} M_{xx}(\tau) & M_{xy}(\tau) \\ M_{yx}(\tau) & M_{yy}(\tau) \end{pmatrix} \begin{pmatrix} B_x^{site2}(\tau) \\ B_y^{site2}(\tau) \end{pmatrix} \tag{2.21}$$

Where B_x^{site1}, B_y^{site1} and B_x^{site2}, B_y^{site2} are the orthogonal horizontal components of magnetic field variations at sites 1 and 2, respectively; and M_{ij} are the elements of the Horizontal Magnetic TF tensor ($\underline{\mathbf{M}}$). In absence of lateral resistivity contrasts, and if the source magnetic field incident at both sites is exactly uniform, the horizontal magnetic components observed at both sites should be the same, resulting in $\underline{\mathbf{M}}$ equals to the identity matrix for all frequencies (Ritter et al., 1998). Lateral contrasts in resistivity generate induced horizontal magnetic fields; therefore under these conditions $\underline{\mathbf{M}}$ is complex and different from the identity matrix (Larsen et al., 1996). However, it is important to remark that HTF is not necessarily related to underground resistivity if the external magnetic field is not homogeneous over the studied sites. Some authors have employed HTF properties to identify the presence of noise in magnetic fields measurements (Ritter et al., 1998; Sokolova and Varentsov, 2005; Muñoz and Ritter, 2013). For example, the *reciprocal criterion* of Sokolova and Varentsov (2005) states that the product of direct and inverse estimates of HTFs between two sites should be close to the identity matrix (2.22), otherwise it

can be interpreted that the magnetic measurements are contaminated by noise:

If $\underline{\mathbf{M}}_{1-2}$ and $\underline{\mathbf{M}}_{2-1}$ are the direct and inverse HTF between two sites:

$$\mathbf{B}^{site1} = \underline{\mathbf{M}}_{1-2}\mathbf{B}^{site2} \text{ and } \mathbf{B}^{site2} = \underline{\mathbf{M}}_{2-1}\mathbf{B}^{site1}$$

then, since the *reciprocal criterion*, the product between these two HTFs:

$$\underline{\mathbf{M}}_{1-2}\,\underline{\mathbf{M}}_{2-1} = \mathbf{R} = \begin{pmatrix} R_{11} & R_{12} \\ R_{21} & R_{22} \end{pmatrix} \longrightarrow \begin{pmatrix} 1 & 0 \\ 0 & 1 \end{pmatrix} \tag{2.22}$$

2.2.6 Estimation of transfer functions

The TFs define bivariate linear equations between input and output signals like:

$$z = ax + by \tag{2.23}$$

where z=output signal; a,b = TFs components; x,y =input signals. To estimate the components of any TF matrix, the difference between the observed output signal and the predicted response is minimized with respect to the TF components (2.24).

$$\min_{a,b}\{\delta z^2\} = \{(observed - predicted)^2\} = \{(z - (ax + by))^2\} \tag{2.24}$$

Using the linear least square method, the TFs that minimize 2.24 are given by (e.g. Simpson and Bahr, 2005):

$$a = \frac{\langle zx^*\rangle\langle yy^*\rangle - \langle zy^*\rangle\langle yx^*\rangle}{\langle xx^*\rangle\langle yy^*\rangle - \langle xy^*\rangle^2} \tag{2.25}$$

$$b = \frac{\langle zy^*\rangle\langle xx^*\rangle - \langle zx^*\rangle\langle xy^*\rangle}{\langle xx^*\rangle\langle yy^*\rangle - \langle xy^*\rangle^2} \tag{2.26}$$

where

$$\langle ij^*\rangle = \sum_{k=1}^{N} i_k j_k^* \equiv \text{power spectra between signals } i \text{ and } j(i, j = x, y, z);$$

$i^* \equiv$ complex conjugate value of i; and $N \equiv$ number of samples

Roughly, TFs are computed by: (i) obtaining the Fourier transform of time series with electromagnetic measurements, (ii) calculating the power spectra between Fourier transformed signals, and (iii) replacing the power spectral terms into the eq. (2.25) and (2.26). The confidence interval (uncertainty) of the TFs estimates can be obtained by different methods. One method is based on assuming that the data follow some statistical distribution, and therefore the uncertainty of the TF estimate is calculated as some estimator associated to the assumed statistical model (see e.g. Weckmann et al., 2005). Other option is the use of non-parametric methods, which are based on the empirical distribution of the data (discussion about advantages and disadvantages of both methods is found in e.g. Chave, 2012).

2.2.7 Modelling: from transfer functions to the resistivity structure

To estimate the spatial distribution of resistivity values which can explain the observed data (transfer functions), forward or inverse modelling can be applied. In forward modelling, the propagation of EM waves within a model of the earth are simulated using numerical approximations which depend on the distribution of resistivity within the model. Following this procedure, the spatial distribution of EM fields are calculated, which allow to compute transfer functions (model responses) at any position of the model (e.g. at the equivalent location of measurements). Inversion modelling is an iterative process, which searches for a model of resistivity distribution that generates responses closer to some target data (e.g. transfer functions computed from measured field data). At each iteration, the response of the model is calculated using the forward modelling approach, and then compared with the target data.

In this thesis, I modelled the MT data using the ModEM program (Egbert and Kelbert, 2012), parallelized using the scheme of Meqbel (2009). ModEM has a modular structure, which allows to invert different types of electromagnetic EM data, and also to perform the inversion processes by using different methods. I used a version of ModEM that applies: the finite differences method to solve numerically Maxwell's equations, and the non-linear conjugate gradients (NLCG) algorithm to solve the minimization problem involved in the inversion process. The following description of the ModEM's basic characteristics is based on Egbert et al. (2011), Egbert and Kelbert (2012), and Kelbert et al. (2014).

To obtain a model of resistivity distribution ($\mathbf{m}$) that can explain adequately the data ($\mathbf{d}$, transfer functions), ModEM minimizes an objective function with respect to the model parameters. The objective function ($\mathbf{\Psi}$) comprises two terms (see (2.27)): a measure of the data misfit (i.e. the disagreement between data and model's response) and a regularization term. Considering that the inversion problem may has non-unique solutions, the regularization term is added in order to reduce the number of possible models that can explain the data and to stabilize the inversion process.

$$\mathbf{\Psi}(\mathbf{m},\mathbf{d}) = \underbrace{(\mathbf{d}-f(\mathbf{m}))^T\mathbf{C}_\mathbf{d}^{-1}(\mathbf{d}-f(\mathbf{m}))}_{\text{data misfit}} + \underbrace{\lambda(\mathbf{m}-\mathbf{m}_0)^T\mathbf{C}_\mathbf{m}^{-1}(\mathbf{m}-\mathbf{m}_0)}_{\text{regularization term}} \tag{2.27}$$

In which $f(\mathbf{m})$ is the forward response of the model (transfer functions), $\mathbf{C_d}$ is the covariance of data errors, λ is a trade-off parameter, $\mathbf{m}_0$ is the prior model, and $\mathbf{C_m}$ is the model covariance. The covariance matrix $\mathbf{C_d}$ contains the inverse of the squared data errors, therefore the calculation of the misfit (and the evolution of the inversion process) depend on the magnitude of the data errors considered. Instead of using the statistical errors obtained for each TF estimate during the data processing, practitioners normally use as data errors in the inversion process some arbitrary values which weight the importance of each TF component on the target data misfit. The regularization term forces the inversion to obtain models that: (i) are smooth (i.e. in which the transition between resistivity structures vary smoothly), and (ii) are as close as possible to the prior model $\mathbf{m}_0$ (but still fitting the data). The trade-off parameter λ controls the contribution of the regularization term to the objective function. The value of λ decreases during the inversion, and is determined by an automatic criterion that depends on the evolution of the

convergence process. The model covariance $\mathbf{C_m}$ partly depends on the parameter α (not shown in eq. (2.27)), which controls the model smoothness in each coordinate direction (the larger the values of α, the smoother the model resulting from the inversion is).

To search for a minimum of the objective function $\mathbf{\Psi}$, at each iteration the NLCG algorithm performs two steps. In the first step, the algorithm calculates the gradient of $\mathbf{\Psi}$ with respect to variations in $\mathbf{m}$, in order to determine a search direction (i.e. the local direction in which $\mathbf{\Psi}$ decreases most quickly). In the second step, the algorithm determines a search step size that reduces $\mathbf{\Psi}$ along the search direction by an expected value, in order to find a local minimum of $\mathbf{\Psi}$ along the search direction. This procedure is repeated until the inversion reaches one of the following predefined stopping criteria: the minimum data misfit, the minimum λ, or the maximum number of iterations.

From the above mentioned parameters, in ModEM the user must provide: the data ($\mathbf{d}$) and data errors, the prior model ($\mathbf{m}_0$), the initial λ, the value to update λ during the inversion, the stopping criteria (i.e. the minimum λ, the minimum data misfit, and the maximum number of iterations), the initial search step size, and the expected value in which λ is reduced during the line search. Additionally, the user can define the value of α, and the regions of the model in which the smoothing conditions are applied. In ModEM the data misfit is calculated using the global Root Mean Square (RMS) value:

$$RMS = \sqrt{\frac{1}{N}\sum_{k=1}^{N}\left(\frac{d_{obs,k} - d_{mod,k}}{e_k}\right)^2} \tag{2.28}$$

where N is the number of all data (TFs) points, $d_{obs,k}$ is the observed data, $d_{mod,k}$ is the calculated data (model response), and e_k is the data error.

Chapter 3

The IPOC Magnetotelluric array

In this chapter the location and instrumentation of the IPOC MT array is presented (section 3.1), the quality of the measured data is discussed (section 3.2), and the processing scheme employed to calculate the MT responses (transfer functions) is described (section 3.3). Section 3.4 presents an analysis of the major patterns observed in transfer functions across the array and a comparison of these patterns with results obtained by previous studies. Finally, section 3.4 also contains a characterization of the temporal variations observed in the IPOC transfer functions from January 2011 to January 2015. The further analyses do not consider the data from sites A01 and PB11, which were not available when writing this thesis.

3.1 Location and instrumentation

The MT IPOC array currently comprises 11 stations, distributed in an area of approx. 400 km x 100 km, with an average distance of 50 km between sites (see Table 3.1). At each MT station, the instruments are oriented using a geomagnetic coordinate system: the X-axis points towards the geomagnetic north, the Y-axis points towards the geomagnetic east, and the Z-axis is positive downwards. EM measurements are carried out at all stations using the following instrumentation:

- Magnetic fields are measured using Geomagnet three-component fluxgate magnetometers.
- The horizontal components of the electric field are measured with non-polarizing Ag/AgCl telluric electrodes (manufactured by the GFZ German Research Centre for Geosciences) and using CASTLE sensor boxes as signal preconditioners. Electrodes are deployed using different dipole configurations (see Table 3.1). Electrodes are installed inside vertical plastic tubes which contain moist bentonite at the contact with the ground. The moist bentonite helps to reduce the contact resistance. In order to avoid the loss of humidity due to evaporation (Brändlein, 2013), the top of the plastic tubes are covered with lids. Electrodes and sensor boxes are connected via coaxial cables, which contain an external metallic shield grounded at the center of the electrode layout. Signals are amplified at the CASTLE sensor boxes by factors of 4 or 10, depending on the signal

amplitude observed at each station.

- The signals of all electromagnetic fields are continuously sampled at a rate of 20 Hz using Earth Data Logger system (EDL) devices. The data are stored on the EDL disk. At sites where satellite transmission is available (i.e. all except A01 and PB11), the data from the EDL are copied via a parallel cable to a computer, which transmits the data to the satellite.

At all sites, additional electronic instruments are installed (e.g. seismometers, GPS, solar panels). To avoid the influence of possible electromagnetic noise generated by these instruments, magnetometers and electrodes were installed at a distance of at least 20 m from any other equipment. To minimize the influence of temperature fluctuations, all sensors and cables are buried at least 30 cm underground.

Table 3.1: Characteristics of IPOC MT sites (location, installation date, length and configuration of electrodes dipoles).

Station	Latitude	Longitude	Elevation (masl)	Starting date	Ex length (m)	Ey length (m)	Dipole configuration
PB01	-21.0432	-69.4874	900	02.05.2007	80.3	81.4	L
PB02	-21.3197	-69.896	1015	03.05.2007	80.9	84.8	T
PB03	-22.0476	-69.7533	1460	07.03.2007	80.4	71.5	L
PB04	-22.3335	-70.1494	1530	10.03.2007	100	101.3	L
PB05	-22.8527	-70.2023	1150	09.03.2007	80	81.3	T
PB06	-22.7058	-69.5717	1440	08.03.2007	79.3	80.8	L
PB07	-21.7266	-69.8861	1560	06.03.2007	81.3	80.5	L
PB09	-21.7964	-69.2419	1530	22.04.2010	80.8	80	L
PB11	-19.761	-69.6558	1410	08.10.2014	99.3	99.7	L
PB15	-23.2083	-69.4709	1830	04.08.2011	80.8	80.7	cross
A01	-20.7636	-69.8887	980	06.10.2014	100.3	99.8	L

3.2 Time series quality

Generally speaking, observed magnetic time series at IPOC sites are stable. Evident problems have been identified only at some sites, but these intervals do not exceed more than a couple of weeks. The most relevant case is a time interval (March 2012 - November 2013) in which channels B_x and B_z at site PB05 were not recorded. This data gap was probably caused by problems in the communication between the magnetometer sensor box and the EDL data-logger.

One of the most challenging problems in MT monitoring is the reliability of electric field time series. Electric field measurements are highly sensitive to instrumental and environmental conditions that are difficult to control, namely contact resistance between the electrode and the soil, and electrochemical reactions within the electrode and at the contact interface (see e.g. Ferguson, 2012). Good electrode contact to the ground is particularly difficult at the extremely arid region of northern Chile, because usually electrolyte leaks and contact resistances are high (in the order of 10^5 Ω). During the first years of the IPOC MT array, different electrode configurations were tested in order to obtain stable electric recordings. A stable electrode configuration is used since January 2011 (Brändlein, 2013), which allows to have approximately four years of continuous electric measurements when writing this thesis. Between

years 2007 and 2010, reliable electric field time series could only be obtained in a few time-limited intervals ($<$ 1 month), which normally occurred after sites were serviced.

To obtain a first order estimation of the long-term stability of electric field records, and to identify problems in measurements, the statistics of each daily time series were examined. Although these statistical estimates are also influenced by processes not related to the stability of electrodes (e.g. transient signals related to natural or cultural sources, long-term electronic drift of amplifiers and data loggers), at least they provide a general idea of the temporal behaviour of the DC level present in the electric measurements. In addition, it is observed that days which exhibit evidence of electrode instability (e.g. jumps in the base level of the time series) are normally characterized by daily averages values that represent outliers in the 4-years statistics. Here it is analysed the 20 Hz sampled rate time series obtained from the EDL data logger, which were corrected by the amplifiers' gains. For the electric channels, these values represent time series of potential difference displayed in their correct physical units. Figure 3.1 show the temporal variation of daily mean and standard deviation of potential difference time series for two exemplary sites. Most of the sites show electric time series that follow a quasilinear long-term drift; more curvy long-term drifts are observed at some sites, in which instrumental problems were identified during service trips. For example, Figure 3.1 shows outlier values of E_x at PB05 in middle 2014 and E_y at PB15 in middle 2013, which can be explained by problems in electrodes found at both sites afterwards (the southern electrode was broken at PB05, while the eastern electrode had dried out at PB15).

Between the service trips of November 2013 and October 2014, daily mean potential differences observed at most of the sites exhibit variations $<$50 mV (see e.g. Figure 3.1), a value which can be interpreted as an estimate of the average annual drift. Previous long-term electric measurements have reported drift in a range between 0.2 and 300 mV per year (e.g. Petiau and Dupis, 1980; Lanzerotti et al., 1993; Perrier et al., 1997; Benz et al., 2012). Although none of these studies were carried out under physical conditions comparable to those observed in the arid environment of northern Chile, it can be said that the annual drift of IPOC electric measurements is within the range of long-term electric measurements found in the literature.

Evident noise patterns observed in time series are periodical and semi-periodical pulses and bursts, which are probably generated by instruments installed at the IPOC stations. Figure 3.2 shows an example of noise patterns related to IPOC instruments. The occurrence of high amplitude pulses observed in electric fields coincides with intervals when the EDL datalogger copies the data from its internal memory to the backup disk. During this operation the EDL requires additional energy from the battery installed at the site, which results in the generation of electrical signals. These pulses are transmitted to the earth via the electrical ground of the station. Due to the highly resistive background at this site, these pulses are not sufficiently attenuated at the place where the electrodes are installed, and therefore these signals are sensed by the electrodes. However, the influence of these noisy signals in the transfer function quality is not relevant, because they are filtered during the processing (compare Figure 3.2a and 3.2b). For example, most of the observed periodical noise patterns have a characteristic period $\leq$1 s, which are not included in the studied period band. Moreover, the observed bursts and pulses normally affect only the electric time series, consequently they represent incoherent noise that is removed by the processing. In

most of the cases, days that exhibit the aforementioned problems are characterized by transfer functions estimates with large confidence intervals (i.e. large error bars). Therefore, intervals of bad data can be identified, and eventually be removed, by examining the statistical error of transfer functions daily estimates.

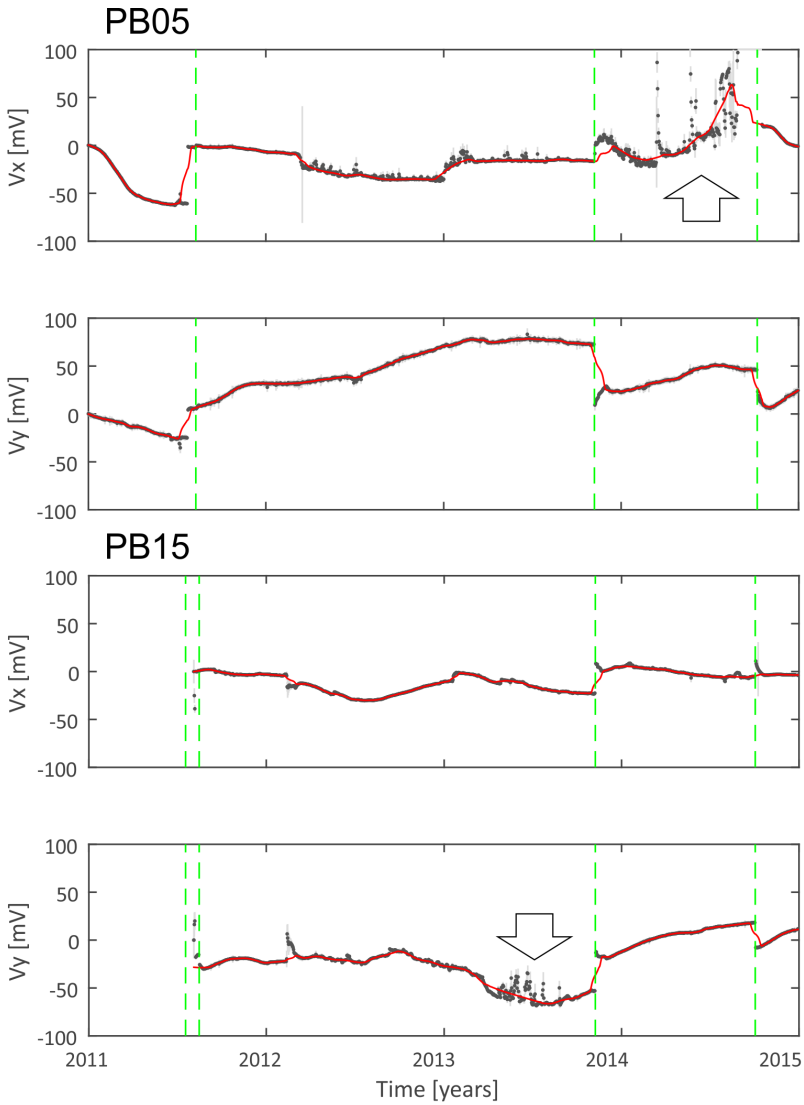

Figure 3.1: Time series showing the long-term behaviour (from January 2011 to December 2015) of electric field measurements at sites PB05 and PB15. Y-axes indicate potential differences along dipoles (Vx = north-south dipole, Vy = east-west dipole). Each black point represents the mean of all potential differences measured during one day, while grey bars are standard deviations associated to each day. Red lines are 30-days moving average of the time series. All values are normalized by the mean value obtained at the first day of the time series. Dashed-green vertical lines represent days when the site was serviced. Arrows indicate intervals with outlier mean daily values. In service trips following these intervals, problems in some electrodes were found at these sites (see the text for details).

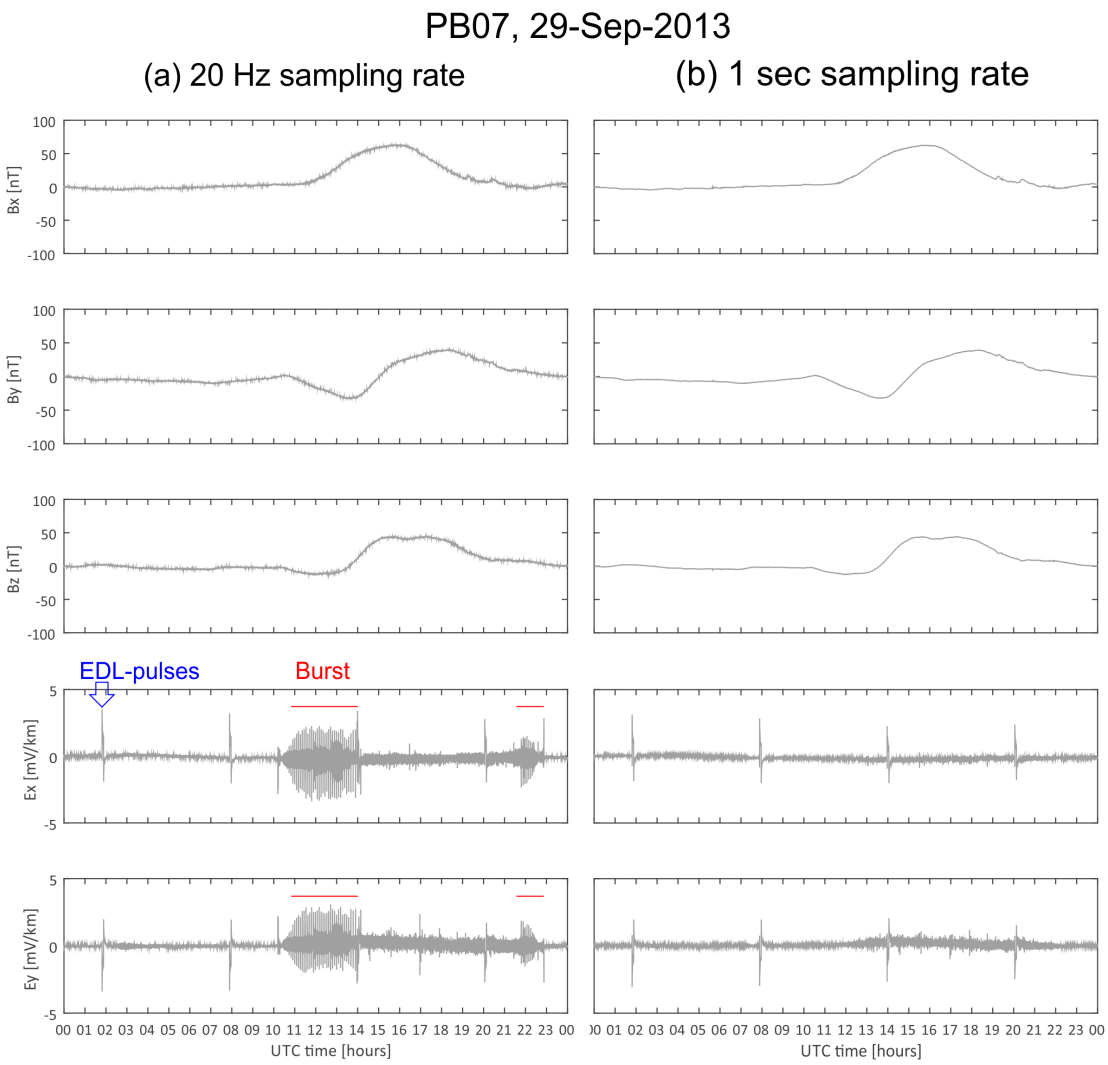

Figure 3.2: Electromagnetic fields time series from 29-September-2013 at site PB07, containing noise patterns (pulses and bursts). (a) original (20 Hz-sampling rate) and (b) 4 s low-pass filtered (sampling rate of 1 s) time series. Note that noise burst between 11:00 and 14:00 in the original time series disappears after filtering. The occurrence of high amplitude pulses observed in electric fields coincides with intervals when the EDL datalogger copies the data from its internal memory to the disk (see the text for more detailed explanation).

3.3 Data processing

The records of electric and magnetic field variations are transmitted via satellite from each station to a data server located at the GFZ-Potsdam, almost in real time. These data are decoded, downloaded and archived on a daily basis to a data repository administrated by the GFZ. Using the EMERALD robust processing package (Ritter et al., 1998; Weckmann et al., 2005; Krings, 2007), the following transfer functions are computed and stored in the data repository: MT transfer function ($\underline{\mathbf{Z}}$), apparent resistivity, phase, vertical magnetic transfer function (VTF) and horizontal magnetic transfer function (HTF). The data processing with the EMERALD package comprises the following general steps:

1. Output data from the EDL data loggers are read and converted to the EMERALD time series file format. When remote-reference technique (Gamble et al., 1979) is applied, time series of local and remote site are subsequently synchronized.

2. Time series are band-pass filtered into narrow period bands following a cascade decimation scheme. The band-passed time series are subsequently divided into short adjacent windows with a fixed number of samples (normally 128 samples).

3. The short windows are multiplied by a cosine taper function (to ensure that the time series vanishes at the windows' margins), and then they are Fourier transformed. These Fourier-transformed segments are called events. The events are divided in frequency sub-bands, centred around evaluation frequencies that are equally distributed on a logarithmic scale.

4. The Fourier coefficients are corrected by the frequency dependent response of the sensors. Actually, only the fluxgate magnetometers have a frequency dependent response; electrodes responses do not depend on frequency.

5. Spectral terms necessary for calculating the transfer functions are computed (see eqs. 2.25 and 2.26). Auto- and cross- spectra between all electromagnetic field components at each sub-band are calculated. Finally, TFs are calculated by stacking the cross- and auto spectra over all time segments (windows). The expressions used for calculating TFs and their confidence intervals are shown in Weckmann et al. (2005). To remove data that can be affected by noise, at this stage it is also possible to select events based on statistical or physical criteria explained in Weckmann et al. (2005). After testing different combination of these criteria on the IPOC data, comparatively better quality TFs are obtained when a coherency criterion with a threshold of 0.9 is applied (see description of this criterion in Weckmann et al., 2005).

6. In order to minimize the influence of outliers (e.g. due to noise), the EMERALD package applies methods based on robust statistics in the stacking process (described in Ritter, 1995). To obtain statistically robust MT responses for periods $>$1000 s, it is necessary to employ at least a 3-days processing interval, i.e. each TF estimate is obtained using 3 consecutive days of time series data.

3.4 The IPOC transfer functions

In the MT and GDS methods it is assumed that TFs depend only on the resistivity structure of subsurface, if some physical conditions are fulfilled (see subsection 2.2.3). Consequently, any changes observed between TFs obtained at different times are thus related to alterations of the internal resistivity structure. Following this concept, the temporal evolution of the resistivity structure in Northern Chile is monitored by analysing the temporal variations of TFs observed at the IPOC MT sites.

3.4.1 Variability of transfer functions and data quality

Temporal variations and long-term average of TFs were obtained by analysing the basic statistics of all daily estimates of TFs calculated at the IPOC array. This statistical analysis shows that the population of daily estimates of TFs tend to be distributed around their statistical median for most of the TFs and periods studied (see examples in Appendix A.1). The variance around the median depend on the quality of the associated EM field measurements. TFs obtained from poor quality data show larger scatter around their median than TFs obtained from EM measurements with high signal-to-noise ratio (e.g. compare histograms of Z_{yx} and Z_{yy} components, and T_x versus T_y in Appendix A.1).

The signal-to-noise ratio of EM measurements is not only influenced by the effect of noise sources, but also by the strength of the (natural) signals. For example, differences in the signal strength observed in electric field measurements components (the signal strength of E_x is lower than E_y) can be explained by the effect of the high resistivity contrast between the ocean and the continent. Measurements of the ocean resistivity show values in a range of $\sim$0.2 - 0.3 Ωm (e.g. Kapinos et al., 2016), while continental areas are characterized on average by significantly higher resistivities (normally 10 - 10,000 Ωm). To illustrate the effect of this resistivity contrast in the measured EM fields, the coastal region can be approximated by two media with highly contrasting resistivity values and infinitely extended along the X-direction (see Figure 3.3 and Berdichevsky and Dmitriev, 2008). Under these conditions, in the resistive (continental) side the electric field component perpendicular to the interface (E_y) increases when approaching the interface (coast) (see Figure 3.3a), due to galvanic effects related to this resistivity contrast. On the contrary, in the resistive side E_x and B_y tend to decrease when approaching the interface due to induction effects (Figure 3.3b). Therefore, the effect of the ocean-continent resistivity contrast lowers the signal strength of E_x and B_y measured in the continent, which partly explains the low signal-to-noise ratios observed in these components. As a result of this phenomenon, TFs estimates which have a stronger dependence on E_x and B_y show comparatively larger statistical errors and larger variability ranges.

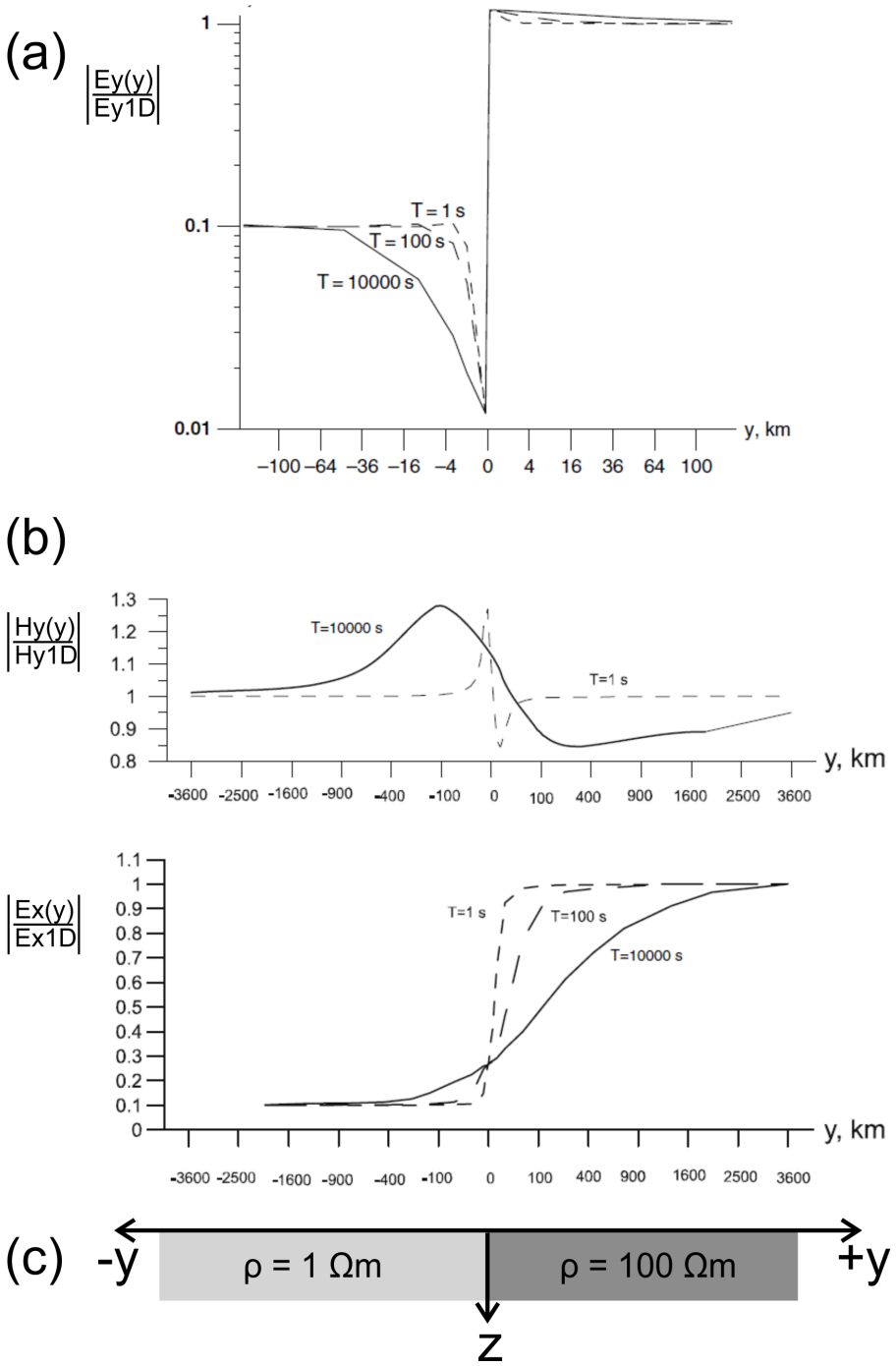

Figure 3.3: Illustration of the ocean effect on EM fields, using the vertical-interface model of Berdichevsky and Dmitriev (2008). (a) E_y and (b) E_x-B_y field variations along a profile perpendicular to the vertical-interface (i.e. parallel to the Y-direction) for different signal periods. (c) The vertical-interface model: two quarter-spaces (1 and 100 Ωm) infinitely extended along the X-direction, separated by a vertical contact (located at Y = 0). Magnitude of EM fields displayed in (a) and (b) are normalized by the value which would be observed in a homogeneous half space of 100 Ωm. Note that vertical and horizontal scales in (a) and (b) are different. Figures (a) and (b) are taken from Berdichevsky and Dmitriev (2008)

3.4.2 Data selection

Daily estimates of TFs at the IPOC array are calculated using single-site (SS) and remote reference processing technique (RR, Gamble et al., 1979). In the further analysis only the RR TFs are considered, because the RR estimates show better quality sounding curves. Site PB01 was employed as reference site, because its magnetic time series exhibit good quality for the studied period band, and this station shows more stable transfer functions. When processing PB01 data, PB09 was employed as reference site, considering its general good data quality. The use of RR improves the quality of $\underline{\mathbf{Z}}$ and VTF estimates, especially in the case of apparent resistivity and phase related to Z_{yy} (see Figure 3.4). In addition, RR sounding curves do not show a drop for periods $<$60 s as single-site processing data do (Figure 3.4). This drop at shorter periods in SS sounding curves is an effect which has been previously described as bias (e.g. Neska, 2006). The use of RR allows also to identify days where long-lasting local noise conditions are present, in which single site processing obtains biased but statistically stable TF estimates (i.e. estimates that have small error bars, but clearly represent outliers).

To avoid the influence of days with noisy measurements, daily estimates of TFs were selected by examining their confidence intervals (statistical errors). Days in which TFs confidence intervals exceeded some threshold values were removed from the analysis. These thresholds (δZ $<$1 [km/s], δT $<$0.02, δM $<$0.02) were empirically chosen, after analysing the statistical distribution and temporal variation of daily estimates of TFs at all sites. The criterion employed to select these values was a qualitative balance between two objectives: to obtain stable long-term TF estimates, and to obtain a significant population of daily estimates. In most of the cases, problems in the time series are observed during days in which the TFs errors exceed the defined thresholds, confirming that these values represent a reasonable selection criterion.

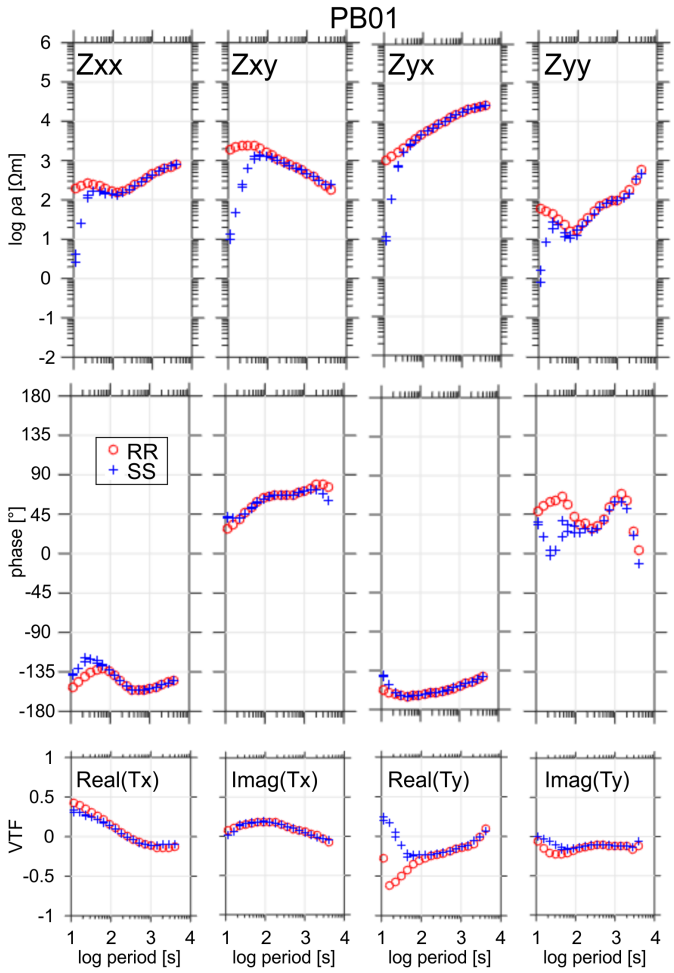

Figure 3.4: Comparison between remote-reference (RR) and single-site (SS) long-term TFs sounding curves for exemplary site PB01. For each period, the displayed value is the median of all daily TF estimates obtained from 2011 to 2015. Daily estimates with confidence intervals exceeding some thresholds (see the text) are not considered for calculating the median value.

3.4.3 Long-term average transfer functions

The population of daily estimates of TFs tend to be distributed around its statistical median (see 3.4.1). These median values define sounding curves which vary smoothly with period, as it is expected for TFs (e.g. Weidelt, 1972). In addition, most of the $\underline{\mathbf{Z}}$ and VTFs median values are consistent with the robust dataset which Brändlein (2013) obtained after processing 150 days of data from the first half of year 2011. Therefore, it is interpreted that the median values of the population of daily estimates represent a long-term average of the TFs. In the following paragraphs, the main patterns observed in the long-term average sounding curves are described, and the reliability of these estimates is discussed.

MT transfer function

Figure 3.5 shows sounding curves for apparent resistivity (ρ_a) and impedance phases (ϕ). The quality of ρ_a and ϕ sounding curves depend on the $\underline{\mathbf{Z}}$ component and the site considered. TFs related to the Z_{yx} component show smoother sounding curves and smaller variance around the long-term median values, because Z_{yx} is associated to the largest electric field component measured at all sites (E_y, see discussion in 3.4.1). On the contrary, smaller signal-to-noise ratio observed in E_x and B_y results in more unstable estimates of Z_{xy} (see related error bars of sounding curves in Appendix A.2). While at all sites ρ_a and ϕ associated to the biggest Z_{yx} component show smooth curves, the Z_{xy} and Z_{xx} components only show smooth curves at sites PB01, PB02, PB05, PB09 and PB15. Low quality Z_{xx} and Z_{xy} sounding curves are obtained at sites characterized by high contact resistance and/or presence of cultural noise sources observed in E_x time series (sites PB03, PB04, PB06 and PB07). TFs associated to Z_{yy} show low quality estimates at almost all sites; exceptionally smooth curves of $\rho_{a,yy}$ and ϕ_{yy} are observed at PB02.

The clearest observed regional pattern is the split of the Z_{xy} and Z_{yx} curves (see Figure 3.5), related to the already mentioned ocean effect. The upwards displacement observed in the $\rho_{a,yx}$ curves relative to $\rho_{a,xy}$ suggests the presence of significant static shift effect at sites PB02, PB03, PB04, PB05 and PB15. Figure 3.6 compiles the long-term median phase tensor skew angle (β) obtained for all sites. At all sites and for most periods, Figure 3.6 shows that β significantly departs from zero, which would indicate the 3-D nature of the resistivity structure (Caldwell et al., 2004). Figure 3.5 shows that ϕ_{xy} sounding curves exceed 90° at sites PB05 (from ∼600 to 1000 s) and PB15 (∼200 to 2000 s), which can also be produced by the presence of a complex 3-D resistivity structure in the subsurface (e.g. Weckmann et al., 2003). Phases over 90° in the Z_{xy} component have been also reported by previous studies in stations located around the Salar Grande, northwest of PB02 (e.g. sites ENG, GER, GLO, PEN and ROJ shown in Lezaeta, 2001; Brasse et al., 2002; Lezaeta and Haak, 2003; Kühn et al., 2014). Consistent with the complex resistivity structure of the Salar Grande region, large values for $\underline{\mathbf{Z}}$ diagonal components are observed at site PB02. Only at site PB09 Z_{xx} and Z_{yy} values are very small for the whole period range (<1 km/s, see Appendix A.2).

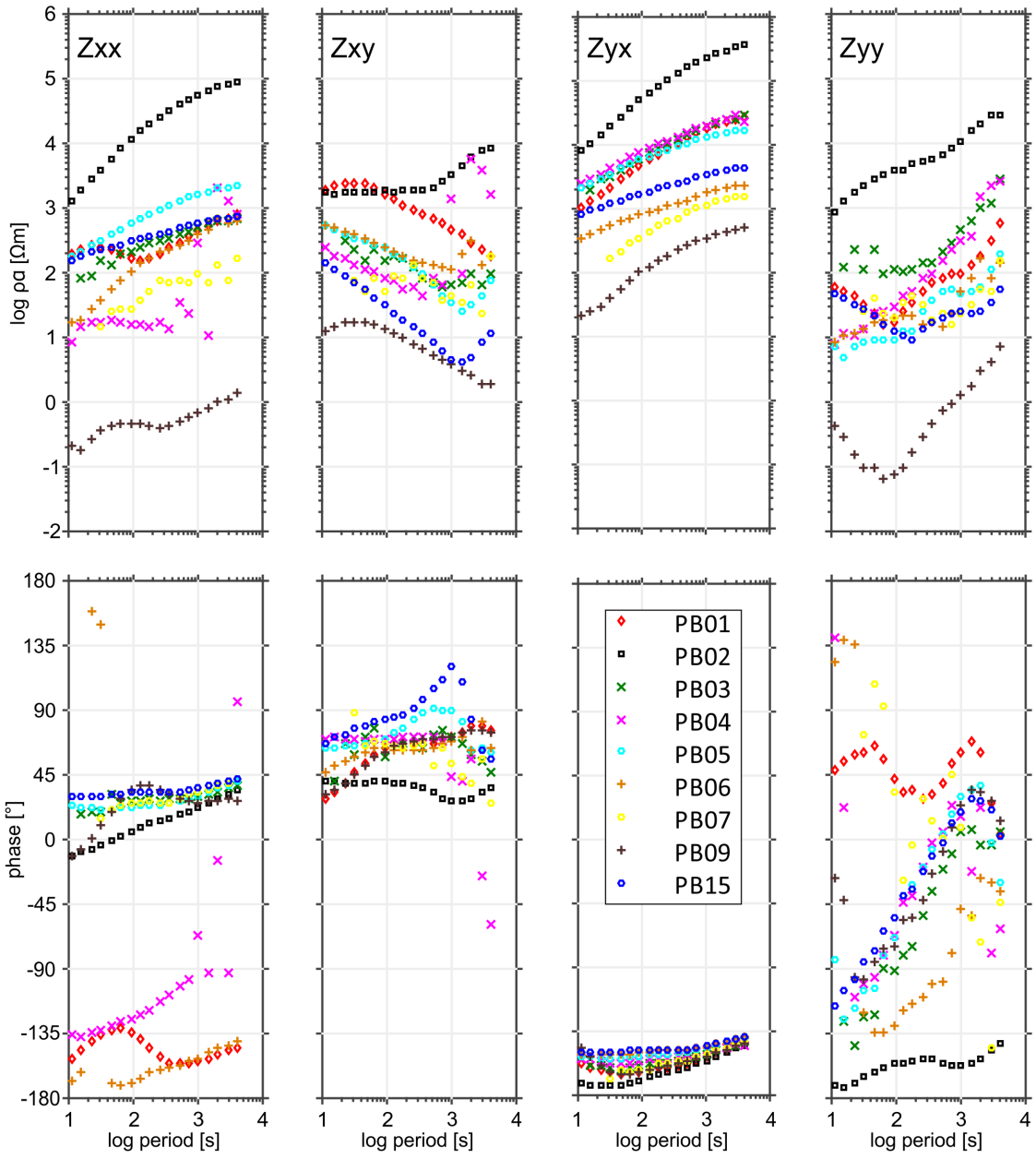

Figure 3.5: Compilation of long-term average apparent resistivity and impedance phase for IPOC sites. For each period, the displayed value is the median of all daily TF estimates obtained from 2011 to 2015. Each daily estimate was calculated using remote reference processing, in which PB01 was employed as remote site (except for PB01, where PB09 was used as remote site). Daily estimates with confidence intervals $\delta Z > 1$ [km/s] were not considered for calculating the median value.

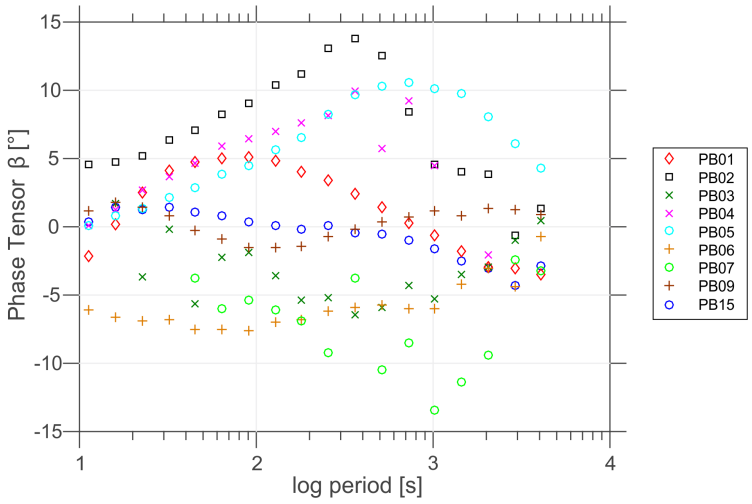

Figure 3.6: Compilation of long-term average phase tensor skew angle β for IPOC sites. For each period, the displayed value is the median of all daily β estimates obtained from 2011 to 2015. Each daily estimate was calculated using remote reference processing, in which PB01 was employed as remote site (except for PB01, where PB09 was used as remote site). Daily estimates with confidence intervals δZ >1 [km/s] were not considered for calculating the median value.

Vertical magnetic transfer function

Figures 3.7 and 3.8 show long-term estimates of VTF for all IPOC sites. Long-term VTF sounding curves are smooth at all sites and for all components. Daily estimates of VTF show smaller variance around their long-term median than **Z** components, which can be explained by the comparatively better quality observed in magnetic measurements. Among the VTF components, daily estimates of T_y show more scatter around the long-term median than T_x estimates, especially at coastal sites and for periods >2000 s (see Appendix A.2). The long term instability of T_y estimates can be explained by its dependency on the B_y component, which shows smaller signal-to-noise ratio than B_x due to the ocean effect (see 3.4.1).

As VTF are sensitive to the size and geometry of resistivity contrasts (when the plane wave assumption is fulfilled), theoretically the high contrast between the ocean and the continent should dominate the behaviour of VTF across the array, unless other significant resistivity contrasts are present in the subsurface. Assuming the dominating effect of the ocean, induction vectors should point away from the coast, which would imply at the IPOC sites to observe positive values of $Real(T_y)$. Induction vectors clearly pointing away from the coast are only observed at sites located closest to the ocean (sites PB04 and PB05 in Figure3.7), which is consistent with the hypothesis of the ocean effect. Other sites located in the Coastal Cordillera (PB02, PB03 and PB07) tend to show positive but small values of $Real(T_y)$ (see Figure 3.8). However, negative values of $Real(T_y)$ observed for most of the period range at some sites located along the Longitudinal Valley (sites PB01 and PB09 in Figure 3.8), would suggest that significant resistivity contrasts are present north-east from the array. The effect of these resistivity contrasts compensate and even exceed the influence of the ocean, as can be inferred from the induction vectors pointing towards the coast at sites PB01 and PB09 (Figure 3.7). A possible source for resistivity contrasts towards the east is the large-scale zone of low resistivity below the Altiplano region, which has been found by several

studies (e.g. Brasse et al., 2002).

The $Real(T_x)$ component exhibits negative values at almost all IPOC sites (Figure 3.8), which explains that induction vectors tend to point towards south in Figure 3.7. Non-zero $Real(T_x)$ components have been systematically described along the Chilean forearc, while $Real(T_x)$ is negative for periods between 10 and 10,000 s at sites in northern Chile (18°S - 23°S, see e.g. Brasse et al., 2002; Brasse and Eydam, 2008; Brändlein, 2013), conversely positive values of $Real(T_x)$ have been reported for periods >1000 s in southern Chile (38°S - 41°S, e.g. Brasse et al., 2009; Kapinos, 2011). It has been suggested that the combined effect of 3-D features and anisotropy present in the resistivity structure may explain the regional character of this trend in $Real(T_x)$ along the Chilean margin (e.g. Kühn et al., 2014; Kapinos et al., 2016).

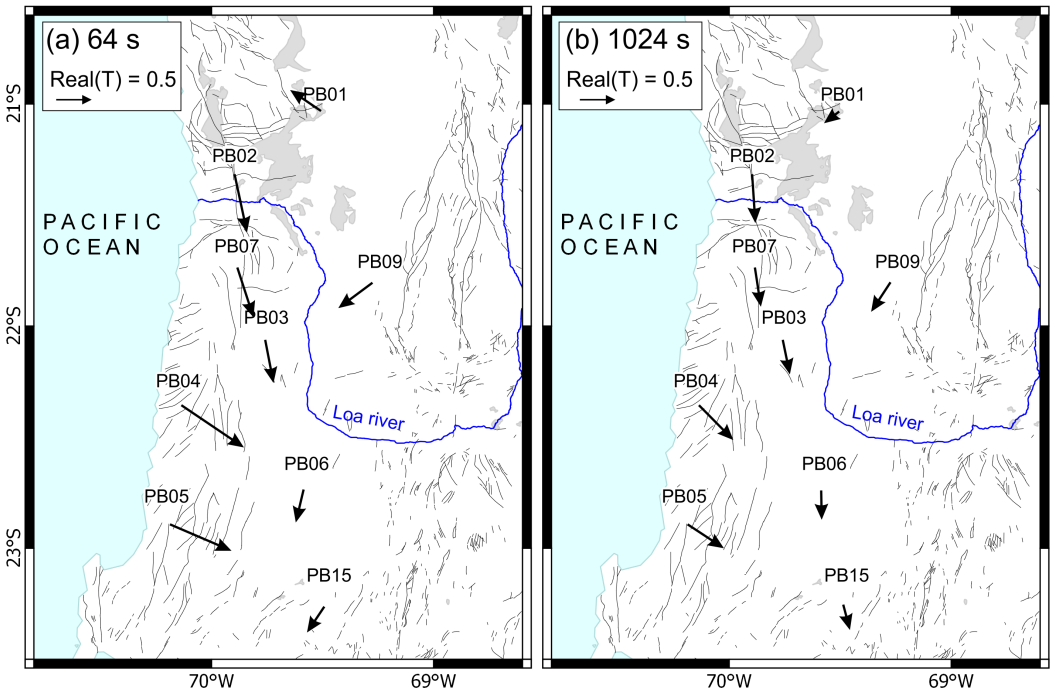

Figure 3.7: Map showing real induction vectors (Wiese convention) for exemplary periods: (a) 64 s, (b) 1024 s. Induction vectors are calculated from the long-term average VTFs shown in Figure 3.8. Grey areas are saltpans, black-thin lines are faults and blue line shows the trace of the Loa river (obtained from Sernageomin, 2003)

.

Horizontal magnetic transfer function

Figure 3.9 shows the HTF sounding curves for all IPOC sites using site PB01 as remote site. In this figure, a value of 1 has been subtracted from $Real(M_{xx})$ and $Real(M_{yy})$, in order to display all $\underline{\mathbf{M}}$ components using the same range along the vertical axes and to facilitate the comparison between them. For periods <20 s, $\underline{\mathbf{M}}$ components show an abrupt drop in their sounding curves and larger variance around the long-term median values, which may be related to the low signal-to-noise ratio that fluxgate magnetometers have for signals with short periods. In addition, larger uncertainties and error bars for $\underline{\mathbf{M}}$ components at shorter periods can also be explained by spatial variability in the magnetic field sources

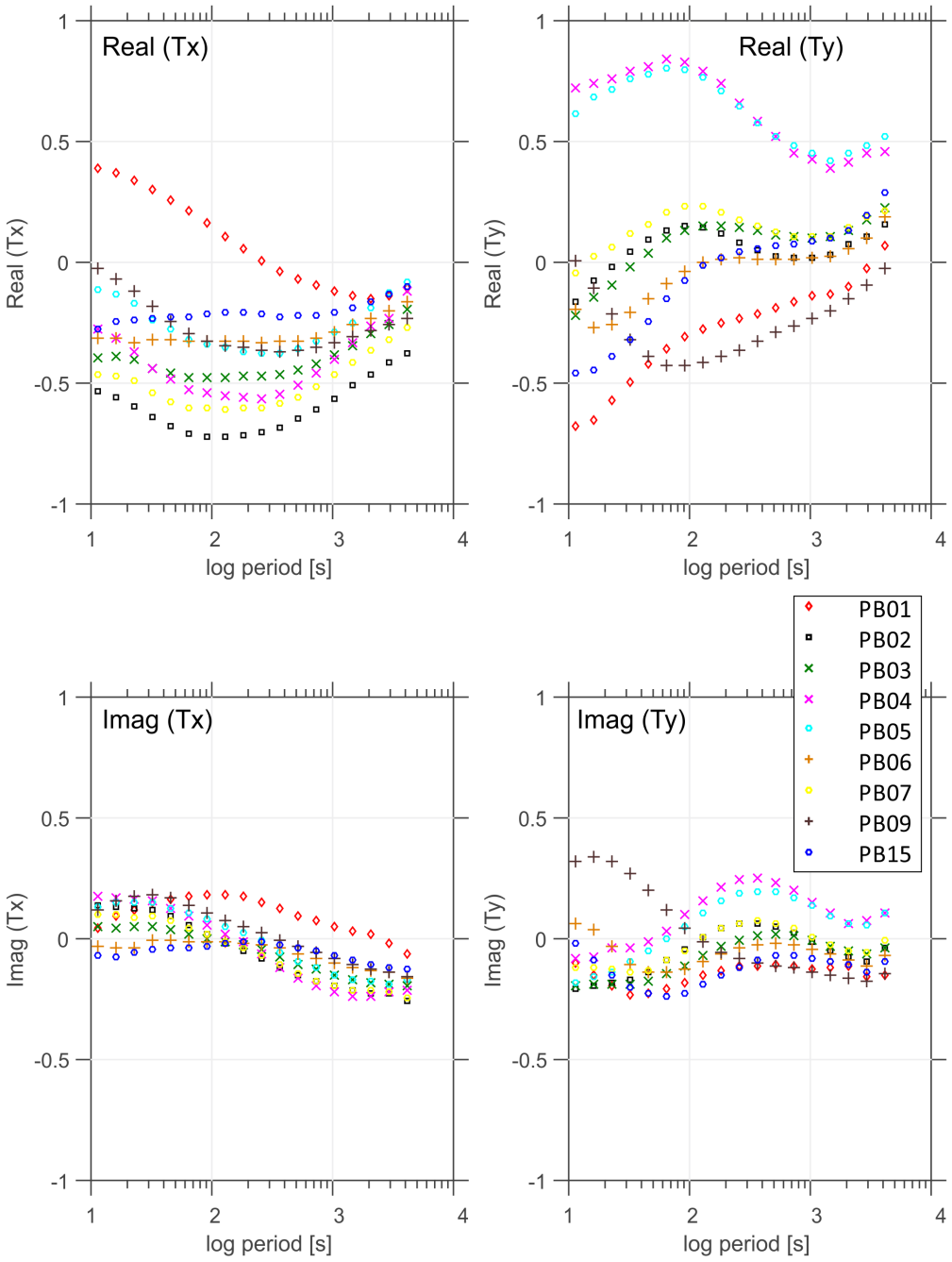

Figure 3.8: Compilation of long-term average VTF for IPOC sites. For each period, the displayed value is the median of all daily TF estimates obtained from 2011 to 2015. Each daily estimate was calculated using remote reference processing, in which PB01 was employed as remote site (except for PB01, where PB09 was used as remote site). Daily estimates with confidence intervals δT >0.02 were not considered for calculating the median value.

between stations. As in the case of VTFs, the most unstable component (M_{yy}) is the one which exhibits higher dependency on B_y fields (see 3.4.1).

Figure 3.10 shows the components of the reciprocal criterion matrix $\mathbf{R}$, obtained after multiplying the direct and inverse HTFs calculated for all sites using PB01 as remote site. Accordingly to the *reciprocal criterion* of Sokolova and Varentsov (2005), deviations of $\mathbf{R}$ from the real identity matrix indicate the presence of noise (see Subsection 2.2.5). In Figure 3.10 a value of 1 has been subtracted from $Real(R_{11})$ and $Real(R_{22})$, in order to facilitate the comparison of different components. Following the *reciprocal criterion*, obtained values of $\mathbf{R}$ suggest that all HTF are biased for periods $<$100 s, especially considering the significant departure of $Real(R_{22})$ and $Real(R_{11})$ from zero in the 10-100 s period range (see Figure 3.10). While for most of the sites the R_{12} and R_{21} components show values close to zero, PB02 exhibits R_{12} and R_{21} shifted from zero throughout the whole period range, suggesting a period-independent bias in HTFs related to this site. Although not as clear as for PB02, the $Real(R_{12})$ component of site PB07 also shows a period-independent deviation from zero.

According to the theory, in absence of lateral resistivity contrasts $\underline{\mathbf{M}}$ is equal to the identity matrix, and therefore sounding curves should be zero in Figure 3.9. Deviations from this pattern (i.e. anomalies) can be interpreted as a consequence of lateral resistivity changes, if external magnetic fields are uniform across the array. A common anomalous pattern observed at all sites is that $Real(M_{yy})$ departs from zero and decreases proportionally with period from 10 to 100 s (Figure 3.9). This pattern resembles the expected theoretical effect in M_{yy} due to the influence of the low resistivity ocean. Following the theoretical example shown in Figure 3.3, the B_y component observed in the continent tend to decrease when approaching to the ocean. In addition, this spatial gradient in the amplitude of B_y tends to decrease for longer periods, when the investigation depth significantly exceeds the thickness of the ocean. Therefore, M_{yy} ($\approx B_y^{local}/B_y^{remote}$) tends to decrease at shorter periods if the local site is closer to the coast than the remote site (as most of the cases shown in Figure 3.9). The clearest exception to this pattern is observed in the HTF between PB09-PB01, where $Real(M_{yy})$ is $>$1 between 20 and 3000 s and reaches a maximum approximately at 100 s. Although $Real(M_{yy})$ $>$1 between PB09-PB01 can be partly explained by the fact that PB09 is farther away from the coast than PB01, it cannot be discarded an additional effect, as is suggested by anomalous values observed also in the M_{xy} and M_{yx} components. Soyer and Brasse (2001) also reported anomalously larger HTFs related to the B_y component at sites located approximately at the same latitude of PB09, for periods between $\sim$100 and 3000 s. These authors interpreted that this anomaly can be related to the presence of a low resistivity zone below the Precordillera. The real parts of M_{xy} and M_{yx} at sites PB02 and PB07 show also an anomalous pattern, which is characterized by an almost period-independent shift of these components from the zero-level. However, HTFs related to these sites may be biased, as is suggested by the results of the *reciprocal criterion* (Figure 3.10).

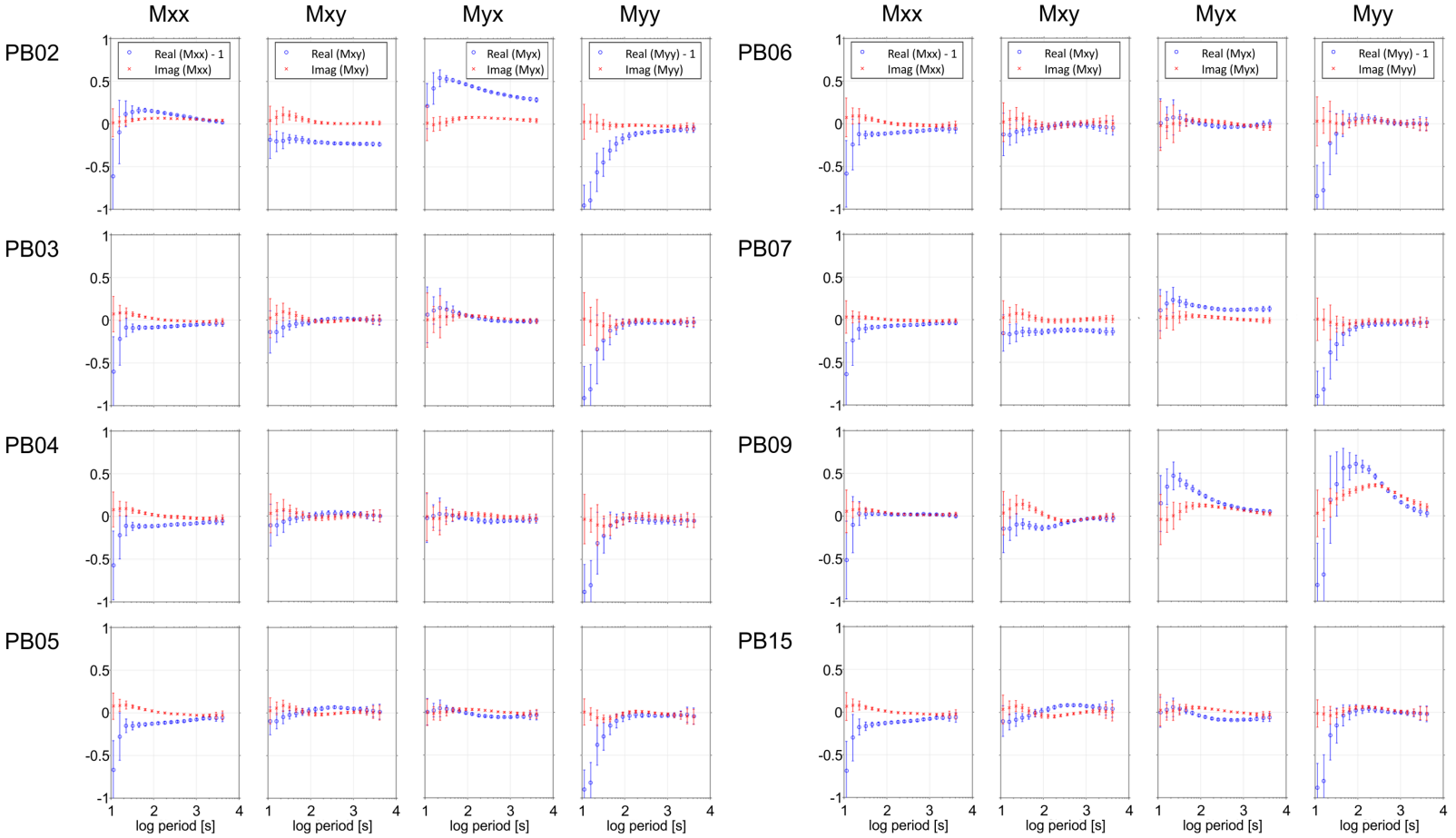

Figure 3.9: Long-term average HTF for IPOC sites, using PB01 as remote site. For each period, the displayed value is the median of all daily TF estimates obtained from 2011 to 2015. Daily estimates with confidence intervals δM >0.02 were not considered for calculating the median value. Note that a value of 1 has been subtracted to $Real(M_{xx})$ and $Real(M_{yy})$, in order to facilitate the comparison of the different components of $\underline{\mathbf{M}}$.

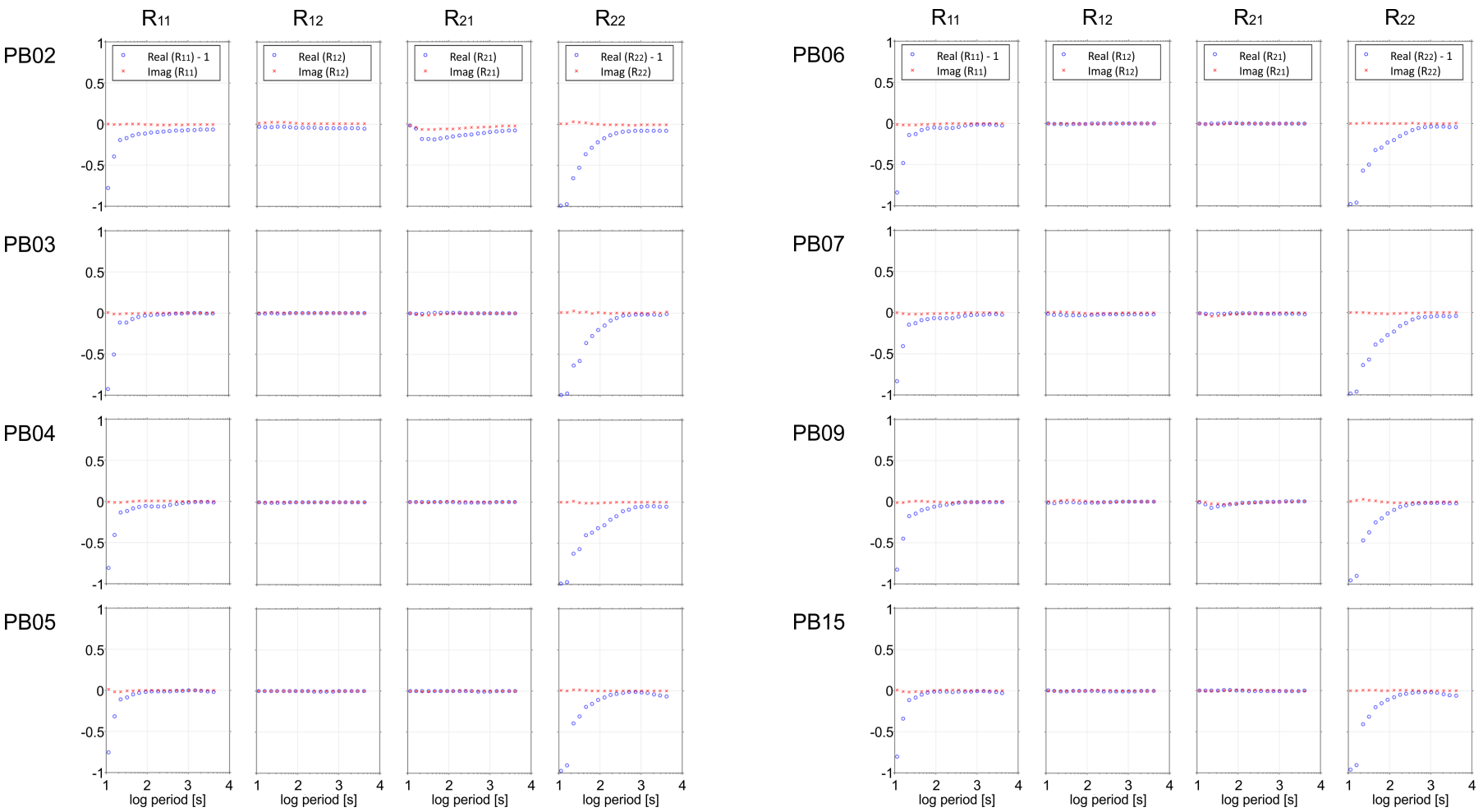

Figure 3.10: Reciprocal criterion matrix ($\mathbf{R}$) of long-term average HTF for IPOC sites using PB01 as remote site. The four components of $\mathbf{R}$ are plotted. Note that a value of 1 has been subtracted to $Real(R_{11})$ and $Real(R_{22})$, in order to facilitate the comparison of the different components of $\mathbf{R}$.

3.4.4 Temporal variation of transfer functions

Daily estimates of IPOC TFs exhibit temporal variations, whose variability range depend on the quality of the associated EM field measurements (see discussion on the influence of data quality in 3.4.1). In order to facilitate the comparison of TFs variations between different sites, here the temporal variability of TFs is analysed by examining deviations of the daily TF estimates from the long-term median value:

$$\Delta TF(\tau) = TF_{daily\ estimate}(\tau) - TF_{long-term\ median}(\tau) \tag{3.1}$$

where TF = transfer functions ($\underline{\mathbf{Z}}$, ρ_a, ϕ, $\mathbf{T}$, $\underline{\mathbf{M}}$), and τ = period [s]. The variability range of TFs tends to be larger in those components that are associated to EM fields with smaller signal-to-noise ratio. Figure 3.11 shows temporal variations of some TFs components for a period of 128 s at two exemplary sites. In this figure, temporal variations of $\underline{\mathbf{Z}}$ and $\mathbf{T}$ are displayed as percentage of the long-term median values, in order to illustrate the relative variability range of these parameters, regardless of their absolute value. As can be seen, daily estimates of TFs components related to more stable EM field measurements (e.g. Z_{yx}, T_x) exhibit smaller variability range around the long-term median than those related to noisier EM field variations (e.g. Z_{xy}, T_y).

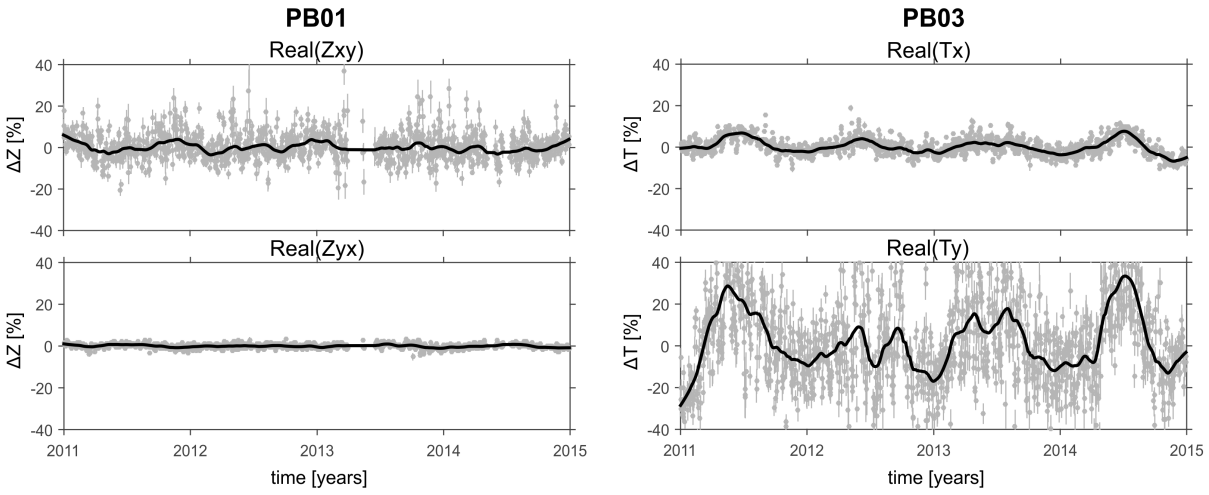

Figure 3.11: Temporal variations of $\underline{\mathbf{Z}}$ and VTF for a period of 128 s. Examples for variations of $Real(\underline{\mathbf{Z}})$ at PB01 (left) and $Real(\mathbf{T})$ at PB03 (right). Temporal variations are displayed as deviations of daily estimates from the statistical median of all daily estimates between 2011 and 2015. Grey dots and grey vertical bars are TFs daily estimates and their associated confidence intervals, respectively. Black lines are the 60-day moving average of the daily estimates. Deviations are displayed as percentage of the absolute value of the long-term median.

The temporal variability of TFs can even exceed ± 100 % of the long-term median value for TFs components and periods characterized by low signal-to-noise ratio. To illustrate this point, Figure 3.12 shows temporal variations of $Real(\underline{\mathbf{Z}})$ and VTFs for all components and periods at the same exemplary sites PB01 and PB03, respectively. Temporal variations are displayed as pseudosections, where each coloured point represents the TF deviation obtained for a specific day (ordered along the horizontal axis) and period (ordered along the vertical axis). As can be seen in Figure 3.12, most daily estimates of large components Z_{yx} and Z_{xx} are within a range of ± 20 % of the median value. However, the variability

range exceed ± 80 % of the median in the smaller components Z_{xy} (only for periods longer than 1000 s) and Z_{yy} (for the whole period range). Even larger variability ranges of daily estimates around the long-term median are observed at sites characterized by contact resistances in the order of 1 MΩ (PB03 and PB07). Figure 3.12 shows that the variability range of T_x is smaller than T_y for all the studied periods. While $Real(T_x)$ deviations do not exceed ± 20 % almost for the whole period band, daily estimates of $Real(T_y)$ show similar variability range only for periods between ~100 and 500 s. It is interesting to note that Z_{yy}, $Imag(T_x)$ and $Real(T_x)$ tend to exhibit positive deviations (i.e. red colours in Figure 3.12) during the middle part of all the studied years. This seasonal pattern will be discussed later.

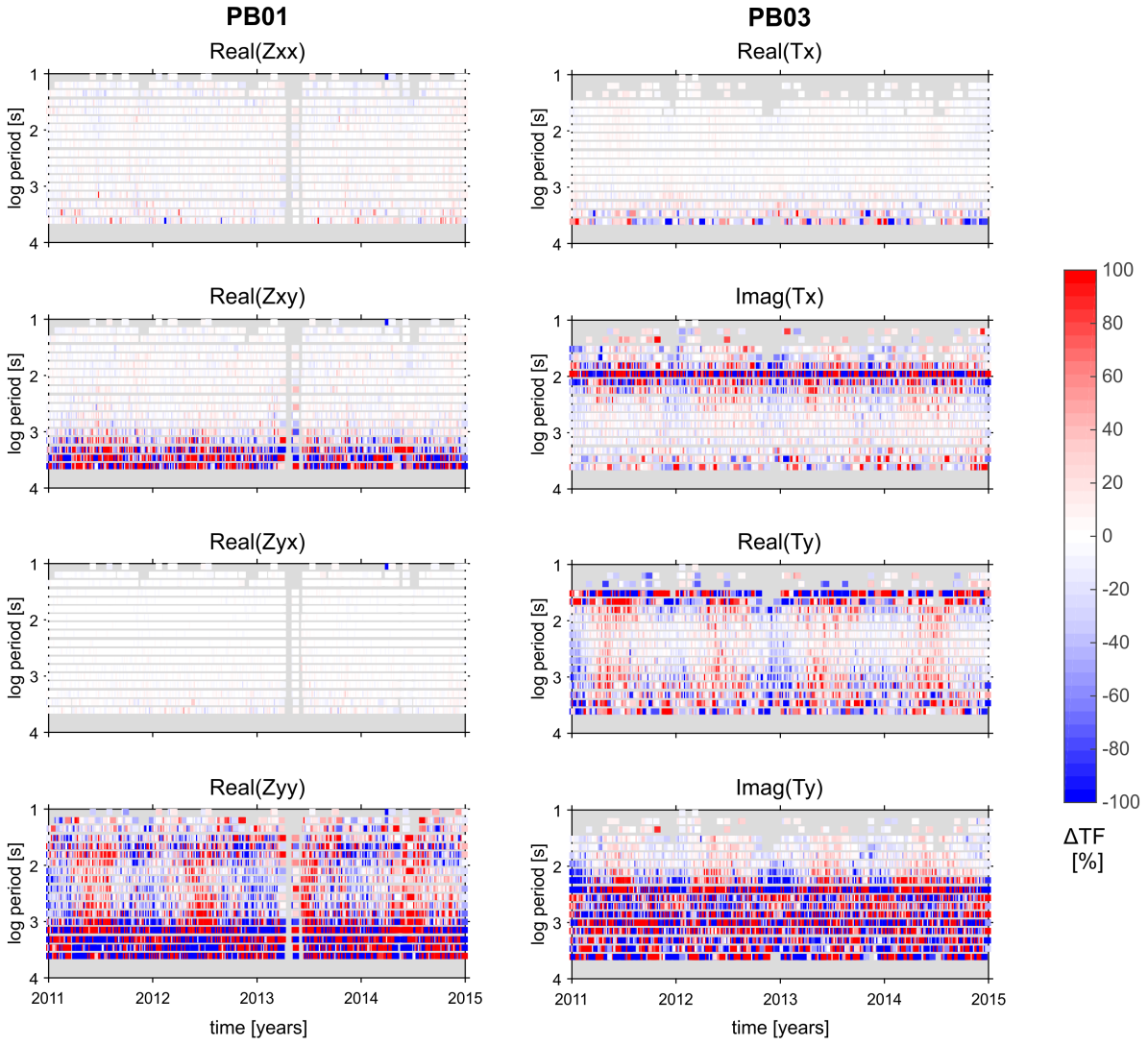

Figure 3.12: Temporal variations of $Real(\underline{\mathbf{Z}})$ (left) and VTF (right) for all periods, sites PB01 and PB03 respectively. Temporal variations are displayed as deviations of daily estimates from the statistical median of all daily estimates between 2011 and 2015. Grey areas represent intervals with no data or days removed from the analysis because TFs estimates showed large errors. Deviations are displayed as percentage of the absolute value of the long-term median. Note that the vertical axis is in logarithmic scale.

The good quality Z_{yx} component for a period of 128 s exhibits on average variability around the long-term median $<10\%$ for $\rho_{a,yx}$ and <3 ° for ϕyx (see examples in Figure 3.13). Deviations exceeding these

average ranges often occur when the EM fields time series show patterns suggesting the influence of noise (e.g. at PB09 during mid 2012 and by beginning of 2013 in Figure 3.13). Previous studies interpreted that apparent resistivity can exhibit long-term temporal deviations that are not necessarily related to changes in the subsurface internal resistivity (e.g. Eisel and Egbert, 2001; Hanekop and Simpson, 2006). These works reported that good quality apparent resistivity components exhibit on average variability in a range from 2 to 5% around the long-term average TF estimate for periods between ∼50 and ∼300 s. The larger average variability range observed in the IPOC TFs could be partly explained by comparatively lower quality EM fields data, which results from the effect of the deep ocean present along the Chilean margin and from the adverse conditions observed in the Atacama desert for electric measurements. However, it cannot be discarded that larger variability in the IPOC TFs may be caused by changes in the underground resistivity related to active tectonic processes which occur in this region.

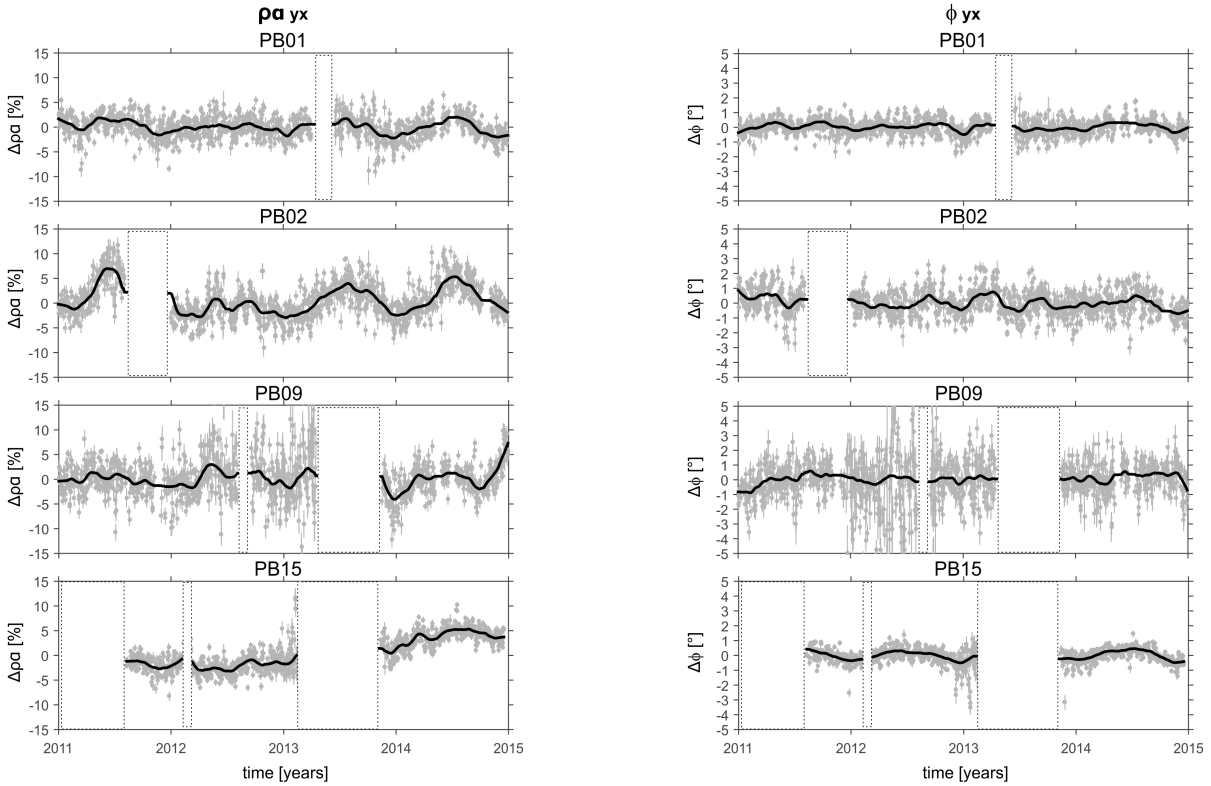

Figure 3.13: Temporal variations of $\rho_{a,yx}$ (left) and ϕ_{yx} (right) for a period of 128 s, sites PB01, PB02, PB09 and PB15. Temporal variations are displayed as deviations of daily estimates from the long-term median (interval from 2011 to 2015). Grey dots and grey vertical bars are TFs daily estimates and their associated confidence intervals, respectively. Black lines are the 60-day moving average of the daily estimates. White rectangles of dashed borders mask intervals with data gaps or where clear problems in the EM fields records were observed. Note that days when $\underline{\mathbf{Z}}$ estimates have confidence intervals $\delta Z > 1$ [km/s] are not included in the analysis.

Daily estimates of VTF normally scatter in a range of ± 0.1 from the long-term median, regardless of the absolute value of the median observed at each site. For this reason, deviations of VTF components from the median (ΔT) shown in the following figures are not divided by the median value. Figure 3.14 shows deviations of the good quality $Real(T_x)$ component for a period of 128 s at four sites. As can be seen, comparatively larger variability around the median is observed in the long-term trend

of temporal variations (black lines in Figure 3.14) at sites PB02 and PB07, which are located in the Coastal Cordillera. Larger variability observed in **T** at sites closer to the coast can be related to noisier measurements of the B_y component, as discussed in 3.4.1. It is important to note that although T_y is the most sensitive component to B_y measurements, the behaviour of B_y affects all VTF components, because power spectral terms of B_y are also used to calculate estimates of T_x (see equations (2.25) and (2.25)).

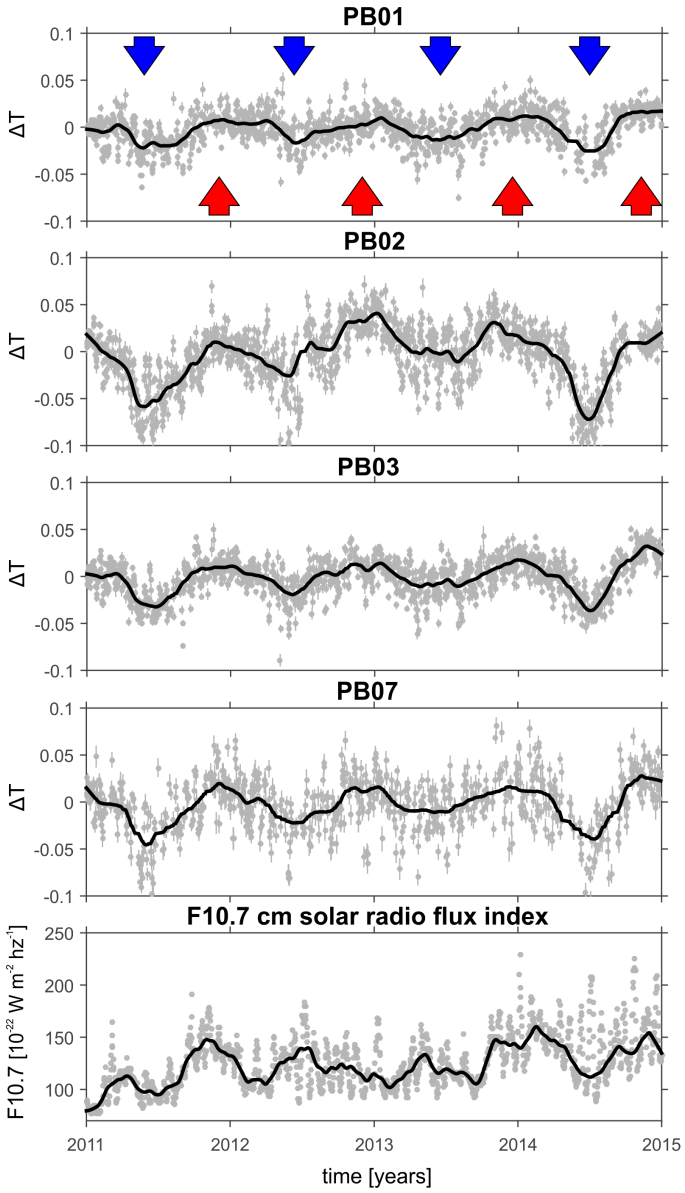

Figure 3.14: The four upper panels show temporal variations of $Real(T_x)$, for a period of 128 s, at sites PB01, PB02, PB03 and PB07. Temporal variations are displayed as deviations of daily estimates from the long-term median (interval from 2011 to 2015). Grey dots and grey vertical bars are TFs daily estimates and their associated confidence intervals, respectively. Black lines are the 60-day moving average of the daily estimates. Red / blue arrows indicate intervals when temporal variations tend to increase / decrease. Note that days when **T** estimates have confidence intervals δT >0.02 are not included in the analysis. The bottom panel shows daily values and the 60-day moving average of the F10.7 cm solar radio flux index (downloaded from http://omniweb.gsfc.nasa.gov), as a proxy for solar activity

Although the variability ranges observed in TFs depend on data quality (and therefore they vary from site to site), temporal variations of TFs exhibit consistently and systematically periodical patterns at all sites. Figure 3.15 shows periodograms of temporal variation of daily estimates of $\underline{\mathbf{Z}}$, VTF, auto-spectra of magnetic fields and HTF at the exemplary site PB01. In most of these TFs, a dominant peak can be observed for periods between 320 and 340 days (i.e. $\sim$1 year). Some components show additional peaks around 10, 27, 40 and 180 days, but the amplitudes for these periods are smaller than the $\sim$1 year peak. The periodical annual variation pattern is observed as a gradually increasing and decreasing trend in the TFs daily estimates which peaks at June and December solstices. In the case of $Real(T_x)$, values of daily estimates tend to increase during December and to decrease during June (red and blue arrows respectively mark these patterns in Figure 3.14). However, the polarity of these fluctuations is different for other components of $\mathbf{T}$. For example, Figure 3.12 shows that daily estimates of $Imag(T_x)$ and $Real(T_y)$ tend to increase at June and decrease at December. Similar patterns suggesting periodic annual variations are also observed in TFs related to $\underline{\mathbf{Z}}$, but here these variations are less evident than in $\mathbf{T}$. For instance, temporal variations of $\rho_{a,yx}$ and ϕ_{yx} tend to exhibit high/low peaks during the middle/beginning of some years (e.g. see $\rho_{a,yx}$ at PB01 and PB02, and ϕ_{yx} at PB15 in Figure 3.13).

Annual variations observed in TFs show correlation with magnetic activity. For instance, the long-term trend of VTFs temporal variations (black lines in four upper panels of Figure 3.14) tend to peak when the F10.7 cm solar radio flux index (*F10.7*) exhibits local maxima or minima (see lowest panel of Figure 3.14). The *F10.7* index is an indicator of the solar activity [1]. As the solar activity controls the ionospheric and magnetospheric current systems that generate the external part of the magnetic fields observed at surface, the *F10.7* can be considered as a proxy for the geomagnetic activity. Periodical seasonal variations in IPOC VTFs were previously documented by Brändlein (2013), who described that seasonal variations are also observed in the B_y component for periods between 100 and 3000 s. Brändlein (2013) interpreted that seasonal variations of VTFs represent a source field effect, based on the correlation observed between magnetic field measurements and the interplanetary electric field (Brändlein et al., 2012), and because VTF seasonal variations exhibit spatially uniform amplitude across the IPOC array. It is important to note that apparent correlation between TFs variability and magnetic activity is not only limited for the annual variations. For example, periodograms of some TFs components and the *F10.7* exhibit dominant peaks at $\sim$27 days (Figure 3.15), which suggests correlation between TFs fluctuations and the solar rotation cycle. In addition, both VTFs and the *F10.7* exhibit also a linearly increasing long-term trend over the studied interval (e.g. compare in Figure 3.14 the VTFs and *F10.7* values observed at the beginning of years 2011 and 2015), which coincides with the ascending trend in the solar activity related to 11-year solar cycle.

[1] http://www.swpc.noaa.gov/phenomena/f107-cm-radio-emissions

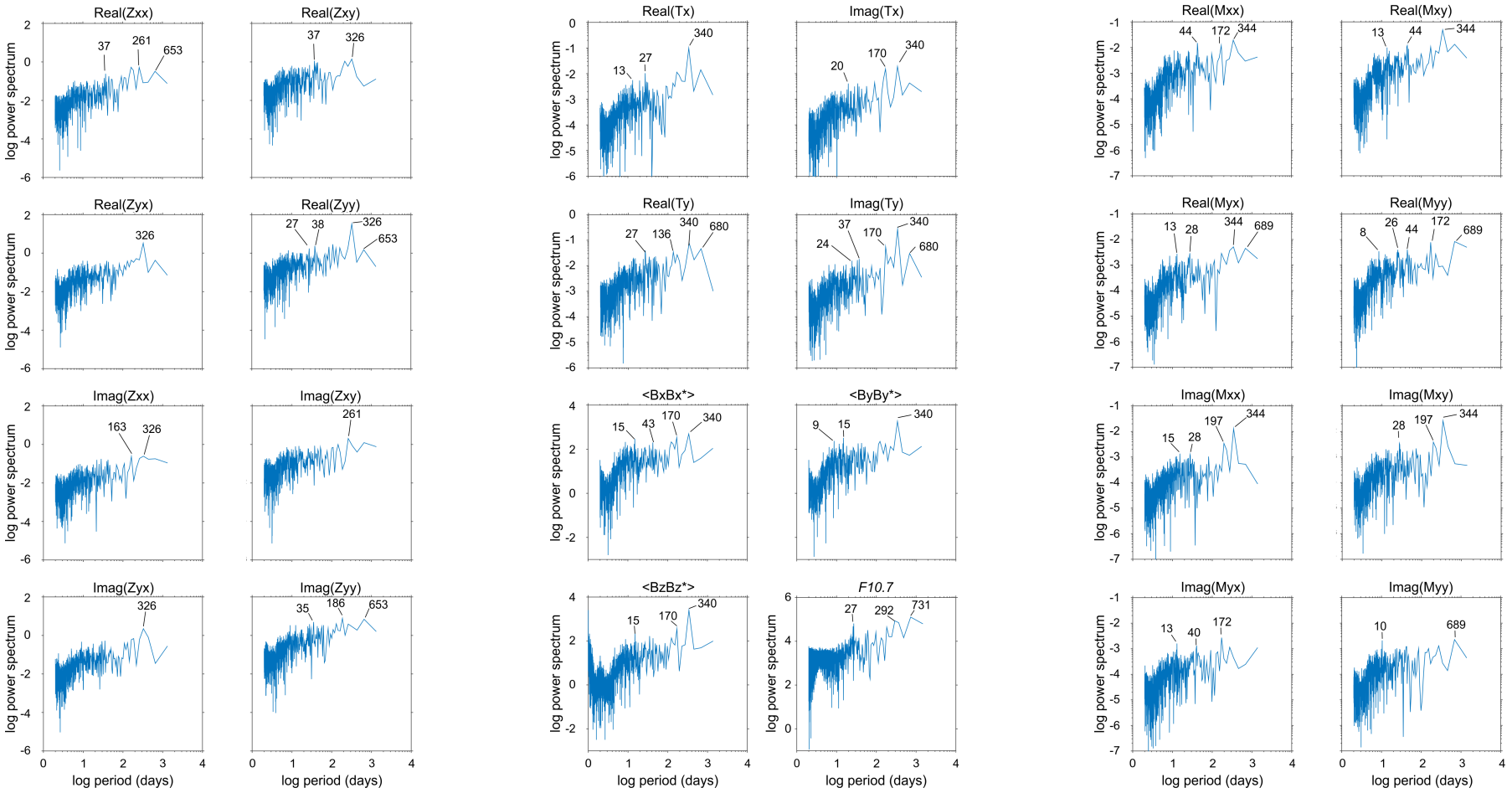

(a) Z **(b)** VTF, B-fields auto-spectra, *F10.7* **(c)** HTF PB01-PB09

Figure 3.15: Periodogram of temporal variations of TFs at a period of 128 s for site PB01: (a)**Z**. (b) VTF and magnetic fields auto-spectra. (c) HTF (between PB01 and PB09). Analysed time series comprise all daily TFs estimates obtained from 2011 to 2015. Days when TFs estimates have confidence intervals $\delta Z > 1$ [km/s], $\delta T > 0.02$ and $\delta M > 0.02$ were not included in the analysis. A number of dominant spectral peaks are marked (period in days, see the text). The spectra of the F10.7 cm solar radio flux index (*F10.7*) is also included in (b).

3.5 Summary

The quality of EM measurements at the IPOC array between 2011 and 2015 varies among sites, period and field components. Magnetic time series show generally good quality at all sites; contamination with external artificial noise or significant problems of the instruments are not observed. However, the statistical error of TFs estimates and shape of TFs sounding curves suggest that the signal-to-noise ratio importantly decreases for periods $<$60 s. This can be explained by the low signal-to-noise ratio of fluxgate magnetometers for measuring magnetic variations at such periods (e.g. Ferguson, 2012).

For periods $>$10 s, time series of electric measurements exhibit relatively good quality at sites PB01, PB02, PB05, PB09 and PB15. Patterns clearly showing the presence of noise in electric field data are observed at sites characterized by contact resistance in the order of MΩ (PB03, PB07) and at sites located close to areas with mining facilities or power lines (PB04, PB06). The long-term trend of electric time series shows generally a linear drift, which exhibits a variability range comparable with previous long-term electric measurements experiments. However, there are some intervals where the fluctuating behaviour of the long-term trend in time series suggests electrode instability or the presence of local noise sources. In most of the cases, days when the EM time series show clear evidence of noise contamination are characterized by TFs estimates with large statistical errors. Therefore, days with bad data quality can be identified and removed by examining the confidence interval of their associated TFs estimates.

The population of daily estimates of TFs tend to be distributed around its statistical median. These median values define sounding curves which vary smoothly with period, and therefore they represent a physically coherent long-term average of the TFs. Patterns observed in sounding curves of long-term median TFs are consistent with the dataset obtained by (Brändlein, 2013) using a long-processing interval, and also with MT data described at similar regions by previous studies (e.g. Lezaeta, 2001; Brasse et al., 2002; Soyer, 2002; Kühn et al., 2014). Long-term median ρ_a and ϕ sounding curves at all IPOC sites show a split in the Z_{xy} and Z_{yx} components related to the effect of the low resistivity ocean. Properties of the long-term median $\underline{\mathbf{Z}}$ tensor suggest that the study area is characterized by a 3-D resistivity structure. Patterns observed in the long-term median VTFs of IPOC sites suggest the presence of low resistivity regions towards the east of the array, which could be related to the Bolivian Altiplano anomaly (e.g. Brasse et al., 2002). The dominant pattern observed in the long-term median HTFs is the decrease of the M_{yy} component for periods $<$100 s, which can be attributed to the effect of the ocean. Anomalous patterns are observed in HTFs at site PB09 between 100 and 3000 s, which could be related to the presence of a low resistivity region below the Precordillera (Soyer and Brasse, 2001).

The reproducibility of TFs over time depends on the quality of the associated EM field measurements. Daily estimates of TFs can occur in a wide range (e.g. exceeding $\pm$ 100% of the long-term median value), at periods and/or sites where EM time series show low signal-to-noise ratio. This condition limits the amount of TFs components that can be used in order to monitor the resistivity structure. In order to monitor other components, it is necessary to enhance the quality of time series (especially E_x and B_y), e.g. by applying additional filtering techniques to the data or by improving measurements conditions.

Temporal variations of all TFs and at all sites show periodical patterns. The amplitude of these patterns

varies among components and sites, and depends on data quality. The most clear periodical pattern is a smooth seasonal fluctuation, which peaks around the June and December solstices. This pattern is especially clear in VTFs, and the polarity of the fluctuation pattern depend on the VTF component. Seasonal variations in VTFs were previously documented by Brändlein (2013), who suggested that they are related to changes in the external magnetic source. Here it is shown that temporal variations of all TFs exhibit some correlation with an indicator of the magnetic activity. In addition, TFs exhibit periodical patterns which are apparently correlated with the 27-day and 11-year solar cycle. All of these observations suggest that estimates of TFs at IPOC sites are not independent of the external (source) magnetic fields conditions, as it is normally assumed by practitioners of the MT and GDS methods. These results motivated to study whether this correlation between TFs variability and geomagnetic activity is a pattern present only in north Chile or a global phenomenon (see analysis of source effects in VTFs presented in chapter 5).

Chapter 4

The electrical resistivity structure of the forearc in Northern Chile

This chapter presents a 3-D model of the electrical resistivity structure of the forearc in Northern Chile (21-23.5°S), and an analysis of the geological implications derived from this model. Section 4.1 reviews common patterns described in the resistivity structure of subduction zones related to the distribution of fluids and deformation processes. The dataset inverted and the modelling parameters chosen are described in sections 4.2 and 4.3, respectively. The preferred model and its datafit is presented in Section 4.4. Section 4.5 describes a series of sensitivity and resolution tests, which were carried out in order to assess the robustness of major resistivity features obtained in the preferred model. The consistency of the preferred model with previous MT studies, the geological interpretation of the obtained resistivity structure, and the geodynamic implications derived from this model are discussed in Section 4.6. Finally, mains results are summarized in Section 4.7. Parts of this chapter are contained in the manuscript "Along-strike segmentation of subduction processes in the central Andes forearc - constraints from the deep electrical resistivity structure", submitted to *Journal of Geophysical Research*.

4.1 Introduction

Results of MT studies conducted in different convergent margins suggest that the resistivity structure of subduction zones exhibits some common patterns (see for example compilation of Pommier, 2014a). In particular, MT studies have consistently imaged zones of low resistivity (LRZs) which suggest the presence of high amount of fluids or partial melts in depth. Major resistivity structures related to fluid processes are described in subsection 1.1.1 and illustrated in Figure 1.1. In the forearc of subduction zones, most MT studies have imaged two major LRZs. One LRZ is usually located between the trench and the coastal region of subduction margins, at depths usually shallower than 15 km. Low resistivities in this region are usually interpreted as evidence of fluids released by the dehydration of clay minerals present in subducted sediments, and often coincides with the updip limit of the interplate seismogenic zone (e.g. Worzewski et al., 2011). Another LRZ is usually imaged between the coastline and the arc, in a

depth range of 20-60 km, and coincides with the forearc mantle wedge interpreted from seismic studies. Low resistivities in this deeper domain are interpreted as evidence of large amount of fluids released by the dehydration of the oceanic crust (Reynard et al., 2011). In turns, this excess of fluids results in hydration of the forearc mantle rocks, altering their mineralogy and generating serpentinite rocks (e.g. Hyndman and Peacock, 2003). In cool subduction zones, the western boundary of the hydrated forearc mantle normally coincides with the downdip limit of the interplate seismogenic zone (e.g. Hyndman et al., 1997).

Comparison of MT studies in Northern Chile, however, suggests that the aforementioned LRZs are not continuous features along the forearc of subduction zones. For instance, Brändlein (2013) interpreted a regional LRZ in the forearc mantle wedge approximately between 21.5° and 22.5°S, a feature which is not observed in models of MT studies between 20° and 21°S (Brasse et al., 2002; Kühn et al., 2014). Recent studies have suggested that the resistivity structure of subduction zones can exhibit significant along-strike variations, and that such spatial variability correlates with first-order segmentation observed in deformation and fluid processes (e.g. Heise et al., 2013; Wannamaker et al., 2014; Hata et al., 2015). In this chapter, factors controlling deformation and fluid processes in the subduction zone of Northern Chile are explored by studying the deep resistivity structure of the forearc. A 3-D model of the resistivity structure is obtained by interpreting long-period MT data collected at nine sites of the IPOC array (see Figure 4.1).

4.2 Dataset inverted

The data inverted comprises estimates of all components of the MT TF ($\underline{\mathbf{Z}}$), VTFs and HTFs. This dataset was obtained after processing one year of time series (from 01-January-2011 to 31-December-2011), using the remote-reference processing and applying the same processing scheme which is described in section 3.3. Site PB15 was installed in August 2011, and therefore only data between 05-August-2011 and 31-March-2012 could be considered. A one-year processing interval was used in order to obtain satisfactory quality for TF estimates which are obtained from EM measurements of low signal-to-noise ratio. Eventually, sounding curves with satisfactory quality were obtained for the period range between 10 and ∼10,000 s at most sites and components. TFs with periods longer than 10,000 s were not considered, as they can be affected by external sources bias (e.g. Shimizu et al., 2011). At site PB07, the Z_{yy} component and some periods of the Z_{xx} and Z_{xy} data were discarded.

Computed estimates of HTFs were evaluated using the *reciprocal criterion* (see (2.22)), in order to detect and discard the influence of source field effects. The *reciprocal criterion* states that the product of direct and inverse estimates of HTFs between any two sites should be close to the identity matrix, otherwise the magnetic measurements are contaminated by noise (Sokolova and Varentsov, 2005). As selection criterion, all HTF components for an specific period were discarded, if their associated *reciprocal criterion* matrix (see (2.22)) deviated by more than 0.1 from the expected identity matrix. Using this procedure, finally HTFs between 16 pairs of stations for a period band between 100 and ∼10,000 s were selected.

Estimates of TFs obtained using the one-year processing interval are very similar to the long-term median

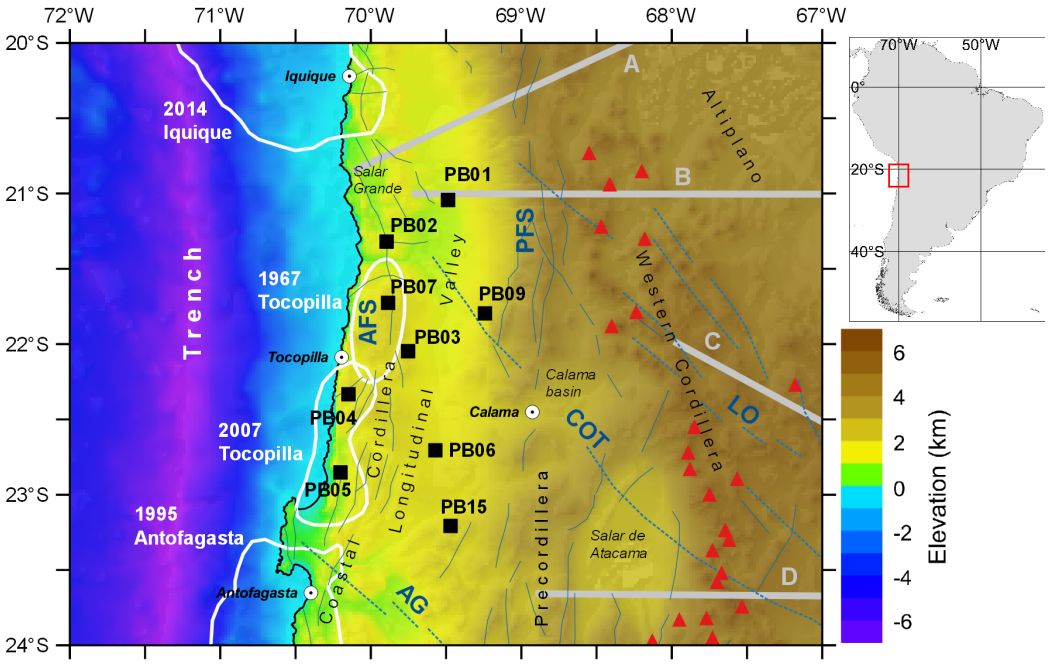

Figure 4.1: Map of the IPOC MT array. Black squares are IPOC MT sites. Red triangles are active volcanoes, obtained from The Smithsonian Institutions Global Volcanism Program (http://volcano.si.edu). White polygons show rupture area interpreted for earthquakes with magnitude $\geq$7.4 during the last 50 years (compiled from Chlieh et al., 2004; Schurr et al., 2012, 2014). Blue lines are major faults (modified from Richards et al., 2001; Sernageomin, 2003). Blue dotted lines are NW-SE regional structural corridors (taken from Richards et al., 2001). Dark blue text indicate major fault systems and NW-SE regional structural corridors: AFS: Atacama Fault System, AG: Archibarca-Galan, COT: Calama-Olacapato-El Toro, LO: Lipez-Coranzuli, PFS: Precordillera Fault System. Grey thick lines are regional MT profiles from previous studies: (A) Pica and (B) ANCORP profiles from Brasse et al. (2002), (C) Comeau et al. (2015), (D) Díaz et al. (2012). Main morphological units are indicated. Elevation data obtained from NOAA (http://www.ngdc.noaa.gov/mgg/topo/topo.html).

of daily TFs described in subsection 3.4.3. This suggests that the TFs contained in the one-year dataset can be considered as estimates of the long-term average of TFs during the interval where the temporal variations of TFs were analysed (from January-2011 to December-2014). Main differences between these two datasets are observed in low-quality components (e.g. Z_{yy}), for which the one-year processing dataset shows better estimates, i.e. sounding curves which vary smoothly with period. Brändlein (2013) obtained a dataset of $\underline{\mathbf{Z}}$ and VTF estimates after processing data from eight IPOC sites (data from PB15 were not included). This author processed 150 days of data (19-February-2011 to 19-July-2011) using the single-site processing technique. Estimates of TFs calculated by Brändlein (2013) are very similar to the TFs obtained in the one-year dataset. Main differences are observed in periods shorter than 100 s, where sounding curves calculated by Brändlein (2013) exhibit a relative drop. This relative drop between the sounding curves of Brändlein (2013) (calculated using single-site processing) and the one-year dataset (calculated using remote-reference processing) may be related to the effect of noise in magnetic measurements, which especially affect TF estimates obtained using the single-site processing technique (e.g. Neska, 2006).

4.3 Inversion setup and model discretization

The preferred inversion setup was determined after testing different values for the parameters which control de inversion process in ModEM (see the description of these parameters in section 2.2.7) and evaluating the related inversion results. Error bounds were used, as this resulted in better overall fit of all TFs components, particularly the general trends at long periods. For all components of VTFs and HTFs fixed error bounds of 0.02 and 0.03 were used, respectively. In the case of $\underline{\mathbf{Z}}$, the errors assigned to each component were calculated as a percentage of its magnitude (Z_{xx} = 15%, Z_{xy} = 3%, Z_{yx} = 7%, Z_{yy} = 20%). A smoothing factor α=0.2 was used, which was applied uniformly in all spatial directions.

The prior and starting models were constructed using the 3d-grid software. The model space consists of a volume of 2369 km x 2369 km x 3193 km in the x, y and z directions, divided in 59 x 59 horizontal cells and 43 vertical layers, respectively (Figure 4.2a). In the core of the model, which is defined by an area of 270 km x 270 km centred on the IPOC array, the cells have a horizontal dimensions of 10 km. In the outer part of the model, the horizontal sizes of the cells increase by a factor of 1.2 with increasing distance from the core. The thickness of the layers starts with 100 m at surface, and then increases with depth by a factor of 1.2. Topography was not considered.

The prior or reference model consists of a homogeneous half space of 50 Ωm and a 0.3 Ωm 3-D body simulating the ocean (Figure 4.2a). The geometry of the ocean body was constrained using bathymetry data from NOAA (http://www.ngdc.noaa.gov/mgg/topo/topo.html). In all tests, the shape and resistivity of the ocean body is fixed in the prior model. After performing a number of tests, it was observed that the inversion tended systematically to create zones of high resistivity in cells in contact with the ocean. It was interpreted that the conductance of the model of the ocean overestimated the real one, resulting in an excess of conductance that the inversion tried to compensate creating unrealistically high resistivities in cells closest to the fixed ocean body. Considering these results, we finally used a prior model in which the bathymetry-constrained ocean body was modified. In this modified ocean body, the coastline and the continental shelf was moved to the west by two or three cells. In order to reduce the computation time required for the inversion processes a nested modelling approach was used (e.g. Meqbel et al., 2014). The nested model subspace considers an area of 385 km x 385 km centred at the array of stations (Figure 4.2b). The average computational time required for completing an inversion test decrease from three weeks (by inverting the complete model) to only three days (by using the nested inversion modelling approach). All inversion tests were calculated using the computer cluster of the GFZ.

In addition to the prior model, ModEM can use a starting model from which the inversion starts to compute the misfit between measured data and model's response (see (2.27)), and which then represents a first guess to initiate the inversion process. The starting model (Figure 4.2c-e) comprises a homogeneous half space of 50 Ωm and three additional bodies:

- A bathymetry-constrained 0.3 Ωm body representing the ocean. Contrary to the prior model (see above), in the starting model the bathymetry-constrained ocean body was not modified. Inclusion of a more realistic model of the ocean in the starting model significantly improved the fit of the data at coastal sites.

- A 1 Ωm body located at the position of the Bolivan Altiplano anomaly (labelled AP in Figure 4.2d-e). The location and vertical extent of the Bolivan Altiplano body (AP) was constrained by LRZs (<1 Ωm) found by independent MT studies of the Altiplano-Puna region between ∼18°S and 23°40S (Brasse et al., 2002; Brasse and Eydam, 2008; Díaz et al., 2012; Kühn et al., 2014; Comeau et al., 2015, see location of MT profiles in Figure 4.1). In areas where MT data are lacking, the shape of the AP body was constrained to regions of high seismic wave attenuation, which were interpreted as evidence for fluids or partial melts at depth by previous studies (e.g. Haberland et al., 2003; Schurr et al., 2003). The main reason to include the AP along strike in the starting model was because all of our previous inversions indicated a huge low resistivity domain somewhere in the eastern part of the model, approximately coincident with the Bolivian Altiplano anomaly.
- A 1000 Ωm body mimicking the geometry of the Nazca lithosphere (labelled NP in Figure 4.2d-e). We assumed an average thickness of 80 km for the Nazca plate. The upper limit was constrained by using the geometry of the Slab 1.0 model (Hayes et al., 2012). Marine MT studies suggest that oceanic lithosphere is characterised by resistivities >1000 Ωm (e.g. Worzewski et al., 2011). Inclusion of the NP resistor in the starting model improved the overall data fit, and helped to better constrained the vertical extent of LRZs located in the lower crust and upper mantle.

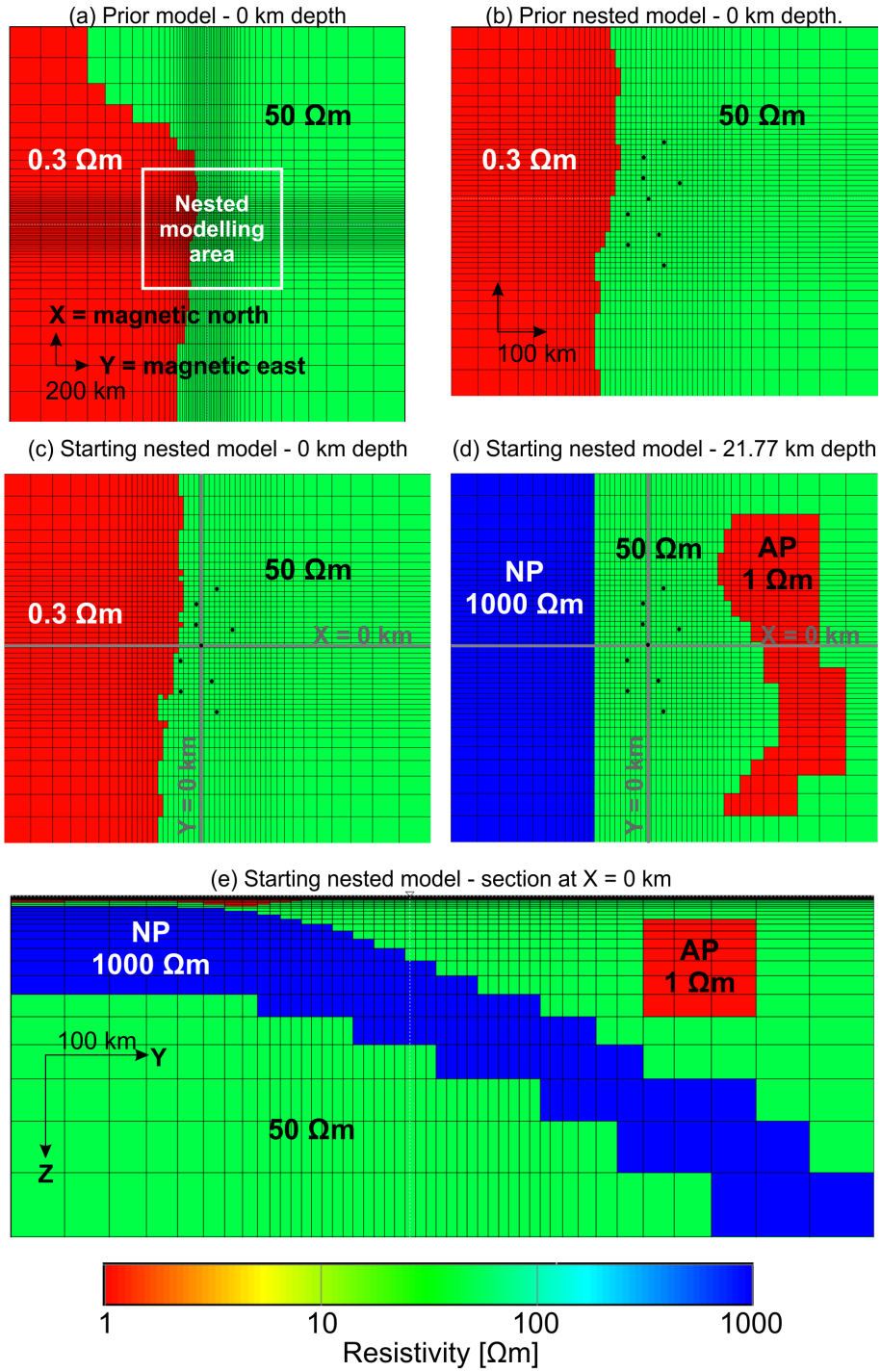

Figure 4.2: Models used in the inversion modelling: (a) Prior model, layer between 0 and 0.1 km depth. Area of nested models is indicated. (b) Prior nested model, layer between 0 and 0.1 km depth. (c) Starting nested model, layer between 0 and 0.1 km depth. (d) Starting nested model, layer between 21.77 and 26.89 km depth. (e) Starting nested model, section at X = 0 km. Black dots in Figures (b), (c) and (d) show the location of sites. The resistivity of the structures included in the prior and starting models is indicated.

4.4 A preferred model

The preferred model was obtained after 110 iterations, in which the global RMS misfit was reduced from 10.43 to a value of 1.82. Figures 4.3 and 4.4 show observed TFs and the respective response of our preferred 3-D resistivity model. The overall data fit is good; the model responses reproduce all major trends in the observations, over the entire period range and for all components of the measured data. Remarkably, the model can reproduce the very high values of $Real(T_y)$ observed at sites PB04 and PB05, the negative values observed in the real parts of T_x at all sites, the trend of diagonal components of the impedance phase (ϕ_{xx} and ϕ_{yy}, Figure 4.3), and the prominent anomaly observed in HTFs at site PB09 (Figure 4.4). Slightly worse fits were obtained for ϕ_{yy} at some sites (e.g. PB01 and PB06 in Figure 4.3) and some of the components of $\underline{\mathbf{M}}$ (e.g. HTF at PB01-PB05 and PB15-PB05 in Figure 4.4).

Figure 4.5 shows horizontal slices of the preferred model at various depths. The outlines of the a priori bodies (ocean, AP and NP) are indicated for reference. The model shows a number of LRZs which together yield a complex 3-D structure in north-south direction. The major features resemble structures included in the starting model: the ocean, the LRZ below the Altiplano and the Nazca lithosphere. However, from these structures only the Altiplano body was significantly modified during the inversion process. This result suggests that the data are sensitive to this structure although the main part of the AP body is located outside of the array. After the inversion the AP anomaly appears to be split into two zones of low resistivity (A1 and A2 in Figure 4.5). The major structure below the IPOC stations is a domain of high resistivity ($>$1000 Ωm) observed along the whole array between the coast and the Precordillera (FHRZ in Figure 4.5b-e). The FHRZ body is clearly observed at least from 5 km depth until the top of the a priori body simulating the Nazca plate; for deeper levels it is not possible to differentiate these two bodies. In addition, the model shows a number of additional distinct LRZs (most of them $<$5 Ωm) which have important implications for the main purposes of this study: two LRZs are located between the upper crust and the top of the slab in the coastal region (C1 and C2 in Figure 4.5b-e), four LRZs are located below the Longitudinal Valley (L1, L2 and L3 in Figure 4.5b-e; M2 in Figure 4.5f-h), and three LRZs appear below the Precordillera region (P1 and P2 in Figure 4.5b-c; M1 in Figure 4.5f-h).

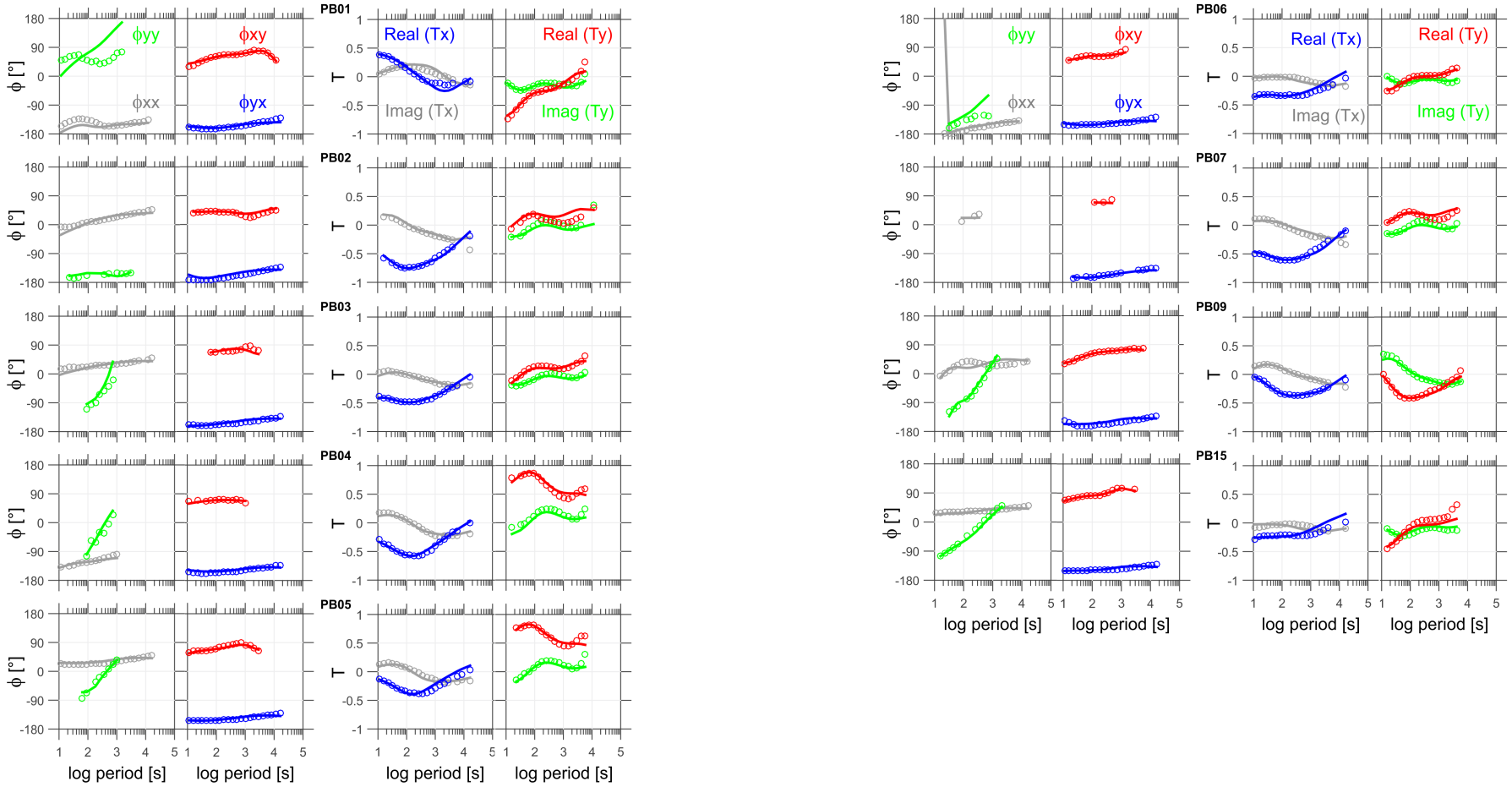

Figure 4.3: Comparison between observed (circles) and calculated (lines) MT response functions. ϕ= impedance phase components, T= vertical magnetic transfer function.

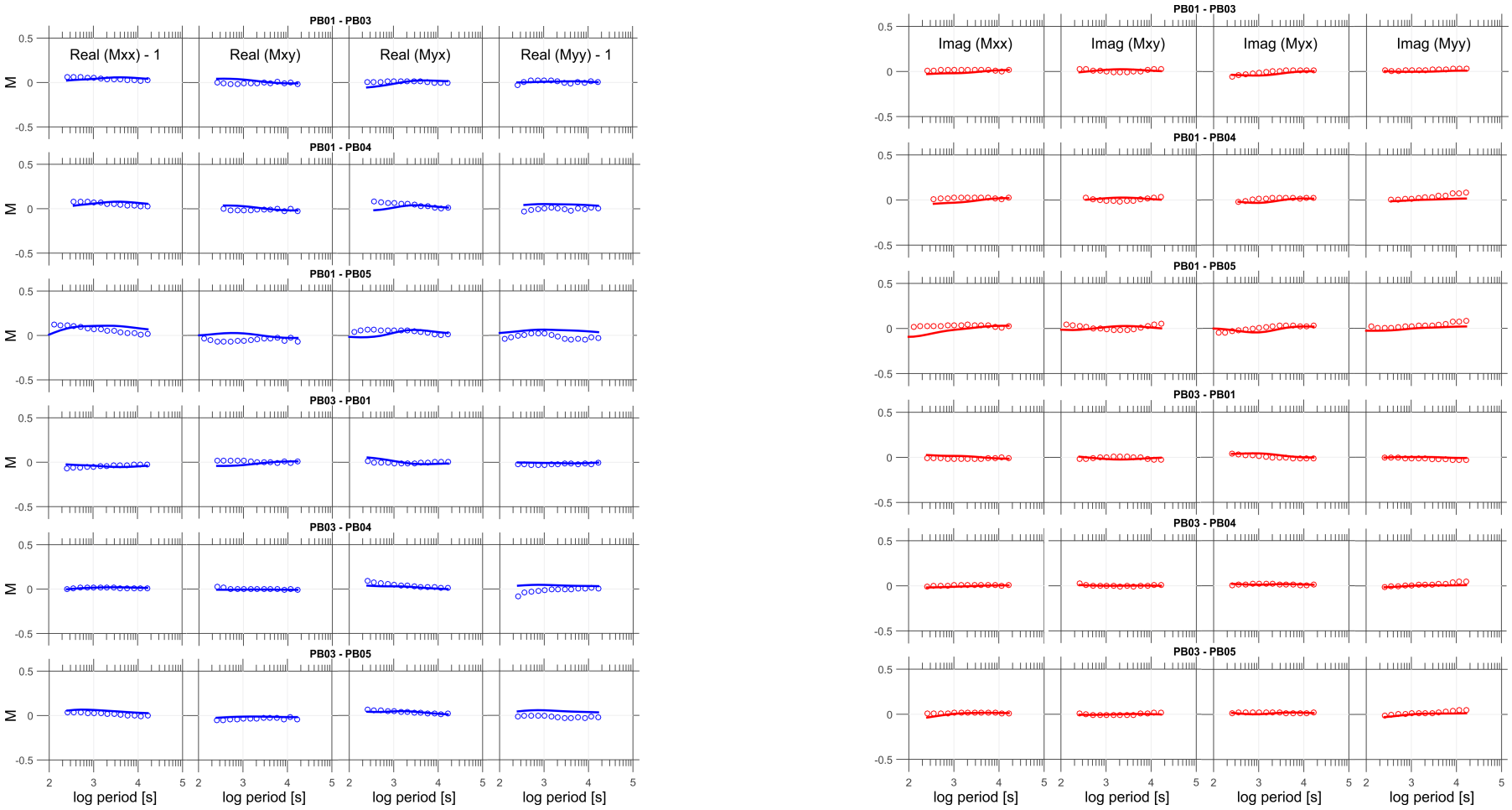

Figure 4.4: Comparison between observed (circles) and calculated (lines) horizontal magnetic transfer functions. Note that a value of 1 was subtracted from the $Real(Mxx)$ and $Real(Myy)$ components in order to show the same Y-axis range as the other components.

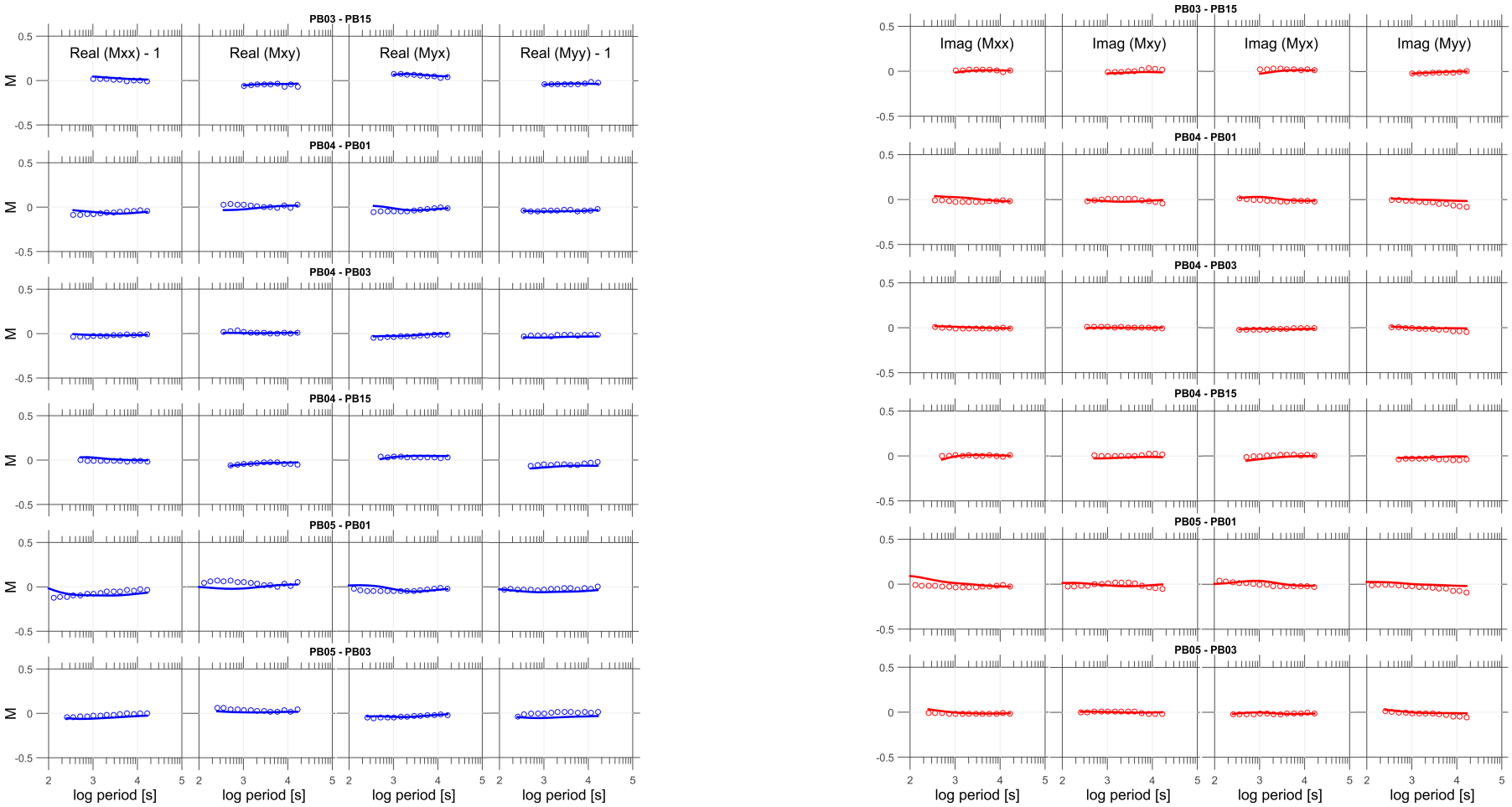

Figure 4.4: Figure 4.4 (Continued.)

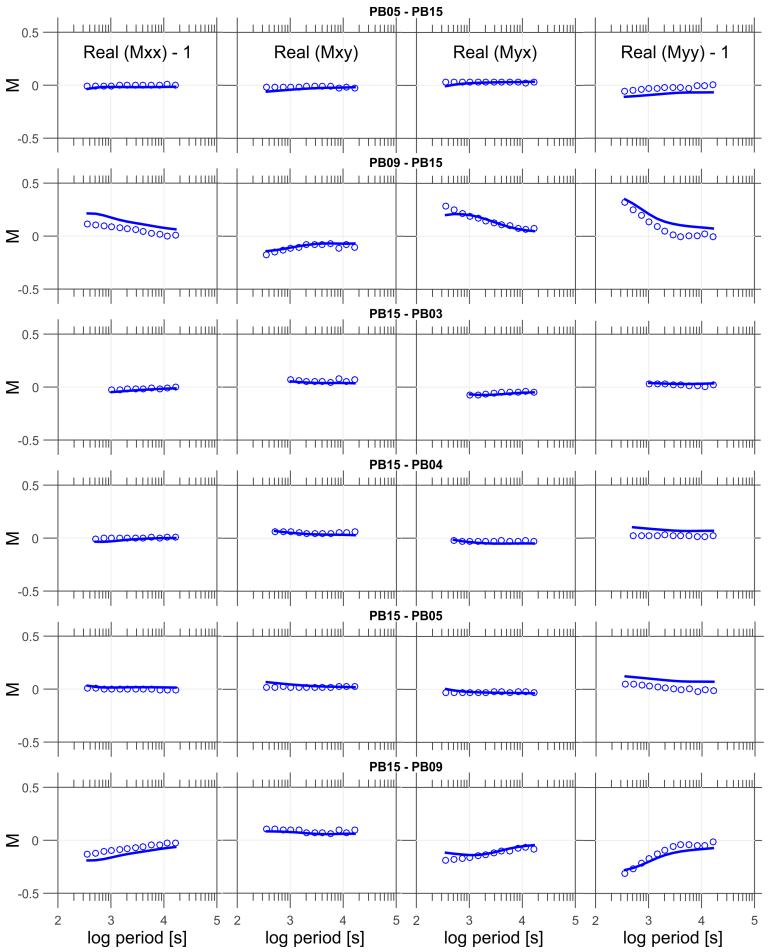

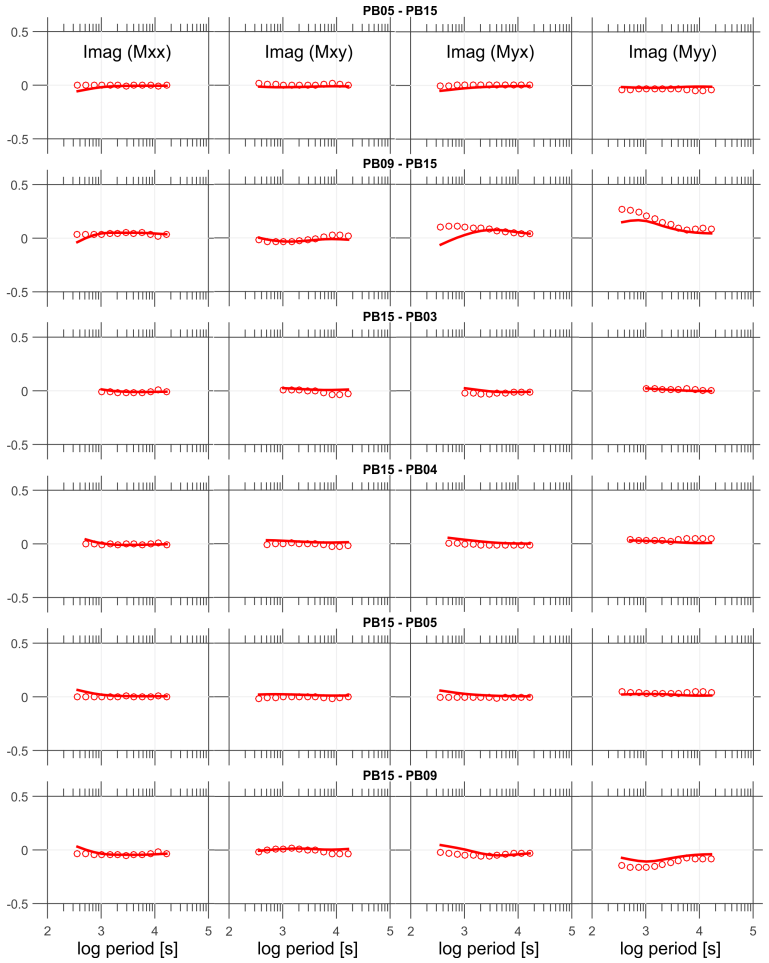

Figure 4.4: Figure 4.4 (Continued.)

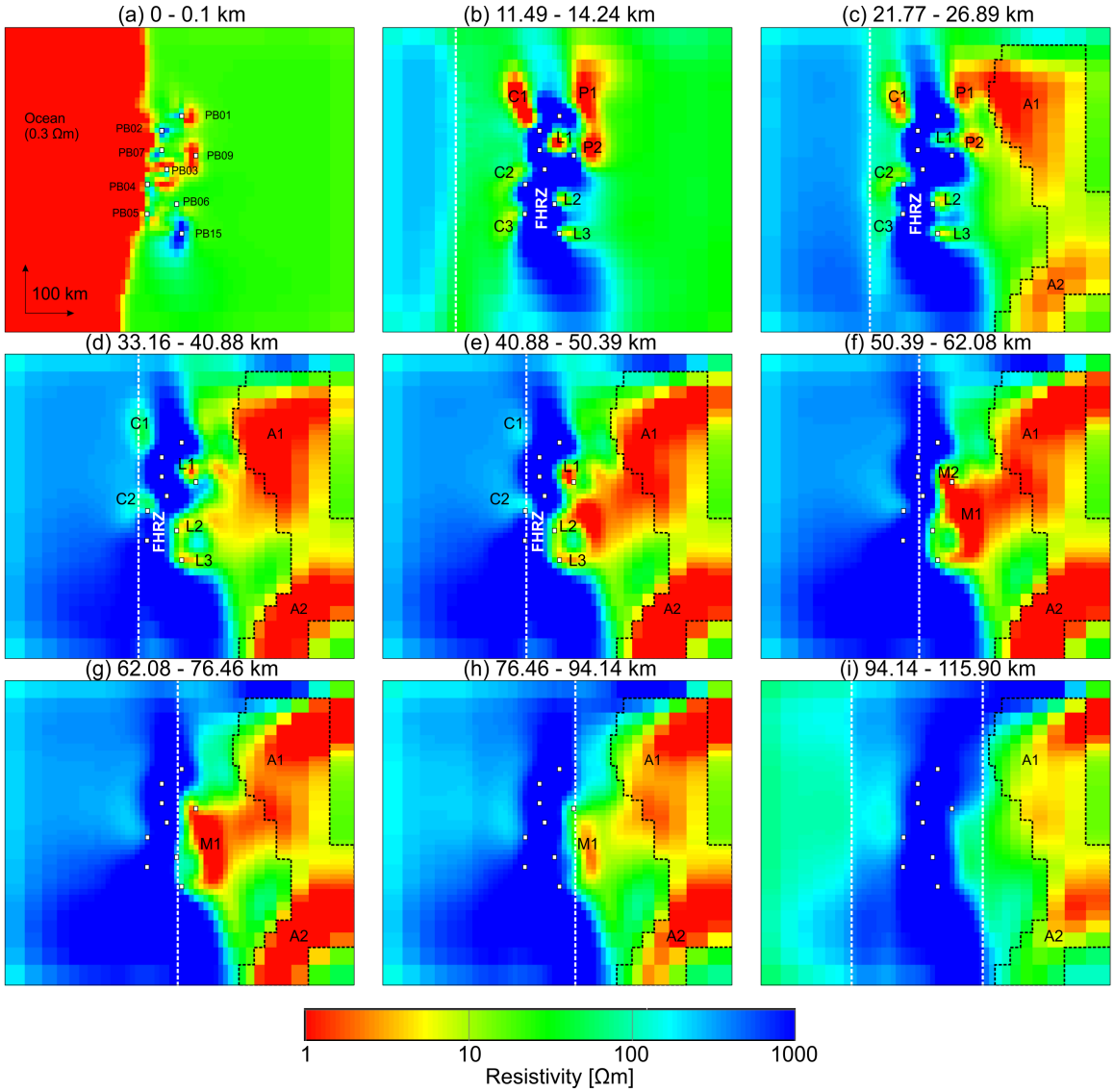

Figure 4.5: Selected horizontal layers of the preferred resistivity model. Resistivity slices are displayed using same color code as Figure 4.2. White squares are IPOC MT sites. White vertical dashed lines indicate western limit of the 1000 Ωm body included in the starting model to simulate the effect of the Nazca lithosphere. The left white vertical dashed lines shown in (i) indicates the eastern limit of the 1000 Ωm body. Polygons of black-dashed borders show the location of the 1 Ωm body included in the starting model to simulate the effect of the Altiplano conductive zone. Major resistivity features described in the text are labelled.

4.5 Sensitivity and resolution tests

Additional inversion modelling tests were run to assess the robustness of the aforementioned major resistivity features found in the preferred model. To test if shape and resistivity of the major features were really required by the data, in these additional tests some changes were introduced in the starting models, but all the other inversion parameters were not changed. The philosophy behind this strategy was to let the inversion decide whether a priori structures are compatible with the data or not. Figure 4.6 summarizes the main results of these additional inversion tests. All of these additional tests resulted in final

models and data fits which were generally very similar to the results obtained with the preferred model. This suggests that the data require a resistivity distribution close to our preferred model, regardless of further perturbations introduced in the starting models. However, the preferred model shows the smallest global RMS. The aim and results of these individual tests are described as follows:

Extent of FHRZ and robustness of C1 and C2 (Test1, global RMS = 2.19)

To test the robustness of the eastern margin of the FHRZ high resistivity domain and to determine if the data require the existence of C1 and C2, which are characterised by resistivities close to the background resistivity of the prior model (50 Ωm), a body of 500 Ωm (i.e. 10 times higher than background resistivity) was included in the starting model between surface and the top of the Nazca lithosphere. This a priori zone of high resistivity covers the region between the Altiplano and the ocean / Nazca plate in the east-west direction, and extends for almost 400 km in north-south direction (see left column of Figure 4.6a). If the data were not sensitive to the eastern margin of the FHRZ or the C1 and C2 anomalies, it was expected that the inversion would keep these regions of high resistivity (i.e. 500 Ωm). However, the inversion recovers a very similar depth section as in the preferred model (compare center and right columns of Figure 4.6a). It is concluded that the LRZ bodies C1 and C2 are required by the data and that the high resistivity of the FHRZ extends eastwards until the Precordillera. C1 is mainly required to fit the Z_{xy} component of site PB02. Unlike other IPOC sites, the ϕ_{xy} component at PB02 tends to increase for long periods $>$1000 s (see Figure 4.3). Such a phase pattern in ϕ_{xy} is consistent with data obtained by previous studies at sites located in the same area (e.g. sites ENG, FOR, GER, GLO, HDN, PEN and ROJ shown in Lezaeta, 2001; Soyer, 2002).

Along-strike extent of P1 and P2 (Test 2, global RMS = 1.89)

The preferred model shows LRZs P1 and P2 north of site PB09 (see Figure 4.5b-c). The aim of Test 2 was to determine whether the along-strike extent of P1 and P2 is a robust feature or just a consequence of a lack of stations in the Precordillera. In this test, the starting model included an a priori body of 1 Ωm extending in north-south direction in the Precordillera region along the entire extent of the array (SP body in left column of Figure 4.6b). The final model of Test 2 shows that the inversion tries to remove the a priori SP body south of PB09 (compare center and right column of Figure 4.6b). However, in contrast to the preferred model, Test 2 still shows some weakly expressed relicts of the a priori SP body south of site PB09 (e.g. east of site PB15 in center column of Figure 4.6b). This result suggests that an along-strike continuous LRZs would be generally compatible with the data, but with a considerably weaker overall resistivity contrast than P1 and P2.

Along-strike extent of M1 and M2 (Test 3, global RMS = 2.22)

A similar strategy was applied to examine the along-strike extent of LRZs associated with the forearc mantle wedge (M1 and M2), which appear in the preferred model approximately between sites PB09 and

PB15 (see Figure 4.5f-h): the starting model included an a priori body of 1 Ωm at similar location and depth as M1 and M2, but extending throughout the entire array (SM body in left column of Figure 4.6c). As before, it was expected that the inversion would keep only those parts of the a priori feature which are compatible with the data. The final model of Test 3 shows that low resistivities (∼1 Ωm) resembling the original extent of the SM body are kept approximately between PB09 and PB15 (see center column of Figure 4.6c). This result suggests that any LRZs in the forearc mantle north of PB09 (∼21.5°S) are incompatible with the data. This result is quite consistent with the along-strike extent of the M1 and M2 bodies of the preferred model. However, it is observed in the final model of Test 3 that the LRZ between PB09 and PB15 appears at the same position and width as SM in the starting model, i.e. it is located west of M1 (compare location of both bodies in center and right columns of Figure 4.6c). Consequently, it is conclude that a low resistivity zone (M1) is required by the data in this region, but its east-west extent is not well constrained. It is interesting to note that the final model of Test 3 (center column of Figure 4.6c) does not show a low resistivity region connecting the Precordillera and Altiplano regions. While such a connection appears in the preferred model (right column of Figure 4.6c), it is probably not well constrained by the data.

Screening effect of P1 and P2 on structures at lower depths (Test 4, global RMS = 2.21)

In the preferred model, the along-strike extent of the M1 body roughly coincides with segments of the Precordillera without any LRZs in the upper crust. Although Tests 2 and 3 suggested that the along-strike extent of P1, P2, M1 and M2 is required by the data, it was not clear if the shallower LRZs P1 and P2 could have a screening effect. To test this hypothesis, in Test 4 the starting model included both the SP and SM a priori bodies (see left and center columns of Figure 4.6d). If LRZs at upper crustal levels in the Precordillera screened resolution for deeper structures, it was expected that the inversion would keep the along-strike extent of the SM a priori body. However, the final model of Test 4 shows that the inversion modified the shape of the SM body significantly north of PB09 (see right column of Figure 4.6d). This result suggests that (i) the data are sensitive to these deep levels below the Precordillera and (ii) LRZs at the mantle wedge depth north of PB09 are inconsistent with the data. In summary, it is concluded that the along-strike extent of M1 is well constrained by the data, even in the northern part of the array where shallow LRZs are observed. Therefore, the existence of LRZs at ∼40 to 70 km depth beneath the Precordillera north of ∼21.3°S can be ruled out. This result is also consistent with the resistivity section along the 21°S shown in Brasse et al. (2002).

Resistivity of the plate interface (Test 5, global RMS = 1.96)

The preferred model shows zones of relatively low resistivity close to the top of the Nazca plate only at some particular regions of the subduction zone. Such segmented distribution of LRZs can be related to key dehydration processes which are interpreted along the subducting slab (e.g. Peacock, 1990). The aim of Test 5 was to evaluate if the distribution of LRZs along the top of the slab in the preferred model was a result of variability in the data resolution. To test the segmented distribution of such resistivity features,

the starting model of Test 5 included a layer of 5 Ωm on top of the oceanic slab (the low resistivity layer is labelled IP in Figure 4.7a). The starting model also included the AP, NP and the ocean bodies. It was expected that the inversion in Test 5 would keep segments of the IP body in areas of low data resolution. The final model obtained in Test 5 is very similar to the preferred model. In particular, no significant differences are observed along the top of the oceanic slab (compare Figures 4.7b and 4.7c). Remarkably, Test 5 shows also the FHRZ in contact with the Nazca plate, suggesting that generally zones of low resistivity along the plate interface are incompatible with the data. As in the preferred model, the final model of Test 5 shows a zone of relatively low resistivity mimicking the plate interface only close to site PB04 (Figures 4.7b and 4.7c).

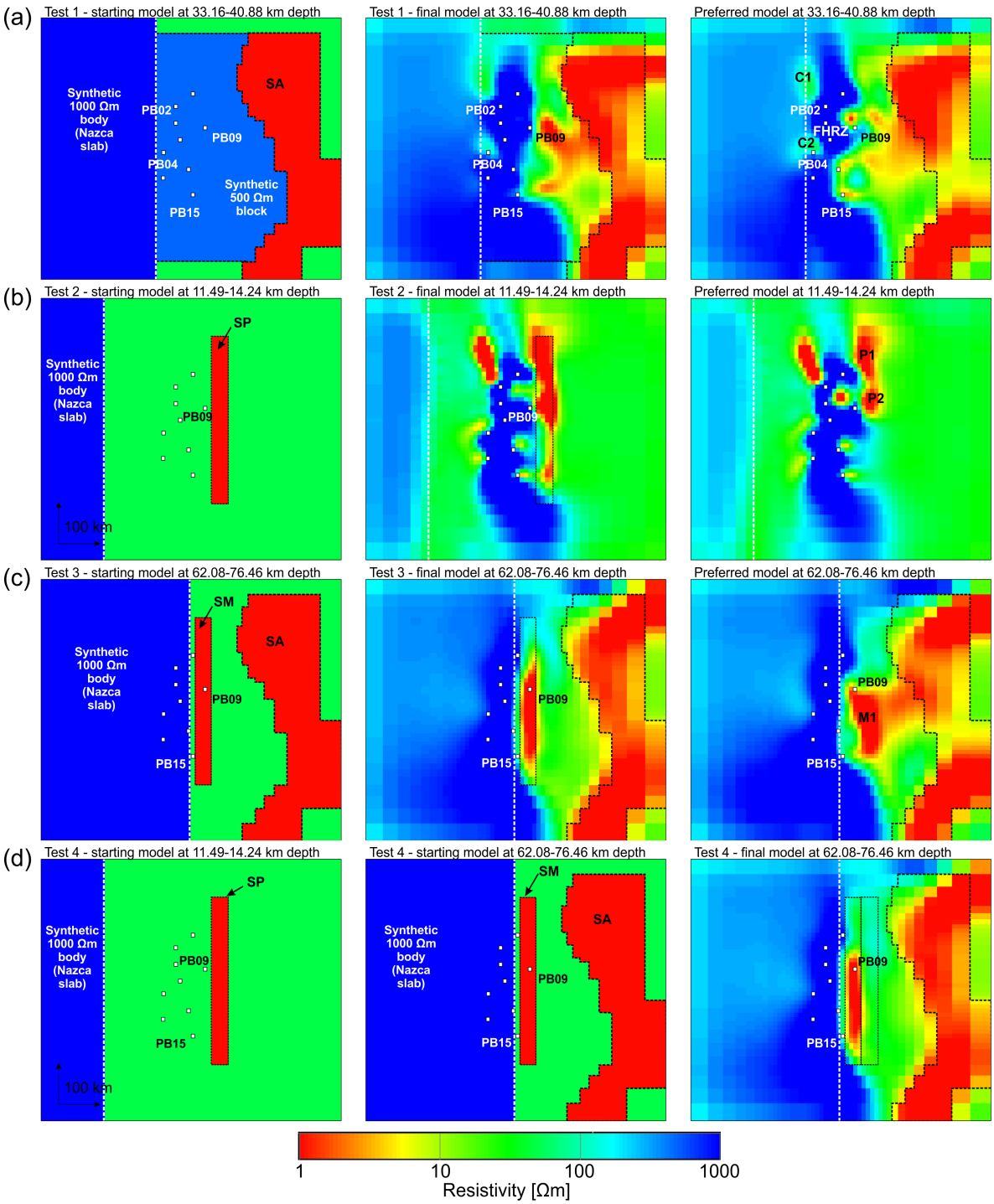

Figure 4.6: Test of major features obtained in the preferred resistivity model. Selected horizontal layers showing starting and final models obtained in alternative tests: (a) Test 1 (resistivity of the forearc and geometry of the C1 and C2), (b) Test 2 (along strike extent of the P1 and P2), (c) Test 3 (along strike extent of M1), and (d) Test 4 (screening effect of P1 and P2 on structures at lower depths). White vertical dashed lines indicate western limit of the 1000 Ωm body included in the starting models to simulate the effect of the Nazca lithosphere. Polygons of black-dashed borders show the location of additional bodies included in the starting models (see the text for details).

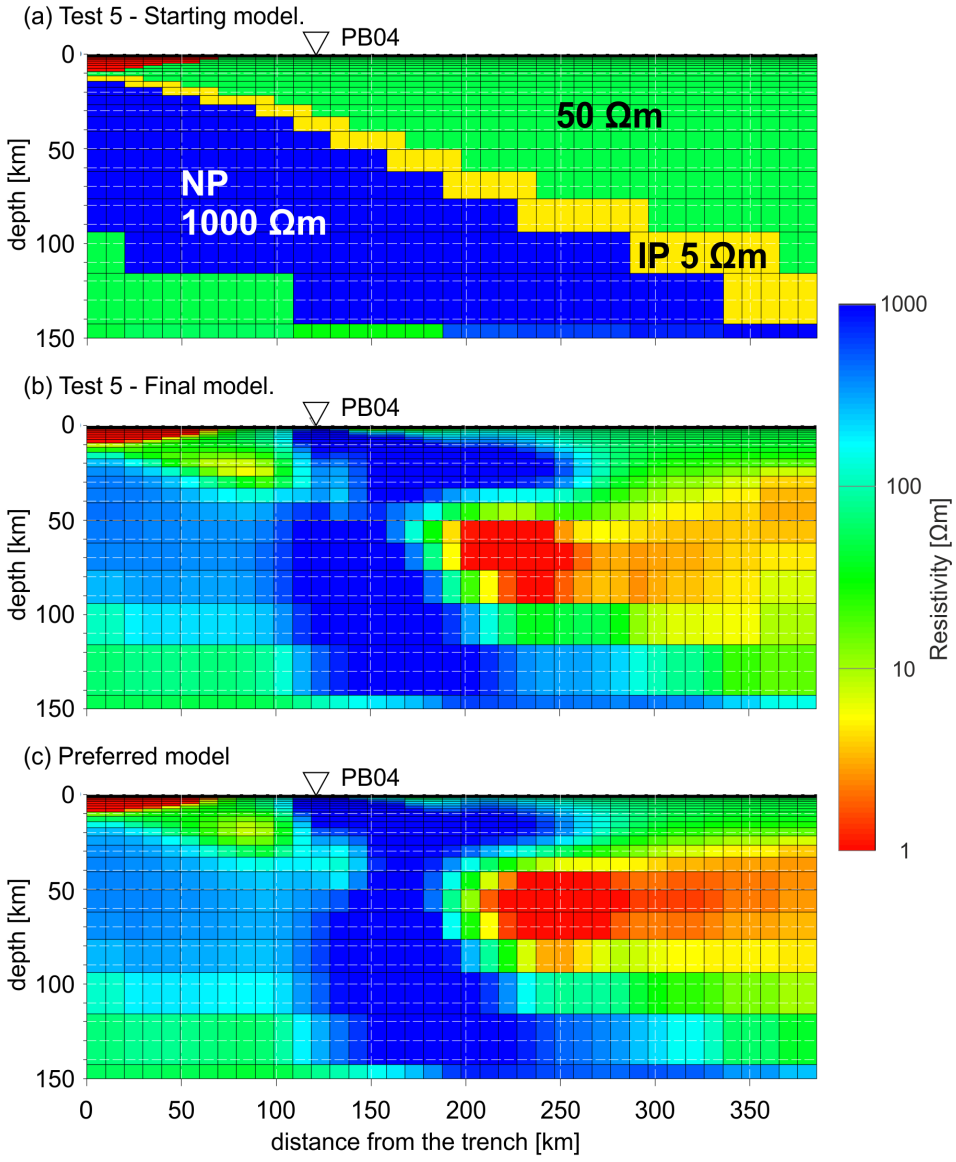

Figure 4.7: Sensitivity Test 5 (resistivity of the plate interface). Section crossing at site PB04 the: (a) starting and (b) final model of Test 5, (c) the preferred model.

4.6 Discussion

4.6.1 Consistency of resistivity model with previous MT studies

Figures 4.8a and 4.8b show depth sections of the preferred inversion model approximately at 21°S in comparison with resistivity models from previous MT studies. The small image on the left side of Figures 4.8a is a section taken from the resistivity model of Kühn et al. (2014) at ∼20.9°S, which was obtained using 3-D inversion modelling of data collected mostly along the Pica and ANCORP profiles (see location in Figure 4.1). The larger image on the right side of Figures 4.8a is taken from Brasse et al. (2002); it was obtained by 2-D inversion modelling of data collected along the ANCORP profile (see location in Figure 4.1). As can be seen from Figures 4.8a and 4.8b, the three sections are generally very consistent. All models exhibit a forearc below the Coastal Cordillera and the Longitudinal Valley which is characterised by high resistivities (>1000 Ωm). Below the Coastal Cordillera, the model of Kühn et al. (2014) shows a LRZ thinner than C1 of the preferred model. Lezaeta (2001) modelled in this region LRZs in a depth range between 0-20 km, which mainly followed branches of the Atacama Fault System (AFS). Along-strike variability in C1 could explain the difference in the vertical extent of the LRZ observed between sections. Both the preferred model and the model of Brasse et al. (2002) coincide in the location and shape of the eastern limit of the resistive forearc. In addition, both models show a LRZ in the upper crust of the Precordillera (approximately at 69°W in Figure 4.8a). The body P1 of the preferred model is larger than the respective LRZ in the model of Brasse et al. (2002), and also larger than the LRZ observed in the 3-D inversion model of the same dataset presented in Kühn et al. (2014) (not shown). This apparent discrepancy is likely caused by the poor site coverage of the IPOC data set. However, along-strike variations in the size of the LRZs located below the Precordillera cannot be ruled out. For instance, Brasse et al. (2002) interpreted a LRZ with a size comparable to the P1 body along the PICA MT profile, which crosses the Precordillera at ∼20°S (see location in Figure 4.1).

Brändlein (2013) obtained a resistivity model of the forearc by 3-D inversion of impedances and VTF data from eight of the IPOC sites; at that time HTFs and data from PB15 were not included. The model of Brändlein (2013) shows a resistive forearc region below the Coastal Cordillera and Longitudinal Valley, which is consistent with the models shown in Figures 4.8a and 4.8b. An important feature interpreted by Brändlein (2013) is a LRZ located at ∼30-70 km depth, extending below the Longitudinal Valley approximately between sites PB02 and PB06. The depth and along-strike extent of this LRZ roughly coincides with M1 of the preferred model. However, M1 is located east of the LRZ found by Brändlein (2013) and it seems to be located on top of the Nazca slab. This distinction in size and location of these bodies in the forearc mantle wedge can probably be attributed to differences in the inversion setups. Brändlein (2013) used a much coarser model discretization (with a minimum cell size of 15 km) and he did not include the resistive Nazca slab as a priori information. The latter seems to be important to constrain the vertical extent of M1 in the preferred model. Another major difference between these two modelling approaches is related to handling the ocean. It is possible that a shift in the LRZ was introduced because the inversion tried to compensate for lack or excess in conductance caused by an over-simplified 2D bathymetry model of the ocean used by Brändlein (2013).

All of the inversion tests conducted in this thesis consistently resulted in models showing LRZs below the Altiplano, even when a priori structures were not included in the starting model. This low resistivity feature is very robust and has an enormous influence on the characteristic of the EM fields observed at the IPOC MT sites. The inclusion of a continuous anomaly simulating the Altiplano LRZ in the starting model (e.g. Figure 4.2d) was not maintained by the inversion. Shape and resistivity of this body was always significantly altered, in most cases two separate LRZs appeared (e.g. A1 and A2 in Figures 4.5c-i). It is interesting to note that A1 is consistent with the LRZs described by Brasse et al. (2002) and Kühn et al. (2014) between 20° and 21°S, while anomaly A2 seems to coincides with the LRZ modelled at ∼23.7°S by Díaz et al. (2012).

4.6.2 Interpretation of main resistivity features

There are remarkable spatial correlations between most of the main resistivity features of the preferred model and major lithospheric structures described by independent geological, geophysical and geochemical studies. Figures 4.8 to 4.12 show sections and maps of the resistivity preferred model in comparison with some of these features. For reference the figures show locations of earthquakes with magnitude >2, registered between January 2007 and December 2013, downloaded from the catalogue of the Centro Sismológico Nacional (CSN, http://www.sismologia.cl), the Chilean Seismological Survey. This time span of seismic activity is comparable with the time of deployment of the IPOC MT array.

Forearc high resistivity zone (FHRZ)

The forearc high resistivity zone (FHRZ) with resistivities >1000 Ωm and a thickness >50 km, located west of the Precordillera, is one of the most important and robust features observed along the entire forearc. While zones of high resistivity are generally not well resolved by the MT method, the FHRZ is well constrained. The east-west extent is defined because the structure is sandwiched by low resistivity structures (e.g. C1 and P1/P2 in Figure 4.8). The general level of resistivity seems robust based on the results of the resolution Test 1 (4.5). The inversion tests show that the FHRZ extends from upper crustal levels to the top of the slab. The FHRZ appears to be a relatively homogeneous crustal block of high resistivity, with poor variability besides the presence of some LRZs structures (see discussion in the next subsection). Structures with similar characteristics to the FHRZ were modelled by other MT studies from different segments of the northern Chile forearc (Lezaeta, 2001; Brasse et al., 2002; Brasse and Eydam, 2008; Díaz et al., 2012).

The FRHZ correlates spatially with distinct density and seismic anomalies, which differentiate this domain from the Precordillera region. The areal extent of the FHRZ coincides with a positive isostatic residual gravimetric anomaly observed along the coastal region of northern Chile (e.g. Götze and Krause, 2002). West of the Longitudinal Valley - Precordillera (LV-PC) boundary, the FHRZ roughly matches comparatively denser blocks modelled by Schaller et al. (2015) in the middle crust (see polygons of white dashed boundaries in Figures 4.9c, 4.10a and 4.10c). East of the LV-PC boundary, the preferred resistivity model shows high resistivity zones at crustal levels in areas where Götze and Krause (2002)

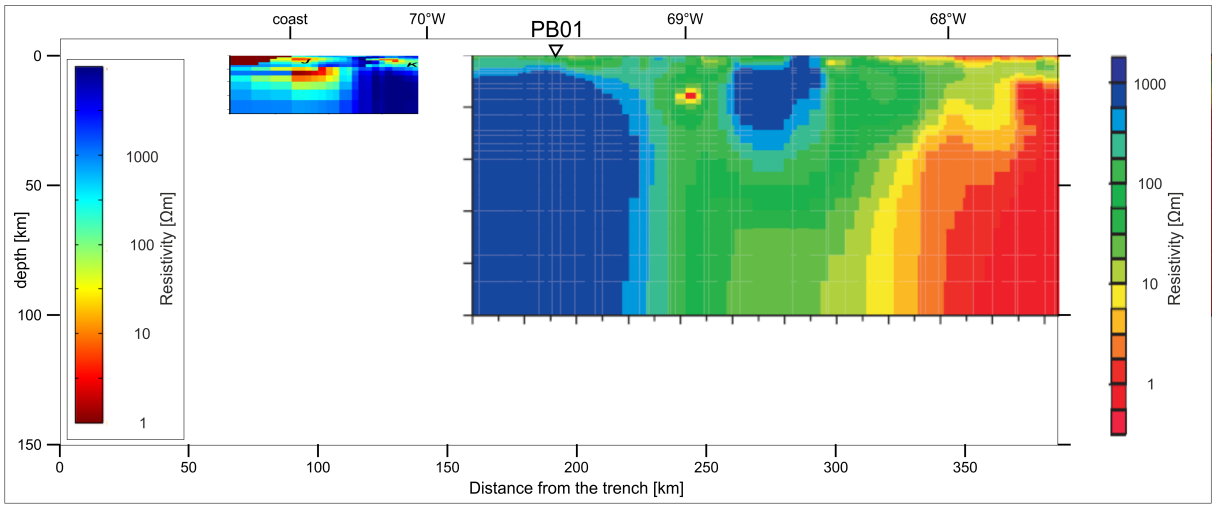

(a) E-W section at ∼21°S MT models: Kühn et al. (2014) (left) and Brasse et al. (2002) (right).

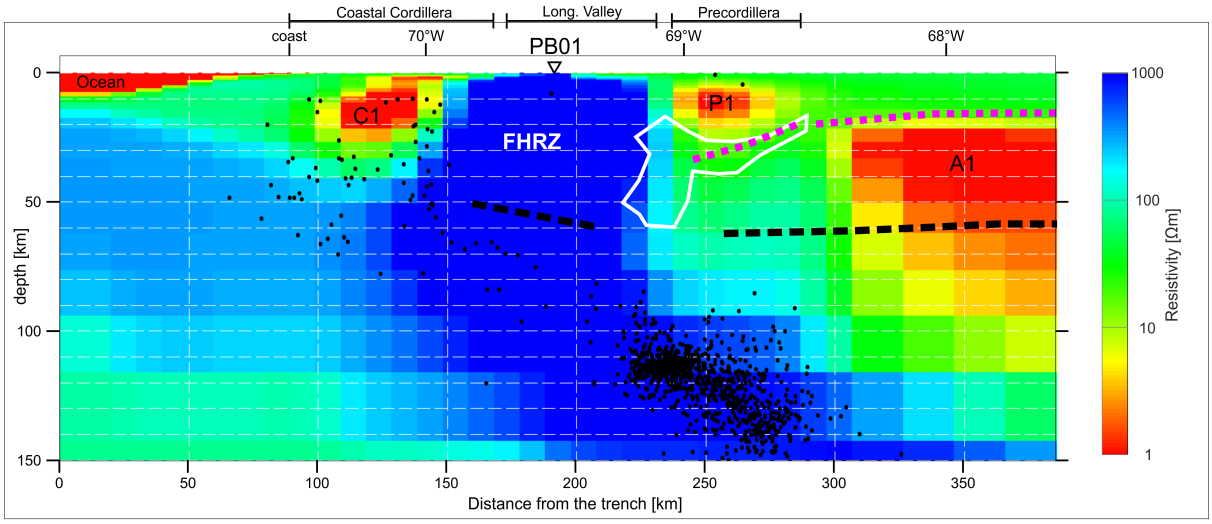

(b) E-W section at 21°S MT model (this work).

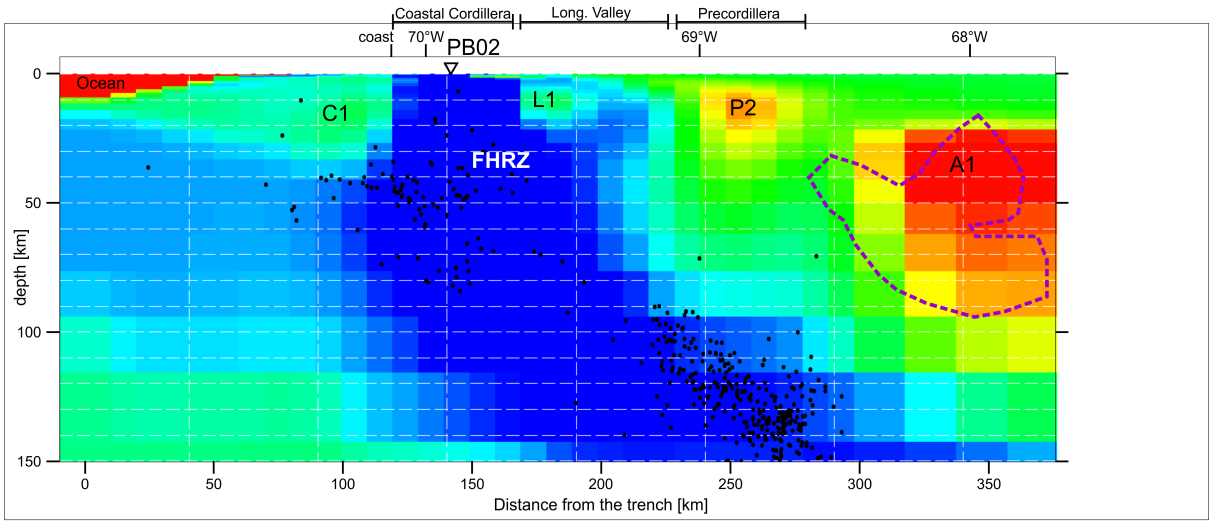

(c) E-W section at 21.3°S MT model (this work).

Figure 4.8: (Caption in next page.)

describe the Central Andean Gravity High (CAGH, see Figures 4.9b-c, 4.10a-c, 4.11c, 4.12a-c), a regional positive anomaly of the isostatic residual gravity, which was explained by a high density body located at depths between 10 and 38 km.

Seismological studies along the central Andes have also documented lateral contrasts in the seismic properties of crustal levels between the Precordillera and the western forearc. Generally, these works describe the western forearc as a domain characterised by comparatively high P and S wave velocities and low seismic wave attenuation (e.g. Schurr et al., 2003; Koulakov et al., 2006). Based on seismic properties of the western forearc and complemented with thermal models of the subduction zone (e.g. Springer, 1999), it was suggested that this region represents a rigid and cold block (e.g. Schurr et al., 2003). In a subduction environment, the arc represents a hot region where more circulation of fluids is expected. Both increasing amount of fluids and increasing temperature are factors that usually tend to decrease the resistivity of rocks. Therefore, the proximity of the Precordillera to the arc may partly explain the contrasting resistivity between this domain and the FHRZ. However, it cannot be rule out that resistivity contrasts between the FHRZ and the Precordillera could also reflect large scale differences in rock composition. Geochemical and gravimetric data suggest that the Coastal Cordillera is characterised by a predominance of bulk mafic composition, which contrasts with a more felsic composition interpreted for the Altiplano-Puna Plateau region (Mamani et al., 2008).

Crustal low resistivity zones below the Coastal Cordillera and Longitudinal Valley

At crustal depths, several low resistivity zones are observed within the FHRZ along the Coastal Cordillera (C1, C2 and C3 in Figures 4.5, 4.8-4.13) and the Longitudinal Valley (L1, L2 and L3 in Figures Figures 4.5, 4.8-4.13). These LRZs are isolated features which cannot be connected as a single LRZs extending along the entire study area, otherwise some patterns observed in the data would not be reproduced. The preferred inversion model shows very low resistivities of <5 Ωm in the upper crust at L1, L2 and L3 (see e.g. Figure 4.11b) which seem to coincide with depocenters along the Longitudinal Valley basin. For instance, L1 spatially coincides with an area where Sáez et al. (1999) interpreted maximum thickness in the Cenozoic infill of the Quillagua-Llamara basin (Figure 4.13). At least the shallow part of C1 could be explained by the occurrence of sediments of the Salar Grande basin (Figures 4.11a and 4.13).

The geological interpretation of C2, C3, and the lower part of C1, is not straightforward. These anomalies

Figure 4.8: (Previous page) Comparison between sections through the preferred resistivity model and independent geological and geophysical information. Panel (a) compiles resistivity sections from Kühn et al. (2014) and Brasse et al. (2002). Resistivity sections in (b) and (c) cross the preferred model at 21°S and 21.3°S, respectively. Black dots in (b) and (c) are hypocentres located within 10 km of the displayed sections. Displayed seismic events are earthquakes with magnitude M >2 registered between January 2007 and December 2013, downloaded from the catalogue of the Centro Sismolgico Nacional (CSN, http://www.sismologia.cl). Black dashed-, purple dotted- and magenta dotted- lines in (b) are the continental Moho, QBBS and top of the ALVZ reflectors taken from ANCORP Working Group (2003) (see the text for details). White polygon indicates high seismic reflectivity zone interpreted by Yoon et al. (2009). Purple dashed line in (c) is the boundary of a high seismic attenuation anomaly, obtained from zones where section at 21.3°S of Schurr et al. (2003) shows values of the seismic quality factor Qp $<$200.

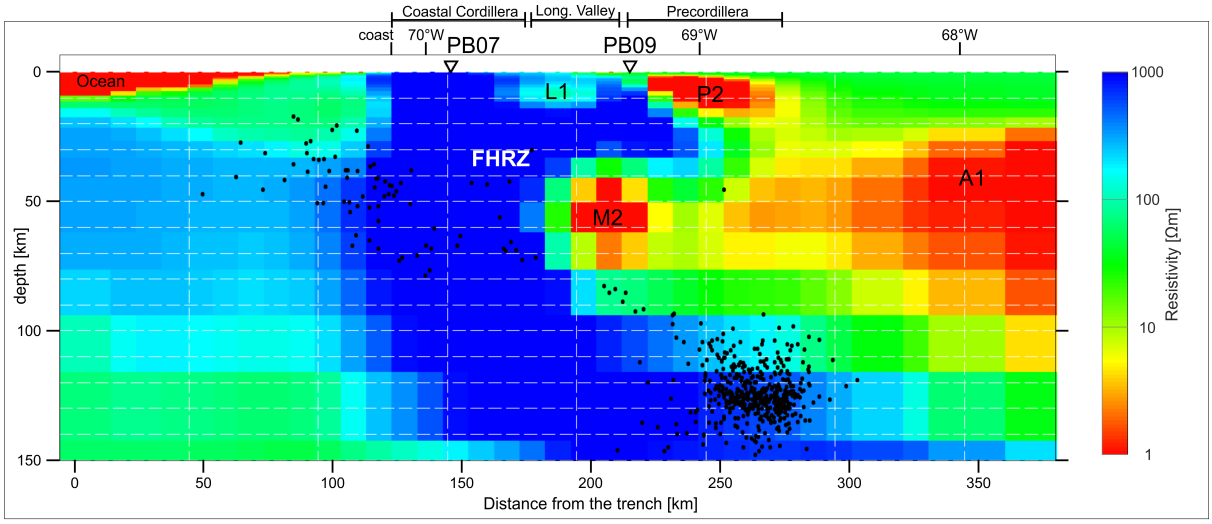

(a) E-W section at ∼21.75°S MT model (this work).

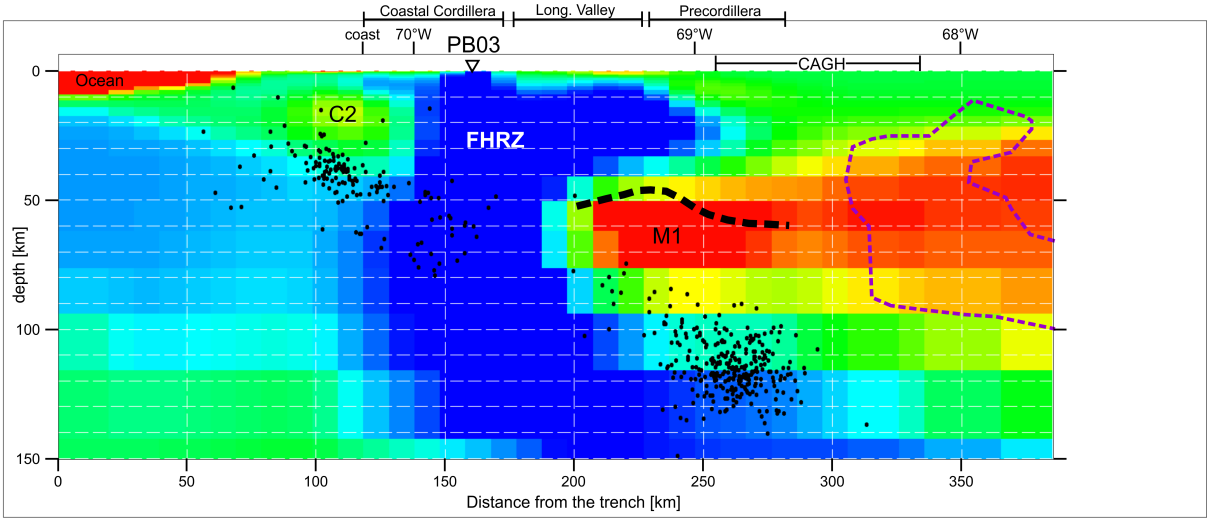

(b) E-W section at 22°S MT model (this work).

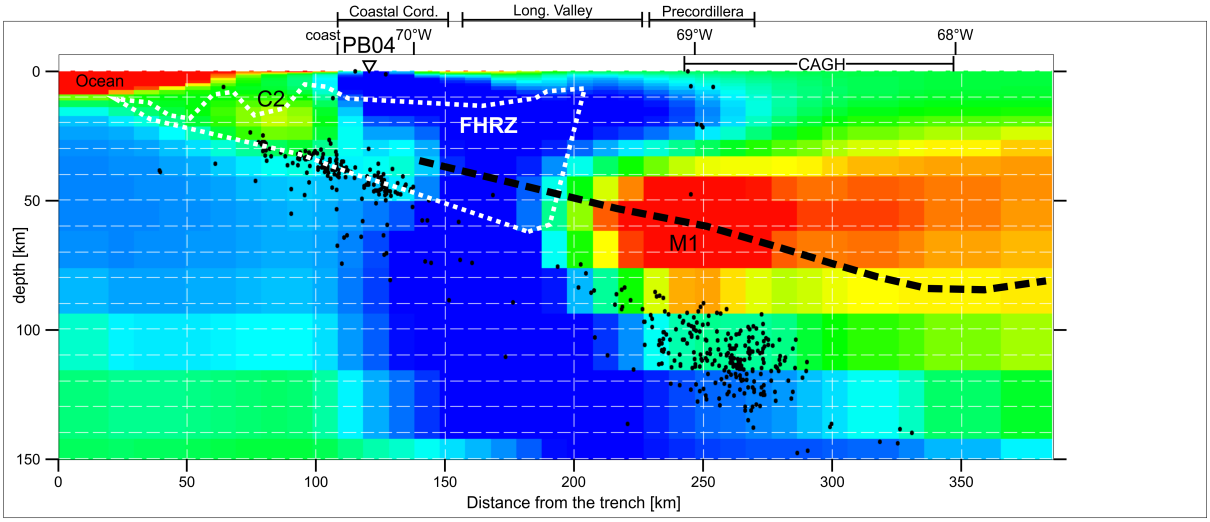

(c) E-W section at ∼22.3°S MT model (this work).

Figure 4.9: (Caption in next page.)

are associated with segments of the Coastal Cordillera where no evident variations in the regional geology are observed. The north-south extent of C2 correlates spatially with the rupture limits of the 1967 M7.4 and the 2007 M7.7 Tocopilla earthquakes (see Figure 4.12b). Similarly, the southern boundary of the 2014 M8.1 Iquique earthquake's rupture area crosses below C1 (see Figures 4.12b). In both cases, the down-dip limit of the earthquakes' rupture area appears spatially correlated with the eastern limits of these low resistivity zones. Although the bottom of a LRZ is difficult to resolve with MT, the results of Test 1 suggest for these LRZs a depth of at least 40 km with resistivities approximately 30 times smaller than the FHRZ (see Figure 4.6a and 4.5). The anomalies C1 and C2 can probably be best explained as high permeability zones in the otherwise rigid and strong forearc, which could contain fluids generated by metamorphic processes at the lower crust or even at the plate interface.

Low resistivity zones in the forearc mantle

The anomalies M1 and M2 define low resistivity zones extending more or less continuously between 21.5°S and 23°S (Figure 4.12 c-e). Their locations and vertical extents coincide roughly with the position of the forearc mantle wedge derived from seismic studies (e.g. Yuan et al., 2000; ANCORP Working Group, 2003; Sodoudi et al., 2011). At 22°S the top of M1 matches the continental seismic Moho found by Sodoudi et al. (2011) (Figure 4.9b), but at 22.3°S and 23.2°S M1 appears to be crossed by the continental Moho found by Yuan et al. (2000) (Figures 4.9c and 4.10c). Both, M1 and M2 coincide with zones of anomalously low Vp and Vs described below the LV-PC boundary by Koulakov et al. (2006) (Figure 4.12d). The spatial match between M1 and the region of low seismic velocities could suggest a common source for both anomalies. Low resistivities ($<$5 Ωm) and relatively low Vp and Vs at the depth range of M1 and M2 can be explained with the presence of fluids and/or melts. M1 and M2 are located farther west of high seismic attenuation anomalies (see purple dashed lines in Figures 4.8c, 4.9b, 4.10a, 4.10b) reported by Schurr et al. (2003), which these authors interpreted as fluid and melt pathways feeding the arc. Therefore, it seems that M1 and M2 are more likely related to fluids. Reynard et al. (2011) suggested that processes associated with dehydration of the slab and serpentinisation of the mantle can release fluids with high salinity and therefore low resistivity, which in turn can explain the low resistivity zones interpreted in the forearc mantle wedge of subduction zones by various studies.

Low resistivity zones in the Precordillera

P1 and P2 define low resistivity zones following roughly the Precordillera Fault system (PFS), north of $\sim$22°S (Figure 4.13). P1 and P2 occur at depths between 10 and 20 km and are characterised by

Figure 4.9: (Previous page) Same as Figure 4.8, but sections at latitudes (a) $\sim$21.5°S, (b) 22°S, (c) $\sim$22.3°S. Black dashed lines in (b) and (c) are the continental Moho reflectors described by Sodoudi et al. (2011) at 22°S and by Yuan et al. (2000) at $\sim$22.4°S, respectively. Purple dashed line in (b) is the boundary of a high seismic attenuation anomaly, obtained from zones where section at 22.1°S of Schurr et al. (2003) shows Qp $<$200. White dashed lines in (c) show the border of the middle-crust high-density block modelled by Schaller et al. (2015) in the forearc at $\sim$22.5°. The segment where sections (b) and (c) cross the CAGH anomaly is indicated.

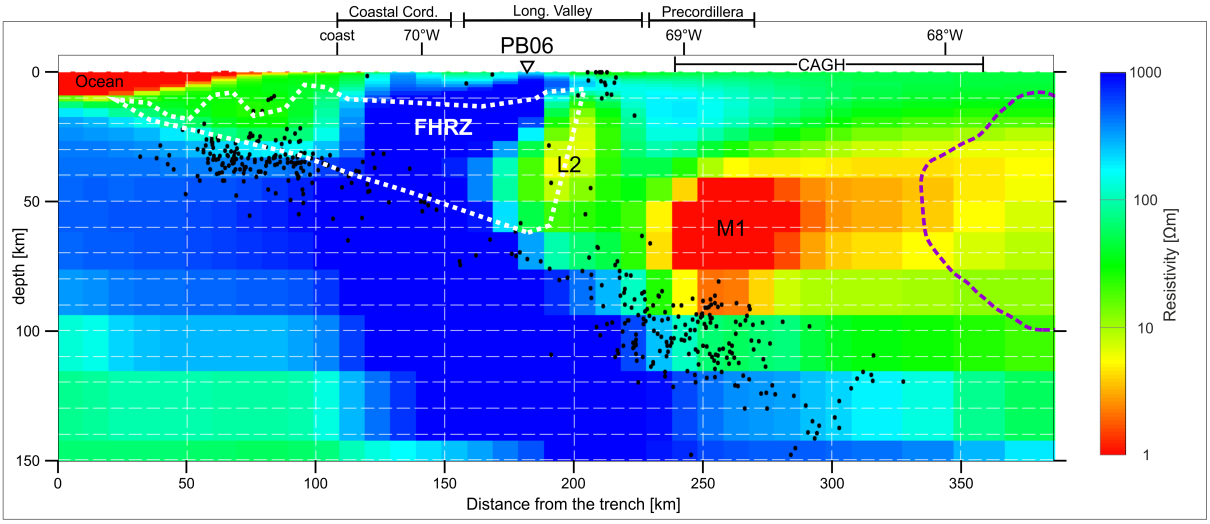

(a) E-W section at ∼21.75°S MT model (this work).

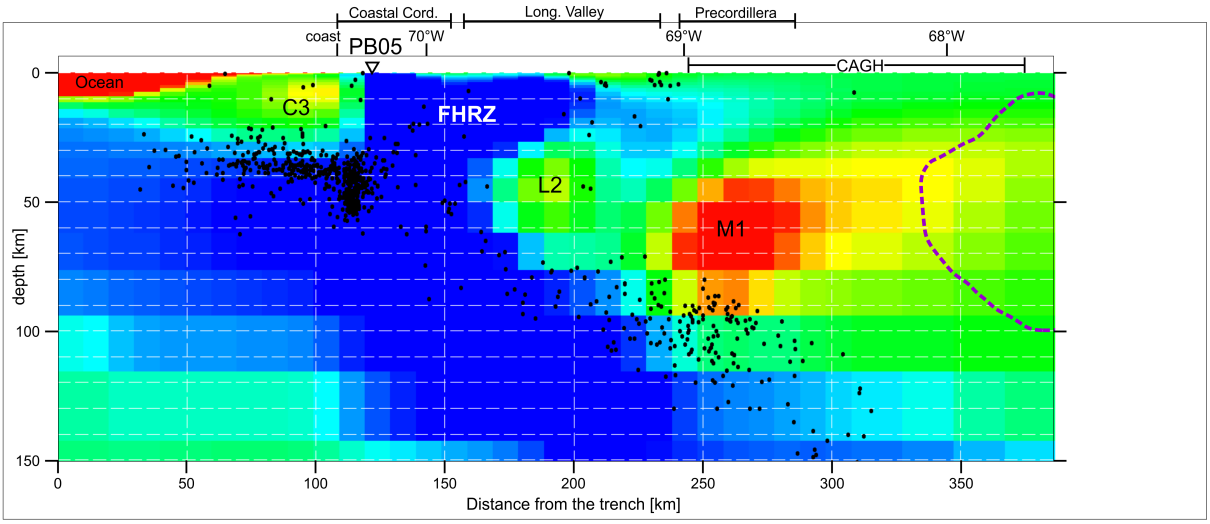

(b) E-W section at 22°S MT model (this work).

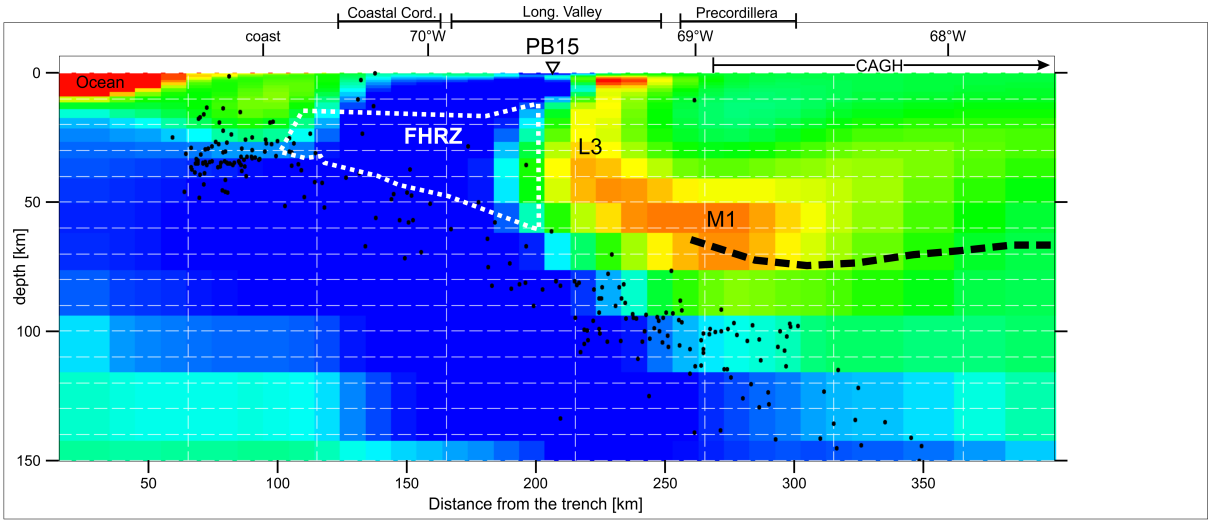

(c) E-W section at ∼22.3°S MT model (this work).

Figure 4.10: (Caption in next page.)

resistivities <5 Ωm (see Figure 4.11c). P1 appears approximately at the same location, but larger in size, as the Precordillera conductor modelled by Soyer and Brasse (2001), Brasse et al. (2002), and Kühn et al. (2014). These regions of low resistivity correspond with clusters of crustal seismicity reported in Salazar (2011) and Bloch et al. (2014). The lower boundary of these seismic clusters occurs at a depth of ∼20 km, which coincides with the top of the high seismic reflectivity anomaly interpreted by Yoon et al. (2009) (see polygon of white boundaries in Figure 4.8b). It has been interpreted that this seismic activity evidences fluids migrating along weak zones in the shallow crust (PFS), fluids which are fed by deep conduits and large scale faults that may reach the plate interface (Yoon et al., 2009; Bloch et al., 2014; Schmelzbach et al., 2016). An abundance of fluids at depths <20 km is consistent with low resistivities and the vertical extent of P1 and P2. However, the preferred model and previous MT studies would be incompatible with a sub-vertical fluid path suggested by Yoon et al. (2009), as it coincides with the transition between the FHRZ and intermediate resistivities observed below the Precordillera at lower crustal levels (see Figure 4.8b).

4.6.3 Large-scale distribution of fluids along the subduction forearc

There is general agreement that large amount of fluids is generated and released along the top of the slab due to dehydration processes of the subducted oceanic lithosphere (e.g. Peacock, 1990). The amount of released fluids increases at regions where key dehydration reactions can occur. Peak production rates of fluids in the forearc are expected for the transition from smectite to illite/chlorite, which occurs approximately at a distance of 100 km from the trench in cool subduction environments (such as northern Chile), and where the porosity of the oceanic crust collapses, approximately between 200 and 250 km from the trench (see e.g. Hyndman and Peacock, 2003). The locations of M1 and M2 are approximately 200 km from the trench (see Figures 4.9 and 4.10) and it is therefore plausible that low resistivities in these regions are associated with high volumes of fluids released by collapse of the slab porosity.

The absence of a low resistivity zone associated with the mantle wedge north of 21.5°S (see Figures 4.8 and 4.12c-e) remains elusive as seismic studies suggest that the forearc mantle at 21°S is serpentinised (e.g. ANCORP Working Group, 2003). To reconcile these observations, here it is speculated that fluid released from the slab were enough to hydrate mantle rocks (explaining seismic models), but free fluid remaining from mantle serpentinisation was insufficient to cause a significant low resistivity anomaly. Figure 4.11c shows that the northern boundary of M1 (approximately at 21.5°S) spatially coincides with a segment of the intermediate-depth seismogenic zone where relatively less and deeper earthquakes are registered. The intermediate-depth seismicity observed in subduction systems could be due to fluids released by dehydration reactions related to eclogitization (e.g. Hacker et al., 2003). This suggests that

Figure 4.10: (Previous page) Same as Figure 4.8, but sections at latitudes (a) ∼22.7°S, (b) 22.9°S, (c) ∼23.2°S. White dashed lines show the border of the middle-crust high-density block modelled by Schaller et al. (2015) in the forearc at (a) ∼22.5°S and (c) ∼23.3°S. Purple dashed line in (a-b) is the boundary of a high seismic attenuation anomaly, obtained from zones where section at 22.8°S of Schurr et al. (2003) shows Qp <200. Black dashed lines in (c) is the continental Moho reflector interpreted by Yuan et al. (2000) at ∼23.4°S. The segment where sections cross the CAGH anomaly is indicated.

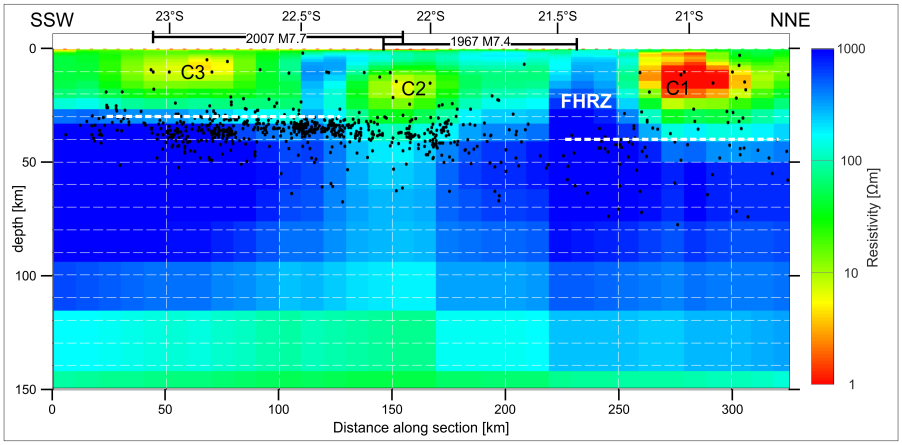

(a) NNE-SSW section crossing the Coastal Cordillera.

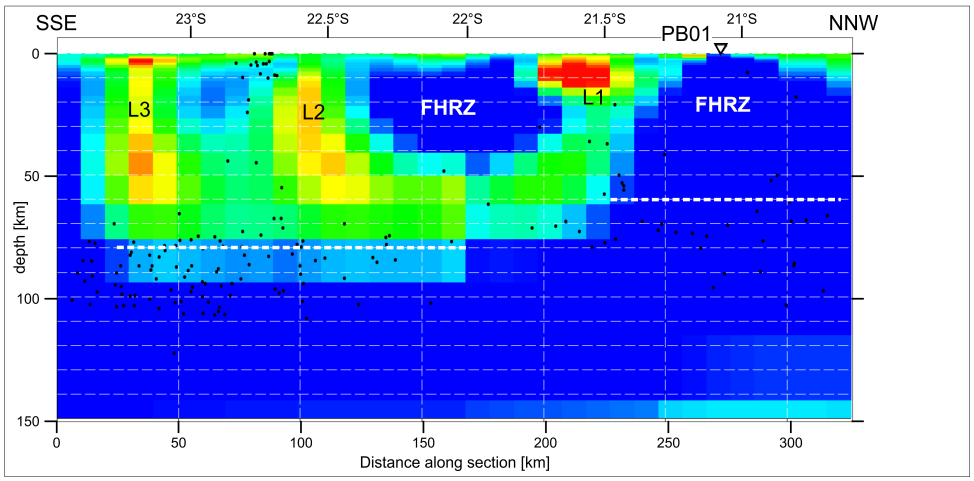

(b) NNW-SSE section crossing the Longitudinal Valley.

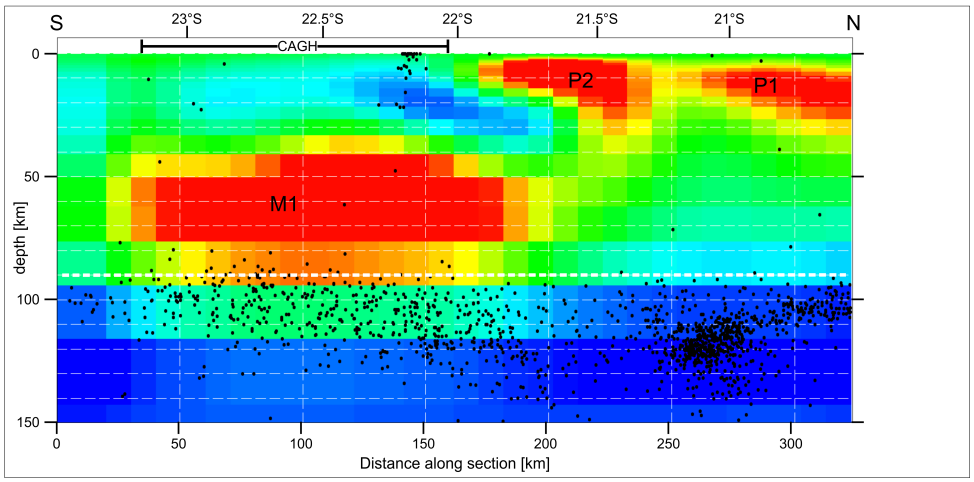

(c) N-S section along the Precordillera at ∼68.9°W.

Figure 4.11: (Caption in next page.)

reasons for a comparatively lower production rate of fluids inferred north of 21.5°S could be related to along-strike variability in the fluid content or in physical properties of the oceanic plate (see Figure 4.14). Völker and Stipp (2015) suggested that along-strike variability in the age and thermal state of the oceanic slab determines significant variations in the amount of fluids released in the forearc region of central and southern Chile. These authors interpreted that larger amounts of fluids are released in the forearc when younger and hotter slab segments are subducted. However, isochrones of the ocean floor (Müller et al., 1997) show that the age of the Nazca plate along the trench does not significantly vary in the study area. Regional heterogeneities of the oceanic lithosphere (e.g. large fault zones) could also cause variations in the amount of fluids transported and released by the slab. However, the inferred transition in the mantle wedge fluid content at ∼21.5°S is not spatially matched by major structural features interpreted in the Nazca plate along northern Chile (e.g. by the Iquique ridge and the Mejillones fault zone, interpreted in Contreras-Reyes and Carrizo, 2011; Maksymowicz, 2015).

The western limit of the FHRZ is located on average at ∼100 km from the trench (see Figures 4.8 to 4.10), at a distance where mineralogical models predict massive production of fluids along the plate interface due to dehydration of clay minerals contained in subducted sediments (e.g. Hyndman and Peacock, 2003). However, the trench of northern Chile is generally depleted of sediments (e.g. von Huene and Ranero, 2003). It has also been suggested that fluids can migrate from the slab into the continental lower crust during episodic fluid flow events triggered by large subduction earthquakes (e.g. Husen and Kissling, 2001). Here it is speculated that the intermediate to low resistivities observed west of the FHRZ are caused by free fluids or minerals associated to current or past migration of fluids, which are generated at the plate interface. The presence of low resistivity zones at along-strike constrained segments of the coastal region (C1, C2 and C3), however, suggests that relatively more favourable conditions to channelize and concentrate such fluids are present at some discrete areas of the continental crust above the plate interface.

4.6.4 Role of crustal heterogeneities in the distribution of fluids and deformation in the crust

The low resistivity zones modelled below the Coastal Cordillera and the Longitudinal Valley correlate spatially with NW-SE trends observed in the distribution of crustal seismicity. This NW-SE trend seems to be concentrated to regions where the generally high seismicity following the Coastal Cordillera branch out towards the east (Figure 4.13). One of these NW-SE oriented branches of high seismicity crosses the LRZs C1 and L1, and coincides spatially with the Calama-Olacapato-El Toro fault system (see labels COT and *trend 1* in Figure 4.13). In the Precordillera and backarc region, previous studies have

Figure 4.11: (Previous page) Same as Figure 4.8, but longitudinal sections crossing the (A) Coastal Cordillera, (B) Longitudinal Valley and (C) Precordillera (see section location in Figure 4.12a). White dashed lines show the top of the oceanic slab since Hayes et al. (2012). Arrows in (A) indicates the approximate rupture length of the 2007 M7.7 and 1967 M7.4 earthquakes. The northern/southern limit of the 1995 M8.0 Antofagasta / 2014 M8.1 Iquique earthquakes rupture area are located approximately at the beginning/end of the section. The segment where the section C crosses the CAGH anomaly (Götze and Krause, 2002) is indicated.

documented concentration of crustal seismicity along structures related to the COT (Schurr et al., 1999; Yáñez et al., 2008). It has been suggested that this regional structural feature must have played a key role in controlling the distribution of deformation, magmatism, and hydrothermal fluid flow at least during the Tertiary and Quaternary (e.g. Richards et al., 2001; Mazzuoli et al., 2008; Yáñez et al., 2008; Acocella et al., 2011; Lanza et al., 2013). In summary, structural corridors such as the COT could represent extended zones of crustal heterogeneities where deformation and transport of fluids is concentrated, especially in areas where these NW-SE trending corridors intersect with major fault systems running sub-parallel to the margin (Figure 4.14).

Basins with thick Cenozoic sedimentary infill have been inferred below areas where the COT intersects the AFS (Salar Grande, e.g. Reijs and McClay, 1998) or the PFS (Calama Basin, e.g. Jordan et al., 2010) (Figure 4.13). Similarly, we explained the low resistivity zones C1 and L1 at least partly as manifestations of (porous) sediments and fluids contained therein. The lower part of C1 and L1 could be caused by conduits of large and deep-reaching faults created at the intersection between the COT and trench-parallel fault systems, which in turn can provide pathways for fluids. The vertical extents of these low resistivity zones (L1, L2, L3, see e.g. Figure 4.11b) seem to reach Moho depths.

Crustal heterogeneities of low permeability can also control deformation and distribution of fluids in the crust. Götze and Krause (2002) suggested that the Atacama high density block, modelled below the CAGH along the Precordillera and Salar de Atacama area, is characterised by low-permeability and high-strength, which in turn explains why records of deformation, magmatic and fluid processes are concentrated along the margins of the Atacama block (e.g. Götze and Krause, 2002; Schurr and Rietbrock, 2004; Yáñez et al., 2008). The upper crustal, low resistivity zones of the Precordillera (P1 and P2) are found only north of the Atacama block (e.g. Figures 4.11c and 4.12a). This spatial correlation suggests that this block may control the along-strike distribution of upper crustal fluids along the Precordillera. Unlike seismic studies, the preferred resistivity model does not suggest significant amounts of fluids at depths of the mantle wedge west of P1 and P2. If fluids inferred for the upper crust of the Precordillera are generated at deeper levels of the forearc, their source would be enigmatic. According to the preferred model, it seems that M1 and P2 are connected through a zone of low resistivity inclined to the south (see Figures 4.11c and 4.14), suggesting that fluids generated at deep subduction levels can follow complex fluid pathways until reaching the continental crust.

Figure 4.12: (Next page) Comparison between horizontal slices of the preferred resistivity model and independent geological and geophysical information. Resistivity slices are displayed with the same color code as Figures 4.8 to 4.11. Brown rectangles are MT sites. Black triangles are active volcanoes. White dots are epicentres of seismic events contained within each model's layer. Black dashed lines in (a) and black arrows in (b-f) indicate sections shown in Figure 4.11. Grey thin lines show the coastline. Dark blue dashed lines in (a-c) show the boundaries of the CAGH (Götze and Krause, 2002). Grey lines in (a-b) are major faults and structural NW-SE lineaments. Gray thick solid lines in (d) delimit zone of anomalously low Vs at 50 km depth since Koulakov et al. (2006). Pink dashed lines in (b-f) are the top of the slab at different depths (taken from Hayes et al., 2012).

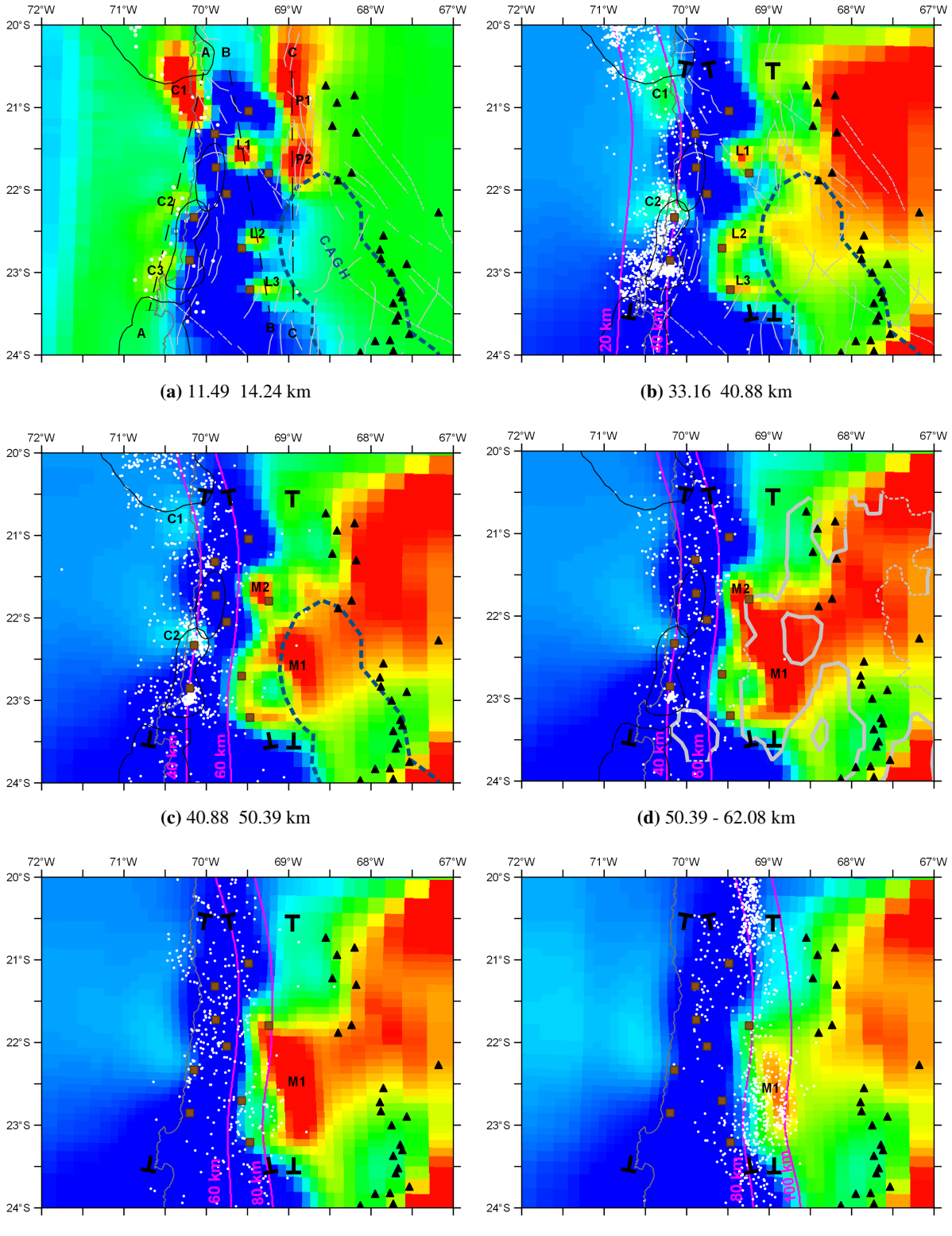

(a) 11.49 14.24 km

(b) 33.16 40.88 km

(c) 40.88 50.39 km

(d) 50.39 - 62.08 km

(e) 62.08 76.46 km

(f) 76.46 94.14 km

Figure 4.12: (Caption in previous page.)

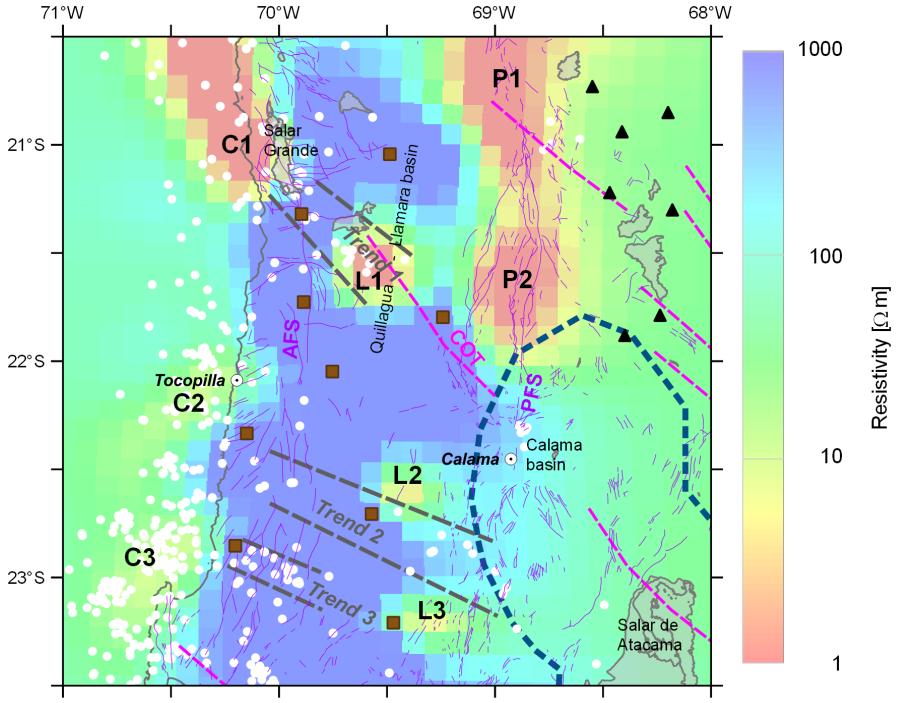

Figure 4.13: Correlation between crustal LRZs, seismicity and NW-SE structural corridors. Map showing horizontal slice of the preferred resistivity model at 11.49-14.24 km depth. Major LRZs are labelled. White dots are epicentres of seismic events located between 10 and 30 km depth. Black triangles are active volcanoes. Pink lines show traces of the regional NW-SE structural corridors (taken from Richards et al., 2001). Purple thin lines and light-grey polygons are observed faults and salt pans taken from Sernageomin (2003). Dark-blue dashed line shows the boundaries of the CAGH (Götze and Krause, 2002). Dark-grey dashed lines indicate NW-SE trends interpreted in the distribution of seismicity (see the text for details).

4.6.5 Along-strike segmentation in the interplate seismogenic zone

The spatial correlation between low resistivity zones found below the coastal region (C1, C2 and C3) and boundaries of rupture areas of the large subduction earthquakes registered during the last 50 years, suggests that concentrations of fluids in the continental crust is linked to deformation processes occurring at the plate interface. Along-strike variability in the amount of fluids below the coastal region can be attributed to variability in the fluid production within the crust and/or to variability in crustal permeability. Along-strike variability in the amount of fluids generated at the plate interface could be related to dehydration of anomalous parts of the slab which are enriched in fluids, such as sedimentary basins or bathymetric features containing serpentinites (e.g. fracture zones). It has been suggested that such localized fluid-rich heterogeneities along the plate interface can control the slip distribution of large subduction earthquakes (e.g. Audet et al., 2009; Audet and Schwartz, 2013; Moreno et al., 2014).

Also long-active NW-SE trending faults, such as the COT, could explain the spatial correlation observed in northern Chile between the rupture boundaries of large earthquakes and the presence of LRZs below the coastal region. Prior studies have suggested that NW-SE trending faults, which show records of deformation processes since the Paleozoic, have constrained the along-strike rupture length of various large subduction earthquakes in south-central Chile (e.g. Melnick et al., 2009; Farías et al., 2011). A

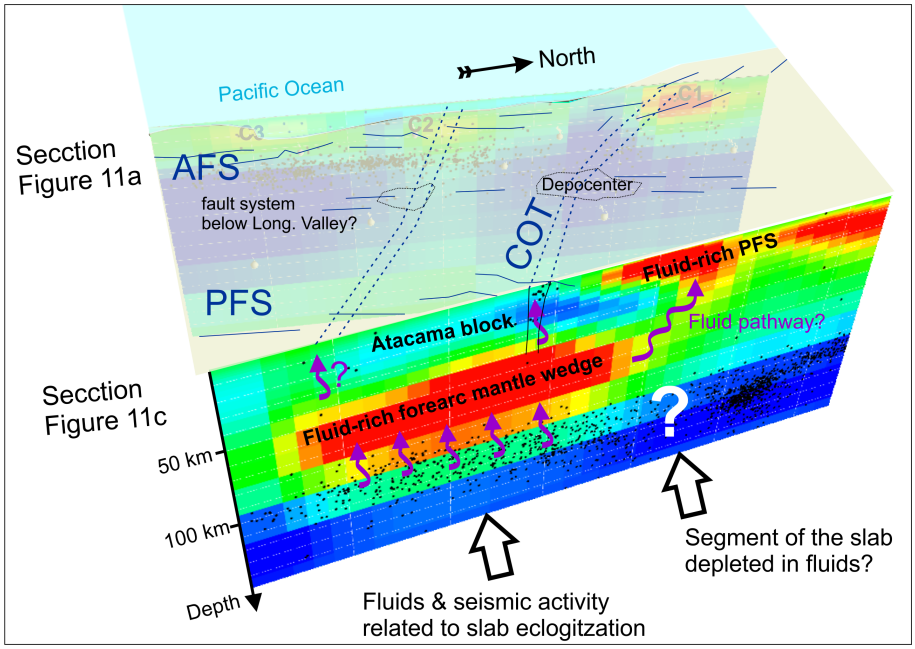

Figure 4.14: Cartoon summarizing along-strike segmentation of large scale distribution of fluids in the forearc of the study area. Resistivity section shown in Figure 4.11c is displayed in the frontal part. Resistivity section shown in Figure 4.11a appears below the surface plane along the coastal area. Resistivity sections are displayed using same color code as Figures 4.8 to 4.11. Major fault systems are indicated along the surface plane. Black dots included in the resistivity sections are hypocenters located within 10 km of the displayed sections.

seismic sequence following the 2010 M8.8 Maule earthquake was documented along one of these faults, in which Farías et al. (2011) suggested likely presence of fluids in depth based on high ratios of the Vp and Vs seismic velocities. These NW-SE faults may represent deep reaching high-permeability zones, which could act as fluid pathways channelizing upward migration of fluids from the plate interface. In turns, such fluid migration processes may release fluid overpressure along the plate interface. Therefore, here it is speculated that areas where the plate interface intersects these high-permeability NW-SE faults may represent relatively strong mechanical segments along the subduction thrust plane (due to comparatively lower fluid pressure), acting as barriers to the rupture propagation along the plate interface.

4.7 Conclusions

A 3-D model of the regional-scale resistivity structure of the subduction zone in Northern Chile was obtained, by inverting data collected a nine IPOC MT sites covering the forearc approximately between 21°S and 23.5°S. A robust and geologically meaningful model was obtained, by inverting estimates of the MT TF (Z), VTF and HTF for a period range of 10-10,000 s, and by including two well-constrained regional structures as a priori resistivity bodies. From these results, can be concluded that:

- The overall data fit is good. The preferred model's responses reproduce all major trends in the observations, over the entire period range and for all components of the measured data.
- The preferred model is generally consistent with resistivity models of the forearc region from

existing MT studies and it reflects major lithospheric structures described by other geological and geophysical studies.

- In terms of size, the predominant structure of the model is a high resistivity zone (>1000 Ωm) observed along the forearc approximately between the coastline and the Longitudinal Valley-Precordillera boundary (69°W) (the forearc high resistivity zone, FHRZ). The FHRZ coincides spatially with a dense, rigid and cold block, identified by gravimetric, seismic and thermal studies. A background of comparatively lower resistivities is observed between the Precordillera and the active volcanic arc.

- The inversion model reveals several low resistivity zones at various depth ranges and segments of the forearc, suggesting an overall complex 3-D resistivity structure. Below the Coastal Cordillera and the Longitudinal Valley, the upper crustal low resistivity zones are associated with Cenozoic sedimentary basins. In areas where regional NW-SE structural lineaments intersect major trench-parallel fault systems, the low resistivity zones reach the lower crust. As these low resistivity zones coincide with regions of high crustal seismicity, here it is interpreted these observations as combination of deep reaching, active faulting and availability of significant amounts of fluids.

- Below the Precordillera, a low resistivity zone was found in the upper crust between 20°-22°S, coinciding with clusters of seismicity which were interpreted by others as fluids circulating in the Precordillera Fault System (PFS). The southern limit of this low resistivity zone coincides with a dense, low-permeability, rigid block.

- The preferred resistivity model exhibits low resistivities associated with forearc mantle wedge between ∼21.5° and 23°S. The along-strike extents of these LRZs was carefully tested and is well resolved.

- The model shows low resisistivities below the Altiplano with a poorly constrained geometry, but they are consistent with resistivity models of previous MT studies.

The complex spatial distribution of low resistivity zones and their interpreted relation with regions characterised by low strength and high amount of fluids, suggests that the distribution of deformation and fluid processes in the forearc of the study area exhibit a first order along-strike segmentation. The presence of large-scale heterogeneities in the lithospheric structure appears to be a first order factor controlling the segmentation of these processes in the crust. In addition, it is observed in the forearc mantle wedge a discrete and constrained low resistivity body which extends for approximately 150 km along the trench axis, suggesting significant along-strike variability in the amount of fluids released from the oceanic slab. In summary, the study area shows several features in the lithosphere's structure which suggest that large-scale deformation and fluid processes associated to subduction systems tend to be concentrated at discrete and along-strike constrained regions of the forearc.

Chapter 5

The influence of source effects on the temporal variability of transfer functions

This chapter contains an analysis of the temporal variability of daily estimates of the vertical magnetic transfer function (VTF), calculated for more than 10 years of data collected at mid-latitude magnetic observatories. The main aim of this analysis was to evaluate the stability of daily VTF estimates, in order to derive a significance interval for monitoring purposes at the IPOC array. The analysis of the IPOC MT data (presented in chapter 3) shows that transfer functions (TFs) exhibit periodic patterns which are correlated with fluctuations in the geomagnetic activity. In this chapter, data from worldwide distributed magnetic observatories are analysed to test whether these patterns observed in the IPOC MT data are present in other regions.

Section 5.1 summarizes previous evidences suggesting that TFs temporal variations at mid-latitudes are not necessarily related to changes in the underground resistivity. The description of the geomagnetic data analysed is contained in section 5.2. The results obtained from this analysis are presented in Section 5.3. Implications of these results are discussed in Section 5.4. Finally, section 5.5 presents the conclusions of this chapter. This chapter has been partly published in Araya Vargas and Ritter (2016).

5.1 Introduction

Generally, practitioners of the magnetotelluric (MT) and geomagnetic deep sounding (GDS) methods assume that external source magnetic fields have a plane wave geometry at mid-latitudes (the *plane wave assumption*, see e.g. Simpson and Bahr, 2005). This assumption implies that transfer functions (TFs) calculated from mid-latitude electromagnetic (EM) data should be reproducible over time, unless the subsurface resistivity structure changes or the data is contaminated with noise (Simpson and Bahr, 2005). Consequently, any changes observed between TFs obtained at different times (i.e. temporal variations of TFs) would then be related to alterations of the internal resistivity structure, if it is provided that the signal-to-noise ratio is adequate.

However, previous studies have shown evidence which suggests that temporal variations of TFs at mid-latitudes are not necessarily connected to changes in the underground resistivity. For instance, Eisel and Egbert (2001) reported that daily estimates of apparent resistivities at two sites in California showed random temporal distribution and exhibited no clear long-term trend during a 2-year interval. Eisel and Egbert (2001) observed that the daily estimates of apparent resistivities deviated from the 2-years average estimates between 2% to 10% for a period range of $\sim$10-2000 s. Apparent resistivity variations of the same order of magnitude were described by Hanekop and Simpson (2006), observed at periods of 57 s and 315 s in a site located in the middle of Australia (a mid-latitude region, far from the coast). Hanekop and Simpson (2006) interpreted that those variations may be related to violations of the plane wave assumption, because subsurface resistivity changes would not be expected for that stable cratonic region. After analysing four years of data from a site in Italy, Romano et al. (2014) identified that apparent resistivity and phases for periods between 20 and 100 s are more stable over time when natural energy source increases.

Some authors have described that VTF estimates can vary significantly depending on the local time of the magnetic data processed (Anderson et al., 1976, 1978; Beamish, 1980; Takeda, 1997), suggesting that those variations can be explained by changes in the external magnetic fields, which are controlled by local time dependent electromagnetic phenomena like geomagnetic pulsation activity and man-made noise sources (e.g. Egbert et al., 2000). Moreover, Beamish (1979) describes that external magnetic field conditions can also influence VTF estimates that are computed from processing several days (i.e. intervals that average different local times), and that these source field effects increase with latitude and period. Ernst and Jankowski (2005) found that source effects become a general problem for sites at latitudes $>50^{\circ}$N, while for lower latitudes the plane wave assumption tends to be violated only during intervals of low magnetic activity. Also Romano et al. (2014) suggested that VTFs estimated at mid-latitude sites can be biased during low global geomagnetic activity (Ap index <5), particularly in the period range 20 - 100 s.

The analysis of the IPOC MT data (chapter 3) reveals that all calculated TFs exhibit systematic periodic patterns which are correlated with fluctuations in the geomagnetic activity. The most prominent periodic pattern is correlated with seasonal variations that Brändlein (2013) interpreted as source field effects. Brändlein (2013) observed systematic seasonal variations affecting daily estimates of the T_y component at periods between 100 and 3000 s, which show significant coherence with the interplanetary electric field. To examine if these variations are influenced by instrumental effects (e.g. temperature drifts) or by source inhomogeneities (e.g. proximity to the equatorial electrojet) only present at the IPOC MT array, geomagnetic data recorded at mid-latitude observatories of the INTERMAGNET network were analysed. This analysis focuses on the temporal variations of VTFs, because only long time series of magnetic data were available.

5.2 INTERMAGNET data and processing

Data from 11 mid-latitude geomagnetic observatories of the INTERMAGNET network were used to calculate long time series of daily estimates of VTFs (see Figure 5.1 and Table 5.1). The criteria to select these observatories were: (i) locations at geomagnetic mid-latitudes in both hemispheres, (ii) minimum data gaps, and (iii) to represent regions with different geographical settings (e.g. coastal and inland regions). Minute-mean magnetic field data from more than 10 years (2003-2013) were downloaded from the INTERMAGNET network website (www.intermagnet.org). Only definitive data were analysed, i.e. data which were corrected for baseline variations and which have had spikes removed (INTERMAGNET, 2011). Time series were analysed using a Cartesian XYZ coordinate system, in which the X-axis is horizontal and points towards magnetic north (assuming the direction of the magnetic field at the first day of the data interval), Y-axis points towards the magnetic east, and Z-axis is positive downwards.

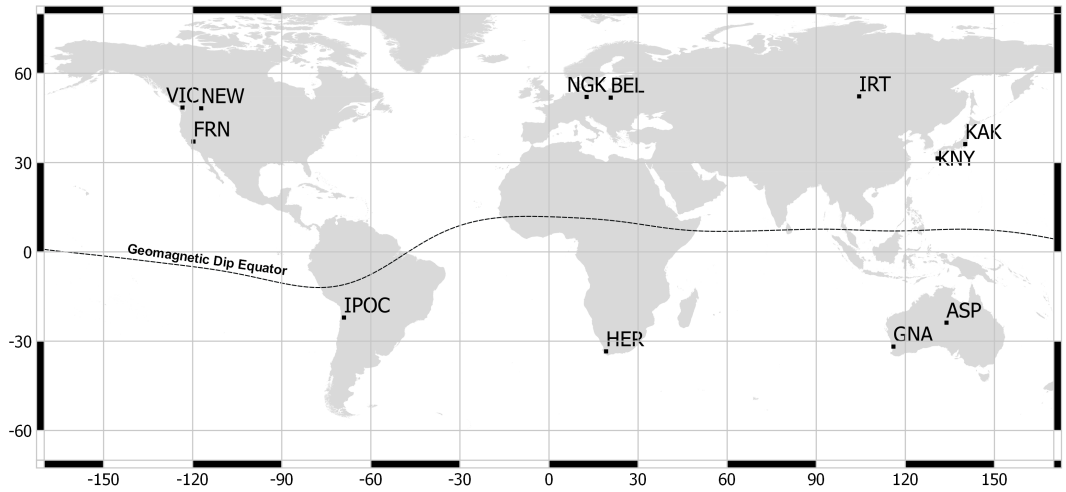

Figure 5.1: Location of the magnetic observatories and sites used for this study. The Geomagnetic Dip Equator is taken from the World Magnetic Model 2015 (ftp://ftp.ngdc.noaa.gov/geomag/wmm/wmm2015/).

Table 5.1: Coordinates of investigated stations (taken from INTERMAGNET, 2011; http://www.ipoc-network.org).

Station	Code	Geographic latitude [°]	Geographic longitude [°]	Geomagnetic latitude [°]	Geomagnetic longitude [°]
Alice Springs	ASP	-23.77	133.88	-32.9	208.2
Belsk	BEL	51.84	20.79	50.2	105.2
Fresno	FRN	37.09	-119.72	43.5	305.3
Gnangara	GNA	-31.8	116	-41.9	188.9
Hermanus	HER	-33.4	19.23	-34	84
IPOC (PB02)	IPOC	-22.05	-69.05	12.04	3.04
Irkutsk	IRT	52.27	104.45	41.9	176.9
Kakioka	KAK	36.23	140.19	27.4	208.8
Kanoya	KNY	31.42	130.88	21.9	200.8
Newport	NEW	48.27	-117.12	54.9	304.7
Niemegk	NGK	52.07	12.68	51.9	97.6
Victoria	VIC	48.52	-123.42	54.1	297.6

Daily estimates of VTFs were calculated using the EMERALD robust processing package (Ritter et al.,

1998; Weckmann et al., 2005; Krings, 2007). To obtain statistically robust VTFs for periods >1000 s, it was necessary to employ a three-days processing interval, i.e. using the same processing scheme employed with the IPOC data (see Section 3.3). Following this scheme, VTFs in a period band between 256 to 4098 seconds were calculated for each day. For any subsequent analysis of temporal variations of the daily estimates, we excluded VTFs with confidence intervals (statistical errors) $\geq$ 0.02 as they can be affected severely by noise.

5.3 Results

Figure 5.2 shows sounding curves for the studied magnetic observatories, which were obtained after computing the median of all daily VTF estimates for each period, using data from years 2003 to 2013. These median sounding curves vary smoothly with period, as is expected for geomagnetic transfer functions (e.g. Weidelt, 1972). For most stations, the daily VTF estimates follow approximately a Normal distribution, centred on their median and mean values (see Figure 5.3, obtained for an exemplary period of 2049 s). Therefore, it can be concluded that the median values represent a long-term average of the VTFs. In order to simplify the comparison of TFs values between different sites, in the following the temporal variability of TFs is analysed by examining deviations of the daily TF estimates from the long-term median value:

$$\Delta T(\tau) = T_{daily\ estimate} - T_{long\ term\ median} \tag{5.1}$$

where T = VTFs and τ = period [s].

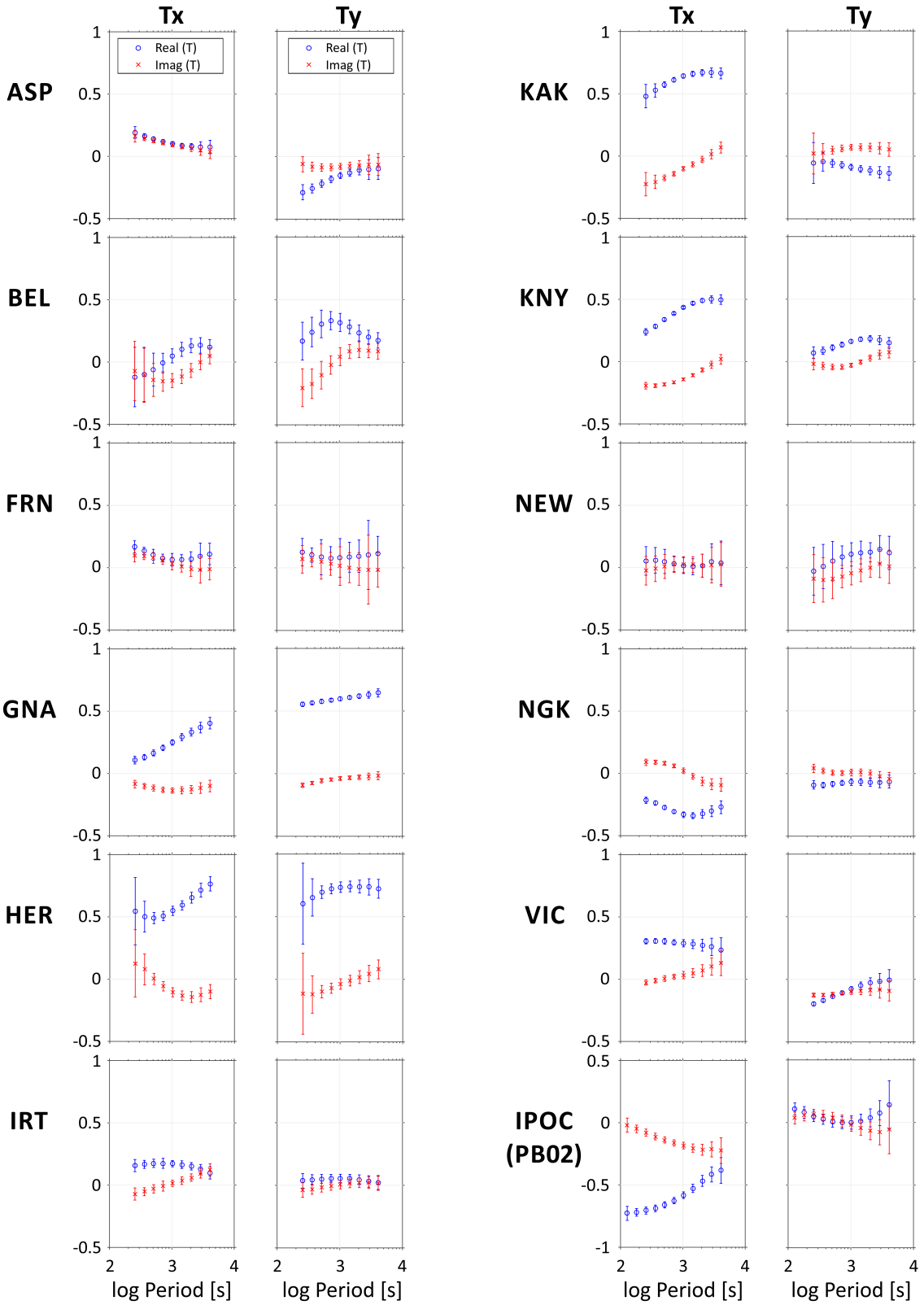

Figure 5.2: VTF sounding curves for the studied magnetic observatories. For each period, the displayed VTF value is the median of all daily VTF estimates obtained for the years 2003 to 2013. Error bars represent 1 standard deviation of the population. VTF sounding curves for IPOC site PB02 are displayed for comparison (daily VTF estimates from 2007 to 2013), but using a different Y-axis range.

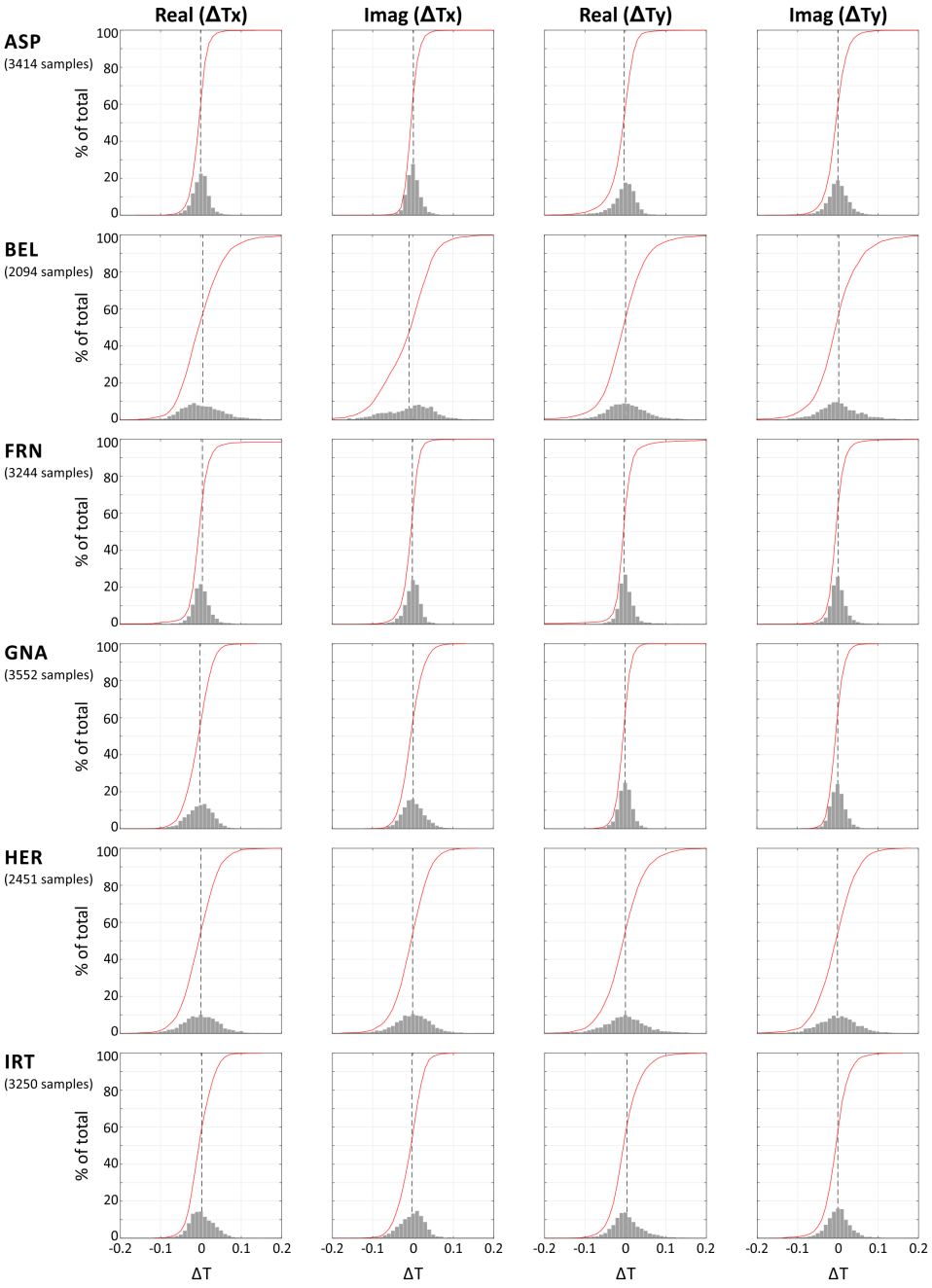

Figure 5.3: Frequency histograms showing the statistical distribution of daily VTF estimates between years 2003 and 2013 for the studied magnetic observatories at a period of 2049 s. Histograms are ordered by sites (along rows) and VTF components (along columns). The X-axes display deviations of daily VTF estimates from the 10-year median values shown in Fig. 1. Y-axes show the frequency of observations as percentage of the total number of samples (daily estimates). Black vertical dashed lines indicate position of the 10-year mean value. Red curves show the cumulative distribution of the daily VTF estimates.

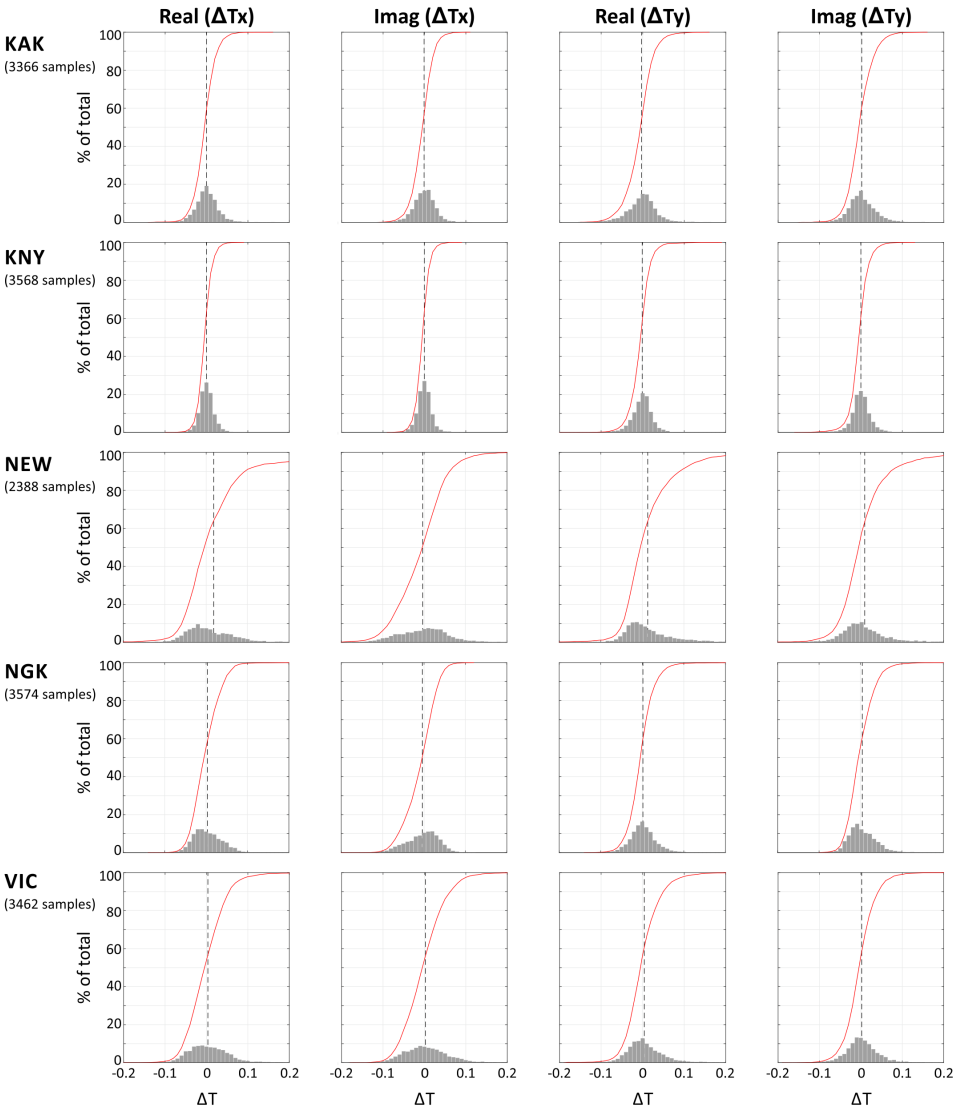

Figure 5.3: (Continued.)

5.3.1 Seasonal dependence

To identify periodical patterns in the VTFs (e.g. seasonal variations, Brändlein et al., 2012), the spectra of the daily VTF estimates was examined. A clear dominant peak can be observed for a period of approximately 356-358 days at all stations (see example in Figure 5.4a). Some components show additional peaks around 11, 27 and 180 days, but the amplitudes for these periods are significantly smaller than the $\sim$1 year peak. Not all VTF periodic fluctuations are related to dominant signals observed in the periodograms of the magnetic field spectra; for instance the peak around 180 days is only visible in the VTFs but has no expression in the magnetic spectra (compare Figure 5.4a and b).

Considering the dominant annual periodical signal, the seasonal variation of daily VTF estimates is analysed. In Figures 5.5 to 5.8 the distribution of all daily VTF deviations from the median with respect their day-of-year (DOY) is plotted for all sites and for a number of periods between 256 and 2049 s. The DOY corresponds to the relative position of each day, starting with DOY = 1 for January 1st of each year. To visualize the first-order trends, the median of all values obtained for each DOY is shown as a black line. Figures 5.5 to 5.8 show that the real parts of the ΔT_x components ($Real(\Delta T_x)$) exhibit maxima around the middle of the year, and this pattern is mirrored in the imaginary parts of T_x ($Imag(\Delta T_x)$). The amplitudes of these patterns tend to increase with increasing latitude: for example, sites located at approximately 50° N show significantly larger seasonal peaks than those sites located at latitudes between 30° and 40° N (see Figures 5.7 and 5.8). Generally, for all components the amplitudes of the seasonal peaks at each site tends to increase if the period increases (e.g. compare the amplitudes of the mid-year peaks between Figs 5.5, 5.6, 5.7 and 5.8).

The T_y components also exhibit seasonal variations, but the effect is not as clear as in T_x. For example, although $Real(\Delta T_y)$ shows a high peak around the middle of the year at most of the sites (exceptions are GNA and HER, see Figures 5.6, 5.7 and 5.8), $Imag(\Delta T_y)$ does not follow a clear trend. In addition, the amplitudes of the seasonal peaks in T_y do not necessarily increase with latitude, as is observed for T_x. For example, the peak-to-peak seasonal amplitude of $Imag(\Delta T_y)$ is comparatively larger at site ASP (23.77° S) than at GNA (31.88° S) for periods between 512 and 2049 s (Figures 5.6 to 5.8). Similarly, when examining other periods, a clear seasonal dependence of ΔT_y is not observed.

It is interesting to note that for each DOY the VTF estimates show a scatter in the range of approximately 0.04, regardless of the period studied (see the distribution of grey points around black lines in Figures 5.5 to 5.8). It is interpreted that this variability around the long-term median represents an empirical confidence range for the repeatability of daily VTF estimates. This scatter could be partly explained either by local noise sources or by cyclic changes in the magnetic source fields which exhibit periodicity shorter than half a year (e.g. peaks around 11 and 27 days observed in Figure 5.4a).

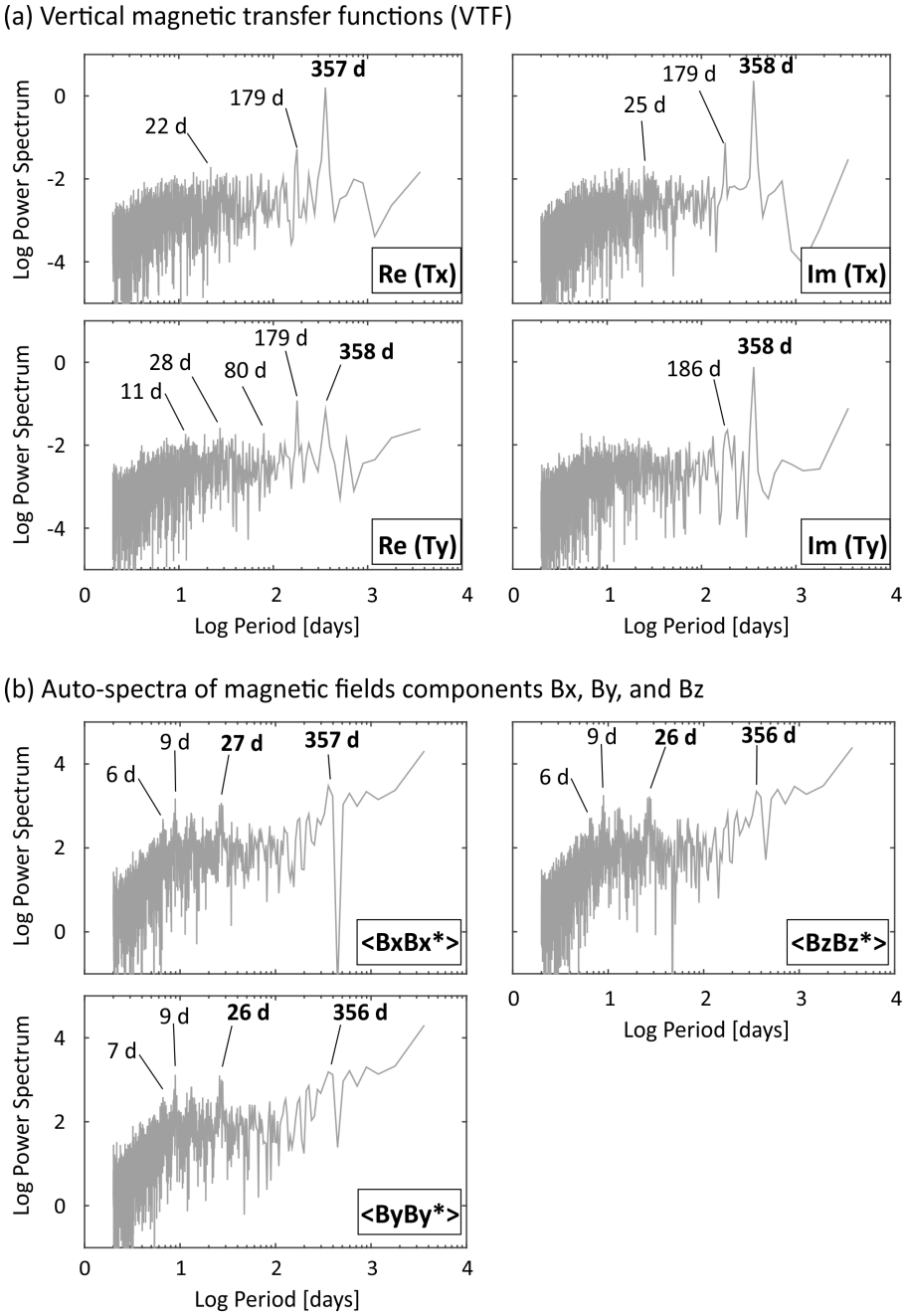

Figure 5.4: Periodograms of (a) VTFs and (b) magnetic field auto-spectra, for an exemplary site (NGK) at a period of 2049 s. Analysed time series comprise daily estimates obtained for the years 2003 to 2013. The magnetic auto-spectra displayed in (b) are stacked spectra used to calculate the VTF (see equations (2.25) and (2.25)). A number of dominant spectral peaks are marked (period in days, see the text).

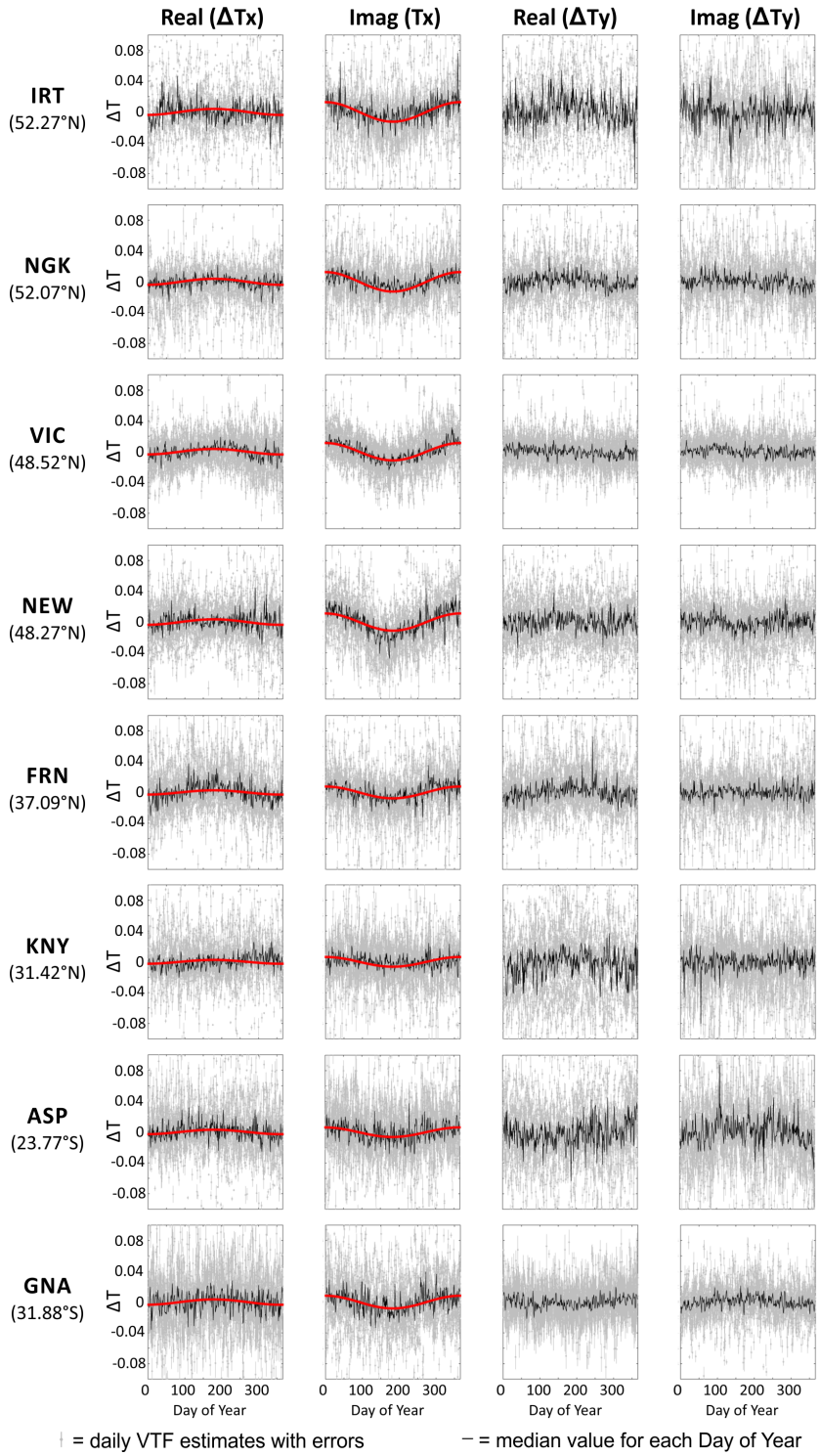

Figure 5.5: Dependence of VTF temporal variations on season, examining data from 2003 to 2013 for a period of 256 s. Plots are ordered by sites (along rows) and VTF components (along columns). X-axes indicate the day-of-year for which the VTF estimates were obtained. Y-axes indicate deviations of the daily VTFs from the 10-year median. Daily VTF estimates and their error bars are displayed as grey dots and grey vertical lines, respectively. The black line is the median value for each day-of-year. The red line is a fit of the seasonal variation in the T_x components calculated using equations (5.3) and (5.4) (see text). The geographical latitude for each site is indicated. Sites BEL, HER and KAK are omitted only in Figure 5.5 because of poor data quality at 256 s.

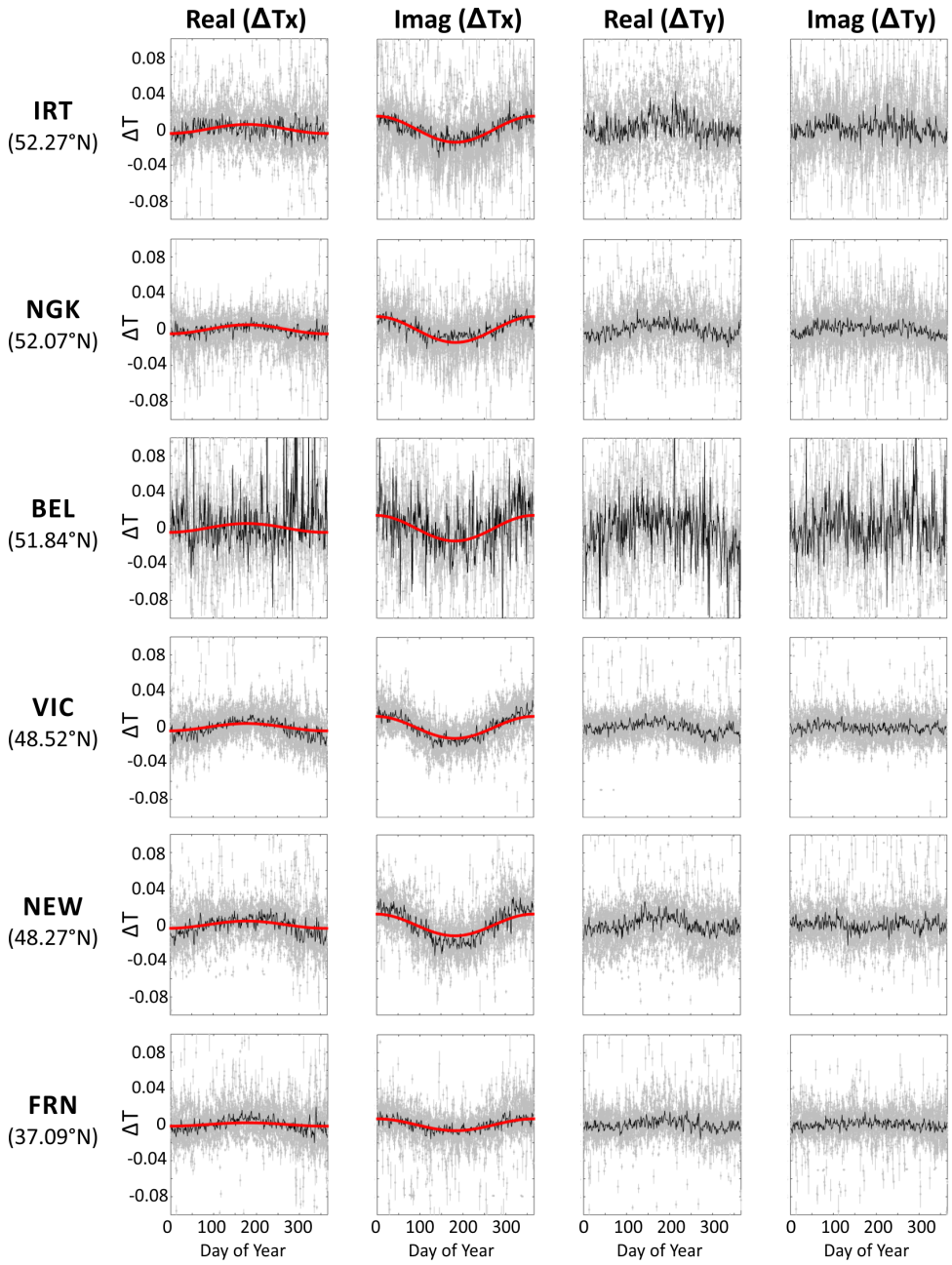

Figure 5.6: Same as Figure 5.5, but for a period of 512 s.

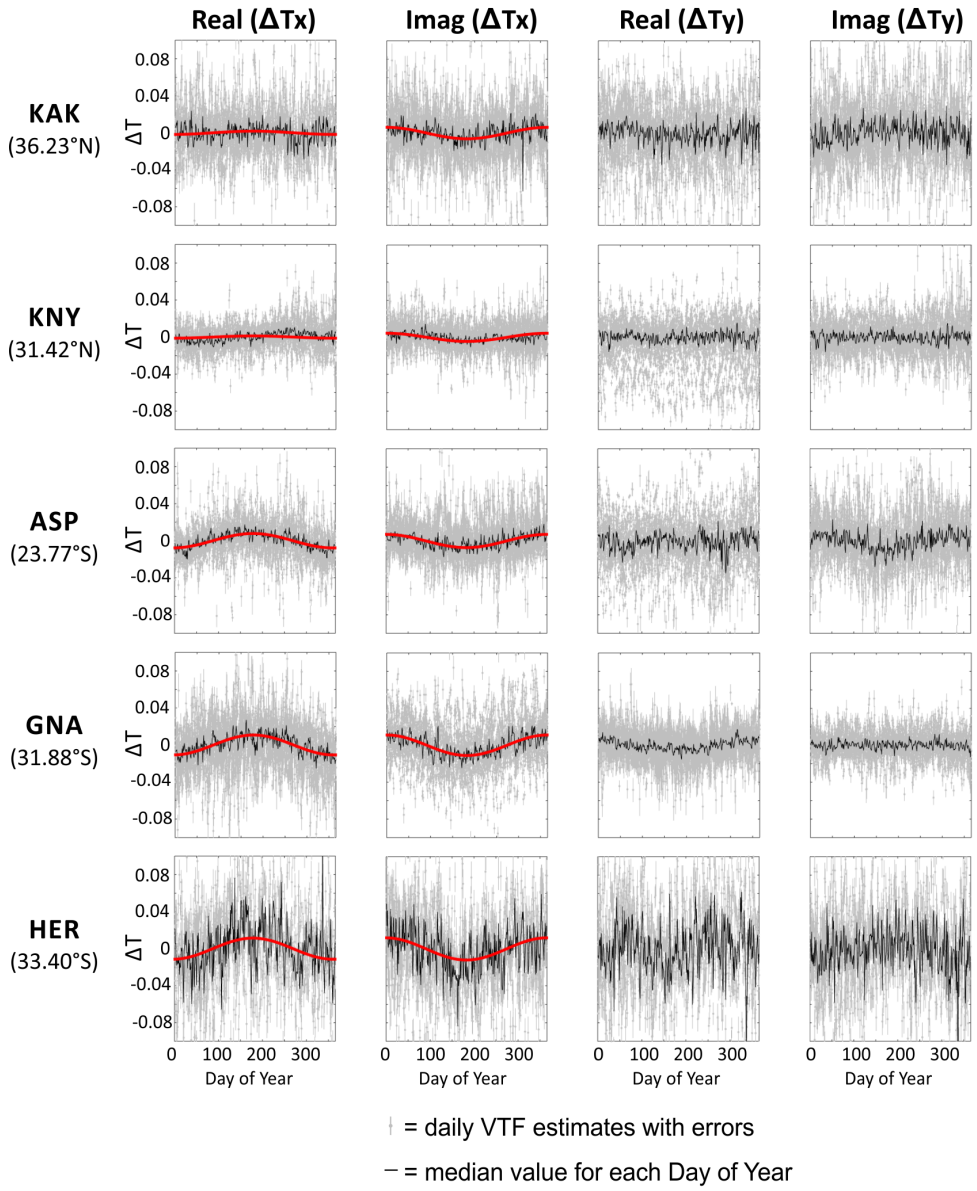

Figure 5.6: (Continued.)

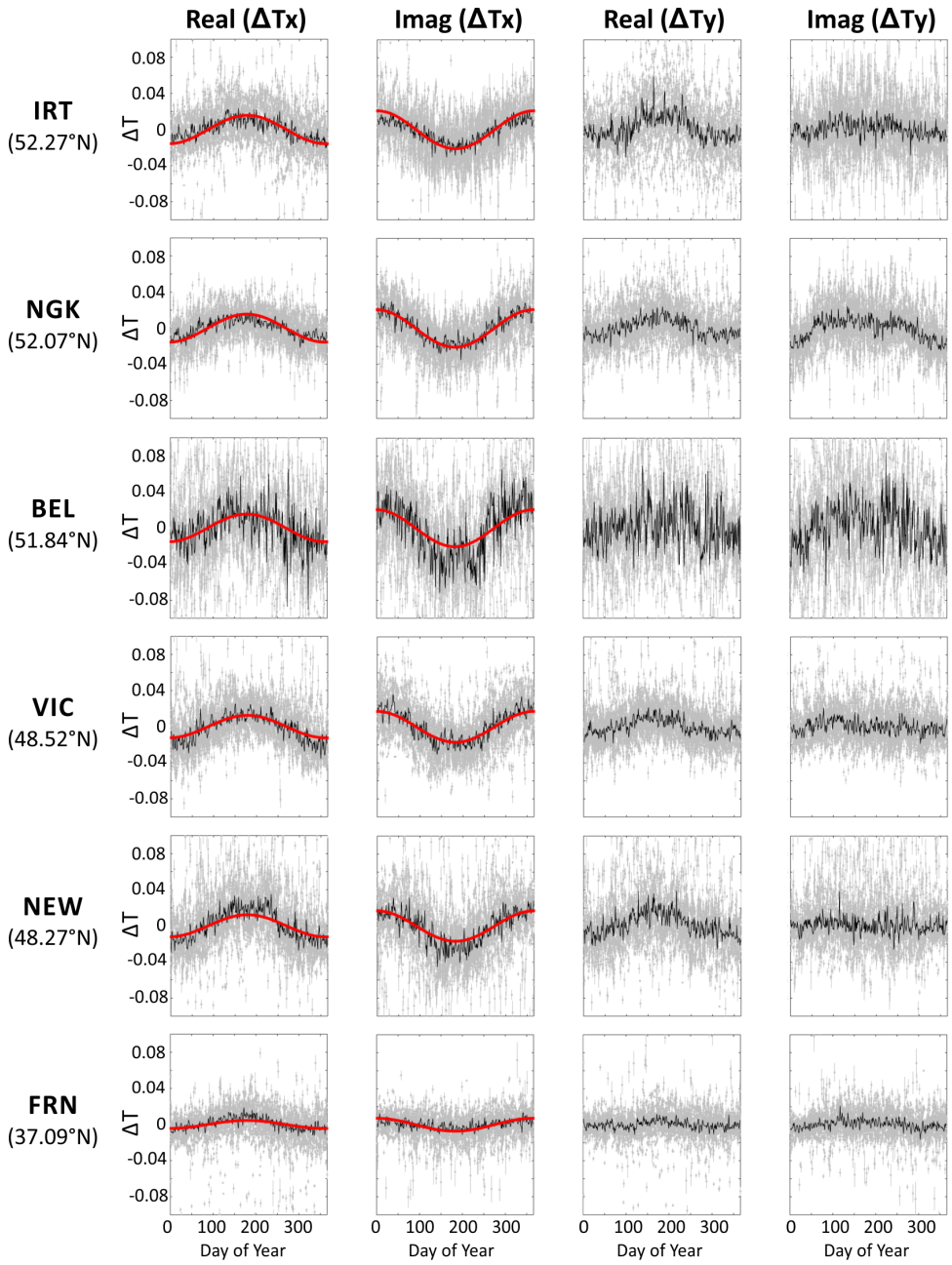

Figure 5.7: Same as Figure 5.5, but for a period of 1024 s.

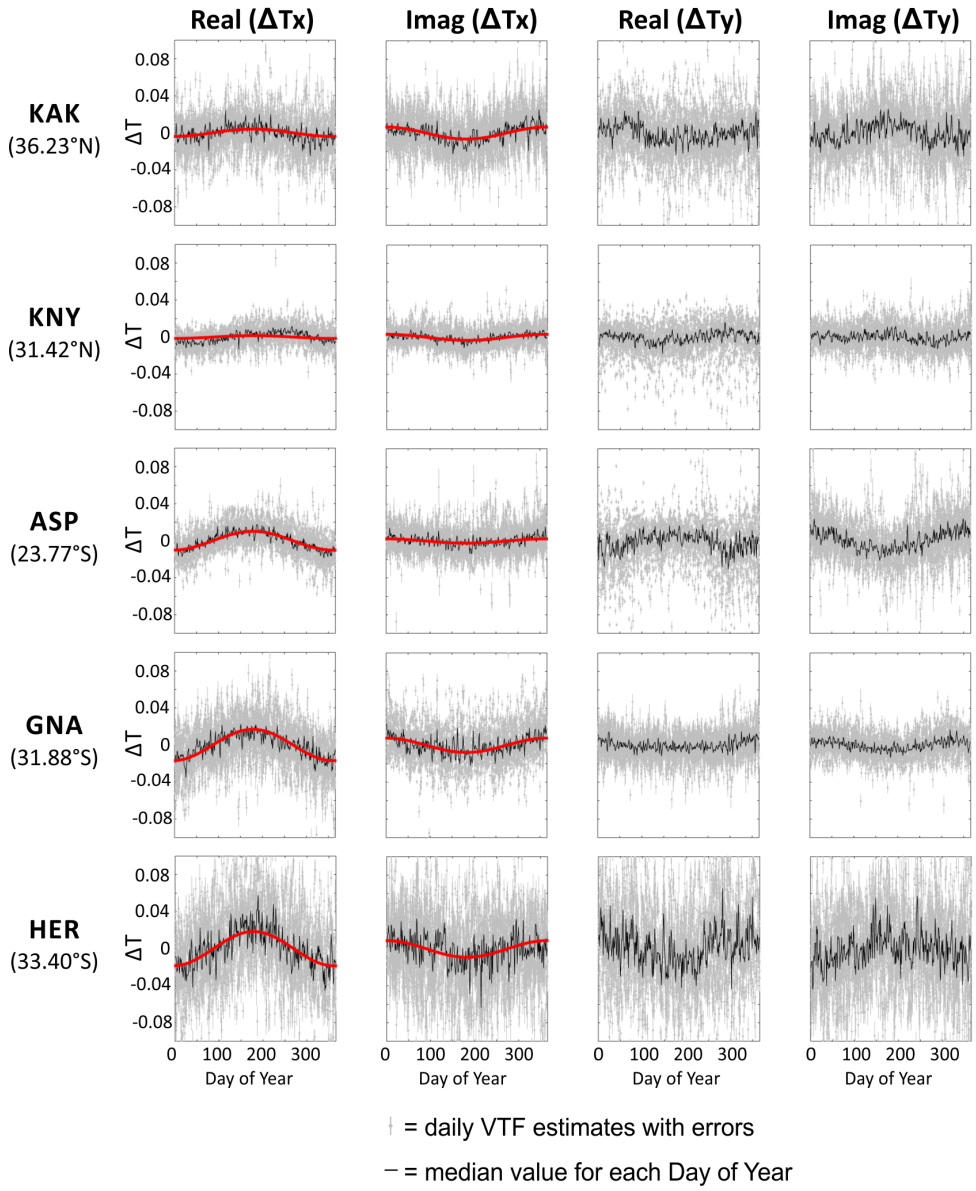

Figure 5.7: (Continued.)

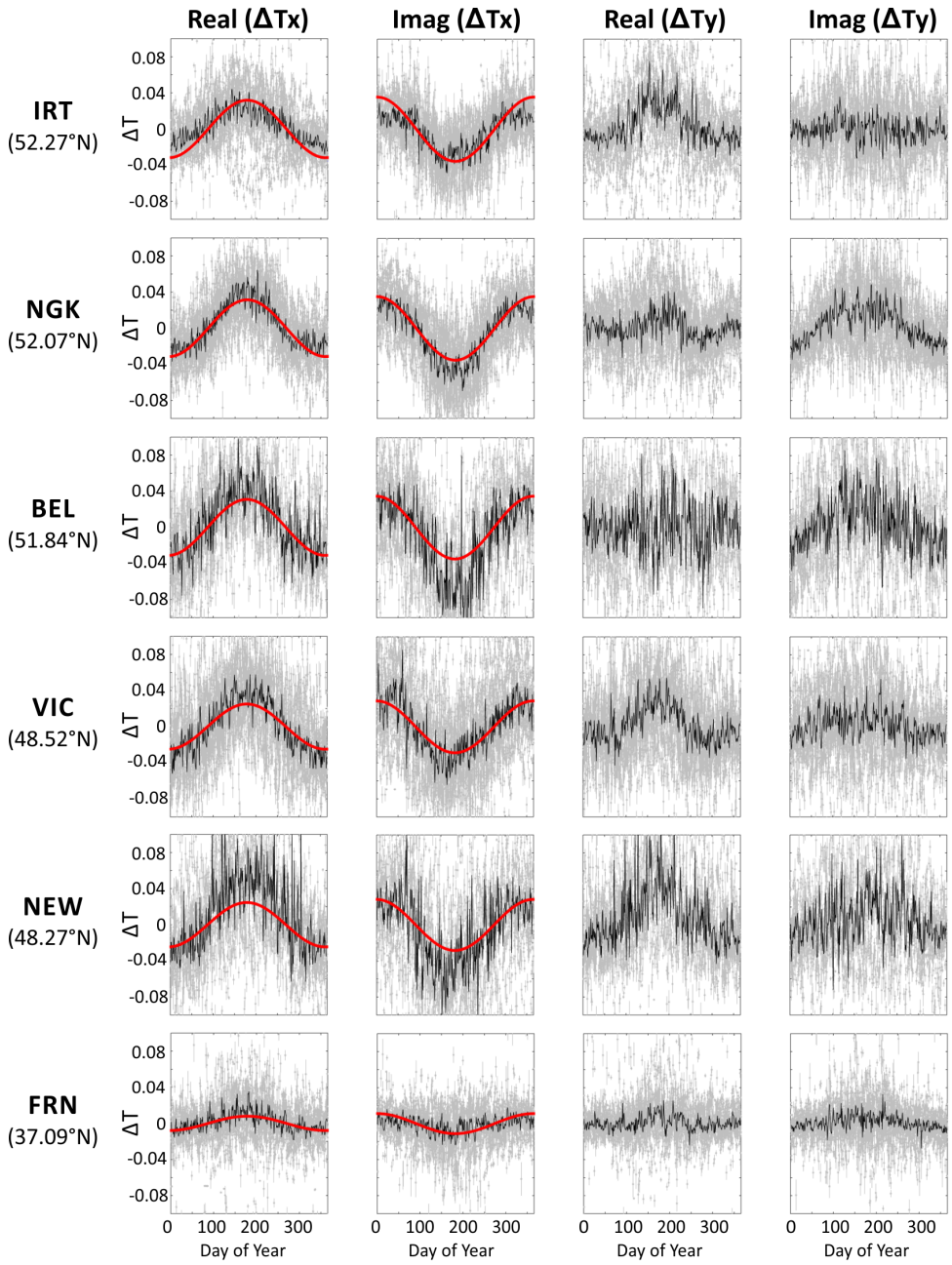

Figure 5.8: Same as Figure 5.5, but for a period of 2049 s.

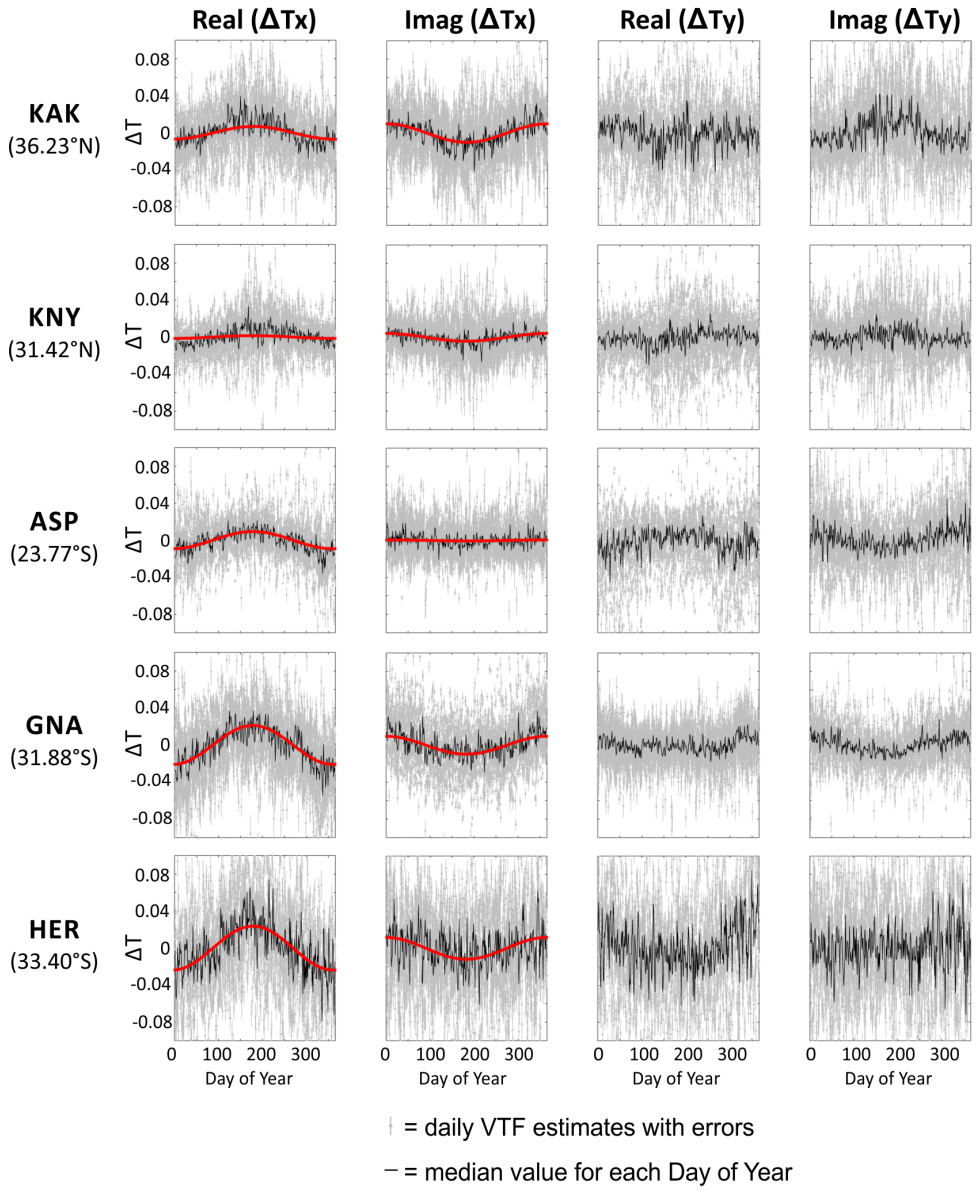

Figure 5.8: (Continued.)

5.3.2 Correlation with the 11-year solar cycle

After processing almost 100 years of GDS data from European observatories, Petrishchev and Semenov (2013) showed that apparent resistivity variability (for periods of 8 hours and 30 days) correlates with the yearly number of sunspots. To test if VTF temporal variations also show correlation with the long term solar activity, 18 years (1995-2013) of magnetic field data were additionally processed, an interval covering partly solar cycles 23 and 24. At the time when this analysis was performed, only some of the selected sites from INTERMAGNET had data available for this interval (BEL, HER, KAK, NGK, VIC). A clear correlation with the 11-year solar cycle could be observed only at some of these sites.

Figures 5.9 to 5.13 show the temporal variability of daily VTF deviations from the 18-years median for a period of 2049 s. For comparison, the F10.7 cm solar radio flux index ($F10.7$) is included as a proxy for the solar activity. To highlight the major trends, a 60-days moving average of VTF deviations and $F10.7$ are plotted as black lines. These figures show that the dominant seasonal variations are modulated by a long term trend, which tends to exhibit a high peak around year 2002 (solar maximum), and which tends to vanish around 1996 and 2009 (solar minima). However, the amplitude of this effect varies among VTF components and sites. For instance, while at site HER the differences between minimum (smoothed) VTF values observed during 2002 and 2009 can reach 0.05 in $Real(T_y)$ and <0.01 in $Imag(T_y)$ (compare location of blue horizontal bars in Figure 5.10), at site KAK the average difference between both years is generally smaller than 0.01 (see Figure 5.11) .

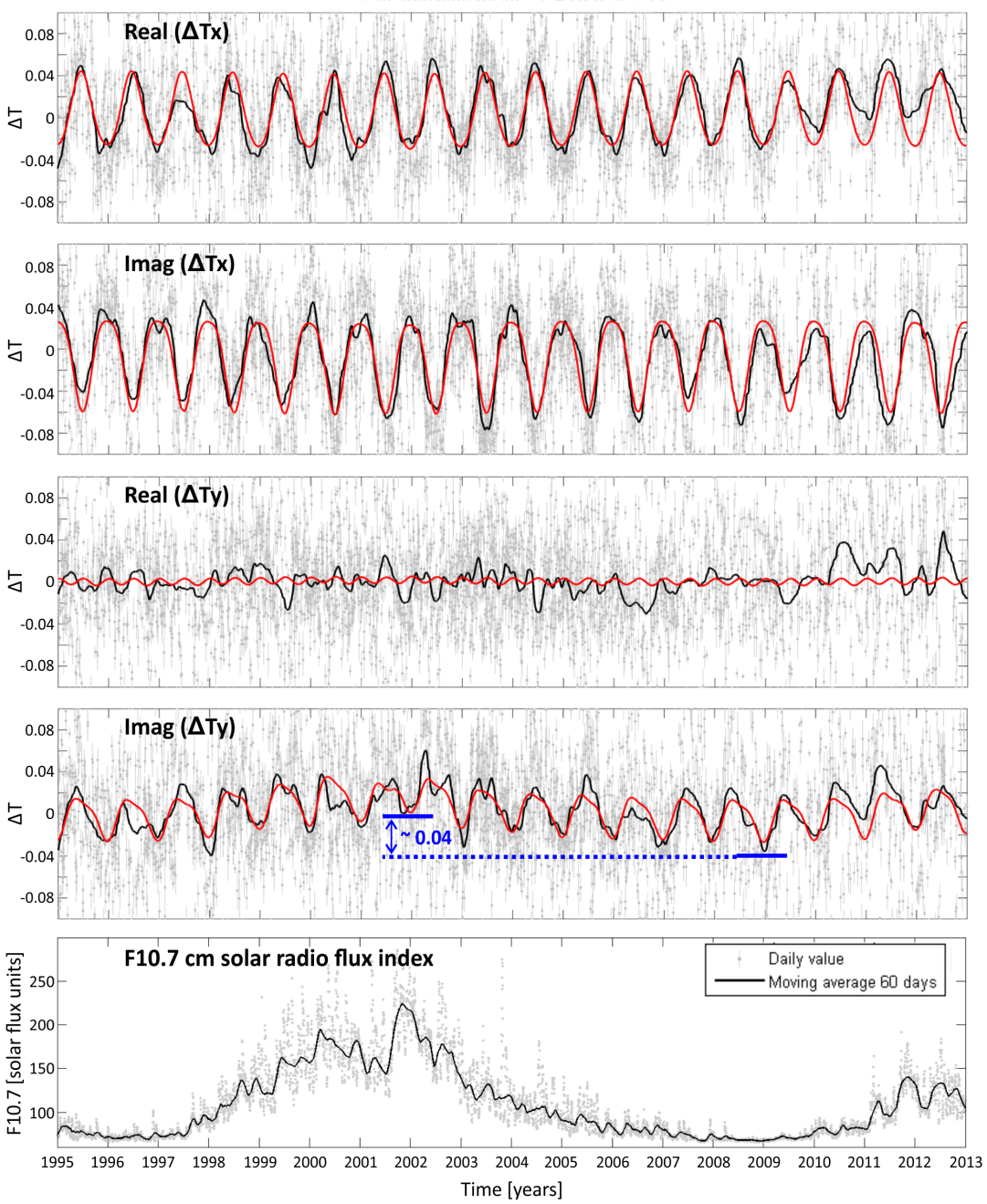

Figure 5.9: Comparison between long-term VTF temporal variations at site BEL and the 11-year solar cycle. The four upper panels show deviations of daily VTF from the median of all estimates between 1995 and 2013, for a period of 2049 s. Daily VTF estimates and their statistical error bars are displayed as grey dots and grey vertical lines, respectively. The red line is a model function that fits the smoothed temporal variations (see text for details). Blue horizontal bars show the minimum smoothed VTF values obtained during solar maximum (2002) and minima (2009). The bottom panel shows daily values of the F10.7 cm solar radio flux index (downloaded from http://omniweb.gsfc.nasa.gov), as a proxy for solar activity.

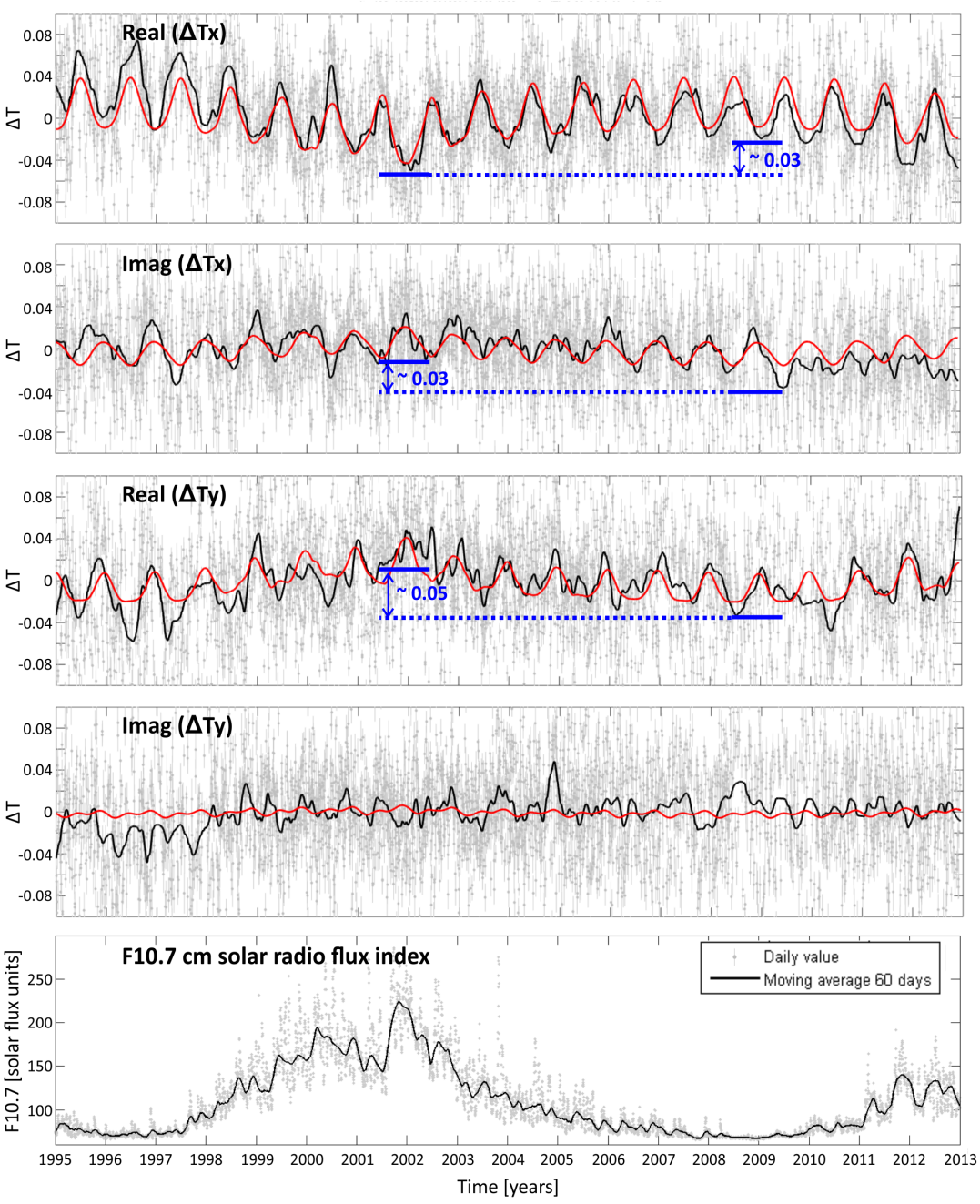

Figure 5.10: Same as Figure 5.9, but for site HER.

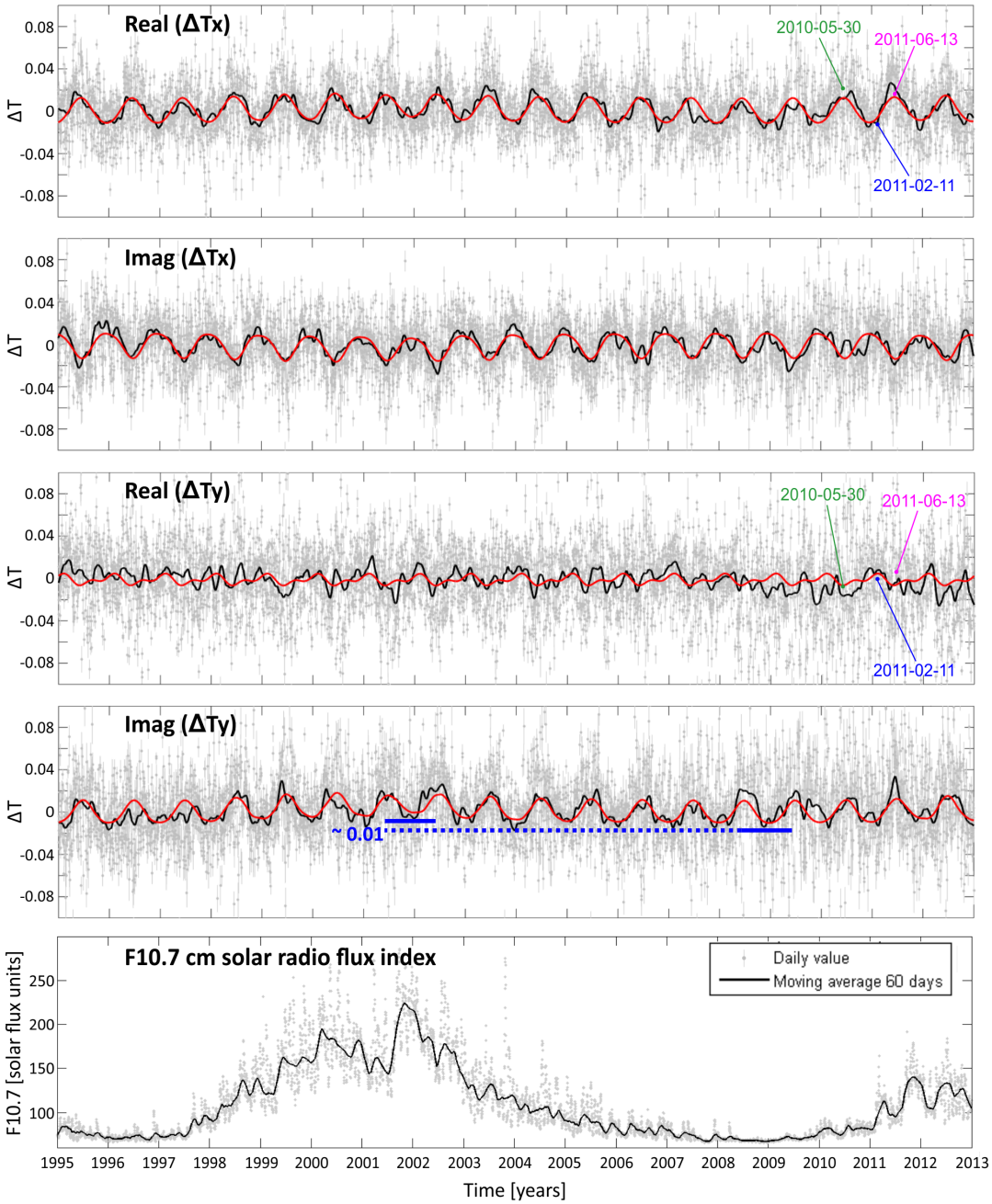

Figure 5.11: Same as Figure 5.9, but for site KAK. The deviations of daily VTF from the median obtained at days 2010-05-30, 2011-02-11 and 2011-06-13 are indicated for the real parts of T_x and T_y components.

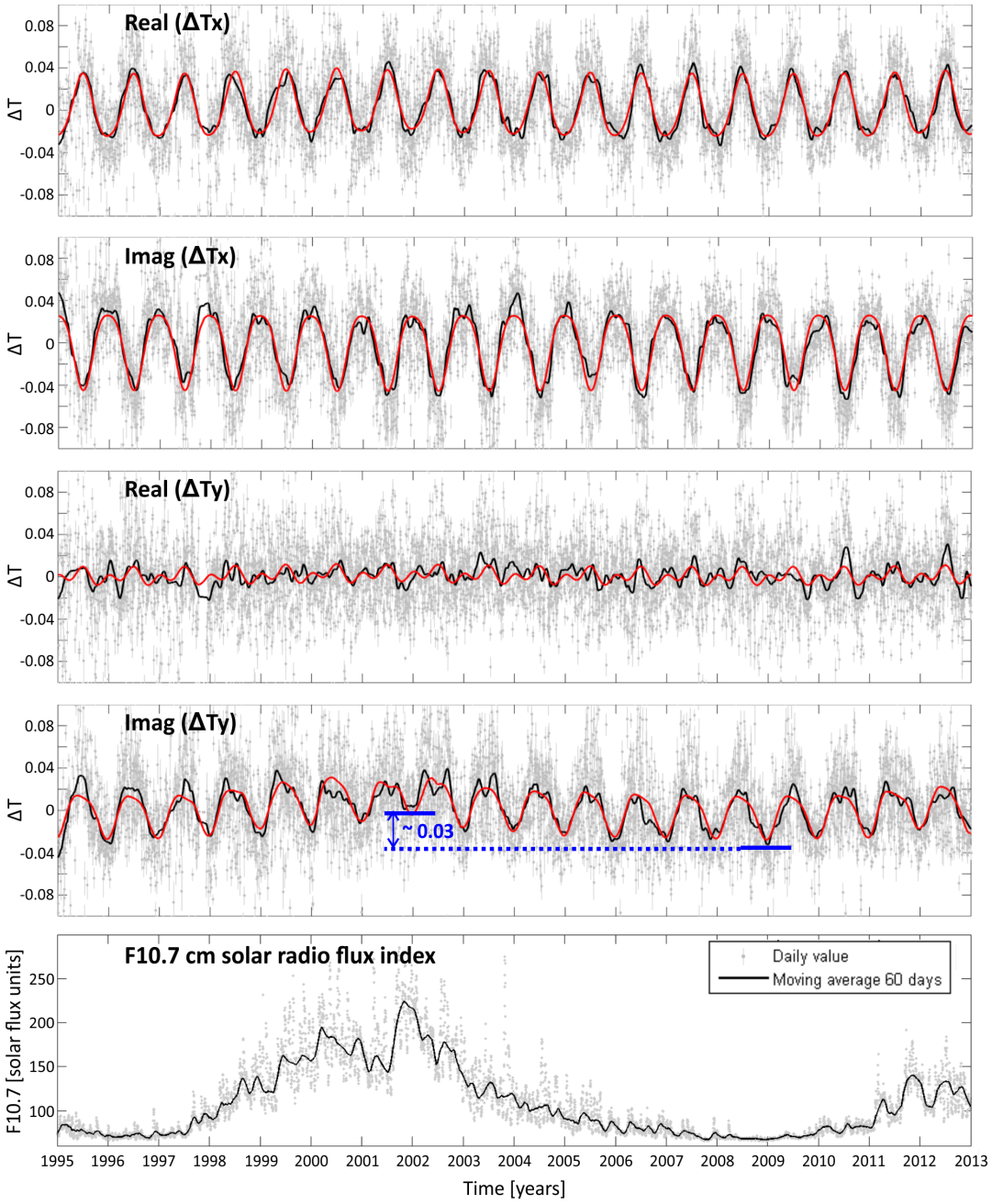

Figure 5.12: Same as Figure 5.9, but for site NGK.

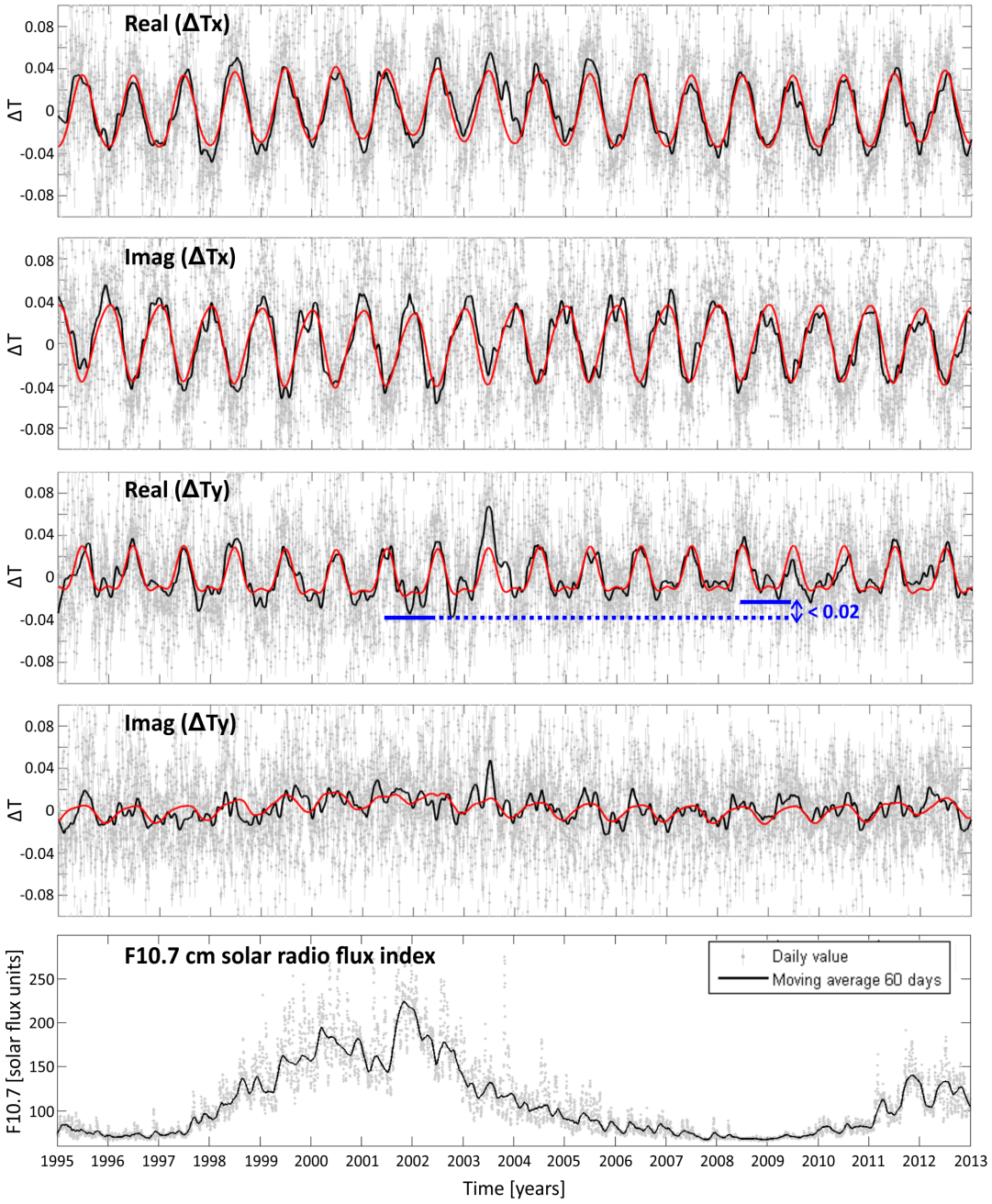

Figure 5.13: Same as Figure 5.9, but for site VIC.

5.3.3 Empirical model of VTF temporal variations

To quantify the amplitude of the seasonal and the 11-year variations in the temporal changes of VTFs, the observed VTF deviations at each site and for each period were modelled using a function with dependence on parameters that control the external magnetic fields (equation (5.2)):

$$\begin{aligned} T_{source\,effects}(DOY, F10.7) = c_1 + c_2 \sin\left(\frac{2\pi \cdot DOY}{365} + c_3\right) + \cdots \\ + c_4 \sin\left(\frac{4\pi \cdot DOY}{365} + c_5\right) + c_6 \cdot F10.7 \end{aligned} \tag{5.2}$$

To account for the seasonal dependence, the model includes sine functions that depend on the DOY of each VTF estimate. The amplitude (c_2, c_4) and phase (c_3, c_5) coefficients of these functions are the sought parameters. Two sine functions are considered, in order to model annual and semi-annual oscillations, which represent the dominant peaks in the spectra of VTF temporal variations (Figure 5.4a). To account for the influence of solar activity, the model includes a coefficient (c_6) which is multiplied with $F10.7$. A normalized value of $F10.7$ is used to adjust the magnitude of c_6 with the amplitude coefficients associated to the sine functions. The long-term trend observed in some components of Figures 5.9 to 5.13 could also be fitted by adding a third sine function (with a period of 11 years), but it was preferred to consider the $F10.7$ index because it is physically related to the solar activity. For each station and period, the 6 coefficients of equation (5.2) were determined by minimizing the differences between data and model using a least squares approach. To examine mid- to long-term trends and to avoid the influence of outliers, the data fitted were the 60-days moving average of the VTF deviations from the median. For consistency, the $F10.7$ time series was smoothed using same procedure.

Figure 5.14 shows coefficients c_2 for temporal variations of $Real(T_x)$ and $Imag(T_x)$ plotted versus geographical latitude. The coefficients were obtained using data between years 2003 and 2013 for the eleven magnetic observatories. These results suggest that the amplitudes of annual variations in T_x tend to increase with increasing latitude, and decrease with decreasing period. As a first approximation, the dependence of the amplitude on latitude can be estimated by a 2nd order polynomial function, which shows a relative symmetry around the geographical equator, especially for the $Imag(T_x)$ component (see grey lines in Figure 5.14). According to this estimate, the amplitudes of annual variations in the T_x components would be consistently >0.01 (i.e. peak to peak differences >0.02) for latitudes higher than ∼35°, and for periods equal to or longer than 1024 s. Although the magnitude of c_2 in T_y tends to be smaller for stations with lower latitudes (not shown), they do not follow a proportional relation with latitude consistent with the T_x component. No clear geographical pattern is observed for the other coefficients.

The coefficient that is multiplied with $F10.7$ (c_6) shows higher values for some VTF components at sites BEL, HER, NGK and VIC. This coefficient controls the long-term fluctuation that the empirical model (red lines) exhibits in Figures 5.9, 5.10, 5.12 and 5.13. In these examples, the empirical model fits properly the VTF temporal variations only if the dependency on F10.7 is considered. An evident

long-term trend correlated with the solar activity is not observed at site KAK (Figure 5.11), which is consistent with small values for coefficient c_6 obtained by the empirical model.

Considering the results obtained for the empirical VTF temporal variation model, the contribution of the seasonal source effect to the absolute value of T_x can be roughly estimated by:

$$Real(\Delta T_x)_{seasonal\ variation}(\tau, DOY, Lat) = a(\tau, Lat) \cdot \sin\left(\frac{2\pi \cdot DOY}{365} - 1.5\right) \tag{5.3}$$

$$Imag(\Delta T_x)_{seasonal\ variation}(\tau, DOY, Lat) = a(\tau, Lat) \cdot \cos\left(\frac{2\pi \cdot DOY}{365}\right) \tag{5.4}$$

Where τ is the period, DOY is day-of-year of the measurement; Lat is the geographic latitude of the studied area; $a(\tau, Lat) = a_1(\tau)Lat^2 + a_2(\tau)Lat + a_3(\tau)$ is a 2nd order polynomial fit, which estimates a global dependency of c_2 with latitude for the real and imaginary parts of T_x (grey lines shown in Figure 5.14, see coefficients in Table 5.2). The functions described by equations (5.3) and (5.4) fit the average seasonal trend of the daily T_x estimates (see red lines in Figures 5.5 to 5.8). It is important to note that daily T_x estimates can deviate from the average seasonal trend due to: (1) the base line of the temporal variations of the studied area, (2) the possible influence of the 11-year solar cycle, and (3) the daily scatter observed around the long-term trends (seasonal and 11-year patterns). As a rule of the thumb, an uncertainty of $\pm$0.02 around the average seasonal trend (i.e. the estimate calculated using equations (5.3) and (5.4)) can be assumed, considering the empirical repeatability range of VTFs obtained in this analysis.

Table 5.2: Coefficients to estimate the global seasonal source effect in the temporal variations of the T_x-components of the VTF (see Figure 5.14).

Coefficient	τ = 256 s		τ = 512 s	
	$Real(T_x)$	$Imag(T_x)$	$Real(T_x)$	$Imag(T_x)$
a_1	0.000001	0.000004	0.000004	0.000007
a_2	-0.000015	-0.000029	-0.00015	-0.000103
a_3	0.001969	0.00328	0.001957	0.000751

Coefficient	τ = 1024 s		τ = 2049 s	
	$Real(T_x)$	$Imag(T_x)$	$Real(T_x)$	$Imag(T_x)$
a_1	0.000011	0.000011	0.000021	0.000019
a_2	-0.00024	-0.000067	-0.000302	-0.000079
a_3	-0.001786	-0.005495	-0.009748	-0.01206

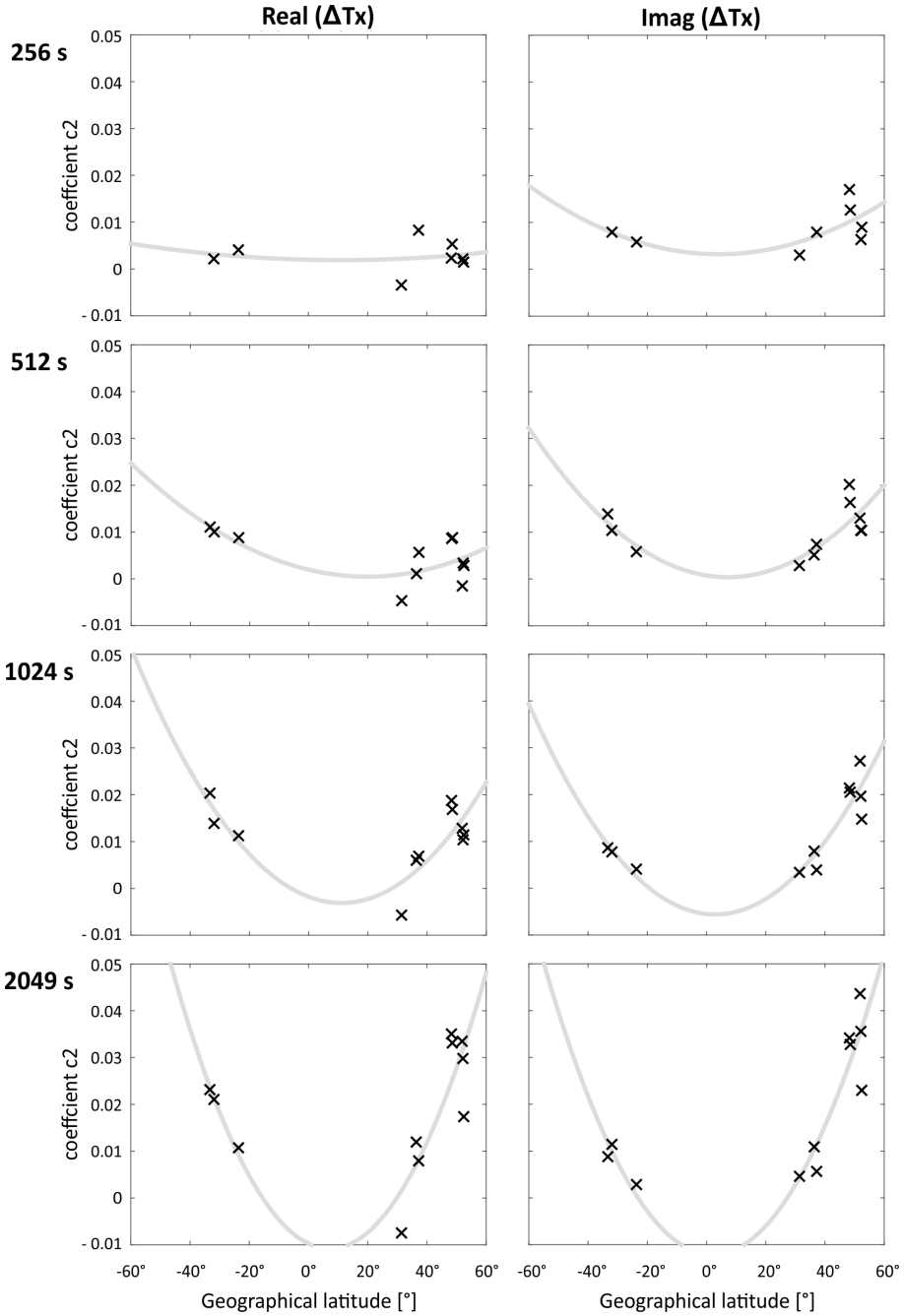

Figure 5.14: Dependency of empirical model coefficient c_2 (amplitude of annual variation) versus geographical latitude. The coefficients c_2 (see text) were obtained by fitting deviations of daily estimates of T_x from the 10-years median using data from 2003 to 2013 for periods of 256 to 2049 s. Crosses mark c_2 values computed for each station. Stations BEL, HER and KAK were excluded in the analysis for the period of 256 s, due to low quality of the estimates. Grey lines are 2nd order polynomial fits, to estimate a global dependency of c_2 with latitude (see equations (5.3) and (5.4), and Table 5.2 for further details).

5.3.4 Similarities of source effects at neighbouring sites

The empirical model defined in equation empirical model VTF can adequately describe the amplitudes of the seasonal variations observed in T_x, which accounts for an important amount of the observed temporal variations. These results would imply that systematic source field effects in T_x are controlled by global phenomena. However, such a trend was not found for the T_y components, at least not for the sites studied here. To test if T_y temporal variations could be related to local phenomena, temporal variations of VTFs recorded at "neighbouring" sites were compared. IPOC sites PB02 and PB05 were also included in this analysis.

Figures 5.15, 5.16 and 5.17 show smoothed temporal variations of all VTF components observed at three pairs of sites, with station distances between 200 and 900 km (NEW-VIC, BEL-NGK and PB02-PB05). For each pair of stations, the main trends observed in VTF deviations are quite similar, particularly the shape and amplitude of the seasonal variations, including T_y. The sites which are closest (PB02 and PB05) exhibit the highest correlated signals ($Imag(T_x)$ and both T_y components between 2010 and 2012, Figure 5.17). These comparisons seem to confirm that T_y temporal variations follow complex patterns, which cannot be properly described by the proposed empirical model. Although NEW-VIC and BEL-NGK are separated by $<5^\circ$ of latitude, both pairs of sites show very different seasonal variations in $Real(T_y)$. While differences between seasonal peaks observed in $Real(T_y)$ at NEW and VIC are close to $\sim$0.05 (Figure 5.15), the amplitude of the annual variation in the same component does not exceed this value at BEL and NGK (Figure 5.16). It is interesting to note that no clear seasonal peak is observed for the T_x temporal variations at sites PB02 and PB05 (Figure 5.17), which is consistent with small amplitudes of seasonal variation predicted by the 2nd order polynomial fit $a(\tau, Lat)$ for a period of 2049 s at latitudes around -20° (see Figure 5.14).

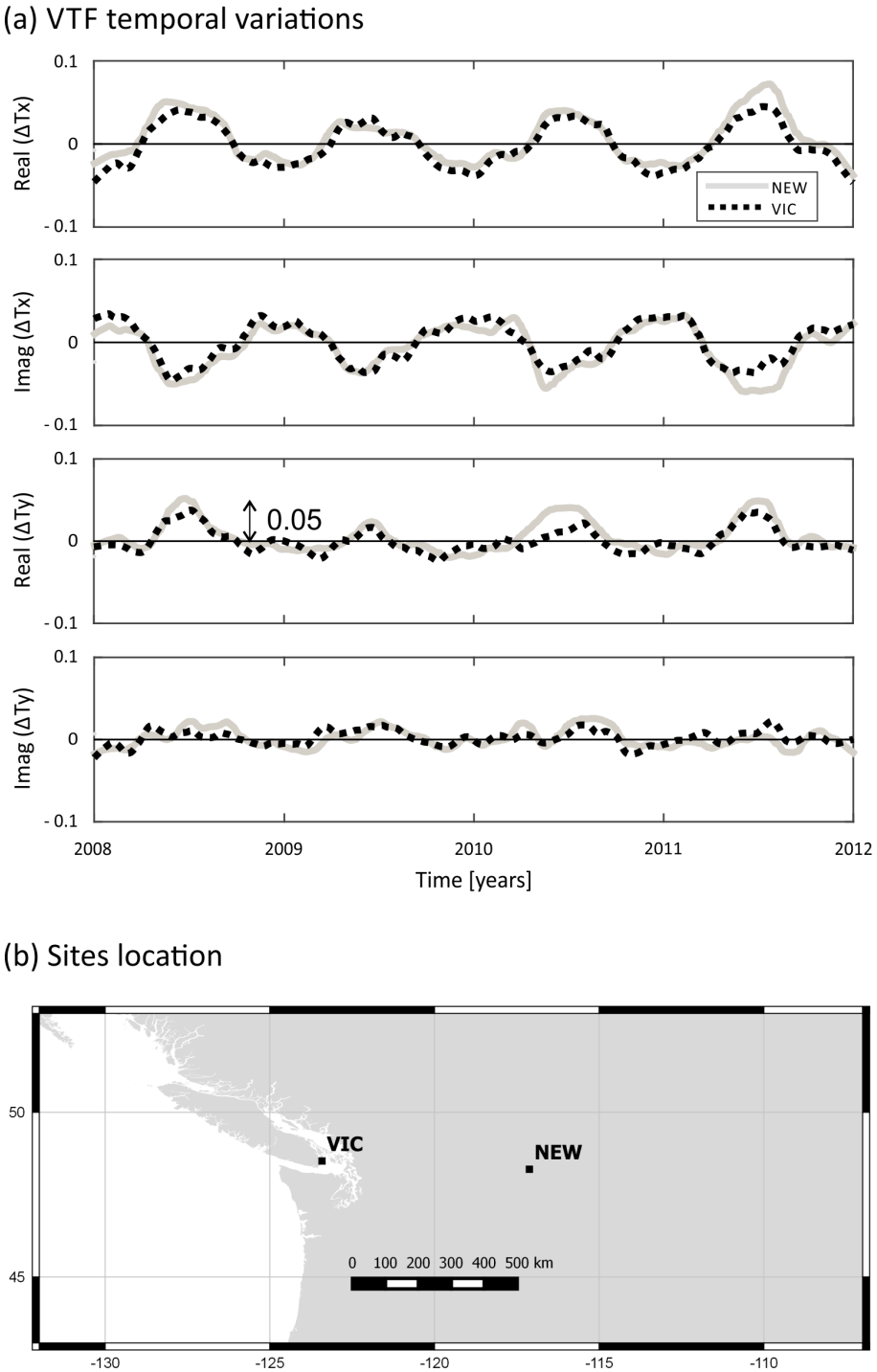

Figure 5.15: (a) Comparison of VTF temporal variations observed at sites NEW and VIC, for a period of 2049 s. Lines are the 60-days moving average of VTF deviations from the 4-years median (2008-2012). (b) Sites location.

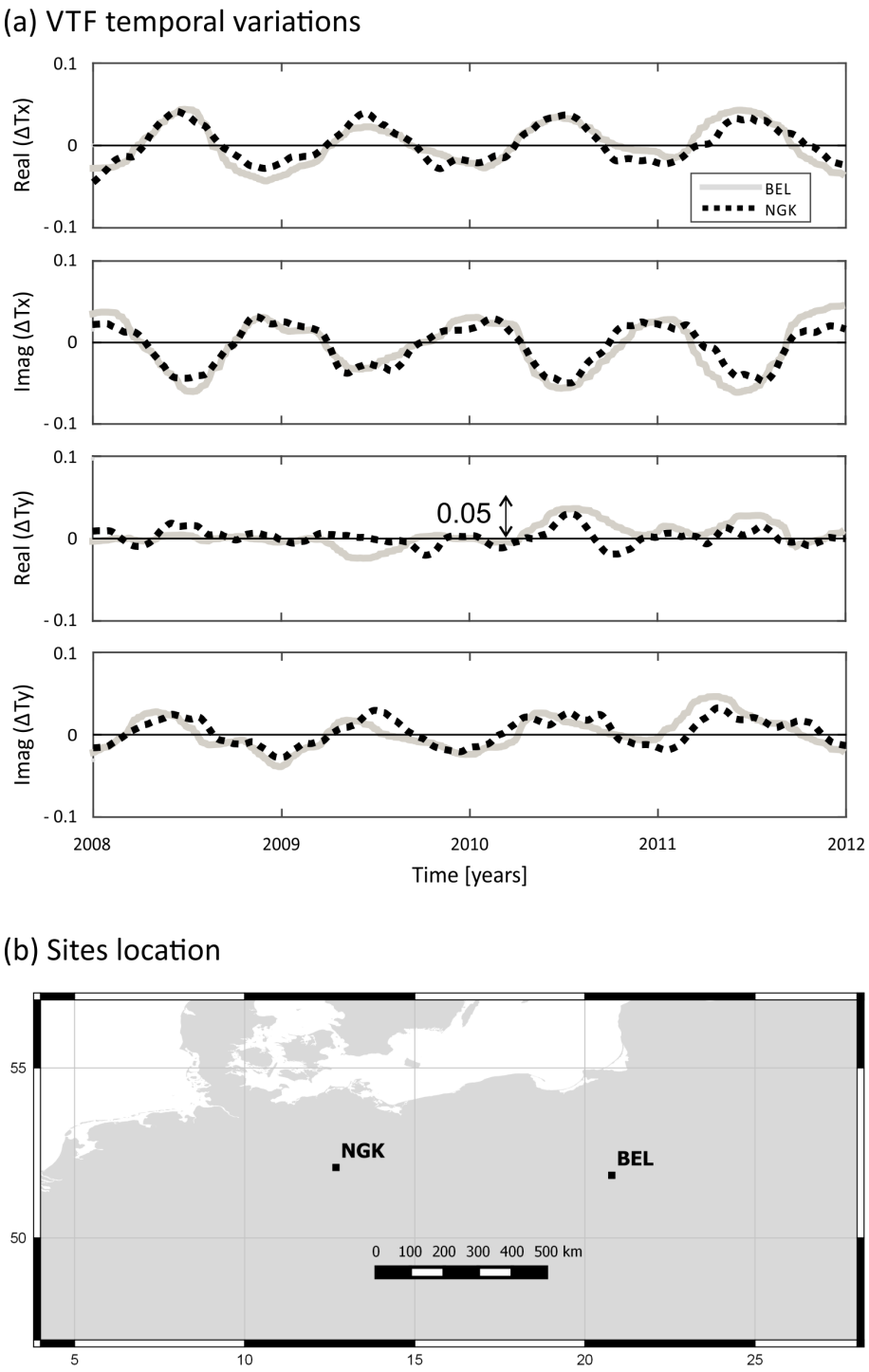

Figure 5.16: (a) Comparison of VTF temporal variations observed at sites BEL and NGK, for a period of 2049 s. Lines are the 60-days moving average of VTF deviations from the 4-years median (2008-2012). (b) Sites location.

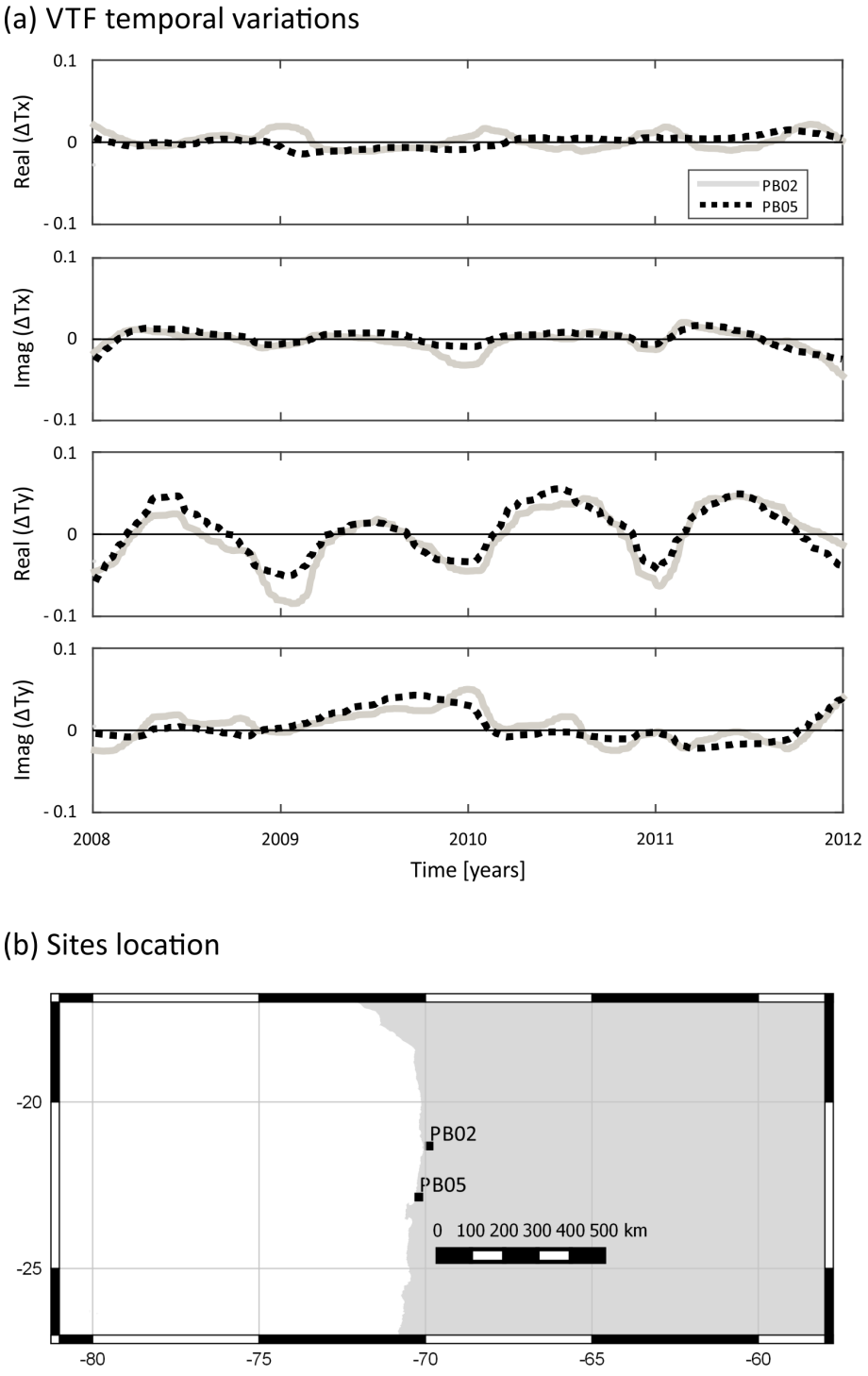

Figure 5.17: (a) Comparison of VTF temporal variations observed at IPOC sites PB02 and PB05, for a period of 2049 s. Lines are the 60-days moving average of VTF deviations from the 4-years median (2008-2012). (b) Sites location.

5.4 Discussion

5.4.1 Influence of data quality on source effects patterns

To evaluate the effect of the data quality on the described source effects, the behaviour of VTF temporal variations between different datasets was compared, in which data were selected considering different thresholds for the confidence interval of daily VTF estimates. The long-term patterns described in VTFs temporal variations do not vanish by applying this procedure, although selecting daily TFs estimates by different error thresholds modifies the amount of analysed days and the associated statistical distribution. Figure 5.18 shows daily VTF deviations from the median at the exemplary site NGK and for the imaginary part of the T_y component, for two subsets of data obtained selecting VTF estimates with errors smaller than 0.04 and 0.01 (i.e. twice and half of the threshold assumed for the previous analyses). As can be seen in Figure 5.18, although changing the threshold error modifies the distribution of points (and subtly their associated median value), the seasonal and 11-year patterns are persistent at both datasets.

A second approach to improve the quality of TF estimates was to use the remote reference processing technique (Gamble et al., 1979). The remote reference processing was not used for the previous analyses because the distance between the studied INTERMAGNET sites exceeds thousands of kilometres in most cases. It is still debated if, and to what extend, the remote reference method can be applied in such circumstances. The remote reference method was applied for processing data of two sites for which there is available neighbouring stations with better data quality: BEL (with NGK as remote site) and NEW (with VIC as remote site). Figures 5.19 and 5.20 compare single-site and remote reference processing results. As can be seen in these figures, the single site and remote reference results do not differ significantly. Again, these figures show that the seasonal variation pattern is clearly observed in both types of results, suggesting that such patterns are robust and systematic features that cannot be explained by fluctuations in the data quality.

5.4.2 Implications of source field effects for MT studies

The results presented in previous sections show systematic patterns in the VTF temporal variations correlating with external magnetic fields changes, obtained at mid-latitudes in different continents and geographical settings (coastal and inland magnetic observatories). The magnitudes of these source field effects can represent an important fraction of the VTF temporal variations. For example, the proposed empirical model suggests that T_x components are modulated by annual variations, which introduce differences between low and high seasonal peaks on the order of 0.04 (and above) in the magnitude of $\mathbf{T}$ at mid-latitudes, for periods $>$200 s. Such variations can even result in a change of sign for $\mathbf{T}$ between seasons, when the absolute value of $\mathbf{T}$ is small. If such an influence of external effects is not taken into account, this can lead to a misinterpretation of the underlying resistivity structure, particularly if long-period geomagnetic data are combined or compared which were acquired at different seasons or years. This potential risk can be illustrated using an example taken from a tectonically active region. Figure 5.21 shows a comparison of real induction vectors obtained at site KAK for three different days:

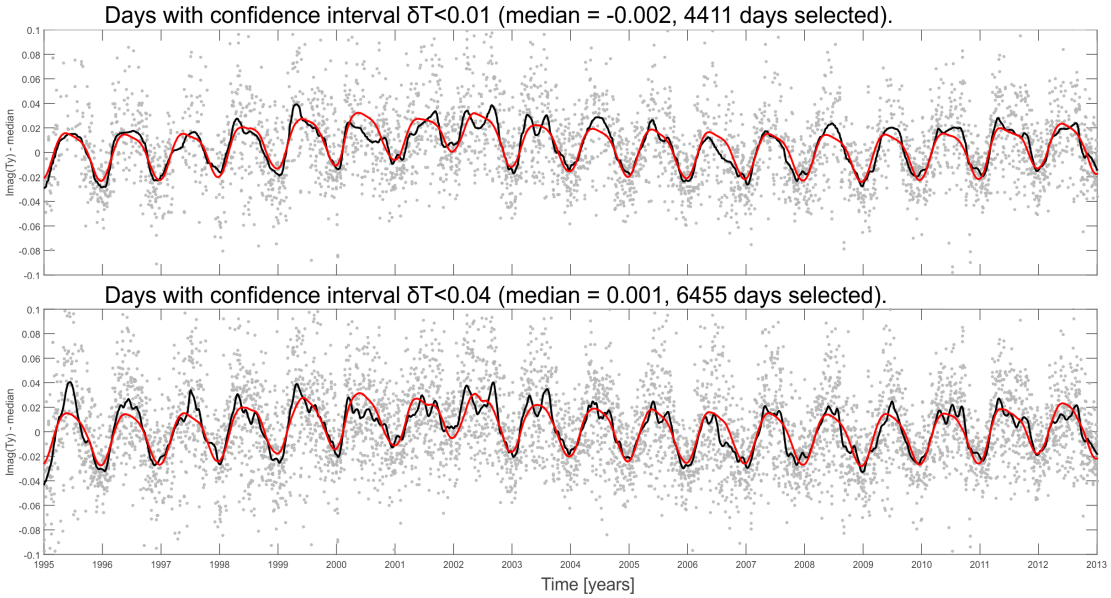

Figure 5.18: Effect of data selection on long-term VTF temporal variations at site NGK. Deviations of daily VTF from the median of all estimates between 1995 and 2013, site NGK, for a period of 2049 s, imaginary part of the T_y component. The data shown are obtained when only daily estimates with confidence intervals smaller than δT <0.01 (upper panel) and δT <0.04 (lower panel) are selected. Grey dots are daily VTF estimates. Black lines are the 60-days moving average of VTF deviations from the 18-years median. The red line is a model function that fits the smoothed temporal variations (see text for details).

two of them were calculated for days around the high peak of the seasonal variations (2010-05-30 and 2011-06-13) and another from a low-peak interval (2011-02-11). The differences in magnitude and direction for this three induction vectors are mainly explained by variations in the $Real(T_x)$ component (the average magnetic declination at KAK for these days is 7.21° W). Changes in the real parts of T_x are within the average variability range (temporal variations of VTF) observed at this site between 1995 and 2013, which are mainly caused by seasonal variations (compare the deviation from the median for these days in Figure 5.11). However, if only VTFs for days 2011-02-11 and 2011-06-13 were available (blue and pink lines in Figure 5.21, respectively), the variation between the observed induction vectors could be misleading. They could, for example, be attributed to a perturbation of the regional resistivity structure triggered by the 2011-03-11 M 9.0 Tohoku earthquake, which took place between both days and which ruptured a large area to the east of site KAK (see Figure 5.21).

To estimate and remove source effects from VTF temporal variations, an effective methodology is to compare VTFs observed at synchronously recording neighbouring sites, located at similar latitude and longitude. The results shown in Figures 5.15 to 5.17 suggest that this comparison can be done at least between sites separated by 5° in latitude and 10° in longitude. It can be concluded that external effects can be identified as those patterns in the VTFs which exhibit similar amplitudes and significant correlation with the geomagnetic activity at all compared sites. Nevertheless, care must be taken to avoid removing VTF patterns generated by internal resistivity changes. Their influence on VTFs can be estimated with forward modelling, in terms of magnitudes and spatial distributions. On the other hand, it should be tested if any remaining patterns, i.e. with source effects removed, could be related to local noise. If synchronous magnetic field observations at similar latitude and less than approximately 10° in longitude

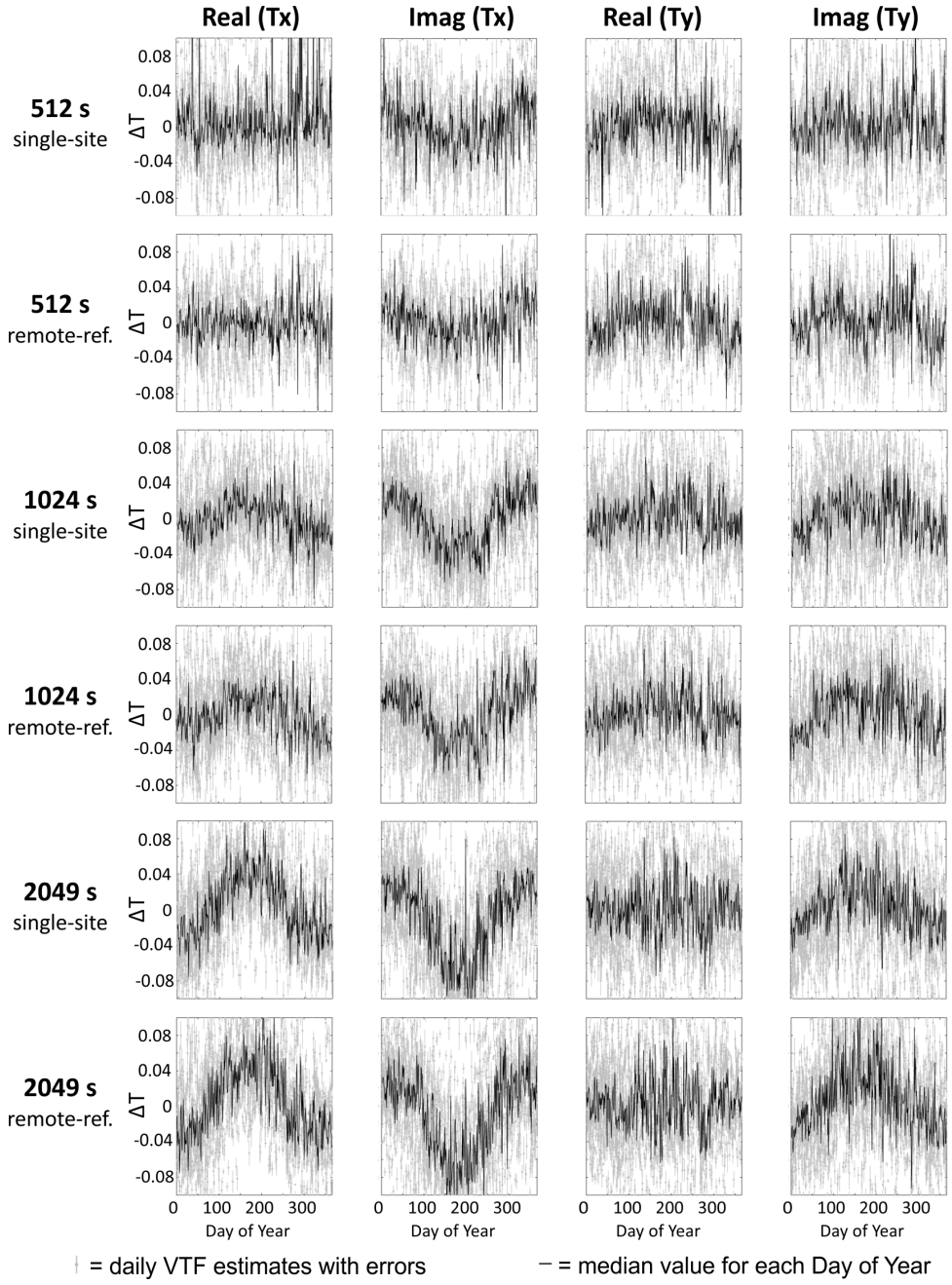

Figure 5.19: Comparison of single site and remote reference processing results obtained for site BEL. Figures show the dependency of daily VTF estimates on season. The remote sites employed was NGK.

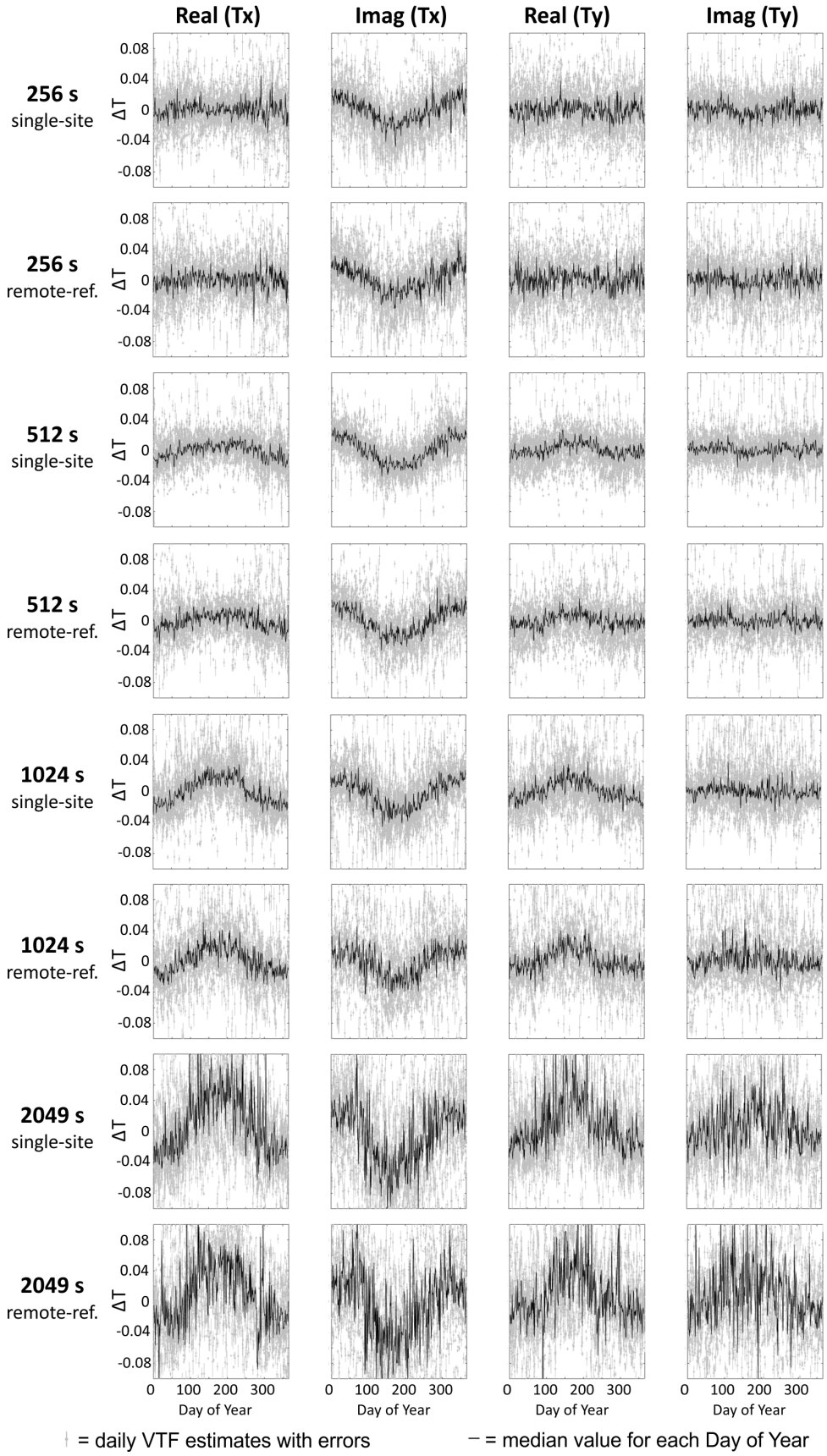

Figure 5.20: Same as Figure 5.19, but for site NEW. The remote site employed was VIC.

are unavailable, the proposed 2nd order polynomial (equations (5.3) and (5.4)) can be used to estimate the amplitude of the seasonal variations in the T_x components.

Smoothed VTF temporal variations (60-days moving average) were analysed to obtain the empirical model and to evaluate if VTFs behave similarly at neighbouring sites. For all stations it was found that daily estimates of VTFs deviate by approximately ± 0.02 from the long-term trends (i.e. annual fluctuation, long-term median value). These results suggest that daily VTF estimates are reproducible within a minimum range of 0.04 around the long-term median. This uncertainty range can be even larger due to the influence of local noise sources and the contribution of the source effects. For electromagnetic deep sounding (e.g. error floors assumed for inversion modelling) and especially for monitoring purposes, this variability range of ± 0.02 represents an empirical minimum threshold for the reproducibility of daily VTF estimates.

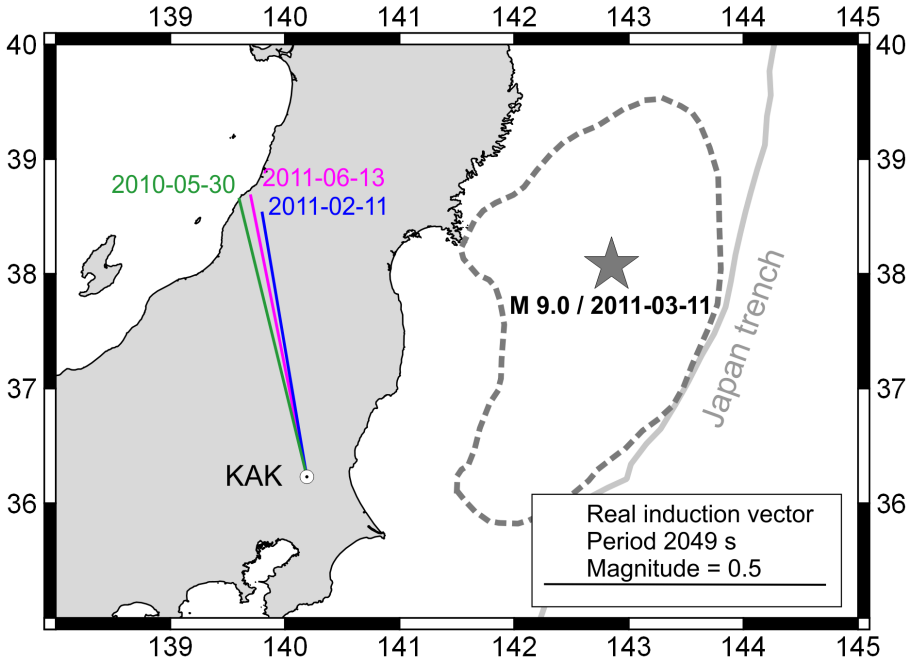

Figure 5.21: Comparison of real induction vectors (period of 2049 s) obtained at site KAK during days 2010-05-30 (green line), 2011-06-13 (blue line) and 2011-02-11 (pink line). The induction vectors are plotted using the Wiese convention, i.e. they tend to point away from areas of low resistivity. The average magnetic declination at KAK for these days is 7.21° W, with a variability below 0.03°. The epicentre location (dark-grey star) and the rupture area (dark-grey dashed line) of the M9.0 2011 Tohoku earthquake were taken from Ozawa et al. (2011). Changes in the real parts of T_x and T_y components between these three days are within the average variability range observed in the temporal variations of VTFs (see the deviation from the median for these days in Figure 5.11).

5.4.3 Origin of source field effects

To evaluate the origin of the source effects observed in VTFs, it was examined the temporal variations and seasonal dependences of the magnetic auto- and cross-spectra used to calculate T_x and T_y (see equations (2.25) and (2.26)). However, it was not possible to identify a clear relationship between the spectral elements and the associated VTFs. It is interesting to note though, that the T_x seasonal variations follow

the same pattern globally (high peaks around the June solstice, lows around the December solstice), while the seasonal patterns of the according auto-spectra depend on the hemisphere of the sites location (high / low peaks at local summer / winter).

Other authors studying seasonal and geomagnetic activity dependence of VTFs suggested that these source field effects can be explained by large-scale external current systems. After analysing the local time dependence of VTFs at fifteen magnetic observatories with a global distribution, Takeda (1997) identified two significant patterns in the real part of T_x ("type 1" and "type 2") for a period of 32 minutes (1920 s). Interestingly, the "type 2" pattern, which he observed at three sites located between 40 and 50°N geomagnetic latitude, exhibits characteristics that we also observe in the temporal variations of daily VTF estimates, namely a seasonal and solar activity dependence (with largest effects during summer and solar maximum), and an increase of the effect with increasing latitude. Takeda (1997) suggested that harmonics of the solar quiet day variation field (Sq) could explain the characteristics and latitudinal distribution of the type 1 and type 2 patterns, which show minimum amplitudes at approximately 40°N geomagnetic latitude. If Sq variations are indeed responsible for the observed source effects (in particular for a period of 2049 s), the dependence of the seasonal variation amplitudes on latitude would not be accurately described by the 2nd order polynomial proposed in equation (5.3) (grey lines in Figure 5.14), because the external Sq current system requires modelling with a more complex spatial structure (e.g. Matsushita and Maeda, 1965). It remains an open question, however, which current system could explain all of the observed source field effects for the T_x- component, particularly at shorter periods (e.g. seasonal peaks for periods of 256 and 512 s at sites FRN, NEW and VIC, see Figures 5.5 and 5.6).

In order to explain the seasonal variations in the T_y component observed in northern Chile, Brändlein et al. (2012) suggested their generation by an external current system that flows in a waveguide constrained to the space between the ionosphere and earth's surface and which does not induce electric fields into earth's subsurface. This current system is driven by interaction between the interplanetary electric field (IEF) and the ionosphere, which would explain the significant signal coherence that these authors observed between some IEF components and electromagnetic fields measured at surface. It would be interesting (but beyond the scope of this study) to test if the model proposed by Brändlein et al. (2012) could explain the seasonal variations which have observed for T_y at some of the investigated sites by calculating the signal coherence between the observatory data and the IEF data.

5.5 Conclusions

The analysis of 10 years (2003-2013) of geomagnetic data obtained at 12 mid-latitude sites, for a period band of 256 to 2049 s, show that:

- Temporal variations of daily estimates of VTFs can exhibit significant systematic periodicity correlated to external magnetic fields changes. Two main patterns can be distinguished: a periodical seasonal fluctuation, and a long-term trend correlated to the 11-year solar cycle.
- The most ubiquitous trend is the seasonal modulation of T_x. This pattern is characterized by a

high peak around the June solstice, and a low peak around the December solstice, in the real part of T_x, regardless of the geographical location of a site. The imaginary part of T_x exhibits the same pattern, but with opposite seasonal polarization. The amplitude of the seasonal variation in T_x increases with increasing latitude and period.

- Seasonal variations are also observed in T_y. However, amplitude and polarization of this periodical pattern does not follow a clear geographical trend, as is observed for T_x.
- At four sites (BEL, HER, NGK and VIC), temporal variations of some VTF components show a long-term trend that is clearly correlated with the 11-year solar cycle. In these cases, the difference between VTFs obtained at solar minima and solar maximum intervals can exceed 0.03 of the absolute value, even after removing seasonal variations.
- Consequently, if the influence of the described source effects is not taken into account, it can lead to wrong interpretations with respect to earth's electrical resistivity structure if VTFs obtained from long-period geomagnetic data acquired at different seasons or years are combined or compared.
- An effective method to estimate and remove such source effects from VTF temporal variations is to compare the VTF variability at neighbouring sites, with site distance smaller than 5° in latitude and smaller than 10° in longitude. Source effects in temporal variations of VTFs can be identified as those patterns which exhibit similar amplitudes and significant correlation with the geomagnetic activity at all neighbouring sites.
- The contribution of the seasonal variation to the absolute value of T_x can be roughly estimated with an empirical model that depends on the latitude of the site and the day of year of the measurements. However, this model cannot describe amplitudes of the seasonal variations observed in T_y components and also not the long-term variation correlated to the 11-year solar cycle which was observed at some sites.

Chapter 6

Temporal evolution of the resistivity structure in Northern Chile

This chapter contains the analysis and modelling of temporal variations of transfer functions (TFs) recorded at the IPOC MT sites, to detect possible regional-scale changes in the resistivity structure of the northern Chile forearc. Section 6.1 reviews phenomena which may generate regional-scale resistivity changes during a seismic cycle. TFs observed from May 2007 to December 2014 are analysed in section 6.2, to identify temporal variations in TFs which can be related to alterations in the resistivity structure. Subsequent modelling tests were performed in order to locate the resistivity changes that would explain the observed TFs variations, and to assess how sensitive are TFs at IPOC sites to resistivity changes above the subduction seismogenic zone, are described in Section 6.3. Finally, results of these analyses are discussed and summarised in sections 6.4 and 6.5, respectively.

6.1 Introduction

The electrical resistivity of rocks depends on physical and chemical factors (e.g. mineral composition, temperature, salinity and amount of fluids), which normally are controlled by processes that operate over geological time scales (e.g. mineral reactions, exhumation/burial of rocks, emplacement and cooling of plutons). However, resistivity-controlling factors such as the amount and interconnectivity of fluids within rocks may be significantly modified in shorter time scales by transient deformation processes (e.g. Honkura et al., 2013). For instance, evidence of shallow hydrologic changes following earthquakes (see e.g. Wang and Manga, 2010) demonstrates that these events can alter the near-surface underground distribution of fluids in time scales of days. It has been also suggested that the permeability of deep levels of the continental crust can be modified by transient events in time scales of 1 to 10^3 years (see e.g. Ingebritsen and Manning, 2010).

The subduction plate interface may represent a low permeability barrier, which prevents the upward flow of fluids that are released from the oceanic crust (e.g. Audet et al., 2009). However, large earthquakes

may break this permeability barrier resulting in a rapid migration of fluids in the plate interface region (Magee and Zoback, 1993). This type of large-scale fluid flow can alter the distribution of fluids in the region located directly above the seismogenic zone. A deep large-scale crustal fluid flow event following the 30-July-1995 Mw 8.0 Antofagasta earthquake was proposed by Husen and Kissling (2001), in order to explain fast temporal variations of the Vp/Vs ratio modelled in the lower crust. Husen and Kissling (2001) describe that the Vp/Vs ratio increase approximately from 1.72 to 1.77 in a region extending from the rupture plane up to 20 km into the overlying South American plate (Figure 6.1). Such variation was revealed after comparing tomographic models obtained by inverting two different datasets of the aftershock sequence: the first starting 19 days after the main shock and encompassing 9 days, the second starting 48 days after the main shock and containing 11 days of observations. These authors interpreted the Vp/Vs changes as a consequence of increasing pore pressure, discarding alternative explanations like changes in rock composition (considering that these variation took place in very short time interval) and increasing crack density (because the Vp/Vs anomaly is located above the rupture plane).

Additional interrelations between fluid flow and seismicity evolution at two other regions were proposed for the 1995 Antofagasta earthquake. Shapiro et al. (2003) suggested that the spatiotemporal distribution of aftershocks along the rupture plane can be partly explained by a diffusive propagation of a pore pressure perturbation, which could be caused by deformation of saturated rocks triggered by the rupture process in the hypocentre. Inside the anomaly of high Vp/Vs modelled by Husen and Kissling (2001), Nippress and Rietbrock (2007) interpreted a seismic swarm that extends $\sim$8 km vertically from the seismogenic interface into the overlying continental crust (see location and spatial extent of this feature in the map of Figure 6.1). Nippress and Rietbrock (2007) suggested that the seismic swarm can be explained either by reactivation of faults zones due to stress relaxation after the main thrust earthquake or by fluid migration mechanisms. Assuming the latter hypothesis and considering the upward migration of aftershocks along the seismic swarm, these authors estimated a fluid flow migrating with 105 to 110 m/day.

Estimations of the permeability of the continental lower crust were obtained by the aforementioned authors, in order to explain the spatial and temporal scale of the fluid flow suggested by their observations. For the region that experienced Vp/Vs changes Husen and Kissling (2001) estimated permeabilities of 10^{-16} to 10^{-17} m^2, which is in the range of values expected for the lower crust (e.g. Ingebritsen and Manning, 2010). Estimation of permeability values by Shapiro et al. (2003) and Nippress and Rietbrock (2007) are 3 to 4 order of magnitude higher ($6 \cdot 10^{-14}$ m^2 and $5 \cdot 10^{-14}$ m^2, respectively), but both studies suggested that the regions in which they interpreted the fluid flow are probably highly permeable fault zones. To explore the relationship between fluid flow and seismic velocity variations suggested by Husen and Kissling (2001), Koerner et al. (2004) modelled numerically the effect of a diffusing pore pressure change on the temporal evolution of hydraulic properties of a 2-D poroelastic medium simulating the continental crust. In the model of Koerner et al. (2004), an initial pore pressure perturbation was introduced along an inclined plane, to simulate the release of fluids from the rupture plane into the overriding continental crust. The simulation results show that the upward migration of the pore pressure perturbation alter the porosity of the medium. The assumed initial porosity of 0.01 increased to values between 0.0135 and 0.02 within a region of the model which is equivalent to the region occupied by the

Vp/Vs anomaly. The model required a permeability of 10^{-13} m^2 in order to reproduce the magnitude and change-rate in Vp/Vs described by Husen and Kissling (2001). To justify the feasibility of this very high value, Koerner et al. (2004) also proposed that the fluid flow could follow a highly permeable pathway in the lower continental crust.

This chapter presents an analysis of the temporal variability of MT data collected at the IPOC array from May 2007 to December 2014. The aim of this analysis was to investigate the temporal evolution of the resistivity structure in northern Chile. To identify variability in the MT data related to changes in the resistivity structure, the temporal variations of TFs are analysed following the monitoring approach derived in chapter 5. As working hypothesis, here it is considered that large-scale fluid relocation events triggered by earthquakes, such as the postseismic fluid flow suggested by Husen and Kissling (2001), could alter significantly the resistivity structure. For instance, Brändlein (2013) interpreted some variations in TFs during years 2008 and 2009, which he suggested as a consequence of resistivity changes in a region located down-dip of the rupture area of the 2007 M7.7 Tocopilla earthquake.

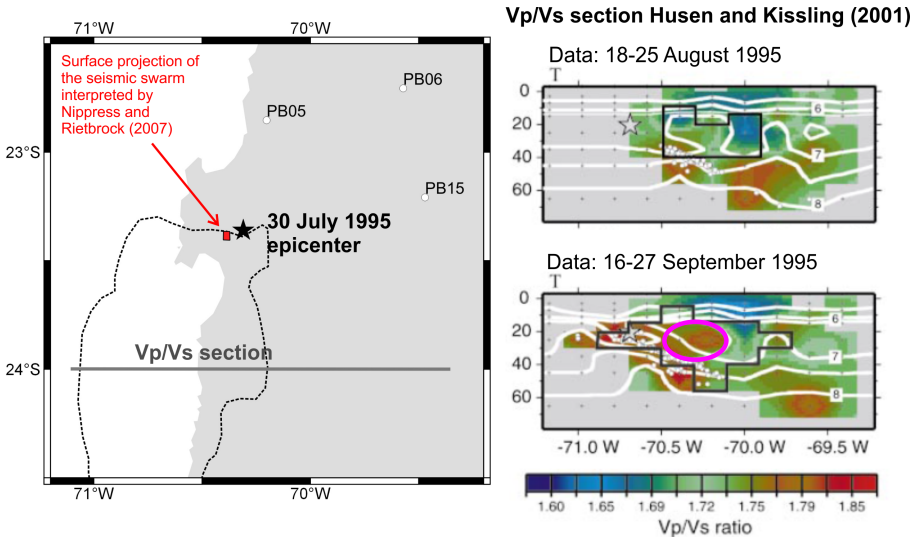

Figure 6.1: Fluid flow phenomena after the 1995 Mw 8.0 Antofagasta earthquake. (Left) Map showing the location of the earthquake area. The black star shows the location of the 1995 Antofagasta main shock epicentre. The dashed black line shows the rupture area of the 1995 Antofagasta earthquake (1 m slip coseismic contour of Chlieh et al., 2004). Red square shows the spatial extent of the seismic swarm interpreted by Nippress and Rietbrock (2007). The thick grey line indicates the trace of the section shown in the right. The location of the three southernmost IPOC MT stations is indicated as reference. (Right) Section showing the temporal changes observed in the Vp/Vs model after the 1995 Antofagasta main shock (Husen and Kissling, 2001). The pink ellipse in the lower section (later dataset) shows the region where the Vp/Vs ratio increased, which Husen and Kissling (2001) interpreted as a consequence of a deep fluid flow.

6.2 Temporal variations of MT transfer functions at the IPOC array

6.2.1 A methodology to reduce temporal variations of transfer functions

Analyses of the temporal variations of TFs presented in previous chapters show that variability of TFs over time can be caused not only by changes in the subsurface resistivity structure, but also by fluctuating noise sources (anthropogenic and instrumental noise, see section 3.4), and variability in external source fields (see chapter 5):

$$\begin{aligned} \text{Observed temporal variations of TFs} \; &= \; \text{effect of resistivity changes} \\ &+ \text{temporal variability of noise sources} \\ &+ \text{temporal variability of external sources fields} \end{aligned} \tag{6.1}$$

To isolate the effect of resistivity changes on temporal variations of TFs, it is necessary to remove contributions related to noise and source field effects. Figure 6.2 summarizes the steps performed to estimate and remove these unwanted contributions from the data (temporal variations of TFs). To minimize the influence of anthropogenic and instrumental noise, as a first step it is removed from the analysis those days where estimates of TFs show confidence intervals exceeding the empirical thresholds described in 3.4.2, and/or days when time series show problems related to instruments malfunction. This criterion restricts significantly the use of TFs which depend on electric field variations ($\underline{\mathbf{Z}}$, apparent resistivity and impedance phase), because electric field data of satisfactory quality are only available since 2011 for some sites. In order to monitor a wider time interval, therefore, only the temporal variations of VTFs are here analysed, as almost continuous recordings of magnetic fields are available since the first sites of the array were installed in 2007.

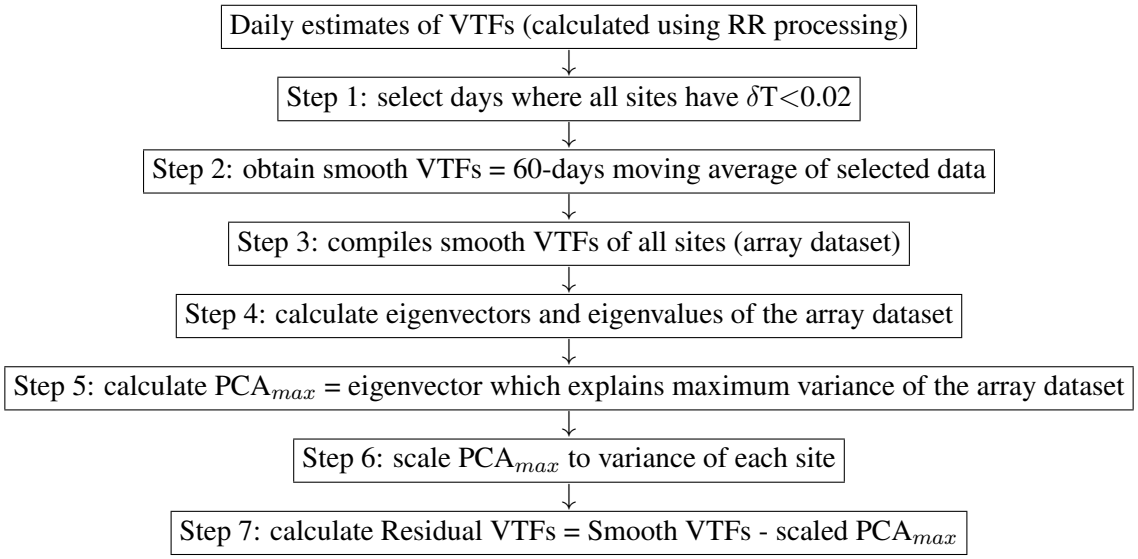

Figure 6.2: Flowchart showing the steps involved in the reduction of temporal variations of vertical magnetic transfer functions (VTFs). RR: remote-reference, δT: confidence interval of VTF estimates.

Temporal variations of VTFs were computed as deviations of daily estimates from a fixed reference sounding curve obtained for each site. The reference sounding curves were taken from the 1-year processing interval dataset described in chapter 4. In order to examine long-term and robust trends, 60-day moving averages of temporal variations were analysed (Step 2 in Figure 6.2). After trying various smoothing windows between 7 and 365 days, it was concluded that a 60-day moving average interval is an appropriate value. The amplitude and shape of the seasonal variation trend was not well observed when using smoothing windows longer than 60 days. Using shorter smoothing windows resulted in residual curves with several local anomalies (i.e. observed only at one site), which are presumably correlated to local noise conditions. Subsequently, a dataset compiling the smooth temporal variations of VTFs at all sites is obtained (the array dataset, Step 3 in Figure 6.2).

As was concluded in chapter 5, source effects observed in the long-term trends of VTF temporal variations at sites separated by hundreds of kilometers tend to exhibit significant similarities, suggesting that source effects can be identified by comparing temporal variations of neighbouring sites. To identify dominant patterns in VTFs variability which are present in the entire array, the array dataset was analysed using the principal component analysis technique (PCA) (Step 4 in Figure 6.2). The PCA is a mathematical technique used to identify linear dependencies between variables of a dataset (see e.g. Preisendorfer and Mobley, 1988). Basically, the PCA decomposes the data into new variables, which can simplify the identification of coherent patterns in the data. In practice, the PCA re-projects the distribution of data points into a set of orthogonal vectors (eigenvectors) which defines a new coordinate system in the data space. These eigenvectors represent directions of maximum variance in the data. Eigenvectors associated to the analysed dataset were calculated with MATLAB [1]. To identify the dominant pattern in the variability of VTFs, I selected the eigenvector that explains the most variance in the dataset (the PCA$_{max}$ model, Step 5 in Figure 6.2). Subsequently, the PCA$_{max}$ is scaled to the TFs variability observed at each site by calculating (6.2) (Step 6 in Figure 6.2):

$$T_{\text{source effect, site i}} = min(T_{\text{site i}}) + \hat{T}\left(\frac{max(T_{\text{site i}}) - min(T_{\text{site i}})}{max(\hat{T}) - min(\hat{T})}\right) \tag{6.2}$$

where $T_{\text{site i}}$ are temporal variations of VTFs at site i, $\hat{T}$ is the PCA$_{max}$ model of temporal variations of VTFs observed at all sites, and $T_{\text{source effect}}$ is the PCA model of T scaled to the variability of site i. This scaling procedure was necessary because the amplitude of the periodical patterns (source effects) observed in the temporal variations of VTFs at the IPOC array depend on the site considered. Relatively larger variability and source effects amplitudes are observed in VTFs at sites located in the Coastal Cordillera (see 3.4.4 and Figure 3.14). Finally, VTFs temporal variations are reduced by discounting the scaled PCA-max time series (6.3) (Step 7 in Figure 6.2). Any residual of this subtraction represents VTFs where source effects and the influence of noise are minimized.

$$T_{residual} = T - T_{\text{source effect}} \tag{6.3}$$

[1] using function *eig*, MATLAB version 8.4.0 (R2014b)

6.2.2 Analysis of temporal variations of VTFs (2007-2014)

Temporal variations of VTFs were analysed in three intervals, constrained by the availability of data (Figure 6.3):

- Interval 1 (07-May-2007 to 30-December-2014, sites PB01, PB02, PB03, PB04, PB07): this interval comprises data from sites that show almost continuous measurements since the IPOC MT array was installed.
- Interval 2 (07-May-2007 to 31-December-2011, sites PB01, PB02, PB03, PB04, PB05, PB07): the main aim of analysing this interval was to study the temporal variability of VTFs around the 2007 Tocopilla earthquake, with especial interest in examining the variations of VTFs at sites PB04 and PB05, which are located above the rupture area.
- Interval 3 (01-January-2011 to 30-December-2014, all IPOC sites except PB05, PB11, A01): during this period a maximum number of sites is available, an interval which comprises the 2014 Iquique earthquake. Site PB05 was not included because of a data gap from March-2012 to November-2013 (see 3.2). Data from PB11 and A01 have not yet been retrieved.

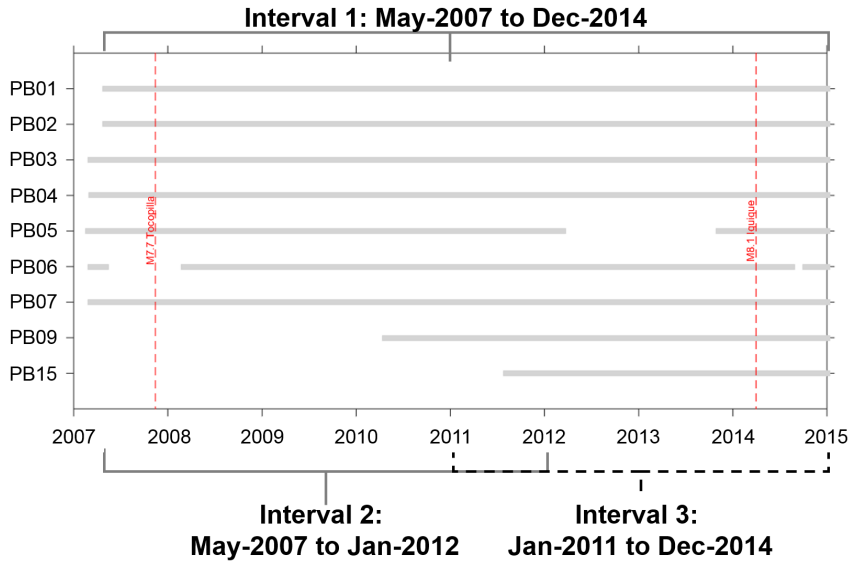

Figure 6.3: Availability of magnetic data at IPOC sites from 2007 to 2015. Intervals where temporal variations of VTFs were analysed are indicated (see the text for details). Red vertical lines indicate the dates of the 2007 M7.7 Tocopilla and 2014 M8.1 Iquique earthquakes.

Generally speaking, residual VTFs at most sites and periods do not deviate significantly from the reference sounding curves. Figures 6.4 to 6.8 show temporal variations for Interval 1 (May-2007 to December-2014) for a number of periods between 64 and 1024 s. As can be seen in these figures, the smooth temporal variations of VTFs (cyan lines) are generally well fitted by the scaled PCA$_{max}$ models (black lines). In particular, it is remarkable how well the PCA$_{max}$ model explains most of the variability observed in the T_y component for periods $\geq$ 256 s. The PCA$_{max}$ models obtained for all components and periods show seasonal variations and long-term trends correlated with fluctuations in

the geomagnetic activity, suggesting that they represent variability in VTFs due to the effect of external source magnetic fields. Therefore, following the methodology presented in 6.2.1, the residual between the data and the PCA_{max} represents VTFs temporal variations where source effects are minimized.

Residual VTFs (pink lines in Figures 6.4 to 6.8) are mostly within a range of ± 0.02 around the reference values. This variability range coincides with the resolution threshold of daily estimates of VTFs (see 5.4.2), and hence are not interpreted as significant deviations from the reference sounding curves. Residual VTFs exceeding this variability range (anomalous residual VTFs) are observed at some sites and periods. Most of the anomalous residual VTFs coincide with seasonal peaks around June and December solstices, suggesting that they represent source effects that were not well fitted by the PCA model. Anomalous residual VTFs observed only at one specific period are also attributed to source effects or noise, because changes in the resistivity structure should result in VTFs that vary smoothly with period (e.g. Weidelt, 1972), and therefore should also depart smoothly from the reference sounding curve over different periods.

The most clear and robust anomalous patterns in the residual VTFs are observed at site PB02, for periods between 64 and 256 s. These patterns consist of long-lasting positive values of residual $Real(T_x)$ observed in two intervals: from approximately mid-2008 to mid-2010, and from early-2012 to late-2013 (anomalous intervals A1 and A2, respectively, which are indicated by red arrows in Figures 6.4, 6.5, 6.6). For periods of 512 and 1024 s, residual VTFs at PB02 show more oscillating behaviour, and an anomalous long-term trend during intervals A1 and A2 is less clear (Figures 6.7 and 6.8). $Imag(T_x)$ shows also consistent negative (during 2008-2010) and positive (during 2012-2014) residual values for periods of 64 and 128 s (Figures 6.4 and 6.5). The persistence of these patterns over years and over periods only at one site suggests that they are not related to source effects, which would be consistently observed at all stations.

The analysis of intervals 2 and 3 (data not shown) resulted in similar conclusions for interval 1. In particular, the anomalies identified at site PB02 are also evident in interval 2 (A1) and 3 (A2). Anomalous values in $Real(T_x)$ were also identified at site PB05 during 2011, but values clearly exceeding the threshold of 0.02 are observed only for one period (64 s), and therefore they were not interpreted as a robust feature. Besides of A1 and A2, additional anomalies are not clearly observed during interval 2, even at PB04 and PB05 which are located above the rupture area of the 2007 M7.7 Tocopilla earthquake.

The anomalies A1 and A2 identified in residual VTFs show consistency over periods and years, and are observed locally at one site. This suggests that these features cannot be attributed to large-scale changes of external electric current systems in the ionosphere or magnetosphere. Therefore, possible candidates to explain these anomalies are alterations in the resistivity structure or long-lasting noise conditions present locally at site PB02 during the intervals where the anomalies are observed. To test whether noise conditions in magnetic field measurements increased during these intervals, the temporal evolution of the *reciprocal criterion* was analysed. Considering that the *reciprocal criterion* is sensitive to the presence of noise in magnetic field measurements (Sokolova and Varentsov, 2005, for details see 2.2.5), it was expected that fluctuating noise conditions should also result in significant temporal variability of the *reciprocal criterion*.

Figure 6.9 shows temporal variations of daily estimates of the *reciprocal criterion* matrix ($\mathbf{R}$) for periods where VTFs show the anomalies A1 and A2 at site PB02. In this figure, temporal variations are displayed as deviations of daily estimates of $\mathbf{R}$ from the long-term statistical median. The long-term median is computed from all daily estimates of $\mathbf{R}$ obtained during the interval considered. Daily values of $\mathbf{R}$ were calculated by multiplying the associated daily estimates of HTFs between sites PB01 and PB02, using equation (2.22). Figure 6.9 shows that daily estimates of $\mathbf{R}$ exhibit temporal variability, which is comparatively larger in the R_{22} component and for a period of 64 s. The smooth temporal variations of $\mathbf{R}$ (blue and red lines in Figure 6.9) exhibit some quasi-periodic patterns, which resemble the seasonal variations described for the VTFs (see chapter 5). However, neither daily estimates nor smooth temporal variations of $\mathbf{R}$ exhibit any significant trend during the intervals of the residual VTF anomalies (denoted by black lines in Figure 6.9), suggesting that noise conditions in magnetic field measurements did not vary much.

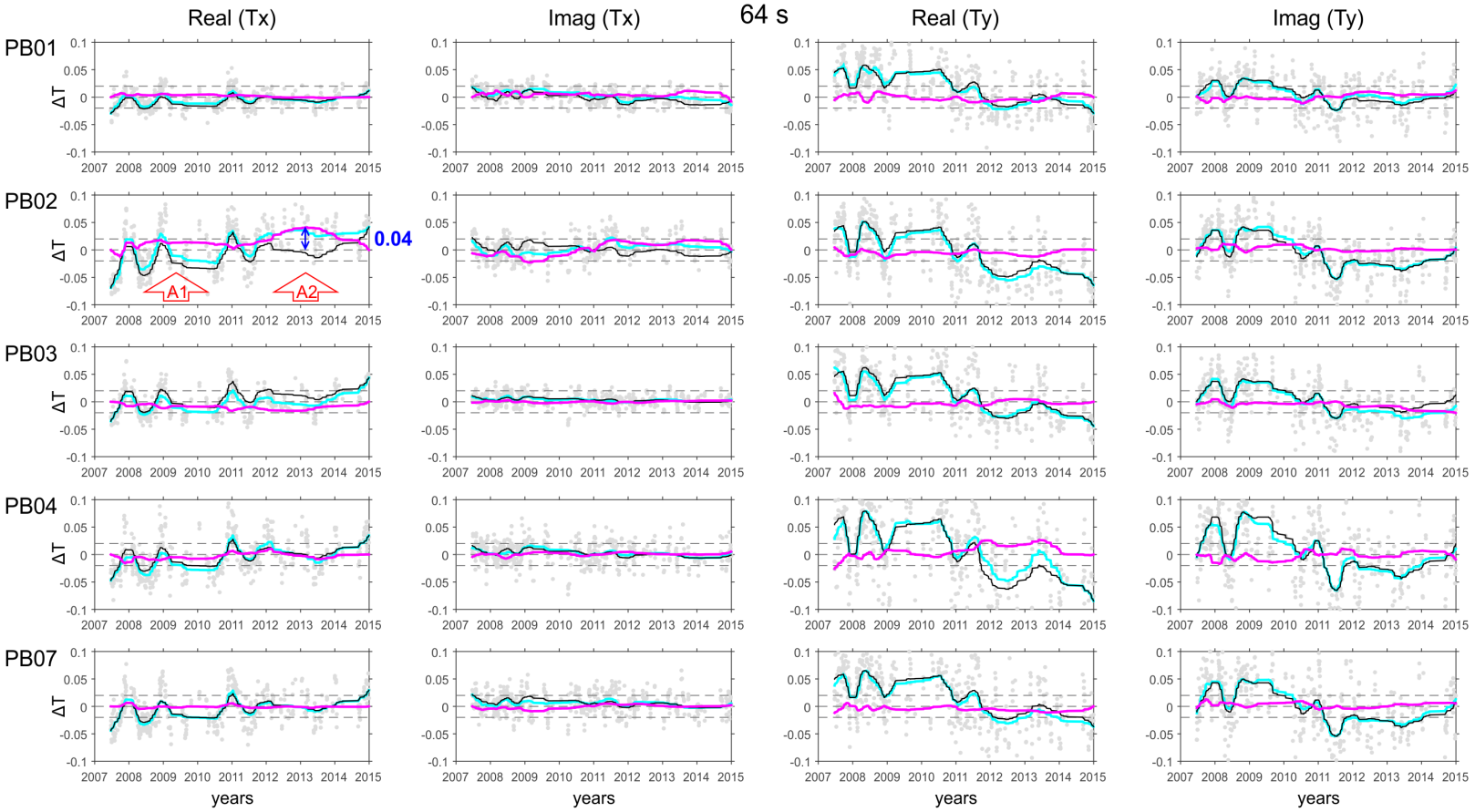

Figure 6.4: Temporal variations 2007-2015 of VTFs, for a period of 64 s. Plots are ordered by sites (along rows) and VTF components (along columns). Temporal variations are displayed as deviations of daily estimates from the reference sounding curves (see the text). Grey dots are daily estimates of VTFs. Cyan lines are 60-day moving average of daily estimates. Black-solid lines are the scaled PCA model of the 60-day moving average (see the text). Pink lines are residual VTFs, obtained after subtracting the scaled PCA model from the 60-day moving average. Black-dashed lines indicate deviations equals to 0.02, 0 and -0.02 as reference. Red arrows indicate residual VTFs anomalies (A1, A2) referred in the text.

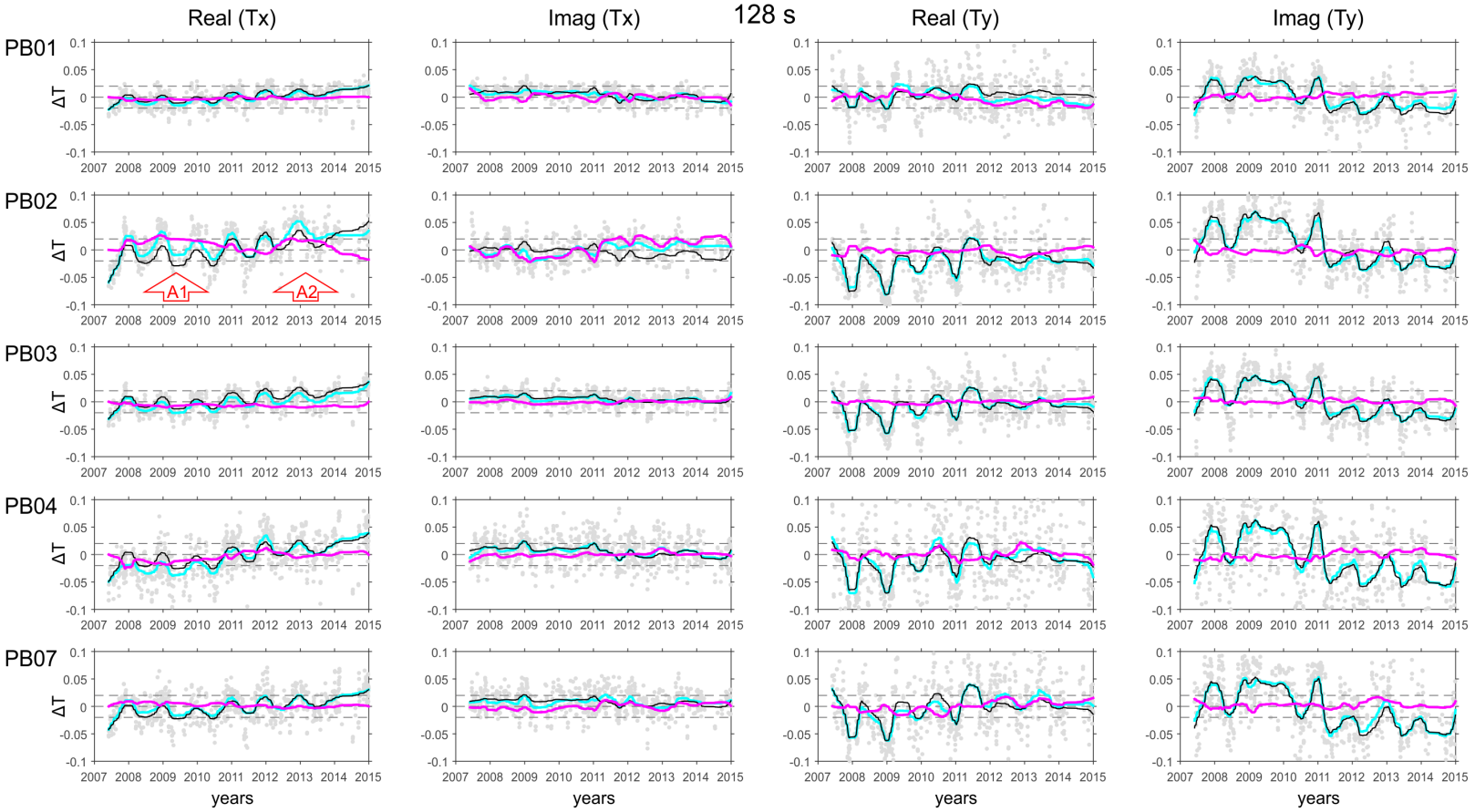

Figure 6.5: Same as Figure 6.4, but for a period of 128 s.

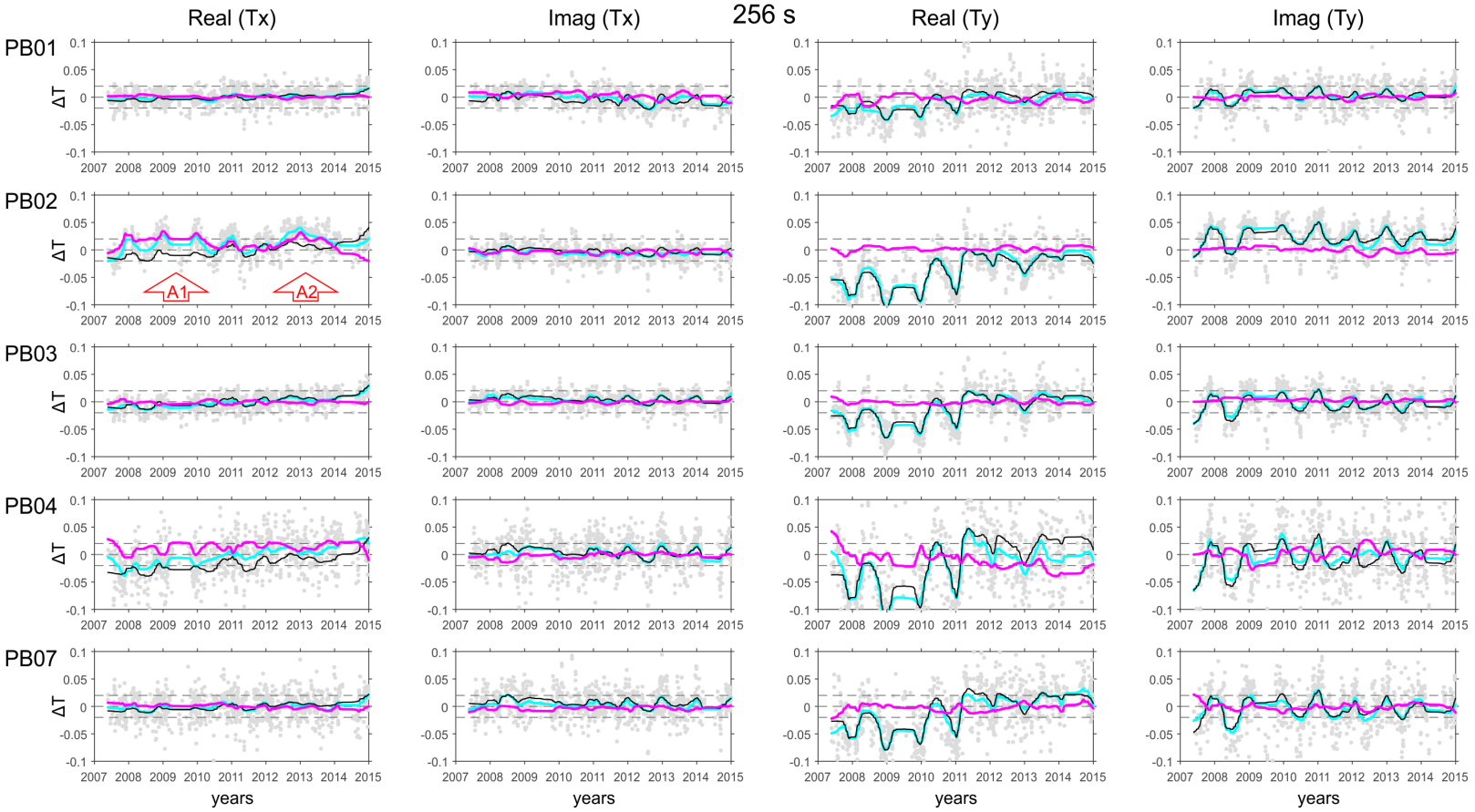

Figure 6.6: Same as Figure 6.4, but for a period of 256 s.

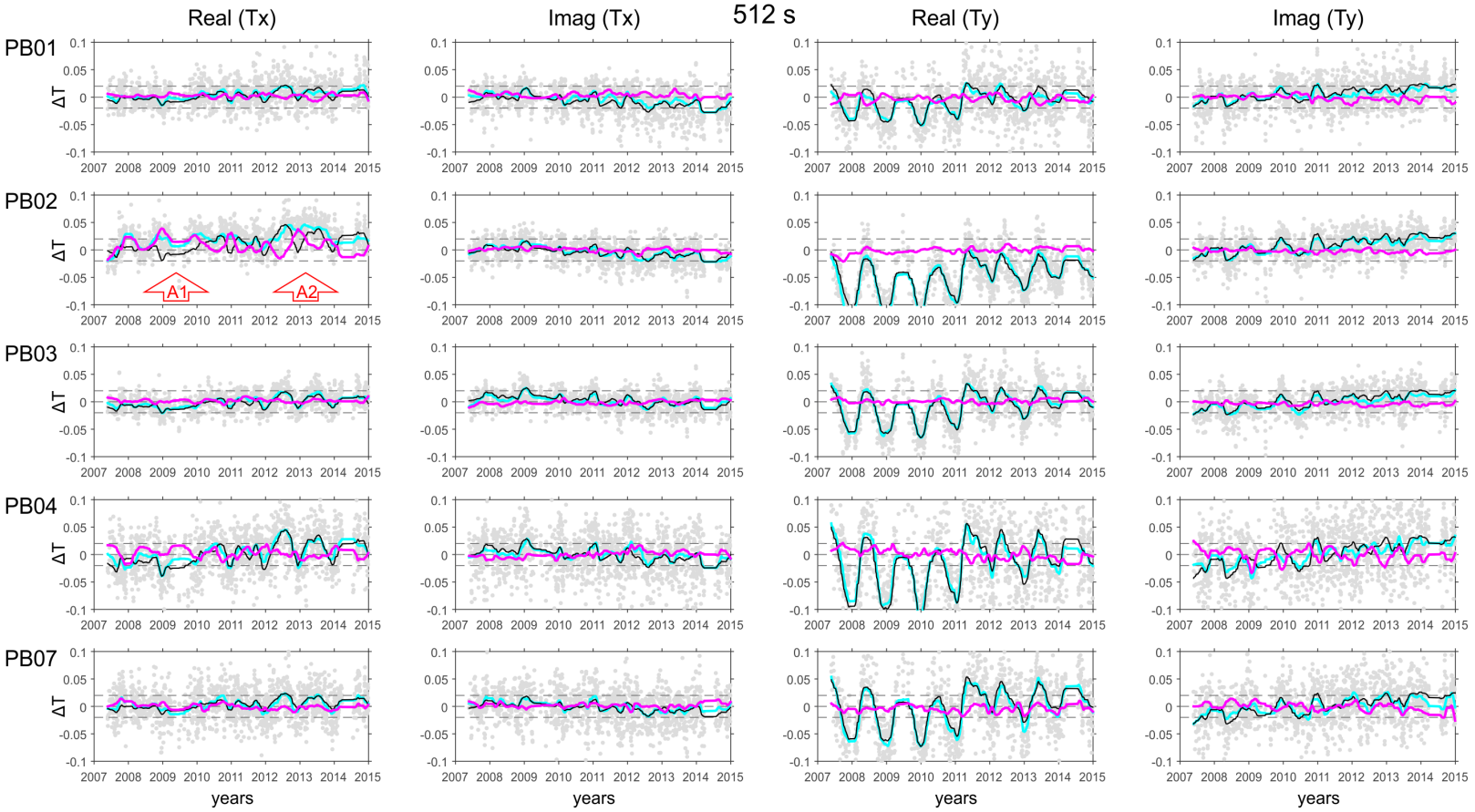

Figure 6.7: Same as Figure 6.4, but for a period of 512 s.

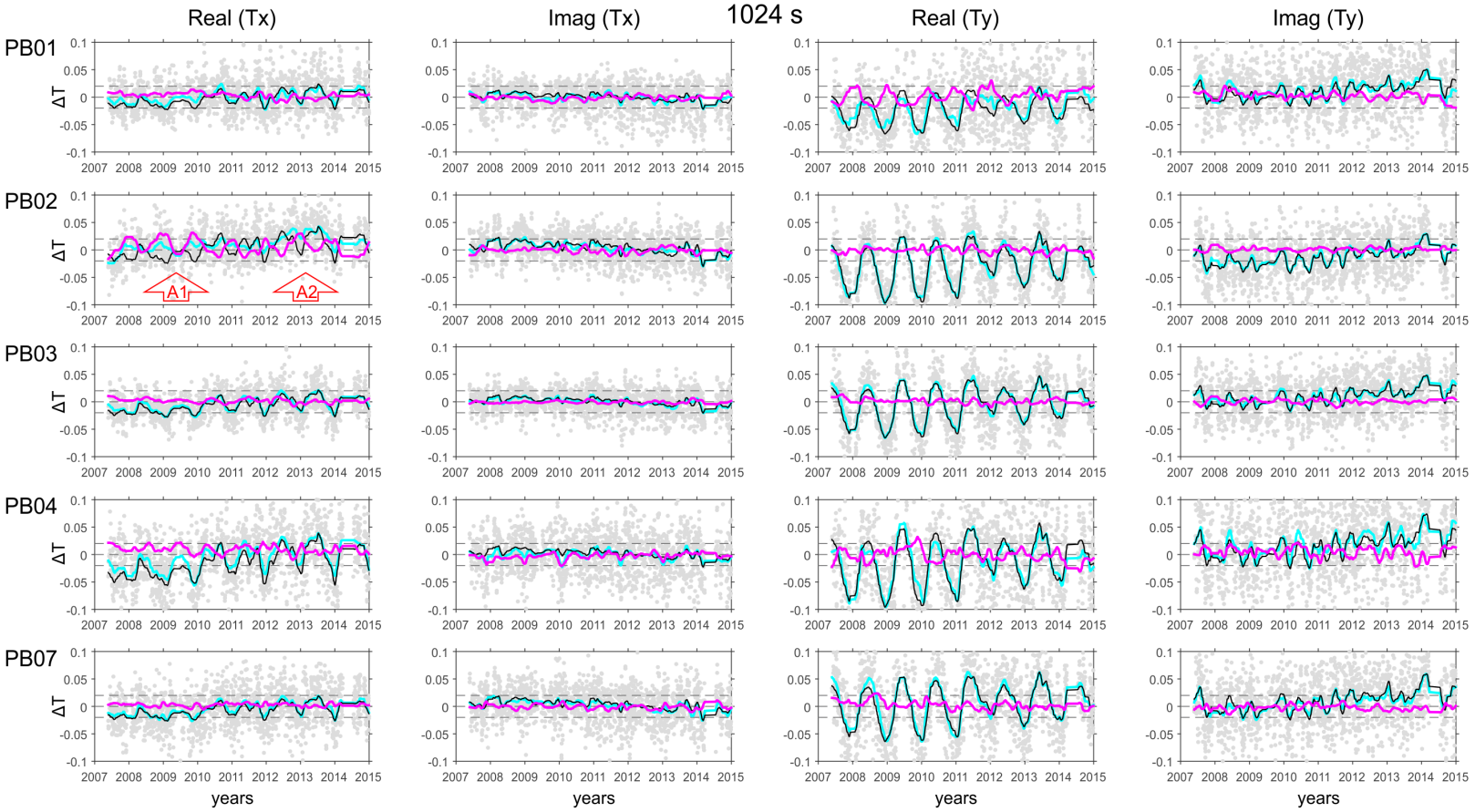

Figure 6.8: Same as Figure 6.4, but for a period of 1024 s.

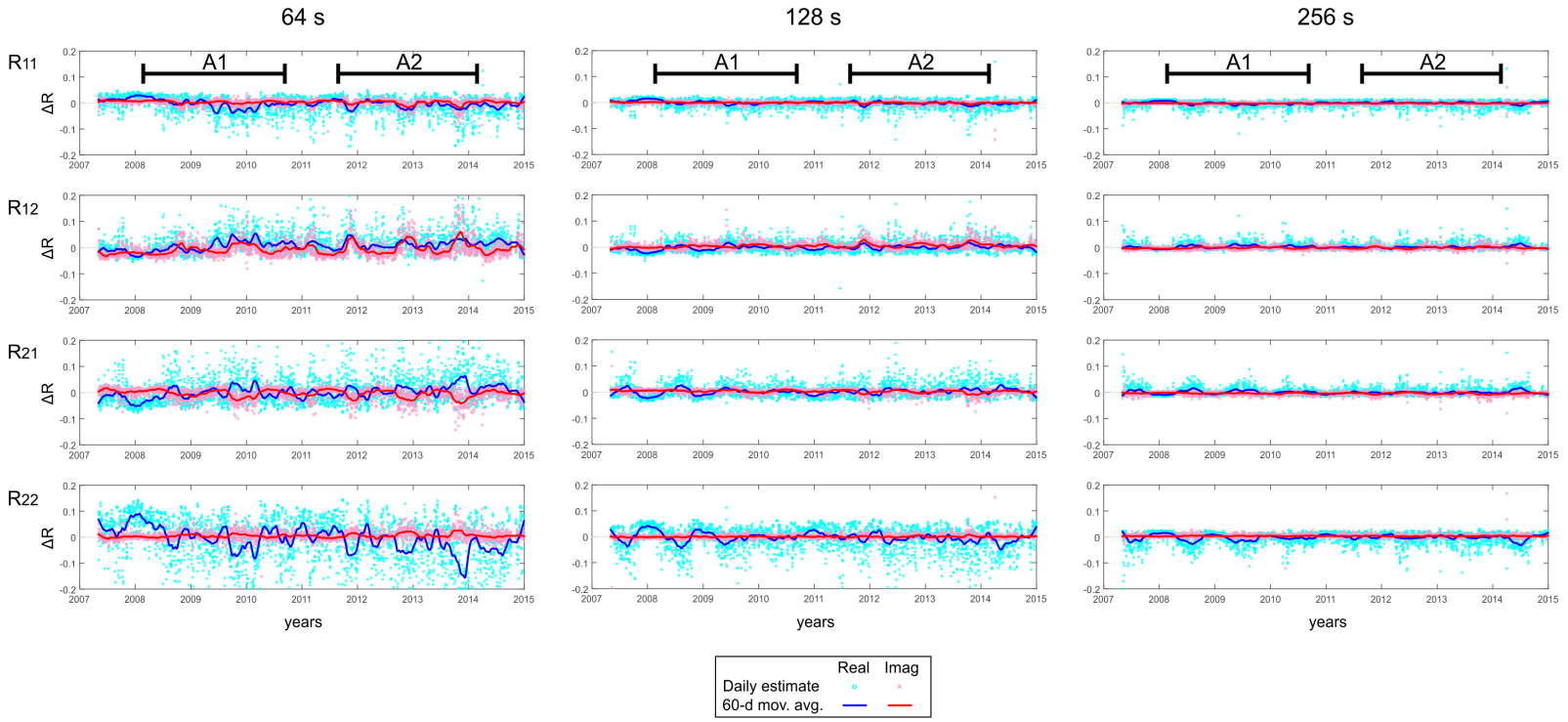

Figure 6.9: Temporal variations 2007-2015 of the reciprocal criterion matrix ($\mathbf{R}$) of HTFs between PB02 and PB01, periods of 64, 128 and 256 s. Plots are ordered by components of $\mathbf{R}$ (along rows) and periods (along columns). Temporal variations are displayed as deviations of daily values of $\mathbf{R}$ from the median of all estimates from 2007 to 2015. Cyan and pink symbols are the real and imaginary parts of daily values of $\mathbf{R}$, respectively. Blue and red lines are the 60-day moving average of the real and imaginary parts of daily values, respectively. Black lines on upper panels labelled A1 and A2 indicate the intervals where anomalies are observed in residual temporal variations of VTFs (see the text)

6.3 Relating transfer function variability with resistivity changes

6.3.1 A model of the resistivity changes causing VTFs anomalies at site PB02

The anomalous temporal variations of VTFs identified in the previous section are most likely related to resistivity changes in the subsurface, as they appear to be uncorrelated with source field effects or varying noise conditions in magnetic measurements. The anomalies were observed only at site PB02 and show significant amplitude for periods <200 s, suggesting that they are related to resistivity changes that affected regions of the upper and middle continental crust relatively close to site PB02. In order to locate the origin of the resistivity changes that can explain such anomalies, a number of alterations in the resistivity structure were simulated by perturbing the preferred resistivity model of chapter 4 (the *reference* model). For all of these hypothetical resistivity change scenarios, the model responses at all IPOC sites were calculated using the ModEM package (see 2.2.7).

The most probable factor to explain resistivity changes within time scales of ∼1 year (as those related to the VTFs anomalies) is the variability in the amount and/or interconnectivity of fluids within the continental crust close to PB02. Here it was assumed that such changes in hydraulic properties of the crust might coincide with similar variability in the seismic activity. Both processes can be connected: while the porosity and resistivity of rocks can be altered during deformation processes (e.g. preceding fracturing, Brace and Orange, 1968), also an increment in the amount of fluids in fault zones can lower the stress necessary to slip (e.g. Scholz, 1998). Therefore, following this hypothesis, most of the resistivity changes were introduced in regions constrained by the rough distribution of earthquakes located within the continental crust (see Figure 6.10).

Figure 6.11 shows a resistivity model (the *modified* model) which can explain the origin of anomaly A2 observed in the residual VTFs at site PB02. To obtain the *modified* model, the resistivity of the *reference* model was modified in a block constrained by a region which roughly comprises most of the crustal earthquakes registered north of site PB02 from 2007 to 2013 (the areal extent of this region is indicated by a polygon with purple boundaries in Figure 6.10). The seismicity in this region appears to be concentrated approximately below the Salar Grande at approximately 5-25 km depth (the vertical extent of the modified block is shown as a polygon of white boundaries in Figure 6.11a). Using the aforementioned block, it was necessary to reduce the original resistivity by a factor of 100 in order to reproduce the maximum amplitude observed in $Real(T_x)$ during the anomaly A2. Among all simulated resistivity changes, the *modified* model shows the best fit of this anomaly.

Figure 6.11b compares VTF responses at PB02 calculated from the *modified* and *reference* models. Here, VTFs are displayed as differences between the *modified* and *reference* model responses. These differences have the same physical meaning as the residual VTFs obtained in section 6.2, because the residual VTFs curves also represent deviations from a reference dataset, which comprises the data inverted to obtain the *reference* model. As can be seen, the differences between the two model responses reproduce the major trend observed in the A2 anomaly over periods, namely maximum deviations in $Real(T_x)$ of ΔT ∼0.04 at 64 s, which abruptly decrease to deviations ΔT <0.02 for periods longer than 200

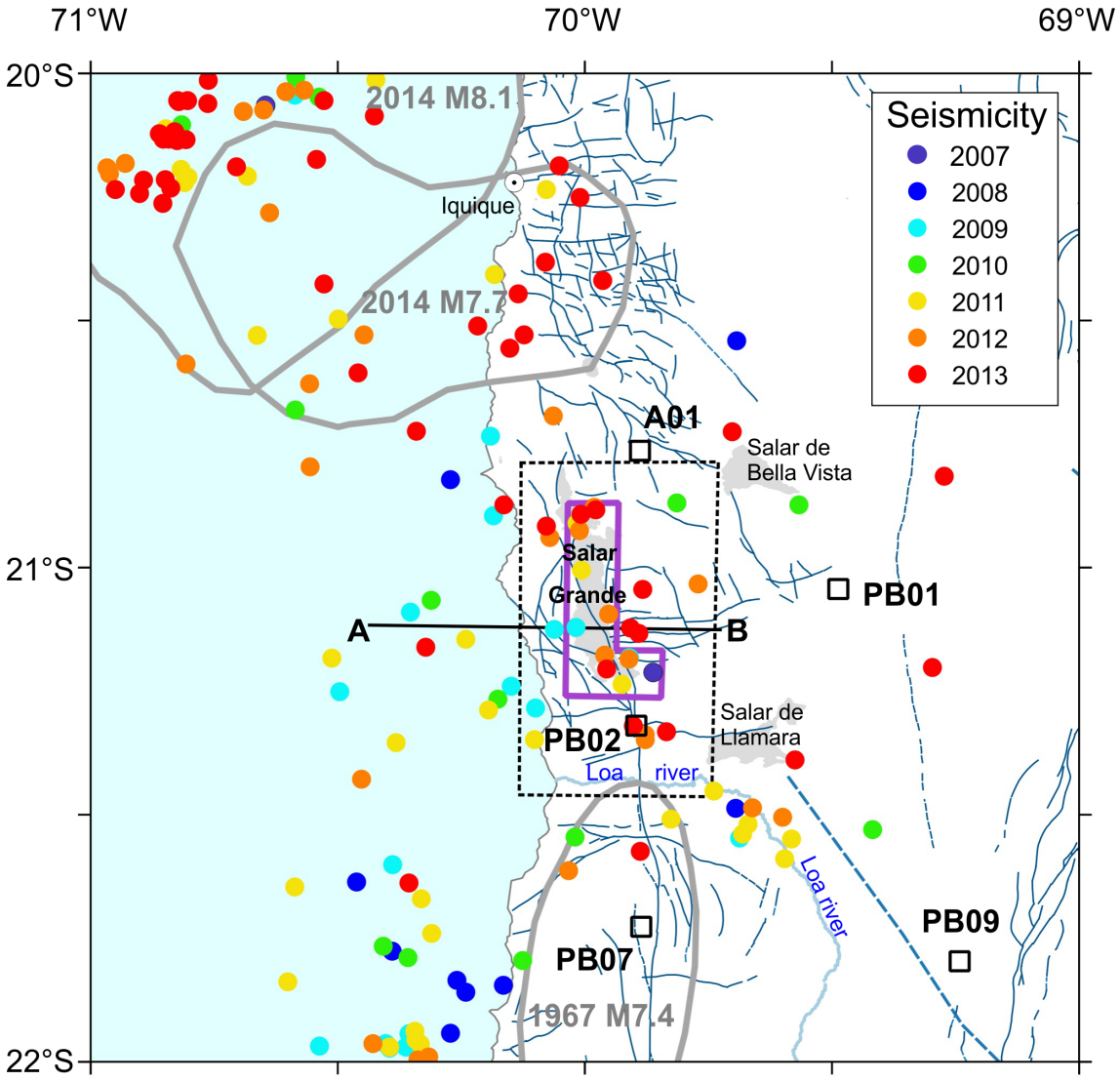

Figure 6.10: Map with temporal distribution of shallow seismicity 2007-2013 at the northern part of the IPOC MT array. Colour-coded dots are epicentres of seismic events from 25-October-2007 to 31-December-2013 which are located between 10 and 30 km depth (downloaded from http://www.sismologia.cl). Polygon with purple boundaries shows the areal extent of the region where resistivity changes were introduced in order to fit the anomalies in VTFs identified at site PB02 (see the text). Black line labelled A-B show the trace of the section shown in Figure 6.11. Polygon of black dashed boundaries surrounds the area considered for the seismic events displayed in Figure 6.21. Dark grey lines show boundaries of the rupture area interpreted for earthquakes with magnitude >7.4 during the last 50 years (compiled from Schurr et al., 2012, 2014). Blue lines are faults (taken from Sernageomin, 2003).

s (compare solid red line with black circles in Figure 6.11b). For the other components of VTFs, the response of the *modified* model deviates less than ΔT <0.02 from the *reference* model response, which is consistent with the amplitude of the residual VTFs obtained at site PB02 for the T_y component and $Imag(T_x)$. The response of the *modified* model reproduces the general trend of the anomaly A1, but does not fit the amplitude and the period where the A1 anomaly peaks (compare solid red line with black triangles in Figure 6.11b). It was not possible to improve significantly the fit of A1 trend by trying different resistivity changes in the same block of the *modified* model. It is possible that resistivity changes within a block with more complex geometry is required to reproduce this anomaly.

Constrained inversion tests of VTFs were also tried to explain the origin of these two anomalies, but it was not possible to obtain a plausible model. In these constrained inversion tests, the dataset inverted was a modified version of the data inverted in chapter 4, in which the residual anomalous changes identified at PB02 were included. Small error bounds (0.01) were set for VTFs in order to fit the residual changes, because the amplitude of these residual variations are very close to the error bounds that were employed to obtain the *reference* model. The *reference* model was used as prior and starting model. The inversion was allowed to modify cells of regions located close to PB02. The vertical extent of these regions was set between 10 and 50 km depth, based on the distribution of hypocentres. Different areal extents were considered, most of them are roughly centred at the Salar Grande and follow the NW-SE corridor suggested by the spatial distribution of epicentres shown in Figure 6.10. However, in all tests the inversion did not converge, and unrealistic resistivity distributions were obtained.

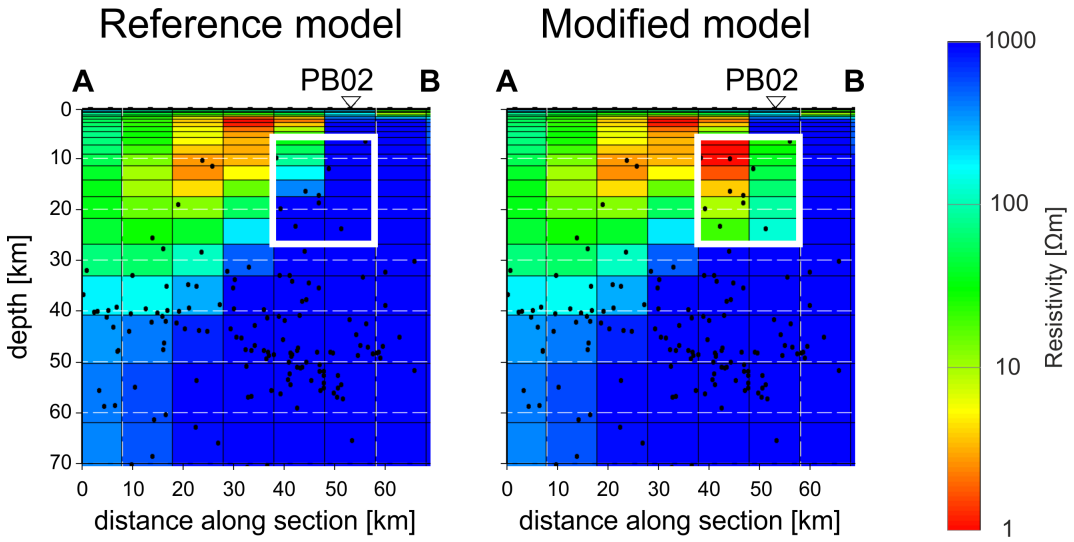

(a) Resistivity structure along section A-B

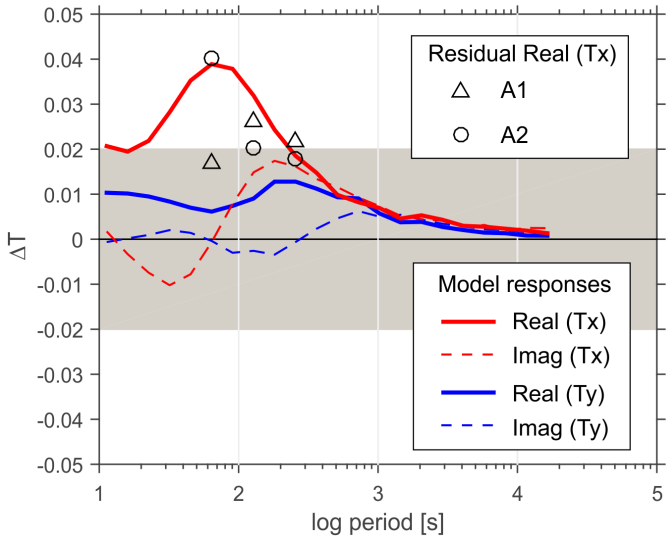

(b) VTF responses at site PB02

Figure 6.11: Resistivity changes simulated below the Salar Grande area in order to reproduce anomalies in VTFs at site PB02. (a) Comparison of the resistivity structure between the reference and modified model along section A-B (see location in Figure 6.10). Polygons with white boundaries indicate the region where resistivity changes were applied. Black dots are hypocentres of seismic events located within 75 km of the sections (events from 01-January-2008 to 31-December-2013 downloaded from http://www.sismologia.cl). (b) Difference of VTF responses at site PB02 between the *modified* and *reference* models. Lines are differences between model responses. Symbols show the maximum amplitudes observed in the $Real(T_x)$ component of residual VTFs during the intervals where the anomalies A1 and A2 were identified. Grey area indicates VTFs differences within a range of ± 0.02.

6.3.2 Sensitivity of the IPOC MT array to possible resistivity changes after large subduction earthquakes

Considering the hypothesis of a postseismic fluid flow event following the 1995 Antofagasta earthquake (Husen and Kissling, 2001), large-scale relocation of fluids could have been triggered by the 2007 Tocopilla or the 2014 Iquique earthquakes. Such large-scale fluid relocation may alter the resistivity structure on a wide scale, resulting in variations of TFs which can be observed over various IPOC sites. However, the analysis of temporal variations of VTFs revealed only two clear anomalies which were interpreted only at one site (PB02). Moreover, anomalies of VTFs at PB02 can be explained by resistivity changes which are spatially and temporally uncorrelated with the large earthquakes of 2007 and 2014. To evaluate whether the IPOC MT array would be sensitive to resistivity changes related to a possible postseismic fluid flow, additional alterations in the resistivity structure were simulated at regions above the interplate seismogenic zone. The thickness of these regions was set to $\sim$15 km, following the dimensions of the Vp/Vs anomaly suggested for the 1995 Antofagasta earthquake (Husen et al., 2000; Husen and Kissling, 2001; Koerner et al., 2004). The locations, depths and areal extents of each tested region were constrained by the rupture zones of the 2007 Tocopilla and 2014 Iquique earthquakes taken from Schurr et al. (2012) and Schurr et al. (2014) (see Figure 6.12). Resistivity changes along the unbroken segment (seismic gap) between the 2014 Iquique and 2007 Tocopilla earthquakes were also tested (polygon C in Figure 6.12), corresponding in length approximately to the locked segments of the margin interpreted by Schurr et al. (2014). The *reference* model was modified by applying changes of 0.1, 0.2, 0.3, 0.5, 2, 5 and 10 times of the original resistivity value at each cell contained within the tested regions.

Figures 6.14, 6.15 and 6.16 show TFs responses at sites where maximum variations were obtained for each test. Significant variations in TFs were not obtained at any site after introducing resistivity changes above the 2014 M7.6 Iquique earthquake rupture area, even at site A01, and therefore these results are not shown. Responses of HTFs are not shown, because significant variations in these TFs were not obtained. In order to facilitate the visualization and comparison of the obtained variations, these figures show differences between the simulation results and the response of the *reference* resistivity model. Overall, the simulation results show that resistivity changes on top of the interplate seismogenic zone would produce measurable changes in the TFs recorded at IPOC stations. As can be expected, the resulting TF variations depend on the site location and the magnitude and distribution of the resistivity change. Maximum TF variations are observed at periods between 90 and 500 s, at sites closely located to the region where the resistivity is modified. In most cases, calculated TF responses represent measurable changes if the resistivity of the *reference* model is reduced more than 3 times in the test-regions. It is interesting to note that these tests produced significant variations in $Real(T_x)$ and Z_{yx}, which are the most stable TF components at the IPOC sites, and therefore seem to be particularly suitable for monitoring purposes.

Among the studied TFs, $\rho_{a,yy}$ and ϕ_{yy} are the most sensitive components to the alterations introduced in the resistivity structure (data not shown). However, the large variability range observed in these TFs is explained because Z_{yy} show values close to zero at almost all sites. The introduced perturbations in the model result in alternating positive and negative values of Z_{yy} over periods. When estimates of $\underline{\mathbf{Z}}$ com-

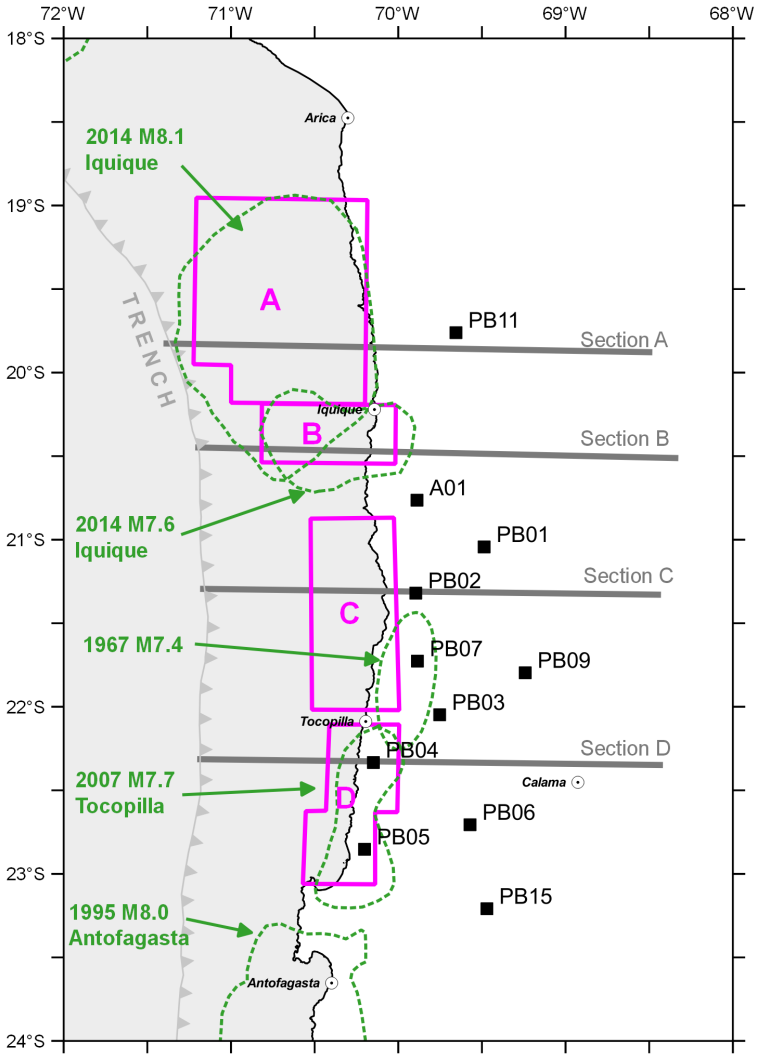

Figure 6.12: Location of synthetic resistivity changes simulated along the interplate seismogenic zone in northern Chile. Polygons with pink boundaries show the approximate areal extent of zones where the *reference* resistivity model was modified: A-2014 M8.1 Iquique earthquake, B-2014 M7.6 Iquique earthquake, C-seismic gap at 21.7°-22°S , D-2007 M7.7 Tocopilla earthquake. Green dashed lines show the rupture area interpreted for earthquakes with magnitude >7.4 during the last 50 years (compiled from Chlieh et al., 2004; Schurr et al., 2012, 2014). Dark grey lines indicate location of sections displayed in Figure 6.13.

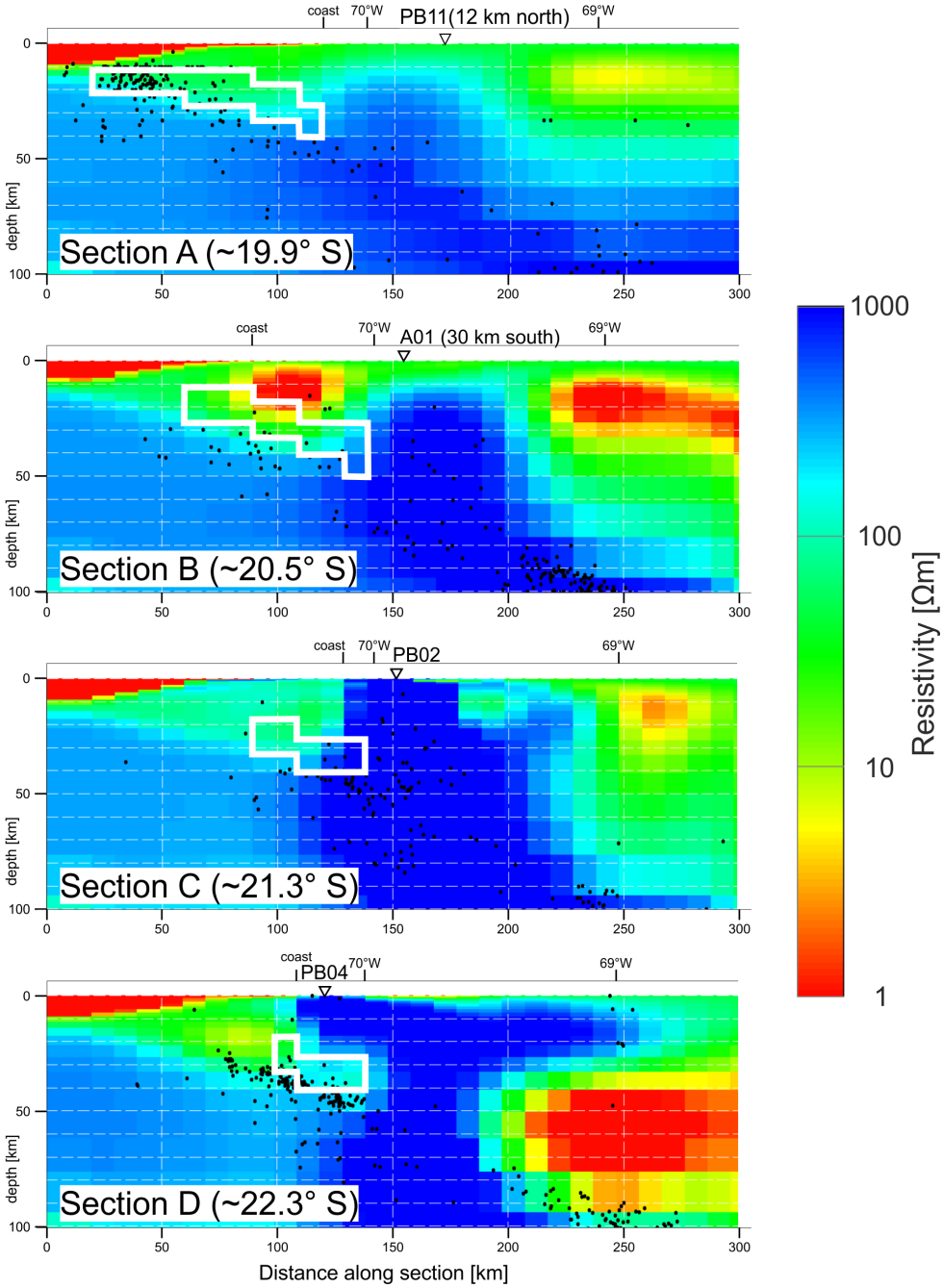

Figure 6.13: Exemplary resistivity sections crossing regions of the *reference* resistivity model which were modified in order to simulate resistivity change scenarios along the interplate seismogenic zone in northern Chile. Polygons white boundaries indicate the modified cells within the *reference* resistivity model. Black dots are hypocentres of earthquakes located 20 km within each section (seismic events from 01-January-2007 to 07-April-2014 downloaded from http://www.sismologia.cl). Sections locations are indicated in Figure 6.12.

ponents change sign over neighbouring periods, the associated apparent resistivity and phase sounding curves can exhibit jumps and cusps, because apparent resistivity and phase values are calculated using mathematical expressions which are highly sensitive to changes in $\underline{\mathbf{Z}}$ components. Small values of Z_{yy} also explains the unstable temporal variations of ρ_{ayy} and ϕ_{yy} observed at IPOC sites, which make impractical to use them for monitoring purposes. Therefore, these TFs components are not considered in the further analysis. Following $\rho_{a,yy}$ and ϕ_{yy}, maximum variations are mostly observed in ρ_a and in the real parts of VTFs. For tests where the closest site is located west of the altered resistivity region, maximum variations are observed in $\rho_{a,xy}$ and $Real(T_y)$ (see e.g. PB04 in 6.16), as these TFs components are highly sensitive to induced currents flowing along the X-axis direction (parallel to the rupture length). As expected, decreasing the resistivity generates larger variations in TFs than increasing the resistivity by the same factor. This can be easily observed in Figures 6.14, 6.15 and 6.16 by comparing the pink and blue lines, which represent responses from models where the resistivity in the tested regions is 10 times smaller or larger than the resistivity of the *reference* model, respectively.

Figure 6.17 shows maps with the spatial distribution of changes in $\rho_{a,xy}$, $\rho_{a,yx}$, ϕ_{xy}, ϕ_{yx}, and real parts of T, if the resistivity of the *reference* model decreases by 10 times at each modified region. Displayed maps show changes at the period where maximum variations in TFs where obtained for each test. To obtain these maps, the model responses where calculated at synthetic sites distributed in a regular mesh of 10 km x 10 km. As can be seen, the magnitudes of TF variations decrease quickly with distance from the region where resistivity changes are introduced (indicated by polygons of black boundaries). Significant variations in TFs are normally observed within less than $\sim$50 km of the modified region. $Real(T_x)$ and ϕ_{xy} seem to be more diagnostic of the north-south extent of the modified regions, as the spatial distribution of these TF variations show a sign change with respect of the location of the anomalous region. Significant variations in $Real(T_y)$ are almost restricted to the areal extent where the resistivity is modified. Obviously, the TF variations strongly depend on the resistivity and size of the volume which is modified and on the resistivity structure of the *reference* model. Changes of bodies with more complex geometry and resistivity values, embedded also in a more complex background resistivity structure, would generate different responses. Denser site coverage is required to obtain a more robust reference resistivity model at 18°-21°S, and therefore to estimate with more precision the effect of resistivity changes at the 2014 Iquique earthquakes or along the northern unbroken segment of the seismic gap.

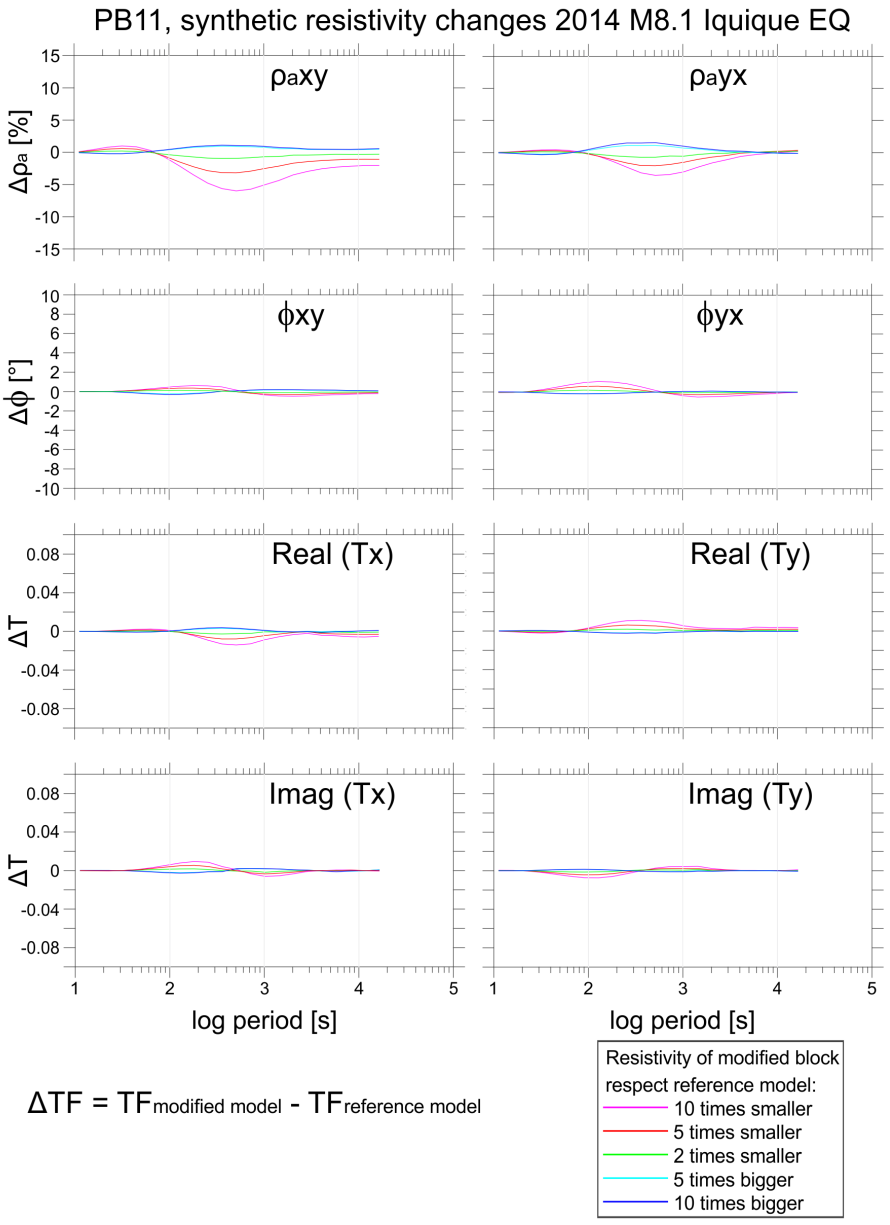

Figure 6.14: TF variations at site PB11 due to resistivity changes simulated above the rupture area of the 2014 M8.1 Iquique earthquake (region A in Figure 6.12). Displayed sounding curves are residuals values, calculated as the differences between the responses of each test and the response of the *reference* model. Colour-coded lines are responses obtained after changing the resistivity of the *reference* model within region A by factors between 0.1 and 10.

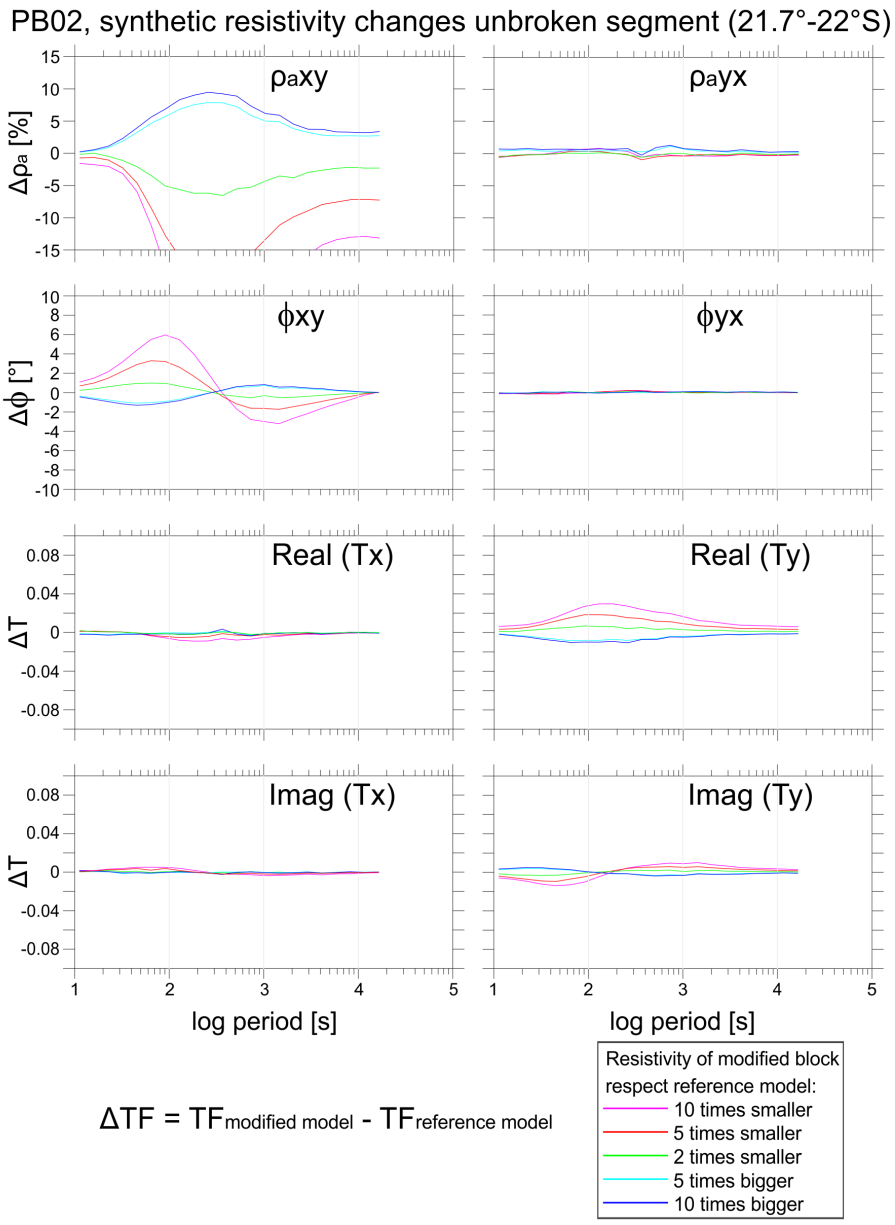

Figure 6.15: Same as Figure 6.14, but TF variations at site PB02 due to resistivity changes simulated above the unbroken segment of the 1877 earthquake between ∼20.9° and 22 °S (region C in Figure 6.12).

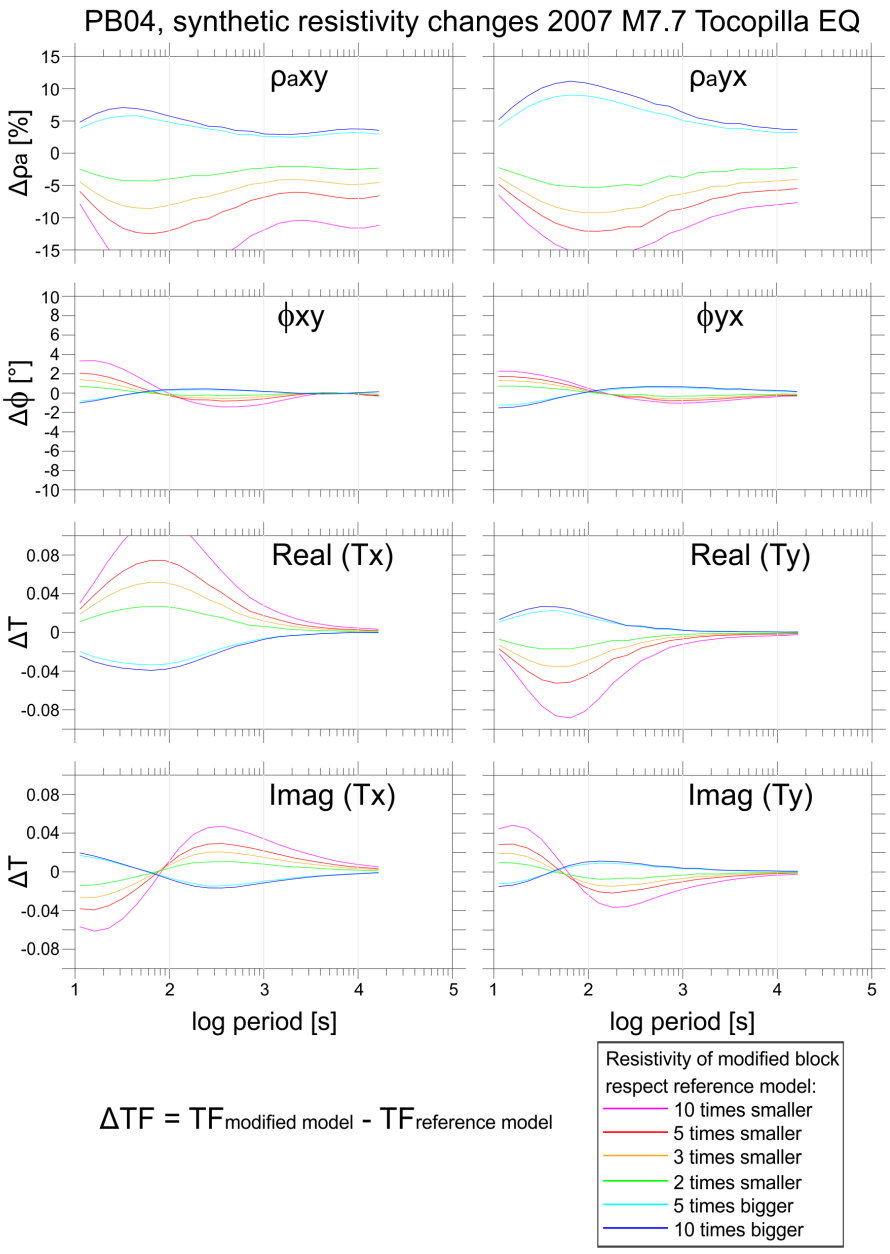

Figure 6.16: Same as Figure 6.14, but TF variations at site PB04 due to resistivity changes simulated above the 2007 M7.7 Tocopilla earthquake (region D in Figure 6.12). Note that TF responses obtained after reducing 3 times the resistivity of the *reference* model are also included.

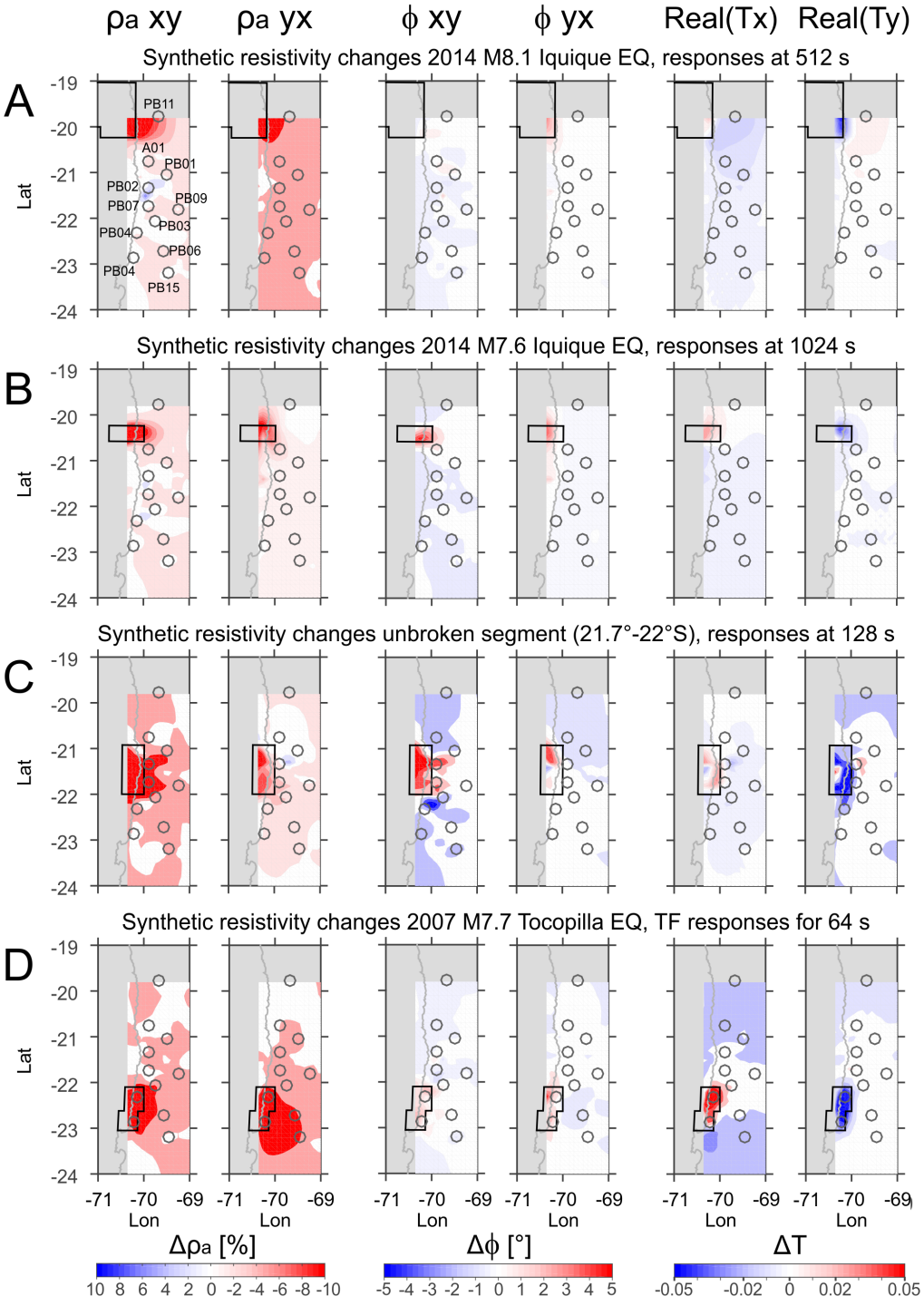

Figure 6.17: Spatial distribution of TF changes obtained by decreasing the resistivity of the *reference* model above the interplate seismogenic zone by a factor of 10. Plots are ordered by modified regions (along rows) and TFs components (along columns). Maps show changes in the TF responses at different periods. The displayed periods are those where maximum variations in TFs where obtained for each test. Polygons of black boundaries indicate the areal extent of the modified regions. Dark grey circles show the location of IPOC MT sites (see top-left plot). Grey lines are the coastline.

6.4 Discussion

6.4.1 Estimate of source effects on TF variations

The contribution of source effects to the temporal variations of VTFs were modelled as the dominant common pattern observed in VTFs variability at all sites during the studied interval (the PCA$_{max}$ model). The PCA$_{max}$ model can explain all major trends in temporal variations of VTFs observed at all IPOC sites. The clearest pattern observed in the PCA$_{max}$ model are seasonal variations. An additional long-term trend can be clearly observed in the smooth deviations of $Real(T_y)$ for periods >256 s (see blue lines in Figures 6.6, 6.7, 6.8): while smooth deviations are dominated by negative values between 2008 and 2010, then they show oscillating positive and negative values between 2011 and 2015. This long-term trend seems to be correlated with the 11-year solar cycle, which showed a solar minimum during 2009 and a solar maximum around 2013. These patterns observed in the PCA$_{max}$ model indicate that major trends in VTF variations at the IPOC array are correlated with fluctuations in the geomagnetic activity, and therefore they are highly probable source effects. Simulations of large-scale resistivity changes above the interplate seismogenic zone show that the magnitude of the associated VTF variations decrease quickly with distance from the perturbed region. Temporal variations of VTFs due to resistivity changes should therefore show significant spatial variability over sites and over periods in a confined region, unless a huge portion of the lithosphere is affected by a significantly large, and maybe unrealistic, resistivity change. These results also suggest that common trends in TF variations observed at all sites, which were estimated by the PCA$_{max}$ model, seem to be source effects.

Brändlein (2013) interpreted an anomalous long-term variation in $Real(T_y)$ at sites PB04 and PB05 for periods between 1500 and 4000 s, which is characterized by a minimum value of $Real(T_y)$ during the year 2009. Brändlein (2013) identified this anomaly after applying a low-pass filter to the temporal variations of VTFs, a filter which removed variability patterns with periodicity only shorter than 1 year. This author attributed such VTF variations to internal resistivity changes, based on the comparatively large effect observed at sites PB04 and PB05. The anomaly interpreted by Brändlein (2013), however, is not present in the reduced temporal variations of VTFs which were obtained in this thesis. Here, minimum values of $Real(T_y)$ during 2009 are well explained by the scaled PCA$_{max}$ model at both sites. Figure 6.18 shows the reduced temporal variations of VTFs for a period of 2049 s during the Interval 2. As illustrated by this figure, residual VTF variations during the whole interval and at all sites are close to zero, because the scaled PCA$_{max}$ model fits very well the VTFs temporal variations. For a period of 2049 s only 161 days during the whole interval show confidence intervals δT <0.02, resulting in a small number of VTF estimates considered in the analysis shown in Figure 6.18. Nevertheless, if all daily estimates of VTFs are analysed (Figure 6.19), again no long-term trends in $Real(T_y)$ are observed during the interval where Brändlein (2013) interpreted anomalous variations. Following the criterion employed to reduce the temporal variations of TFs in this thesis, low values of $Real(T_y)$ observed during 2009 at all IPOC sites are explained by source field effects, which show a minimum correlated with a solar minimum in the 11-year solar cycle. Larger amplitudes of VTF variations at sites PB04 and PB05 can be explained by the comparatively larger variability around the long-term median that is observed in daily

estimates of TFs at these sites, and which is maybe related to the effect of the ocean on the quality of TF estimates (see 3.4.4).

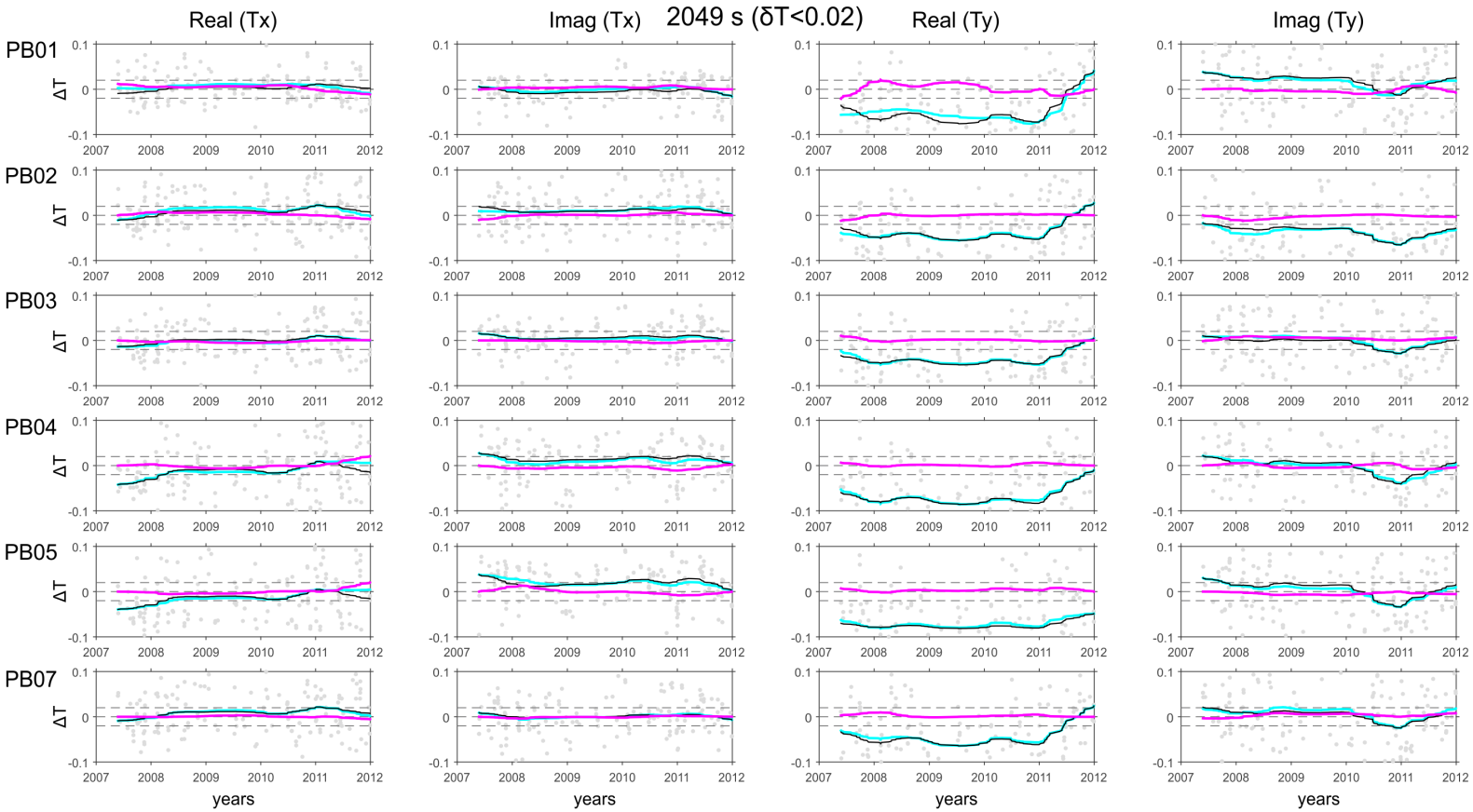

Figure 6.18: Same as Figure 6.4, but for a period of 2049 s and considering VTF temporal variations from 2007 to 2012 (Interval 2, see the text). Days when T estimates have confidence intervals δT >0.02 were excluded.

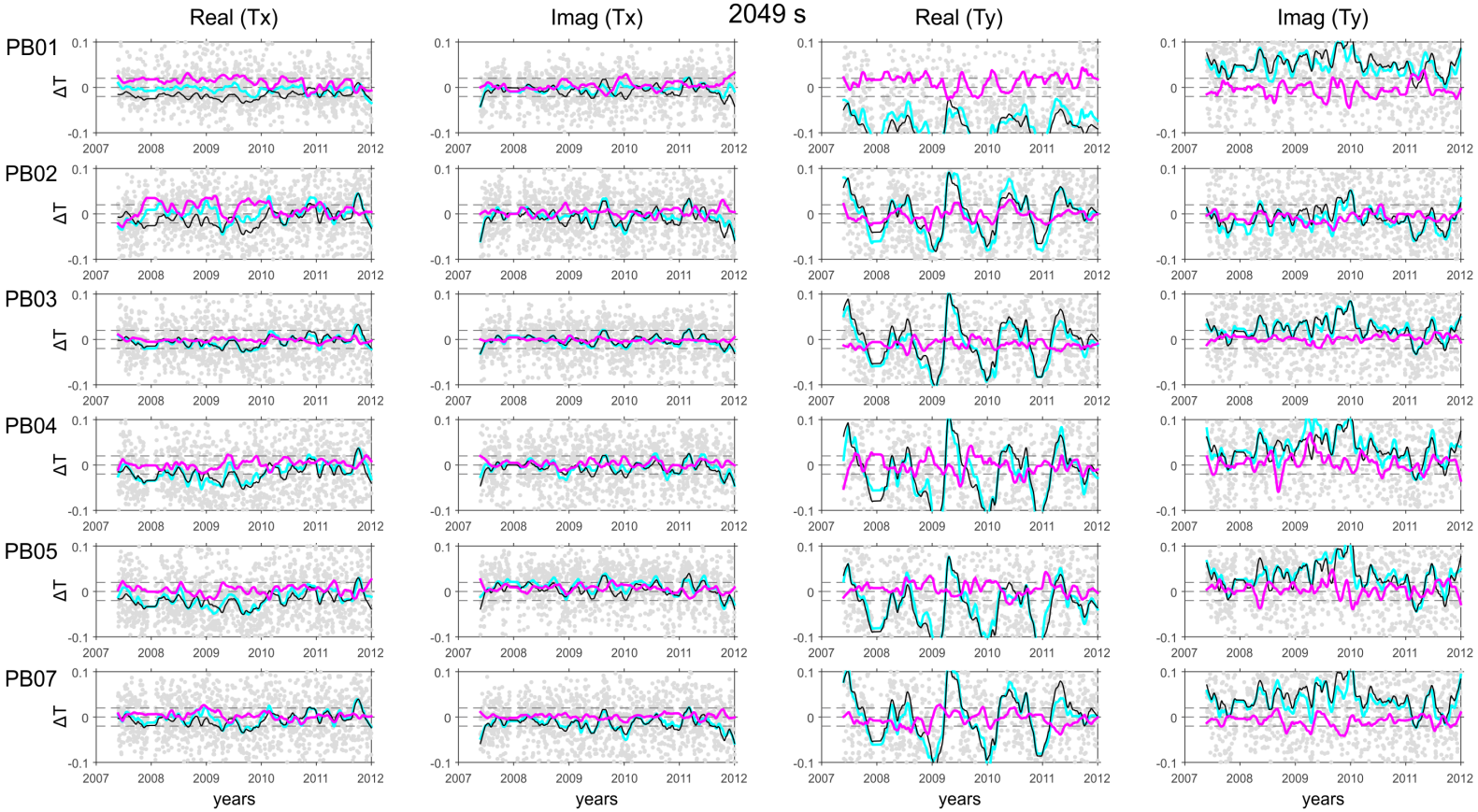

Figure 6.19: Same as Figure 6.18, but days when T estimates have confidence intervals δT >0.02 are included.

6.4.2 Large-scale changes of resistivity and hydraulic properties of the crust

In order to fit the maximum amplitude of the VTF anomaly A2, it was necessary to decrease the resistivity of the *reference* model by 100 times in a region below the Salar Grande (see Figures 6.10 and 6.11). The amount and resistivity of fluids necessary to explain the inferred resistivity change can be estimated by using mixing laws of multi-phase materials. To calculate these models, a resistivity of 1000 Ωm was assumed for the resistive phase, considering the dominant high resistivity values observed within the modified block (see left panel of Figure 6.11a). A resistivity of 0.1 Ωm was assumed for the fluid phase, which represents an average value (in logarithmic scale) of the resistivity range interpreted for crustal fluids (e.g. 0.01-1 Ωm Nesbitt, 1993). Figure 6.20 shows bulk resistivity changes obtained for different amounts of fluids, which were calculated using Archie's law (Archie, 1942), the model of Hermance (1979), and the Hashin-Shtrikmann lower and upper bounds (Hashin and Shtrikman, 1962) (see description of these models in section 2.1). In this figure, the bulk resistivity (ρ_{bulk}) is normalized by the resistivity of the resistive phase (ρ_{matrix}). If the average resistivity of the *reference* model below the Salar Grande area is approximated by ρ_{matrix}, any deviation of the ratio $\rho_{\text{bulk}}/\rho_{\text{matrix}}$ from unity can be interpreted as a modification of the average resistivity. To obtain a bulk resistivity 100 times smaller than ρ_{matrix} (i.e. $\rho_{\text{bulk}}/\rho_{\text{matrix}}) = 0.01$) requires a fluid fraction of at least 0.01, as Archie's law with a cementation exponent m = 1 suggests (pink line in Figure 6.20). For scenarios where pores are not well interconnected, it is necessary a fluid fraction of approximately 0.1 (see e.g. bulk resistivities calculated using the model of Hermance, 1979, or the Archie's law with cementation exponent m = 2).

Porosities in a range of ∼0.01-0.1 would be necessary to obtain the amount of fluids estimated from resistivity changes modelled below the Salar Grande area. These values seem to be high, as middle to low crustal levels are characterized by average porosities of a few percent (e.g. Marquis and Hyndman, 1992). However, it is likely that high porosity rocks are present below the Salar Grande area. This area exhibits a complex history of sedimentation and deformation (Reijs and McClay, 1998; González et al., 2008), which suggests that fractured sedimentary rocks may be present at depth. For instance, porosities on the order of 0.1 have been measured in borehole samples crossing sedimentary rocks within fracture zones adjacent to large scale faults (e.g. Hamahashi et al., 2013). Active seismicity below the Salar Grande area suggests that faulting processes are taking place in depth, processes which may contribute to sustain (or even increase) high porosities. Moreover, such faulting processes may enhance the interconnectivity between pores containing fluids, a mechanism which can also contribute to decrease the bulk resistivity of the crust (e.g. see bulk resistivity curves in Figure 6.20 which were calculated using the Archie's law with cementation exponent m close to 1). Obviously, if lower contrasts between the resistivity of the matrix and fluid were assumed, higher fluid fractions and porosities would be required in order to explain a decrease in the bulk resistivity equivalent to the modelled resistivity change below the Salar Grande area.

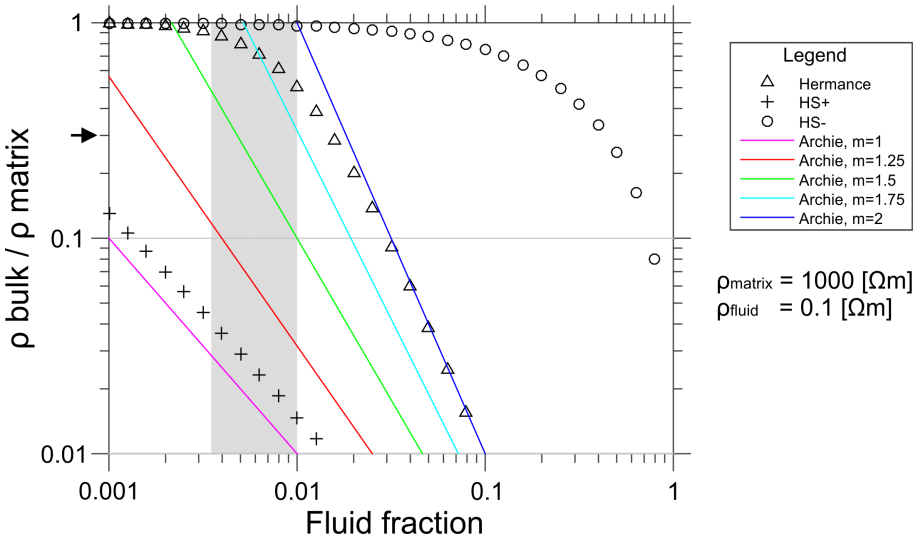

Figure 6.20: Bulk resistivity as a function of fluid fraction, for a rock composed by two phases: a matrix of 1000 Ωm and a fluid of 0.1 Ωm. X-axis indicates the fluid fraction. Y-axis indicates the ratio between the bulk resistivity (ρ_{bulk}) and the resistivity of the matrix (ρ_{matrix}). Symbols and coloured-coded lines are bulk resistivities calculated with different models: Hermance = Hermance (1979); HS+, HS- = Hashin-Shtrikmann lower and upper bounds, respectively (Hashin and Shtrikman, 1962); Archie = Archie's law (Archie, 1942), assuming different values of the cementation exponent m (see the text for details). Grey area indicates the variation of porosity modelled by Koerner et al. (2004) in order to reproduce the Vp/Vs anomaly identified following the 1995 Antofagasta earthquake (see the text). Black arrow on the left-hand side of the plot indicates when ρ_{bulk} is one third of ρ_{matrix}.

6.4.3 Variability in the large-scale fluid distribution during the seismic cycle

Anomalous variations in VTFs identified at PB02 can be explained by resistivity changes within a region coincident with seismic activity during the analysed interval. The most probable candidate to explain such perturbations in the resistivity structure is a change in the hydraulic properties of the crust, which may be associated with the recorded seismicity. It has been suggested that the development of seismic sequences can be related to temporal changes in the hydraulic properties of the crust. For instance, Miller et al. (2004) proposed that aftershocks of large earthquakes may be triggered by migration of fluids through high permeability zones created by the mainshock. Figure 6.21 compares temporal variations of $Real(T_x)$ for a period of 64 s at site PB02 (upper panel) with the spatiotemporal distribution of the seismicity below the Salar Grande area (lower panel). According to Figure 6.21, the recorded seismic activity below the Salar Grande area increased since 2011, in particular within the depth range where the resistivity changes were modelled (indicated by blue dotted lines in Figure 6.21b). Some clusters of hypocentres suggest a sequential upward migration of seismic events with time. Here it is speculated that episodic migration of fluids can explain both the spatiotemporal distribution of seismicity and the resistivity changes modelled below the Salar Grande area at 5-25 km depth, in particular the resistivity changes related to the anomaly A2. Following the mechanism proposed by Miller et al. (2004), earthquakes of larger magnitudes at the plate interface (red squares at ∼50 km depth in Figure 6.21b) may contributed to generate the sequence of seismicity and the inferred upward migration of fluids. A more precise re-location of hypocentres would be necessary to confirm if the spatiotemporal distribution of local seismicity can support the proposed hypothesis of upward migration of fluids from the plate inter-

face into the upper crust below the Salar Grande area. Interestingly, anomalous temporal variations of VTFs vanish by the end of 2014 (Figure 6.21a), suggesting that the resistivity structure in the area tended also to return to the resistivity distribution estimated with the *reference* model. It remains open which processes operated in the upper crust after the inferred relocation of fluids took place, in order to re-establish the hydraulic property conditions present before the perturbation. It remains also elusive why the recorded seismic activity in this region significantly increased since 2011, and if such phenomena could have some association with the rupture processes related to the 2014 Iquique earthquake.

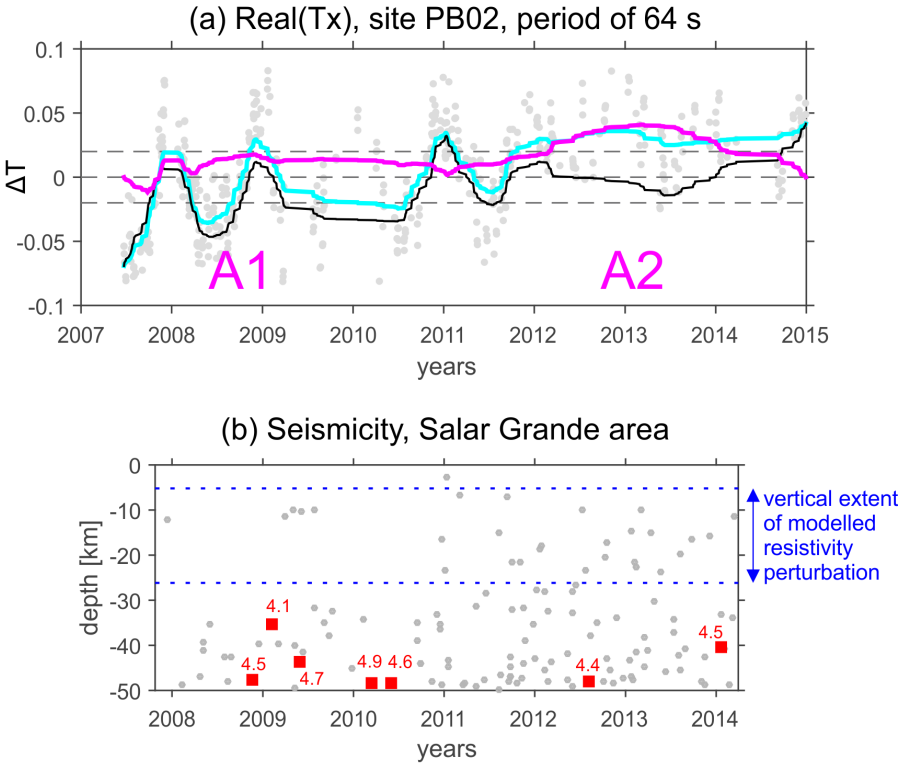

Figure 6.21: Comparison of temporal variations of VTFs at site PB02 with spatiotemporal distribution of seismicity below the Salar Grande area. (a) Reduction of temporal variations 2007-2015 of $Real(T_x)$, for a period of 64 s. Temporal variations are displayed as deviations of daily estimates from the reference sounding curves. Grey dots are daily estimates of VTFs (only days with confidence intervals δT <0.02). Cyan lines are 60-day moving average of daily estimates. Black lines are the scaled PCA model of the 60-day moving average. Pink lines are residual VTFs, obtained after subtracting the scaled PCA model from the 60-day moving average. A1 and A2 indicate approximately the interval where maximum amplitude is observed in anomalous residual VTFs. (b) Distribution of hypocentres over time and depth. Grey dots are seismic events with magnitude 1.5≤M≤4. Red squares are events with magnitude M>4 (red numbers indicate the magnitude of these events). Displayed hypocentres are seismic events from 01-January-2007 to 07-April-2014 downloaded from http://www.sismologia.cl, which are located within the polygon of black dashed boundaries indicated in Figure 6.10. Blue dotted lines indicated the boundaries of depth range where resistivity changes were modelled.

No significant changes were identified in reduced VTFs temporal variations at sites PB04 and PB05 during the intervals analysed for each station (2007-2014 and 2007-2012, respectively). According to results of the simulation tests, to generate measurable changes in TFs at site PB04 it would be necessary to decrease the resistivity along the continental crust above the 2007 Tocopilla earthquake rupture area at least by 3 times (see Figure 6.16). Therefore, it can be inferred that no resistivity changes greater in size and magnitude than such perturbation in the resistivity structure have occurred, otherwise they would

have been detected by the array. As can be seen in Figure 6.20, to decrease the resistive background present below the Coastal Cordillera by $\sim$3 times requires a fluid fraction in a range of $<$0.001 to 0.02 (such reference minimum and maximum values are defined by pink and blue lines in Figure 6.20). This fluid fraction range encompasses the increment in the porosity which Koerner et al. (2004) interpreted in the region affected by the postseismic fluid flow proposed for the 1995 Antofagasta earthquake (porosities between 0.0035 and 0.01, indicated with a grey area in Figure 6.20). Consequently, it seems unlikely that following the 2007 Tocopilla earthquake has taken place a rapid regional-scale fluid flow with the characteristics such as Husen and Kissling (2001) and Koerner et al. (2004) suggested for the 1995 Antofagasta earthquake. However, it cannot be excluded that a massive relocation of fluids is taking place after the 2007 Tocopilla or 2014 Iquique events. The permeability of the lower crust or the upper mantle is not well constrained, and therefore it is unknown at which time rate the migration of fluids can occur at those depths. Consequently, the acquisition and analysis of long-term observations is the only way to constrain the variability in the distribution of fluids and its possible interactions with major deformation processes.

Obviously, fluid flow phenomena affecting smaller volumes of the crust could have also taken place, as they should result in smaller resistivity changes that cannot be detected by the array. For instance, re-distribution of fluids along the plate interface or along local faults (as was also suggested for the 1995 Antofagasta earthquake, e.g. Shapiro et al., 2003; Nippress and Rietbrock, 2007), may also be not sensed. As the simulation tests showed, resistivity changes above the interplate seismogenic zone can produce significant anomalies in TFs, but their magnitudes decrease quickly with distance from the anomalous region (Figure 6.17).

Some constraints on the temporal distribution of fluids can also be derived by examining the *reference* resistivity model. The analysis of TFs temporal variations suggests that this model has not experienced significantly large changes during the studied interval, at least within the area covered by the IPOC MT array. Therefore, it is likely that major features of the *reference* resistivity model represent structures that have been produced by geological processes over several seismic cycles. For instance, a predominance of high resistivities ($\geq$1000 Ωm) in most of the forearc suggests that rocks in this region present small amounts of interconnected fluids, which may reflect unfavourable conditions to channel or trap fluids generated at depth (e.g. by metamorphic processes). The occurrence of clusters of seismicity and major faults within or adjacent to low resistivity zones of large vertical extent, on the contrary, may suggest the presence of high-permeability zones in the continental crust where deformation and fluid processes are focused during geological time scale. The aforementioned correlations, together with the resistivity changes inferred below the Salar Grande area and the lack of evidence suggesting a massive relocation of fluids following the 2007 Tocopilla earthquake, may imply that rapid large-scale migration of fluids within the continental crust occurs mainly in discrete regions of the forearc, where exceptionally high permeabilities are present. The distribution of such regions may be controlled by the spatial coincidence of three geological elements: segments of the plate interface where significantly large amount of fluids are released from the oceanic plate (source of the fluids), fault zones of large vertical extent which reach the base of the continental crust (fluid channels), and high-permeability regions of the upper to middle crust along which fluids are distributed (fluid traps). The temporal evolution of hydraulic properties

within these regions can be partly controlled by episodic upward migration of fluids generated at the plate interface. Assuming this hypothesis, monitoring the temporal evolution of seismicity and physical properties within these regions, using arrays of geophysical stations locally deployed, may give insights about coupled hydrogeologic and tectonic processes occurring at the plate interface.

6.5 Conclusions

From the analysis of the temporal variations of VTFs at IPOC sites over the interval from May-2007 to December-2014, it is concluded that:

- Variability of daily estimates of VTFs show similar long-term trends at all IPOC sites. The dominant trend in VTFs present at all studied sites was modelled using the principal component analysis method. Major patterns in this model (PCA_{max}) are correlated with seasonal variations and the 11-year solar cycle, suggesting that they represent source field effects.
- Residual VTFs were obtained after subtracting from time series of VTFs the PCA_{max} model scaled to the variability range observed at each site. Residual VTFs during the studied interval show values normally within a range of ± 0.02 around a reference long-term estimate of VTFs, i.e. within the expected variability range of daily estimates of VTFs (see chapter 5). Residual VTFs exceeding this variability range (anomalous residual VTFs) are usually correlated with peaks in the seasonal variation pattern, and therefore they were interpreted as source effects which were not well fitted by the PCA_{max} model.
- Clear and robust anomalous residual VTFs patterns were identified at site PB02, for a period range between 64 and 256 s. These anomalous patterns consist in long-lasting positive values of residual $Real(T_x)$ which smoothly vary during two intervals (2008-2010 and 2012-2013), reaching maximum values around early-2009 and early-2013, respectively. The effect of possible magnetic noise sources was evaluated and can be ruled out.
- Results from forward modelling tests suggest that the general trend of the anomalous VTF variations at site PB02 can be explained by resistivity changes below the Salar Grande area. To reproduce the maximum amplitude observed in these anomalies, it was necessary to decrease the resistivity of the *reference* model by 100 times within a region at approximately 5-25 km depth located below the Salar Grande area, a region where intensive seismicity was recorded during the studied interval.

To evaluate whether the IPOC MT array would be sensitive to resistivity changes related to possible postseismic fluid flow events, alterations in the resistivity structure were simulated at regions above the subduction seismogenic zone. The simulation results show that:

- A massive change of resistivity affecting the continental lower crust along the rupture area of a large subduction thrust earthquake would produce measurable variations in the TFs recorded at IPOC stations, if the resistivity decrease by a factor of ≥ 3 or increase by a factor of ≥ 5. If such

resistivity changes occurred, maximum variations should be observed in a period range of 90-500 s at sites located in the Coastal Cordillera. These simulation tests produced significant variations in the $Real(T_x)$ and Z_{yx}, which are the best determined TF components at the IPOC sites.

- Significant changes in the VTF at site PB04 would be obtained, if the region above the 2007 Tocopilla earthquake rupture area was perturbed by an increase in the fluid content comparable to the porosity increment which Koerner et al. (2004) suggested for the 1995 Antofagasta earthquake.
- According to the simulation results, and together with the absence of significant changes in temporal variations of reduced VTFs at sites PB04 and PB05, it is likely that resistivity changes greater than 3 times have not occurred within the lower continental crust along the 2007 Tocopilla earthquake rupture area, otherwise they would have been detected by the array.

Chapter 7

General conclusions and outlook

Results obtained in this thesis have implications for the understanding of tectonic processes of the subduction zone in Northern Chile, and for the application of geophysical electromagnetic methods for monitoring purposes. Main conclusions and outlook concerning each of these topics are outlined as follows:

The regional-scale electrical resistivity structure of the forearc in Northern Chile and its tectonic implications

The regional-scale resistivity structure along the forearc of Northern Chile (21°S-23.5°S) was derived from 3-D inversion of long-period magnetotelluric (MT) data collected at the IPOC array. This model shows that:

- The main structure along the entire forearc is a domain of high resistivity ($>$1000 Ωm) found in the continental South American plate, approximately between the coastline and 69°W, an area which was previously described as a dense, rigid and cold block. The model shows significantly lower resistivities ($<$100 Ωm) in the continental lithosphere between the Precordillera (69°W) and the position of the active volcanic arc. The model exhibits additionally a number of low resistivity zones (LRZs, $<$10 Ωm) at various depths and segments of the forearc suggesting a complex overall 3-D resistivity distribution.
- Below the Coastal Cordillera and the Longitudinal Valley, the model shows upper crustal LRZs coincident with Cenozoic sedimentary basins observed at surface. These LRZs can exhibit large vertical extents, even reaching the continental lower crust in areas where regional NW-SE structural lineaments intersect major trench-parallel fault systems such as the Atacama Fault System. In these areas, clusters of crustal seismicity are observed within the LRZs. The spatial correlation between LRZs and evidence of past and active deformation suggests that these areas represent long-active highly-permeable regions of the continental crust containing significant amounts of fluids, in which deformation and fluid processes have been concentrated over geological time scale.

Below the Chilean Precordillera, an upper crustal LRZ at 20-22°S matches a cluster of seismicity which was interpreted as evidence of fluids circulating along the Precordilleran Fault System. The southern limit of this LRZ correlates with a low-permeability rigid block in the continental lithosphere previously suggested by gravimetric and seismic studies (e.g Götze and Krause, 2002; Schurr and Rietbrock, 2004).

- In the forearc mantle wedge, the model exhibits a well constrained LRZ which extends for 150 km along the trench axis (approximately between 21.5°S and 23°S). The extent of this LRZ correlates spatially with a segment of the mantle where the top of the intermediate-depth seismogenic zone is relatively shallow. This discrete LRZs suggests significant along-strike variability in the amount of fluids released from the oceanic slab at the forearc mantle wedge.

Overall, the spatial correlation between resistivity structures, major fault systems and active seismicity suggests that accumulation/circulation of fluids is concentrated at highly-permeable discrete regions of the subduction forearc, which are controlled by regional-scale structures in the continental and oceanic crust. Future work should extend the model of the regional-scale resistivity structure to other segments of the South American subduction margin, in order to identify major lithospheric structures which may control the spatial distribution of deformation processes and fluids. A priority area to study is the forearc in Northern Chile between 18°S and 21°S, a region which comprises seismotectonic segments at different stages of a seismic cycle. To extend the resistivity model obtained in this study towards north, the data collection can follow a site spacing similar to the IPOC MT array.

The resistivity model obtained in this thesis has revealed regional-scale LRZs which seem to be loci of recurrent deformation and fluid processes over geologic time. Future studies should characterize with more detail the anatomy of these LRZs (e.g. the Salar Grande area), in order to determine the geometry of fluid-rich regions and to identify the geological structures controlling the distribution of fluids. Such models can provide more precise information on the interplay between fluid systems and deformation processes. Determining the spatial distribution and nature of these geological fluids may also be relevant for the assessment of hydrological, geothermal and mineral resources.

Significant along-strike segmentation in the amount of fluids released at the forearc mantle wedge was interpreted. Analysis of the spatial distribution of petrological or geochemical evidence (e.g. magmas, minerals related to metamorphic or metasomatic processes) can provide constraints to test the validity of such interpretation. To determine the controlling factors for this segmentation would require to characterize in more detail the structure of the Nazca plate in the study area. Along-strike variability in the physical properties of the oceanic slab could be identified by analysing existing marine magnetic data (e.g. EMAG2 global magnetic grid, Maus et al., 2009), but it would be ideal to acquire new offshore geophysical information (e.g. MT, seismic, gravity, magnetic) following a 3-D layout.

Detectability of variations in the deep subduction fluid system

The ability to detect a large-scale fluid relocation with the IPOC MT data was assessed by evaluating the effect of alterations in the resistivity structure on TFs recorded at IPOC sites. Changes of resistivity were simulated along the continental lower crust overlying the interplate seismogenic zone, emulating similar characteristics of the fluid flow event following the 1995 Antofagasta earthquake which was proposed by Husen and Kissling (2001). Forward modelling responses of these synthetic models show that:

- Alterations in the resistivity structure above the interplate seismogenic zone can produce measurable variations in the TFs recorded at IPOC stations. The amplitude of the simulated TF responses exceeded the significance interval of TF daily estimates at IPOC sites when the resistivity in the perturbed region decreases by a factor of $\geq$3 or increases by a factor of $\geq$5 with respect to the reference resistivity model.
- Maximum changes in TFs usually were obtained at a period range of 90-500 s at IPOC sites located in the Coastal Cordillera. The magnitude of TF variations decreases quickly with distance from the region where resistivity changes were introduced.
- Significant variations were obtained in the $Real(T_x)$ and Z_{yx} components. These parameters are the best determined TF components at the IPOC sites, suggesting that they are suitable for monitoring changes of resistivity above the seismogenic zone.

These results confirm quantitatively that the MT monitoring component of the IPOC array is useful in order to detect and constrain variability in the deep fluid distribution of the subduction zone. The high variability of the amplitude of the TF changes with distance from the perturbed region highlights the importance of covering the entire segment of the 1877 seismic gap with new permanent MT sites. As a first step, MT stations at IPOC sites A01 and PB11 were installed in order to monitor the forearc along the segment which was broken by the 2014 Iquique earthquake. The permeability of the lower crust or the upper mantle is not well constrained, and therefore it is unknown in which time scale major relocation of fluid can occur at these depths. Consequently, the acquisition and analysis of long-term observations is the only way to constrain the variability in the distribution of fluids and its possible interactions with major deformation processes.

The obtained results are applicable to resistivity changes above the interplate seismogenic zone and are highly dependent on the reference resistivity model employed. Future work should evaluate the effect on IPOC TFs of resistivity changes at other regions of the subduction zone (e.g. in the upper mantle above the intermediate-depth seismogenic zone, in the continental crust along deep-reaching LRZs). Due to the complex 3-D resistivity structure modelled in the study area, it is likely that perturbations simulated in other regions can generate non-trivial TF responses at IPOC stations. For instance, Brändlein (2013) suggested that a decrease in the resistivity of the western part of the forearc mantle wedge can generate significant VTF changes over various IPOC sites and at periods longer than 1000 s. Acquisition of new MT data would be necessary in order to improve the accuracy of the resistivity model, in particular to resolve with more detail the spatial extent of the modelled LRZs. This can be achieved by using a denser layout of temporal stations along the IPOC array.

Temporal evolution of the regional-scale resistivity structure between 2007-2014 and its tectonic implications

The analysis of geomagnetic data collected at the IPOC array from May-2007 to December-2014 shows that:

- Overall temporal variability of daily estimates of the vertical magnetic transfer function (VTF) shows similar long-term trends at all IPOC sites. These long-term patterns in VTFs correlate with fluctuations in the geomagnetic activity, suggesting that they represent source field effects.
- Anomalous temporal variations of VTFs not related to source effects were identified at site PB02, for a period range between 64 and 256 s. These anomalous values in VTF variations are consistently observed during two intervals (2008-2010 and 2012-2014), reaching maximum amplitude around early-2009 and early-2013, respectively. The effect of local noise in magnetic records at site PB02 was evaluated and can be ruled out.
- In order to reproduce the anomalous variations in VTFs at site PB02, a decrease in resistivity was modelled below the Salar Grande area at 5-25 km depth, a region where intensive seismicity was recorded during the anomalous interval. An episode of fluid migration from the plate interface into the continental middle-upper crust is suggested to explain the spatiotemporal correlation between the distribution of seismicity and changes in resistivity.
- No significant and robust variations of VTFs were identified at sites PB04 (from 2007 to 2014) and PB05 (2007-2012). These results, together with the modelling tests simulating perturbations in the resistivity structure, suggests that detectable resistivity changes have not occurred within the lower continental crust along the 2007 M7.7 Tocopilla earthquake rupture area.

Significant changes in the resistivity structure of the forearc in Northern Chile were interpreted at the Salar Grande area, a region where spatial correlation is observed between regional LRZs, seismic activity along NW-SE structural lineaments, and the southern boundary of the 2014 M7.6 Iquique earthquake. The spatiotemporal distribution of seismicity and the large vertical extent of the LRZ at the Salar Grande area suggest that the temporal evolution of hydraulic properties within this region is partly controlled by episodic upward migration of fluids generated at the plate interface. Future work should study with local arrays the temporal evolution of seismicity and physical properties within deep-reaching LRZs located above the seismogenic zone. Monitoring these parameters at these regions can be used to detect large-scale relocation of fluids from the plate interface into the continental crust. Such fluid flow events can give insights about the temporal evolution of fluid pressure conditions along the plate interface, a parameter which several authors have interpreted as a key factor controlling the rupture propagation of megathrust earthquakes (e.g. Moreno et al., 2014). In Northern Chile, priority regions to study are the Salar Grande area and the northern margin of the 2007 Tocopilla earthquake, as they roughly define the along-strike boundaries of one of the segments which remains unbroken since the 1877 earthquake.

The use of long-period electromagnetic data for monitoring changes in the resistivity structure of the solid earth

Temporal variations of electromagnetic transfer functions (TFs) was analysed for two groups of mid-latitude sites. The analysis of both datasets reveals that changes in external magnetic fields can have significant influence on temporal variability of TFs for long-period data. Consequently, to use TF variations for monitoring the temporal evolution of the resistivity structure requires to identify and remove beforehand contributions related to source fields effects.

There is an increasing number of studies using MT in order to monitor the resistivity structure at shallow depths. Such experiments rely on TFs for periods usually between 10^{-3} s and 100 s. It is also fundamental to quantify the influence of source effects on MT TFs and VTFs at such period band, in order to interpret correctly temporal variations of these parameters as indicators for changes in the resistivity structure.

IPOC magnetotelluric array

The analysis of temporal variability of TFs for a period range between approximately 30 and 4000 s, obtained at sites of the IPOC MT array during 2007-2014, reveals that:

- IPOC TFs exhibit significant temporal variations, whose amplitude can exceed sometimes 100% of their absolute value. The population of daily estimates of TFs tend to be distributed around its statistical median, although the variability range around this long-term value depends on the quality of the associated electromagnetic (EM) field measurements.
- Temporal variations of TFs at all IPOC sites show periodical patterns, whose periodicity coincides with indicators of geomagnetic activity. The most ubiquitous pattern is a seasonal modulation of daily estimates of TFs that peaks around the June and December solstices. Brändlein (2013) described this pattern affecting VTFs of the IPOC data, and showed that it exhibits significant correlation with changes in external magnetic fields. In this thesis it was shown that seasonal variations are also observed in temporal variations of the impedance ($\underline{\mathbf{Z}}$), apparent resistivity, impedance phase, and horizontal magnetic (HTF) transfer functions. TFs exhibit additionally periodical patterns which seem to be correlated with the 27-day and the 11-year solar cycle.

Daily estimates of TF components can occur in a wide range at some periods and/or sites where EM time series show low signal-to-noise ratio. This condition restricts the amount of parameters which can be used in order to analyse the temporal evolution of the resistivity structure. In order to monitor more TFs components, future work should pursue to enhance the quality of time series, by improving measurement conditions and/or by applying additional processing techniques. To improve the quality of electric field data, major issues to deal with are low signal strength in the north-south electric field component (E_x) and instability of moisture conditions at the contact between electrodes and the ground. Automatic periodical measurements of contact resistance can give a quantitative indicator of electric field measurements conditions, and therefore may help to detect intervals with electrodes' malfunction. The

use of multivariate processing schemes (e.g. Egbert, 1997) may help to remove the influence of source effects in TFs, as such source effects should represent coherent noise present at all sites.

Geomagnetic Deep Sounding studies at mid-latitudes

The analysis of up to 18 years (1995-2013) of geomagnetic data acquired at 11 mid-latitude magnetic observatories of the INTERMAGNET network, located in different continents and tectonic settings, shows that:

- Temporal variations of daily estimates of VTFs for a period range of 256-2049 s exhibit systematic periodical patterns correlated with changes in external magnetic fields. The most ubiquitous trend is the seasonal modulation of the T_x VTF component. This pattern is characterized by a high peak around the June solstice (low peak around the December solstice) in the real part of T_x, regardless of the geographical location of a site. The imaginary part of T_x exhibits the same pattern, but with opposite seasonal polarization. The amplitude of the seasonal variation in T_x increases with increasing latitude and period. Seasonal variations are also observed in the T_y VTF component, but the amplitude and polarization of this periodical pattern do not follow a clear geographical trend as is observed for T_x.
- Temporal variations of some VTF components at some INTERMAGNET sites show a long-term trend that is clearly correlated with the 11-year solar cycle. The difference between VTFs obtained at solar maximum and solar minima intervals can exceed a value of 0.03, even after removing seasonal variations.
- An effective method to estimate and remove such source effects from temporal variations of VTFs is to compare the VTF variability at neighbouring sites. Source effects in temporal variations of VTFs can be identified as those patterns which exhibit similar amplitudes and significant correlation with the geomagnetic activity at all neighbouring sites.

The origin of these source effects on VTFs remains open. In order to gain a better understanding on these effects, future work should expand this analysis by studying geomagnetic data from more geographical locations and for periods shorter than 200 s. This analysis can characterize with more precision the dependence of source effects on geographical location and on period range. With this characterization, the variations of source effects over space and period can be modelled in order to identify the external current systems that generate them.

Bibliography

Acocella, V., Gioncada, A., Omarini, R., Riller, U., Mazzuoli, R., and Vezzoli, L. (2011). Tectonomagmatic characteristics of the back-arc portion of the Calama–Olacapato–El Toro Fault Zone, Central Andes. *Tectonics*, 30(3).

Allmendinger, R. W. and González, G. (2010). Invited review paper: Neogene to Quaternary tectonics of the coastal Cordillera, northern Chile. *Tectonophysics*, 495(1):93–110.

Allmendinger, R. W., Jordan, T. E., Kay, S. M., and Isacks, B. L. (1997). The evolution of the Altiplano-Puna plateau of the Central Andes. *Annual Review of Earth and Planetary Sciences*, 25(1):139–174.

Amilibia, A., Sàbat, F., McClay, K., Muñoz, J., Roca, E., and Chong, G. (2008). The role of inherited tectono-sedimentary architecture in the development of the central Andean mountain belt: Insights from the Cordillera de Domeyko. *Journal of Structural Geology*, 30(12):1520–1539.

ANCORP Working Group (2003). Seismic imaging of a convergent continental margin and plateau in the central Andes (Andean Continental Research Project 1996 (ANCORP'96)). *Journal of Geophysical Research: Solid Earth (1978–2012)*, 108(B7).

Anderson, C., Lanzerotti, L., and Maclennan, C. (1976). Local time variation of induction vectors as indicators of internal and external current systems. *Geophysical Research Letters*, 3(8):495–498.

Anderson, C., Lanzerotti, L., and Maclennan, C. (1978). Local time variation of geomagnetic induction vectors. *Journal of Geophysical Research: Solid Earth (1978–2012)*, 83(B7):3469–3484.

Angermann, D., Klotz, J., and Reigber, C. (1999). Space-geodetic estimation of the Nazca-South America Euler vector. *Earth and Planetary Science Letters*, 171(3):329–334.

Arabasz, W. J. (1971). *Geological and geophysical studies of the Atacama Fault Zone in Northern Chile*. PhD thesis, California Institute of Technology.

Araya Vargas, J. and Ritter, O. (2016). Source effects in mid-latitude geomagnetic transfer functions. *Geophysical Journal International*, 204(1):606–630.

Archie, G. E. (1942). The electrical resistivity log as an aid in determining some reservoir characteristics. *Transactions of the AIME*, 146(01):54–62.

Armijo, R. and Thiele, R. (1990). Active faulting in northern Chile: ramp stacking and lateral decoupling along a subduction plate boundary? *Earth and Planetary Science Letters*, 98(1):40–61.

Arriagada, C., Roperch, P., Mpodozis, C., and Cobbold, P. R. (2008). Paleogene building of the Bolivian Orocline: Tectonic restoration of the central Andes in 2-D map view. *Tectonics*, 27.

Audet, P., Bostock, M. G., Christensen, N. I., and Peacock, S. M. (2009). Seismic evidence for overpressured subducted oceanic crust and megathrust fault sealing. *Nature*, 457(7225):76–78.

Audet, P. and Schwartz, S. Y. (2013). Hydrologic control of forearc strength and seismicity in the Costa Rican subduction zone. *Nature Geoscience*, 6(10):852–855.

Barazangi, M. and Isacks, B. L. (1976). Spatial distribution of earthquakes and subduction of the Nazca plate beneath South America. *Geology*, 4(11):686–692.

Barrientos, S. E. (2007). Earthquakes in Chile. In Moreno, T.; Gibbons, W., editor, *The Geology of Chile*, pages 263–287. The Geological Society, London.

Beamish, D. (1979). Source field effects on transfer functions at mid-latitudes. *Geophys. J. R. astr. Soc.*, 58(1):117–134.

Beamish, D. (1980). Diurnal characteristics of transfer functions at pulsation periods. *Geophys. J. R. astr. Soc.*, 61(3):623–643.

Benz, S., Bahr, K., and Einecke, U. (2012). Construction and Comparison of Ag/AgCl Electrodes for long-period Magnetotellurics. In *Proceedings 21st International Workshop on Electromagnetic Induction in the Earth, Darwin, Australia*.

Berdichevsky, M. N. and Dmitriev, V. I. (2008). *Models and methods of magnetotellurics*. Springer Science & Business Media.

Bilek, S. and Lay, T. (2002). Tsunami earthquakes possibly widespread manifestations of frictional conditional stability. *Geophysical Research Letters*, 29(14):18–1.

Bilek, S. L. (2010). Invited review paper: Seismicity along the South American subduction zone: Review of large earthquakes, tsunamis, and subduction zone complexity. *Tectonophysics*, 495(1):2–14.

Bloch, W., Kummerow, J., Salazar, P., Wigger, P., and Shapiro, S. (2014). High-resolution image of the North Chilean subduction zone: seismicity, reflectivity and fluids. *Geophysical Journal International*, 197(3):1744–1749.

Brace, W. and Orange, A. (1968). Electrical resistivity changes in saturated rocks during fracture and frictional sliding. *Journal of Geophysical Research*, 73(4):1433–1445.

Brändlein, D. (2013). *Geo-electromagnetic monitoring of the Andean Subduction Zone in Northern Chile*. PhD thesis, Freie Universität Berlin, Germany.

Brändlein, D., Lühr, H., and Ritter, O. (2012). Direct penetration of the interplanetary electric field to low geomagnetic latitudes and its effect on magnetotelluric sounding. *Journal of Geophysical Research: Space Physics (1978–2012)*, 117(A11).

Brasse, H. and Eydam, D. (2008). Electrical conductivity beneath the Bolivian Orocline and its relation

to subduction processes at the South American continental margin. *Journal of Geophysical Research: Solid Earth (1978–2012)*, 113(B7).

Brasse, H., Kapinos, G., Li, Y., Muetschard, L., Soyer, W., and Eydam, D. (2009). Structural electrical anisotropy in the crust at the South-Central Chilean continental margin as inferred from geomagnetic transfer functions. *Physics of the Earth and Planetary Interiors*, 173(1):7–16.

Brasse, H., Lezaeta, P., Rath, V., Schwalenberg, K., Soyer, W., and Haak, V. (2002). The Bolivian altiplano conductivity anomaly. *Journal of Geophysical Research: Solid Earth (1978–2012)*, 107(B5):EPM–4.

Cahill, T. and Isacks, B. L. (1992). Seismicity and shape of the subducted Nazca plate. *Journal of Geophysical Research: Solid Earth (1978–2012)*, 97(B12):17503–17529.

Caldwell, T. G., Bibby, H. M., and Brown, C. (2004). The magnetotelluric phase tensor. *Geophysical Journal International*, 158(2):457–469.

Carmichael, R. S. (1989). *Physical properties of rocks and minerals*. CRC Press.

Charrier, R., Pinto, L., and Rodríguez, M. P. (2007). Tectonostratigraphic evolution of the Andean Orogen in Chile. In Moreno, T.; Gibbons, W., editor, *The Geology of Chile*, pages 21–114. The Geological Society, London.

Chave, A. D. (2012). Estimation of the magnetotelluric response function. In Chave, A. D. and Jones, A. G., editors, *The Magnetotelluric Method: Theory and Practice*, pages 165–218. Cambridge University Press, New York.

Chave, A. D. and Jones, A. G. (2012). *The magnetotelluric method: Theory and practice*. Cambridge University Press.

Chlieh, M., De Chabalier, J., Ruegg, J., Armijo, R., Dmowska, R., Campos, J., and Feigl, K. (2004). Crustal deformation and fault slip during the seismic cycle in the North Chile subduction zone, from GPS and InSAR observations. *Geophysical Journal International*, 158(2):695–711.

Coira, B., Davidson, J., Mpodozis, C., and Ramos, V. (1982). Tectonic and magmatic evolution of the Andes of northern Argentina and Chile. *Earth-Science Reviews*, 18(3):303–332.

Comeau, M. J., Unsworth, M. J., Ticona, F., and Sunagua, M. (2015). Magnetotelluric images of magma distribution beneath Volcán Uturuncu, Bolivia: Implications for magma dynamics. *Geology*, 43(3):243–246.

Comte, D. and Pardo, M. (1991). Reappraisal of great historical earthquakes in the northern Chile and southern Peru seismic gaps. *Natural Hazards*, 4(1):23–44.

Constable, C. (2016). Earths Electromagnetic Environment. *Surveys in Geophysics*, 37:27–45.

Contreras-Reyes, E. and Carrizo, D. (2011). Control of high oceanic features and subduction channel on earthquake ruptures along the Chile–Peru subduction zone. *Physics of the Earth and Planetary Interiors*, 186(1):49–58.

Daglis, I., Thorne, R. M., Baumjohann, W., and Orsini, S. (1999). The terrestrial ring current: origin, formation, and decay. *Reviews of Geophysics*, 37:407–438.

Díaz, D., Brasse, H., and Ticona, F. (2012). Conductivity distribution beneath Lascar volcano (Northern Chile) and the Puna, inferred from magnetotelluric data. *Journal of Volcanology and Geothermal Research*, 217:21–29.

Echternacht, F., Tauber, S., Eisel, M., Brasse, H., Schwarz, G., and Haak, V. (1997). Electromagnetic study of the active continental margin in northern Chile. *Physics of the Earth and Planetary Interiors*, 102(1):69–87.

Egbert, G. D. (1997). Robust multiple station magnetotelluric data processing. *Geophysical Journal International*, 130(1):475–496.

Egbert, G. D., Eisel, M., Boyd, O. S., and Morrison, H. F. (2000). DC trains and Pc3s: Source effects in mid-latitude geomagnetic transfer functions. *Geophysical Research Letters*, 27(1):25–28.

Egbert, G. D. and Kelbert, A. (2012). Computational recipes for electromagnetic inverse problems. *Geophysical Journal International*, 189(1):251–267.

Egbert, G. D., Kelbert, A., and Meqbel, N. (2011). Modular System for Electromagnetic Inversion. ModEM user manual.

Eisel, M. and Egbert, G. D. (2001). On the stability of magnetotelluric transfer function estimates and the reliability of their variances. *Geophysical Journal International*, 144(1):65–82.

Ernst, T. and Jankowski, J. (2005). On the plane wave approximation of the external geomagnetic field in regional induction studies. *Izvestiya Physics of the Solid Earth*, 41(5):363–370.

Everett, J. and Hyndman, R. (1967). Geomagnetic variations and electrical conductivity structure in south-western Australia. *Physics of the Earth and Planetary Interiors*, 1(1):24–34.

Farías, M., Charrier, R., Comte, D., Martinod, J., and Hérail, G. (2005). Late Cenozoic deformation and uplift of the western flank of the Altiplano: Evidence from the depositional, tectonic, and geomorphologic evolution and shallow seismic activity (northern Chile at 19°30' S). *Tectonics*, 24(4).

Farías, M., Comte, D., Roecker, S., Carrizo, D., and Pardo, M. (2011). Crustal extensional faulting triggered by the 2010 Chilean earthquake: The Pichilemu Seismic Sequence. *Tectonics*, 30(6).

Ferguson, I. J. (2012). Instrumentation and field procedures. In Chave, A. D. and Jones, A. G., editors, *The Magnetotelluric Method: Theory and Practice*, pages 421–479. Cambridge University Press, New York.

Forbes, J. M. (1981). The equatorial electrojet. *Reviews of Geophysics*, 19(3):469–504.

Friedel, S. (1997). Elektromagnetische Tiefensondierungen in Nordchile unter Berücksichtigung der Sq-Variationen und des EEJ. Diploma thesis, Freie Universität Berlin, Germany.

Gamble, T., Goubau, W. M., and Clarke, J. (1979). Magnetotellurics with a remote magnetic reference. *Geophysics*, 44(1):53–68.

Glover, P. W., Hole, M. J., and Pous, J. (2000). A modified Archie's law for two conducting phases. *Earth and Planetary Science Letters*, 180(3):369–383.

González, G., Gerbault, M., Martinod, J., Cembrano, J., Carrizo, D., Allmendinger, R., and Espina, J. (2008). Crack formation on top of propagating reverse faults of the Chuculay Fault System, northern Chile: Insights from field data and numerical modelling. *Journal of Structural Geology*, 30(6):791–808.

Götze, H.-J. and Krause, S. (2002). The Central Andean gravity high, a relic of an old subduction complex? *Journal of South American Earth Sciences*, 14(8):799–811.

Haberland, C., Rietbrock, A., Schurr, B., and Brasse, H. (2003). Coincident anomalies of seismic attenuation and electrical resistivity beneath the southern Bolivian Altiplano plateau. *Geophysical Research Letters*, 30(18).

Hacker, B. R., Peacock, S. M., Abers, G. A., and Holloway, S. D. (2003). Subduction factory 2. Are intermediate-depth earthquakes in subducting slabs linked to metamorphic dehydration reactions? *Journal of Geophysical Research: Solid Earth (1978–2012)*, 108(B1).

Hamahashi, M., Saito, S., Kimura, G., Yamaguchi, A., Fukuchi, R., Kameda, J., Hamada, Y., Kitamura, Y., Fujimoto, K., Hashimoto, Y., Hina, S., and Eida, M. (2013). Contrasts in physical properties between the hanging wall and footwall of an exhumed seismogenic megasplay fault in a subduction zonean example from the Nobeoka Thrust Drilling Project. *Geochemistry, Geophysics, Geosystems*, 14(12):5354–5370.

Hanekop, O. and Simpson, F. (2006). Error propagation in electromagnetic transfer functions: what role for the magnetotelluric method in detecting earthquake precursors? *Geophysical Journal International*, 165(3):763–774.

Hashin, Z. and Shtrikman, S. (1962). A variational approach to the theory of the effective magnetic permeability of multiphase materials. *Journal of Applied Physics*, 33(10):3125–3131.

Hata, M., Oshiman, N., Yoshimura, R., Tanaka, Y., and Uyeshima, M. (2015). Three-dimensional electromagnetic imaging of upwelling fluids in the Kyushu subduction zone, Japan. *Journal of Geophysical Research: Solid Earth*, 120(1):1–17.

Hayes, G. P., Wald, D. J., and Johnson, R. L. (2012). Slab1. 0: A three-dimensional model of global subduction zone geometries. *Journal of Geophysical Research: Solid Earth (1978–2012)*, 117(B1).

Heise, W., Caldwell, T. G., Bertrand, E. A., Hill, G. J., Bennie, S. L., and Ogawa, Y. (2013). Changes in electrical resistivity track changes in tectonic plate coupling. *Geophysical Research Letters*, 40:5029–5033.

Hermance, J. F. (1979). The electrical conductivity of materials containing partial melt: a simple model from Archie's law. *Geophysical Research Letters*, 6(7):613–616.

Honkura, Y., Oshiman, N., Matsushima, M., Barış, Ş., Tunçer, M. K., Tank, S. B., Çelik, C., and Çiftçi,

E. T. (2013). Rapid changes in the electrical state of the 1999 Izmit earthquake rupture zone. *Nature communications*, 4.

Husen, S. and Kissling, E. (2001). Postseismic fluid flow after the large subduction earthquake of Antofagasta, Chile. *Geology*, 29(9):847–850.

Husen, S., Kissling, E., and Flueh, E. R. (2000). Local earthquake tomography of shallow subduction in north Chile: A combined onshore and offshore study. *Journal of Geophysical Research: Solid Earth (1978–2012)*, 105(B12):28183–28198.

Hyndman, R., Yamano, M., and Oleskevich, D. (1997). The seismogenic zone of subduction thrust faults. *The Island Arc*, 6(3):244–260.

Hyndman, R. D. and Peacock, S. M. (2003). Serpentinization of the forearc mantle. *Earth and Planetary Science Letters*, 212(3):417–432.

Ingebritsen, S. and Manning, C. (2010). Permeability of the continental crust: dynamic variations inferred from seismicity and metamorphism. *Geofluids*, 10(1-2):193–205.

Isacks, B. L. (1988). Uplift of the central Andean plateau and bending of the Bolivian orocline. *Journal of Geophysical Research: Solid Earth (1978–2012)*, 93(B4):3211–3231.

Jacques, J. (2003). A tectonostratigraphic synthesis of the Sub-Andean basins: implications for the geotectonic segmentation of the Andean Belt. *Journal of the Geological Society*, 160(5):687–701.

Jiracek, G. R. (1990). Near-surface and topographic distortions in electromagnetic induction. *Surveys in Geophysics*, 11(2-3):163–203.

Jordan, T., Nester, P., Blanco, N., Hoke, G., Dávila, F., and Tomlinson, A. (2010). Uplift of the Altiplano-Puna plateau: A view from the west. *Tectonics*, 29(5).

Jordan, T. E., Isacks, B. L., Allmendinger, R. W., Brewer, J. A., Ramos, V. A., and Ando, C. J. (1983). Andean tectonics related to geometry of subducted Nazca plate. *Geological Society of America Bulletin*, 94(3):341–361.

Kapinos, G. (2011). *Amphibious Magnetotellurics at the South-Central Chilean Continental margin*. PhD thesis, Freie Universität Berlin.

Kapinos, G., Montahaei, M., Meqbel, N., and Brasse, H. (2016). Three-dimensional electrical resistivity image of the South-Central Chilean subduction zone. *Tectonophysics*, 666:76–89.

Kaufman, A. A. and Keller, G. V. (1981). *The magnetotelluric sounding method*. Elsevier Scientific.

Kelbert, A., Meqbel, N., Egbert, G. D., and Tandon, K. (2014). ModEM: a modular system for inversion of electromagnetic geophysical data. *Computers & Geosciences*, 66:40–53.

Kley, J., Monaldi, C., and Salfity, J. (1999). Along-strike segmentation of the Andean foreland: causes and consequences. *Tectonophysics*, 301(1):75–94.

Koerner, A., Kissling, E., and Miller, S. (2004). A model of deep crustal fluid flow following the Mw= 8.0 Antofagasta, Chile, earthquake. *Journal of Geophysical Research: Solid Earth (1978–2012)*, 109(B6).

Koulakov, I., Sobolev, S. V., and Asch, G. (2006). P-and S-velocity images of the lithosphere-asthenosphere system in the Central Andes from local-source tomographic inversion. *Geophysical Journal International*, 167(1):106–126.

Krings, T. (2007). The influence of robust statistics, remote reference, and horizontal magnetic transfer functions on data processing in magnetotellurics. Diploma thesis, Westfälische Wilhelms-Univ. Münster, Munster, Germany.

Kühn, C., Küster, J., and Brasse, H. (2014). Three-dimensional inversion of magnetotelluric data from the Central Andean continental margin. *Earth, Planets and Space*, 66(1):1–13.

Lanza, F., Tibaldi, A., Bonali, F., and Corazzato, C. (2013). Space–time variations of stresses in the Miocene–Quaternary along the Calama–Olacapato–El Toro Fault Zone, Central Andes. *Tectonophysics*, 593:33–56.

Lanzerotti, L., Chave, A., Sayres, C., Medford, L., and Maclennan, C. (1993). Large-scale electric field measurements on the Earth's surface: A review. *Journal of Geophysical Research: Planets (1991–2012)*, 98(E12):23525–23534.

Larsen, J. C., Mackie, R. L., Manzella, A., Fiordelisi, A., and Rieven, S. (1996). Robust smooth magnetotelluric transfer functions. *Geophysical Journal International*, 124(3):801–819.

Lezaeta, P. (2001). *Distortion analysis and 3-D modeling of magnetotelluric data in the Southern Central Andes*. PhD thesis, Freie Universität Berlin.

Lezaeta, P. and Haak, V. (2003). Beyond magnetotelluric decomposition: Induction, current channeling, and magnetotelluric phases over 90°. *Journal of Geophysical Research: Solid Earth (1978–2012)*, 108(B6).

Lomnitz, C. (2004). Major earthquakes of Chile: a historical survey, 1535-1960. *Seismological Research Letters*, 75(3):368–378.

Magee, M. E. and Zoback, M. D. (1993). Evidence for a weak interplate thrust fault along the northern Japan subduction zone and implications for the mechanics of thrust faulting and fluid expulsion. *Geology*, 21(9):809–812.

Maksaev, V. and Zentilli, M. (1999). Fission track thermochronology of the Domeyko Cordillera, northern Chile; implications for Andean tectonics and porphyry copper metallogenesis. *Exploration and Mining Geology*, 8(1-2):65–89.

Maksymowicz, A. (2015). The geometry of the Chilean continental wedge: Tectonic segmentation of subduction processes off Chile. *Tectonophysics*, 659:183–196.

Mamani, M., Tassara, A., and Wörner, G. (2008). Composition and structural control of crustal domains in the central Andes. *Geochemistry, Geophysics, Geosystems*, 9(3).

Marquis, G. and Hyndman, R. D. (1992). Geophysical support for aqueous fluids in the deep crust: seismic and electrical relationships. *Geophysical Journal International*, 110(1):91–105.

Matsushita, S. and Maeda, H. (1965). On the geomagnetic solar quiet daily variation field during the IGY. *Journal of Geophysical Research*, 70(11):2535–2558.

Maus, S., Barckhausen, U., Berkenbosch, H., Bournas, N., Brozena, J., Childers, V., Dostaler, F., Fairhead, J., Finn, C., Von Frese, R., Gaina, C., Golynsky, S., Kucks, R., Lhr, H., Milligan, P., Mogren, S., Mller, R., Olesen, O., Pilkington, M., Saltus, R., Schreckenberger, B., Thbault, E., and Tontini, F. C. (2009). EMAG2: A 2–arc min resolution Earth Magnetic Anomaly Grid compiled from satellite, airborne, and marine magnetic measurements. *Geochemistry, Geophysics, Geosystems*, 10(8).

Mazzuoli, R., Vezzoli, L., Omarini, R., Acocella, V., Gioncada, A., Matteini, M., Dini, A., Guillou, H., Hauser, N., Uttini, A., and Scaillet, S. (2008). Miocene magmatism and tectonics of the easternmost sector of the Calama–Olacapato–El Toro fault system in Central Andes at ˜24°S: Insights into the evolution of the Eastern Cordillera. *Geological Society of America Bulletin*, 120(11-12):1493–1517.

McPherron, R. L. (2005). Magnetic pulsations: their sources and relation to solar wind and geomagnetic activity. *Surveys in Geophysics*, 26(5):545–592.

Melnick, D., Bookhagen, B., Strecker, M. R., and Echtler, H. P. (2009). Segmentation of megathrust rupture zones from fore-arc deformation patterns over hundreds to millions of years, Arauco peninsula, Chile. *Journal of Geophysical Research: Solid Earth*, 114(B1).

Meqbel, N. M., Egbert, G. D., Wannamaker, P. E., Kelbert, A., and Schultz, A. (2014). Deep electrical resistivity structure of the northwestern US derived from 3-D inversion of USArray magnetotelluric data. *Earth and Planetary Science Letters*, 402:290–304.

Meqbel, N. M. M. (2009). *The electrical conductivity structure of the Dead Sea Basin derived from 2D and 3D inversion of magnetotelluric data*. PhD thesis, Freie Universität Berlin.

Miller, S. A., Collettini, C., Chiaraluce, L., Cocco, M., Barchi, M., and Kaus, B. J. (2004). Aftershocks driven by a high-pressure CO2 source at depth. *Nature*, 427(6976):724–727.

Moreno, M., Haberland, C., Oncken, O., Rietbrock, A., Angiboust, S., and Heidbach, O. (2014). Locking of the Chile subduction zone controlled by fluid pressure before the 2010 earthquake. *Nature Geoscience*, 7(4):292–296.

Mpodozis, C. and Ramos, V. A. (1989). The Andes of Chile and Argentina. In G. Ericksen, M. C. and Reinemund, J., editors, *Geology of the Andes and its relation to hydrocarbon and mineral resources*, pages 59–89. Circum-Pacific Council for Energy and Mineral Resources Earth Science Series, Houston.

Müller, R. D., Roest, W. R., Royer, J.-Y., Gahagan, L. M., and Sclater, J. G. (1997). Digital isochrons of the world's ocean floor. *Journal of Geophysical Research: Solid Earth (1978–2012)*, 102(B2):3211–3214.

Muñoz, G. and Ritter, O. (2013). Pseudo-remote reference processing of magnetotelluric data: a fast and efficient data acquisition scheme for local arrays. *Geophysical Prospecting*, 61(s1):300–316.

Muñoz, N. and Charrier, R. (1996). Uplift of the western border of the Altiplano on a west-vergent thrust system, northern Chile. *Journal of South American Earth Sciences*, 9(3):171–181.

Nesbitt, B. E. (1993). Electrical resistivities of crustal fluids. *Journal of Geophysical Research: Solid Earth (1978–2012)*, 98(B3):4301–4310.

Neska, A. (2006). *Remote Reference versus Signal-Noise Separation: a least-square based comparison between magnetotelluric processing techniques*. PhD thesis, Freie Universität Berlin, Germany.

Nester, P. (2008). *Basin and paleoclimate evolution of the Pampa del Tamarugal forearc valley, Atacama Desert, northern Chile*. PhD thesis, Cornell University.

Nippress, S. and Rietbrock, A. (2007). Seismogenic zone high permeability in the Central Andes inferred from relocations of micro-earthquakes. *Earth and Planetary Science Letters*, 263(3):235–245.

Nocquet, J.-M., Villegas-Lanza, J., Chlieh, M., Mothes, P., Rolandone, F., Jarrin, P., Cisneros, D., Alvarado, A., Audin, L., Bondoux, F., et al. (2014). Motion of continental slivers and creeping subduction in the northern Andes. *Nature Geoscience*, 7(4):287–291.

Oncken, O., Hindle, D., Kley, J., Elger, K., Victor, P., and Schemmann, K. (2006). Deformation of the central Andean upper plate system – Facts, fiction, and constraints for plateau models. In Oncken, O., Chong, G., Franz, G., Giese, P., Götze, H., Ramos, V., Strecker, M., and Wigger, P., editors, *The Andes*, pages 3–27. Springer.

Ozawa, S., Nishimura, T., Suito, H., Kobayashi, T., Tobita, M., and Imakiire, T. (2011). Coseismic and postseismic slip of the 2011 magnitude-9 Tohoku-Oki earthquake. *Nature*, 475(7356):373–376.

Peacock, S. A. (1990). Fluid processes in subduction zones. *Science*, 248(4953):329–337.

Perrier, F. E., Petiau, G., Clerc, G., Bogorodsky, V., Erkul, E., Jouniaux, L., Lesmes, D., Macnae, J., Meunier, J. M., Morgan, D., et al. (1997). A one-year systematic study of electrodes for long period measurements of the electric field in geophysical environments. *Journal of Geomagnetism and Geoelectricity*, 49(11-12):1677–1696.

Petiau, G. and Dupis, A. (1980). Noise, temperature coefficient, and long time stability of electrodes for telluric observations. *Geophysical Prospecting*, 28(5):792–804.

Petrishchev, M. S. and Semenov, V. Y. (2013). Secular variations of the Earth's apparent resistivity. *Earth and Planetary Science Letters*, 361:1–6.

Pommier, A. (2014a). Geophysical assessment of migration and storage conditions of fluids in subduction zones. *Earth, Planets and Space*, 66(1):1–11.

Pommier, A. (2014b). Interpretation of magnetotelluric results using laboratory measurements. *Surveys in Geophysics*, 35(1):41–84.

Pommier, A., Gaillard, F., Pichavant, M., and Scaillet, B. (2008). Laboratory measurements of electrical conductivities of hydrous and dry Mount Vesuvius melts under pressure. *Journal of Geophysical Research: Solid Earth (1978–2012)*, 113(B5).

Preisendorfer, R. W. and Mobley, C. D. (1988). *Principal component analysis in meteorology and oceanography*, volume 425. Elsevier Amsterdam.

Price, A. (1962). The theory of magnetotelluric methods when the source field is considered. *Journal of Geophysical Research*, 67(5):1907–1918.

Pritchard, M. and Simons, M. (2006). An aseismic slip pulse in northern Chile and along-strike variations in seismogenic behavior. *Journal of Geophysical Research: Solid Earth (1978–2012)*, 111(B8).

Reijs, J. and McClay, K. (1998). Salar Grande pull-apart basin, Atacama fault system, northern Chile. *Geological Society, London, Special Publications*, 135(1):127–141.

Reutter, K.-J., Scheuber, E., and Chong, G. (1996). The Precordilleran fault system of Chuquicamata, northern Chile: Evidence for reversals along arc-parallel strike-slip faults. *Tectonophysics*, 259(1):213–228.

Reynard, B., Mibe, K., and Van de Moortèle, B. (2011). Electrical conductivity of the serpentinised mantle and fluid flow in subduction zones. *Earth and Planetary Science Letters*, 307(3):387–394.

Richards, J. P., Boyce, A. J., and Pringle, M. S. (2001). Geologic evolution of the Escondida area, Northern Chile: a model for spatial and temporal localization of porphyry Cu mineralization. *Economic Geology*, 96(2):271–305.

Ritter, O. (1995). *An audiomagnetotelluric investigation of the Southern Upland Fault: novel instrumentation, field procedures and 3D modelling*. PhD thesis, University of Edinburgh.

Ritter, O., Junge, A., and Dawes, G. J. (1998). New equipment and processing for magnetotelluric remote reference observations. *Geophysical Journal International*, 132(3):535–548.

Romano, G., Balasco, M., Lapenna, V., Siniscalchi, A., Telesca, L., and Tripaldi, S. (2014). On the sensitivity of long-term magnetotelluric monitoring in Southern Italy and source-dependent robust single station transfer function variability. *Geophysical Journal International*, 197(3):1425–1441.

Sáez, A., Cabrera, L., Jensen, A., and Chong, G. (1999). Late Neogene lacustrine record and palaeogeography in the Quillagua–Llamara basin, Central Andean fore-arc (northern Chile). *Palaeogeography, Palaeoclimatology, Palaeoecology*, 151(1):5–37.

Saffer, D. M. and Tobin, H. J. (2011). Hydrogeology and mechanics of subduction zone forearcs: fluid flow and pore pressure. *Annual Review of Earth and Planetary Sciences*, 39:157–186.

Salazar, P. (2011). *The upper crustal microseismicity image from the North Chilean subduction zone: implications for tectonics and fluid migration*. PhD thesis, Freie Universität Berlin.

Schaller, T., Andersen, J., Götze, H.-J., Koproch, N., Schmidt, S., Sobiesiak, M., and Splettstößer, S.

(2015). Segmentation of the Andean margin by isostatic models and gradients. *Journal of South American Earth Sciences*, 59:69–85.

Scheuber, E. and González, G. (1999). Tectonics of the Jurassic-Early Cretaceous magmatic arc of the north Chilean Coastal Cordillera (22–26 S): A story of crustal deformation along a convergent plate boundary. *Tectonics*, 18(5):895–910.

Schilling, F. R., Partzsch, G. M., Brasse, H., and Schwarz, G. (1997). Partial melting below the magmatic arc in the central Andes deduced from geoelectromagnetic field experiments and laboratory data. *Physics of the Earth and Planetary Interiors*, 103(1):17–31.

Schmelzbach, C., Kummerow, J., Wigger, P., Reshetnikov, A., Salazar, P., and Shapiro, S. (2016). Microseismic reflection imaging of the Central Andean crust. *Geophysical Journal International*, 204(2):1396–1404.

Scholz, C. H. (1998). Earthquakes and friction laws. *Nature*, 391(6662):37–42.

Schurr, B., Asch, G., Hainzl, S., Bedford, J., Hoechner, A., Palo, M., Wang, R., Moreno, M., Bartsch, M., Zhang, Y., Oncken, O., Tilmann, F., Dahm, T., Victor, P., Barrientos, S., and Vilotte, J.-P. (2014). Gradual unlocking of plate boundary controlled initiation of the 2014 Iquique earthquake. *Nature*, 512(7514):299–302.

Schurr, B., Asch, G., Rietbrock, A., Kind, R., Pardo, M., Heit, B., and Monfret, T. (1999). Seismicity and average velocities beneath the Argentine Puna plateau. *Geophysical Research Letters*, 26(19):3025–3028.

Schurr, B., Asch, G., Rietbrock, A., Trumbull, R., and Haberland, C. (2003). Complex patterns of fluid and melt transport in the central Andean subduction zone revealed by attenuation tomography. *Earth and Planetary Science Letters*, 215(1):105–119.

Schurr, B., Asch, G., Rosenau, M., Wang, R., Oncken, O., Barrientos, S., Salazar, P., and Vilotte, J.-P. (2012). The 2007 M7. 7 Tocopilla northern Chile earthquake sequence: Implications for along-strike and downdip rupture segmentation and megathrust frictional behavior. *Journal of Geophysical Research: Solid Earth (1978–2012)*, 117(B5).

Schurr, B. and Rietbrock, A. (2004). Deep seismic structure of the Atacama basin, northern Chile. *Geophysical Research Letters*, 31(12).

Schwalenberg, K., Rath, V., and Haak, V. (2002). Sensitivity studies applied to a two-dimensional resistivity model from the Central Andes. *Geophysical Journal International*, 150(3):673–686.

Schwarz, G., Chong Diaz, G., Krüger, D., Martinez, E., Massow, W., Rath, V., and Viramonte, J. (1994). Crustal high conductivity zones in the southern Central Andes. In *Tectonics of the Southern Central Andes*, pages 49–67. Springer.

Sernageomin (2003). *Mapa Geológico de Chile escala 1:1.000.000*. Servicio Nacional de Geología y Minería.

Shapiro, S., Patzig, R., Rothert, E., and Rindschwentner, J. (2003). Triggering of seismicity by pore-pressure perturbations: Permeability-related signatures of the phenomenon. *Pure and Applied Geophysics*, 160(5-6):1051–1066.

Shimizu, H., Yoneda, A., Baba, K., Utada, H., and Palshin, N. A. (2011). Sq effect on the electromagnetic response functions in the period range between 10^4 and 10^5 s. *Geophysical Journal International*, 186:193–206.

Simpson, F. and Bahr, K. (2005). *Practical magnetotellurics*. Cambridge University Press.

Sodoudi, F., Yuan, X., Asch, G., and Kind, R. (2011). High-resolution image of the geometry and thickness of the subducting Nazca lithosphere beneath northern Chile. *Journal of Geophysical Research: Solid Earth*, 116(B4).

Sokolova, E. Y. and Varentsov, I. M. (2005). RRMC Technique Fights Highly Coherent EM Noise. In *Protokoll uber das 21. Kolloquium Elektromagnetische Tiefenforschung*, pages 124–136.

Soyer, W. (2002). *Analysis of geomagnetic variations in the Central and Southern Andes*. PhD thesis, Freie Universität Berlin, Germany.

Soyer, W. and Brasse, H. (2001). A magneto-variation array study in the central Andes of N Chile and SW Bolivia. *Geophysical Research Letters*, 28(15):3023–3026.

Spinelli, G. A. and Saffer, D. M. (2007). Trench-parallel fluid flow in subduction zones resulting from temperature differences. *Geochemistry, Geophysics, Geosystems*, 8(9).

Springer, M. (1999). Interpretation of heat-flow density in the Central Andes. *Tectonophysics*, 306(3):377–395.

Stern, C. R. (2004). Active Andean volcanism: its geologic and tectonic setting. *Revista Geológica de Chile*, 31(2):161–206.

Stoerzel, A. (1996). Estimation of geomagnetic transfer functions from nonuniform magnetic fields induced by the equatorial electrojet: A method to determine static shifts in magnetotelluric data. *Journal of Geophysical Research: Solid Earth (1978–2012)*, 101(B8):17917–17926.

Takeda, M. (1997). Local time variation of geomagnetic transfer functions. *Geophysical Journal International*, 130(3):765–770.

Tassara, A., Götze, H.-J., Schmidt, S., and Hackney, R. (2006). Three-dimensional density model of the Nazca plate and the Andean continental margin. *Journal of Geophysical Research: Solid Earth (1978–2012)*, 111(B9).

Taylor, G. K., Dashwood, B., and Grocott, J. (2005). Central Andean rotation pattern: Evidence from paleomagnetic rotations of an anomalous domain in the forearc of northern Chile. *Geology*, 33(10):777–780.

Tilmann, F., Zhang, Y., Moreno, M., Saul, J., Eckelmann, F., Palo, M., Deng, Z., Babeyko, A., Chen, K.,

Baez, J., Schurr, B., Wang, R., and Dahm, T. (2016). The 2015 Illapel earthquake, central Chile: A type case for a characteristic earthquake? *Geophysical Research Letters*, 43.

Unsworth, M. and Rondenay, S. (2013). Mapping the distribution of fluids in the crust and lithospheric mantle utilizing geophysical methods. In *Metasomatism and the Chemical Transformation of Rock*, pages 535–598. Springer.

Victor, P., Oncken, O., and Glodny, J. (2004). Uplift of the western Altiplano plateau: Evidence from the Precordillera between 20° and 21° S (northern Chile). *Tectonics*, 23(4).

Viljanen, A. (2012). Description of the magnetospheric/ionospheric sources. In Chave, A. D. and Jones, A. G., editors, *The Magnetotelluric Method: Theory and Practice*, pages 96–121. Cambridge University Press, New York.

Völker, D. and Stipp, M. (2015). Water input and water release from the subducting Nazca Plate along southern Central Chile (33° S–46° S). *Geochemistry, Geophysics, Geosystems*.

von Huene, R. and Ranero, C. (2003). Subduction erosion and basal friction along the sediment-starved convergent margin off Antofagasta, Chile. *Journal of Geophysical Research: Solid Earth*, 108(B2).

Wait, J. R. (1954). On the relation between telluric currents and the earth's magnetic field. *Geophysics*, 19(2):281–289.

Wang, C.-Y. and Manga, M. (2010). *Earthquakes and Water*. Springer.

Wannamaker, P. E., Evans, R. L., Bedrosian, P. A., Unsworth, M. J., Maris, V., and McGary, R. S. (2014). Segmentation of plate coupling, fate of subduction fluids, and modes of arc magmatism in Cascadia, inferred from magnetotelluric resistivity. *Geochemistry, Geophysics, Geosystems*, 15(11):4230–4253.

Weckmann, U., Magunia, A., and Ritter, O. (2005). Effective noise separation for magnetotelluric single site data processing using a frequency domain selection scheme. *Geophysical Journal International*, 161(3):635–652.

Weckmann, U., Ritter, O., and Haak, V. (2003). A magnetotelluric study of the Damara Belt in Namibia: 2. MT phases over 90° reveal the internal structure of the Waterberg Fault/Omaruru Lineament. *Physics of the Earth and Planetary Interiors*, 138(2):91–112.

Weidelt, P. (1972). The inverse problem of geomagnetic induction. *J. Geophys.*, 38:257–289.

Weidelt, P. and Chave, A. (2012). The magnetotelluric response function. In Chave, A. D. and Jones, A. G., editors, *The Magnetotelluric Method: Theory and Practice*, pages 122–162. Cambridge University Press, New York.

Wiese, H. (1962). Geomagnetische Tiefentellurik Teil II: die Streichrichtung der Untergrundstrukturen des elektrischen Widerstandes, erschlossen aus geomagnetischen Variationen. *Geofisica pura e applicata*, 52(1):83–103.

Worzewski, T., Jegen, M., Kopp, H., Brasse, H., and Castillo, W. T. (2011). Magnetotelluric image of the fluid cycle in the Costa Rican subduction zone. *Nature Geoscience*, 4(2):108–111.

Yáñez, G. and Cembrano, J. (2004). Role of viscous plate coupling in the late Tertiary Andean tectonics. *Journal of Geophysical Research: Solid Earth (1978–2012)*, 109(B2).

Yáñez, G., Rivera, O., Comte, D., Pardo, M., Baeza, L., and Vera, E. (2008). Damage zone and the occurrence of world-class porphyry copper deposits in the active margin of Chile: Geophysical signatures and tectonomagmatic inferences. In *International Symposium on Andean Geodynamics*, number 7, pages 592–593.

Yoon, M., Buske, S., Shapiro, S., and Wigger, P. (2009). Reflection image spectroscopy across the Andean subduction zone. *Tectonophysics*, 472(1):51–61.

Yuan, X., Sobolev, S., Kind, R., Oncken, O., Bock, G., Asch, G., Schurr, B., Graeber, F., Rudloff, A., Hanka, W., et al. (2000). Subduction and collision processes in the Central Andes constrained by converted seismic phases. *Nature*, 408(6815):958–961.

Appendix A

IPOC Transfer Functions

A.1 Histograms daily estimates of TFs IPOC

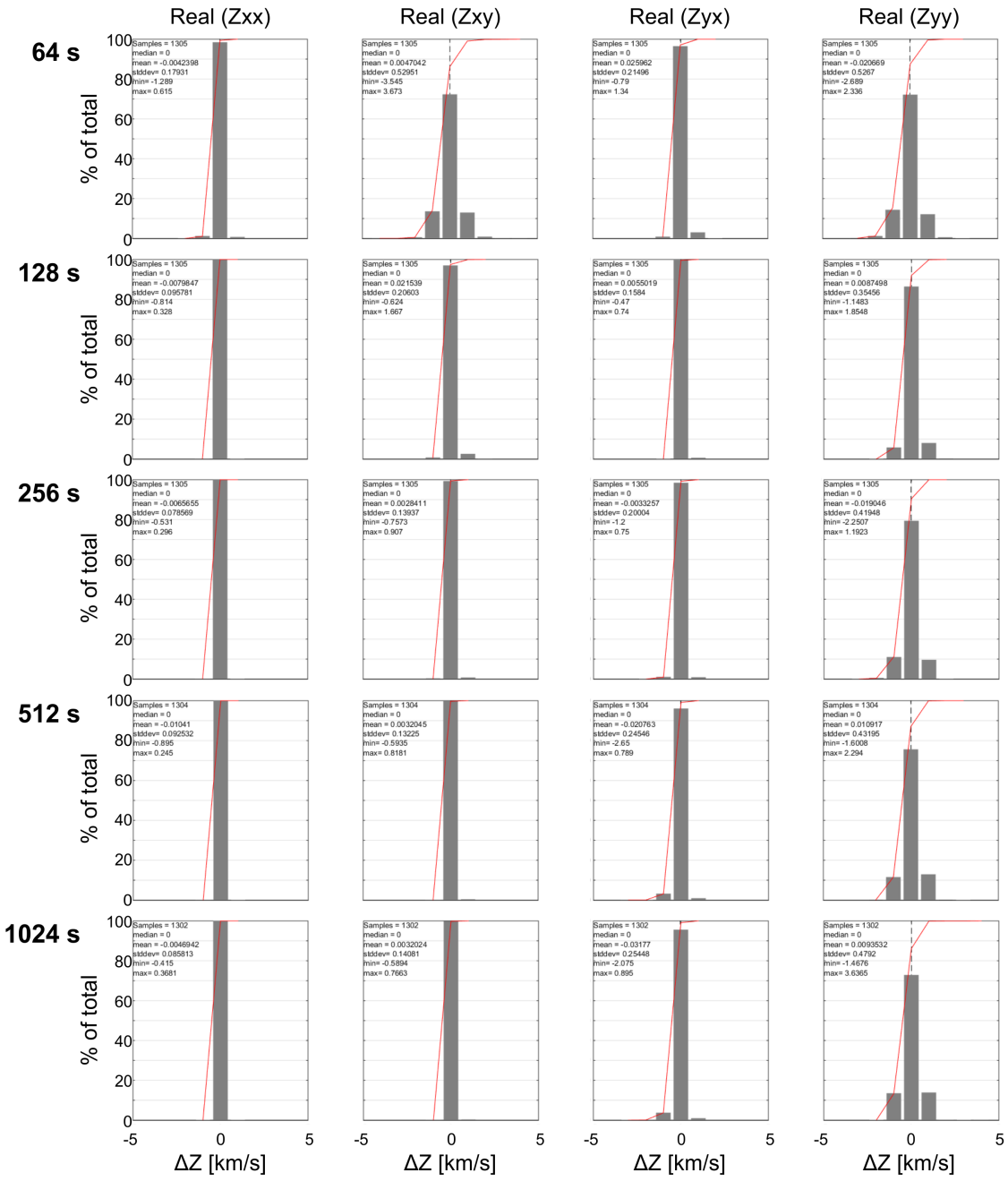

Figure A.1: Frequency histograms showing the statistical distribution of daily $Real(Z)$ estimates between years 2011 and 2015 for the exemplary IPOC site PB01 (remote reference processing, remote site PB09). Histograms are ordered by periods (along rows) and TF components (along columns). The X-axes display deviations of daily TF estimates from the 4-year median values (ΔZ). Y-axes show the frequency of observations as percentage of the total number of samples (daily estimates). Black vertical dashed lines indicate position of the 4-year mean value. Red curves show the cumulative distribution of the daily TF estimates.

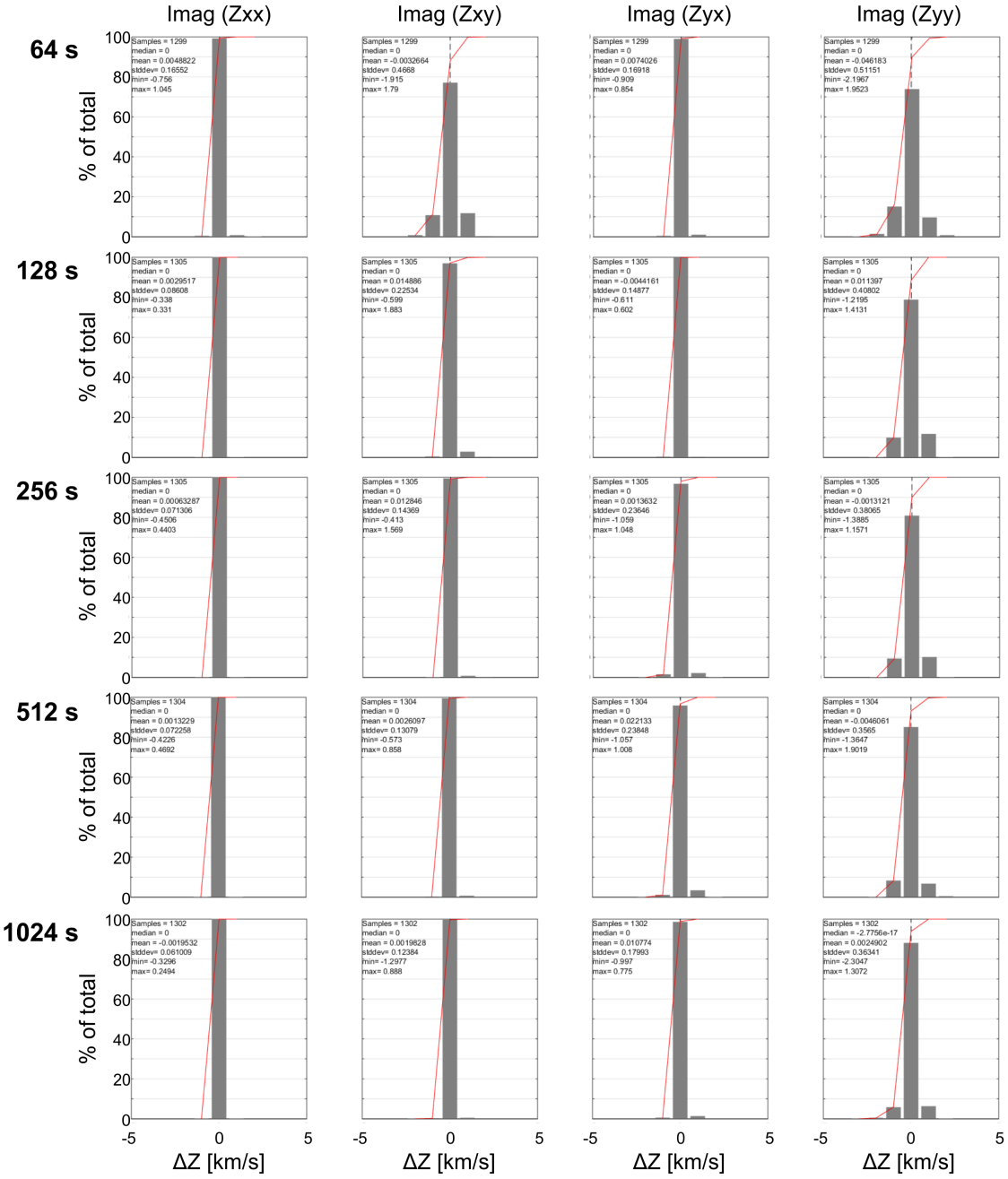

Figure A.2: Same as Figure A.1, but for $Imag(Z)$.

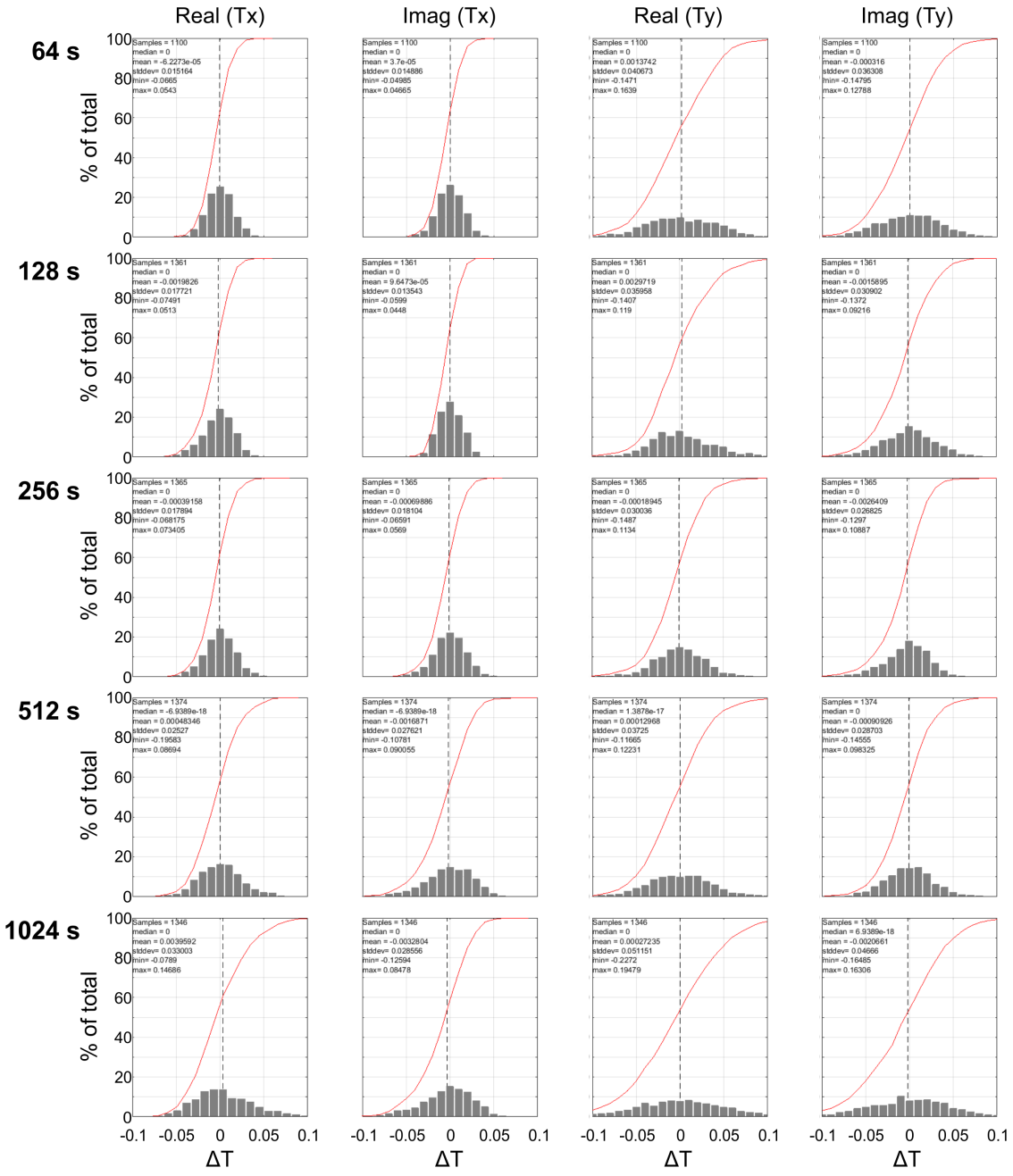

Figure A.3: Same as Figure A.1, but for VTF.

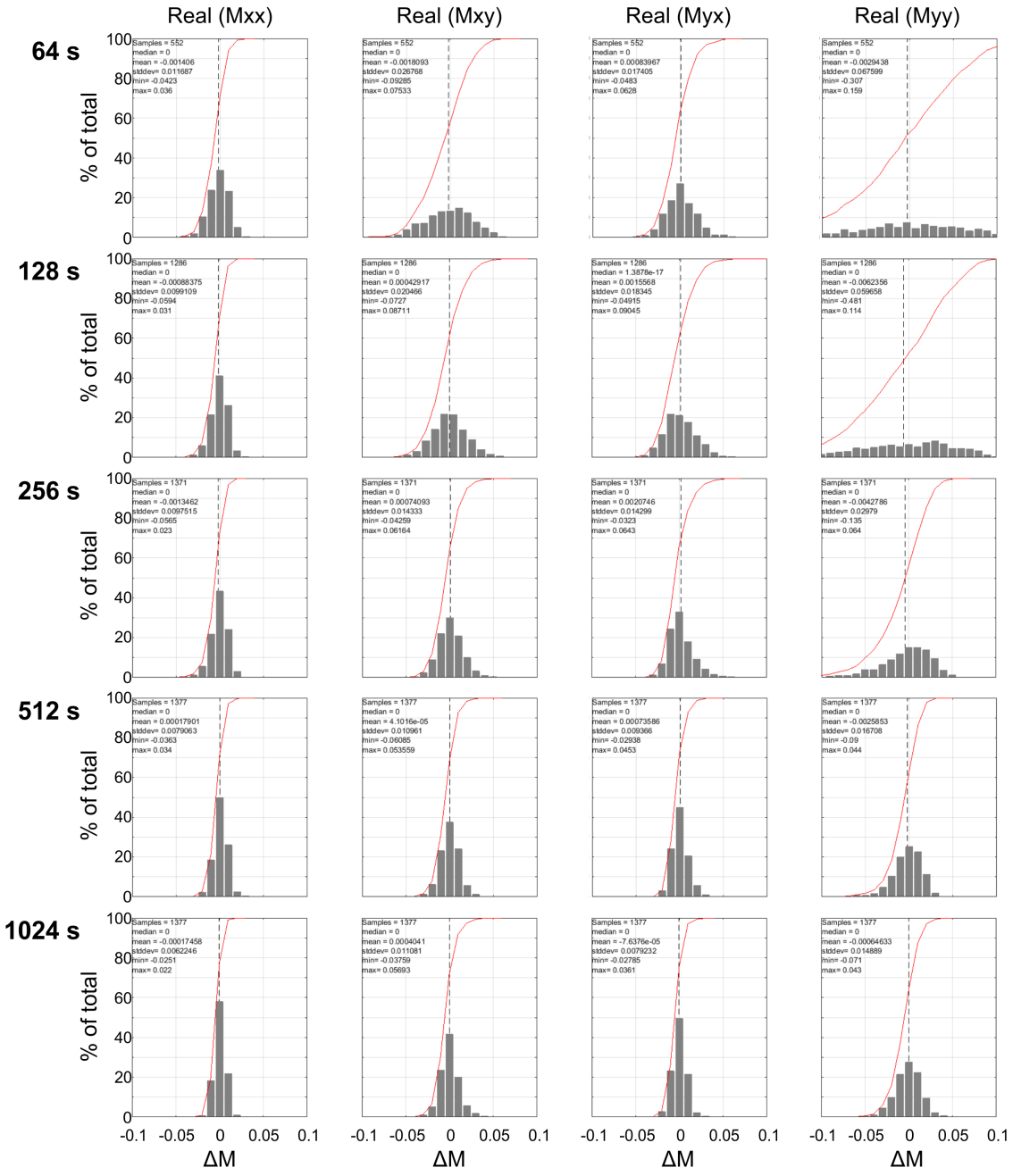

Figure A.4: Same as Figure A.1, but for HTF PB09-PB01, $Real(M)$.

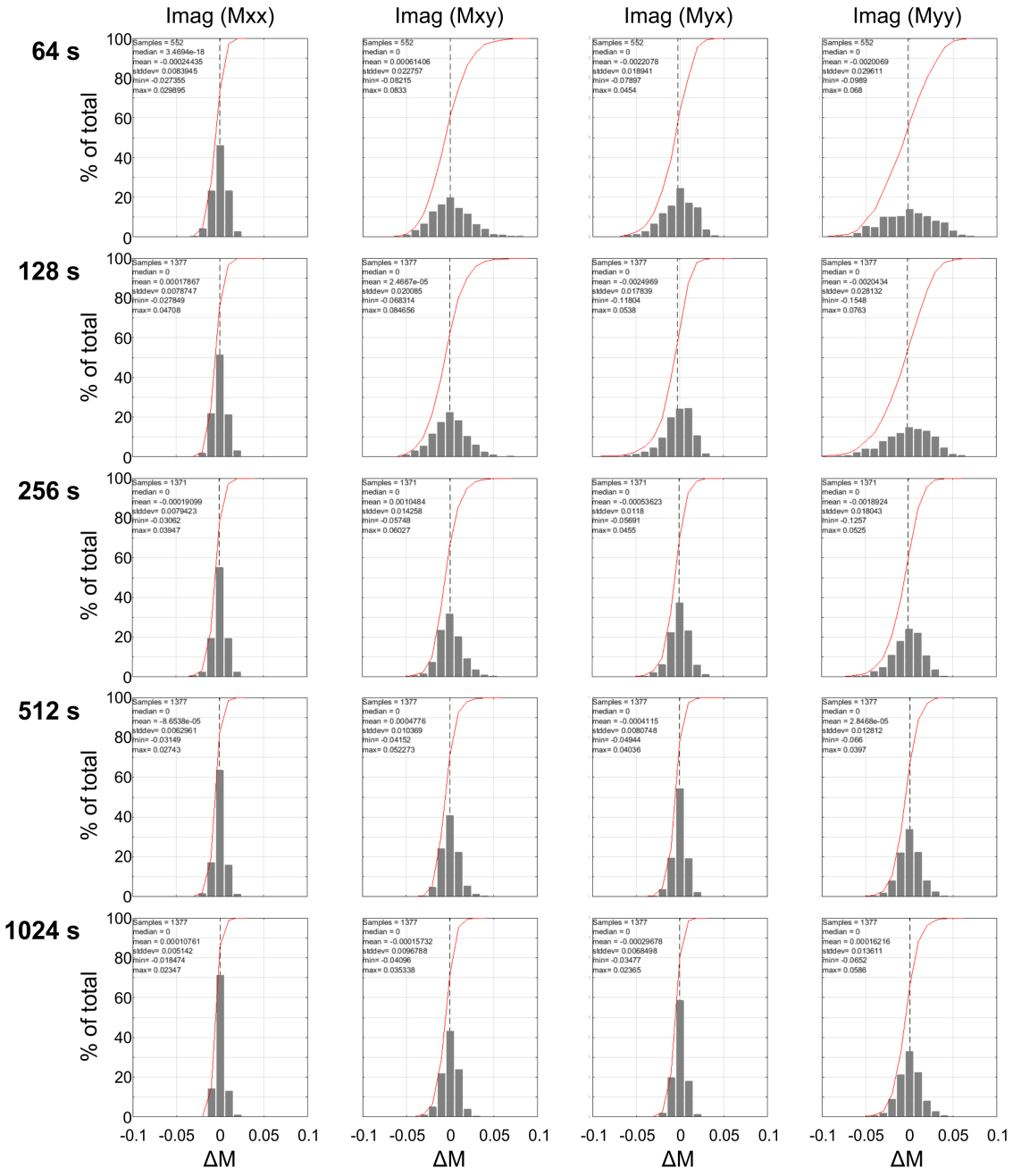

Figure A.5: Same as Figure A.1, but for HTF PB09-PB01, $Imag(M)$.

A.2 Long-term average sounding curves

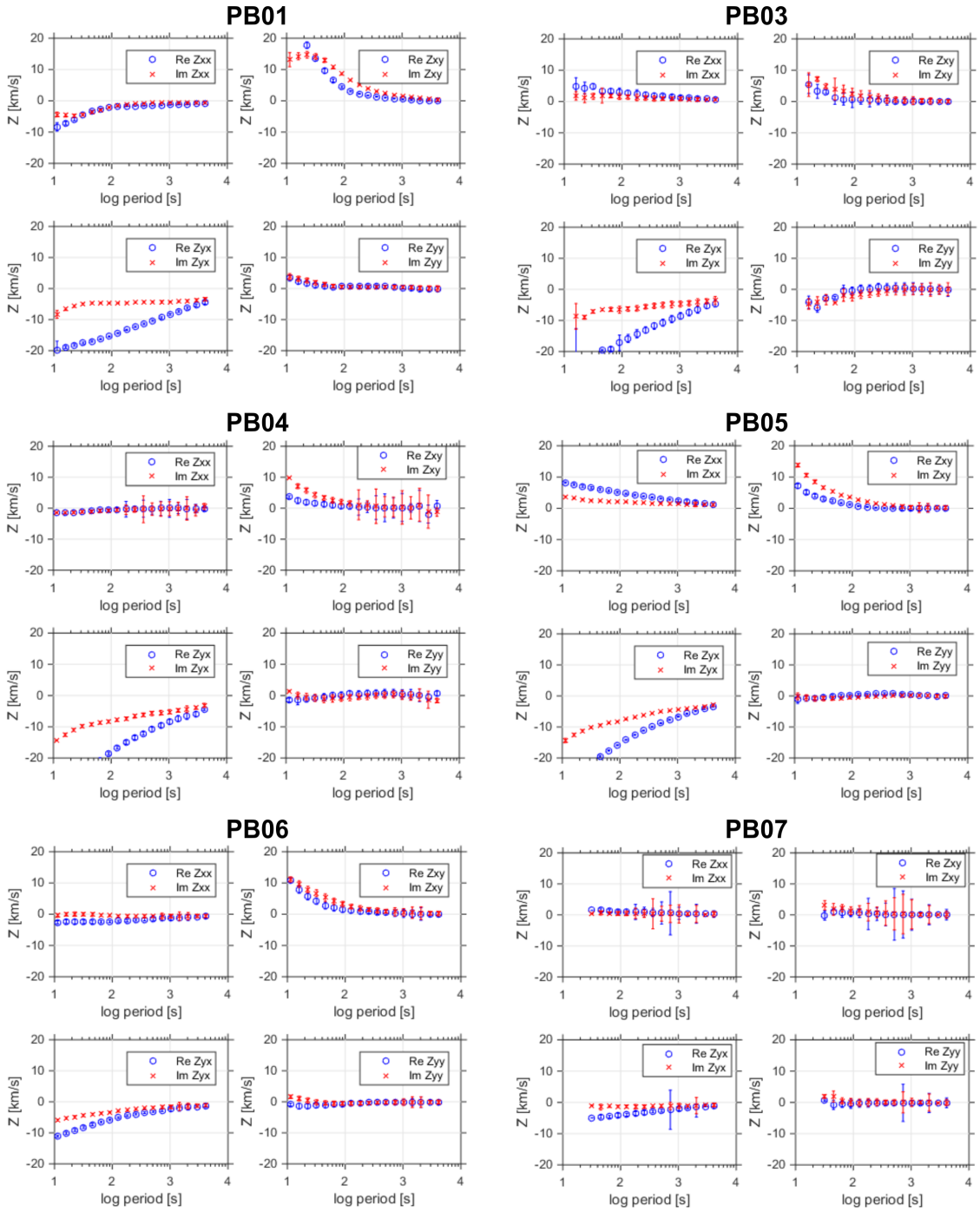

Figure A.6: Long-term average impedance sounding curves for IPOC sites PB01 to PB07. For each period, the displayed value is the statistical median of all daily TF estimates obtained from 2011 to 2015, excluding those days which exhibit confidence intervals $\delta Z > 1$ [km/s]. Error bars are 1 standard deviation of the population.

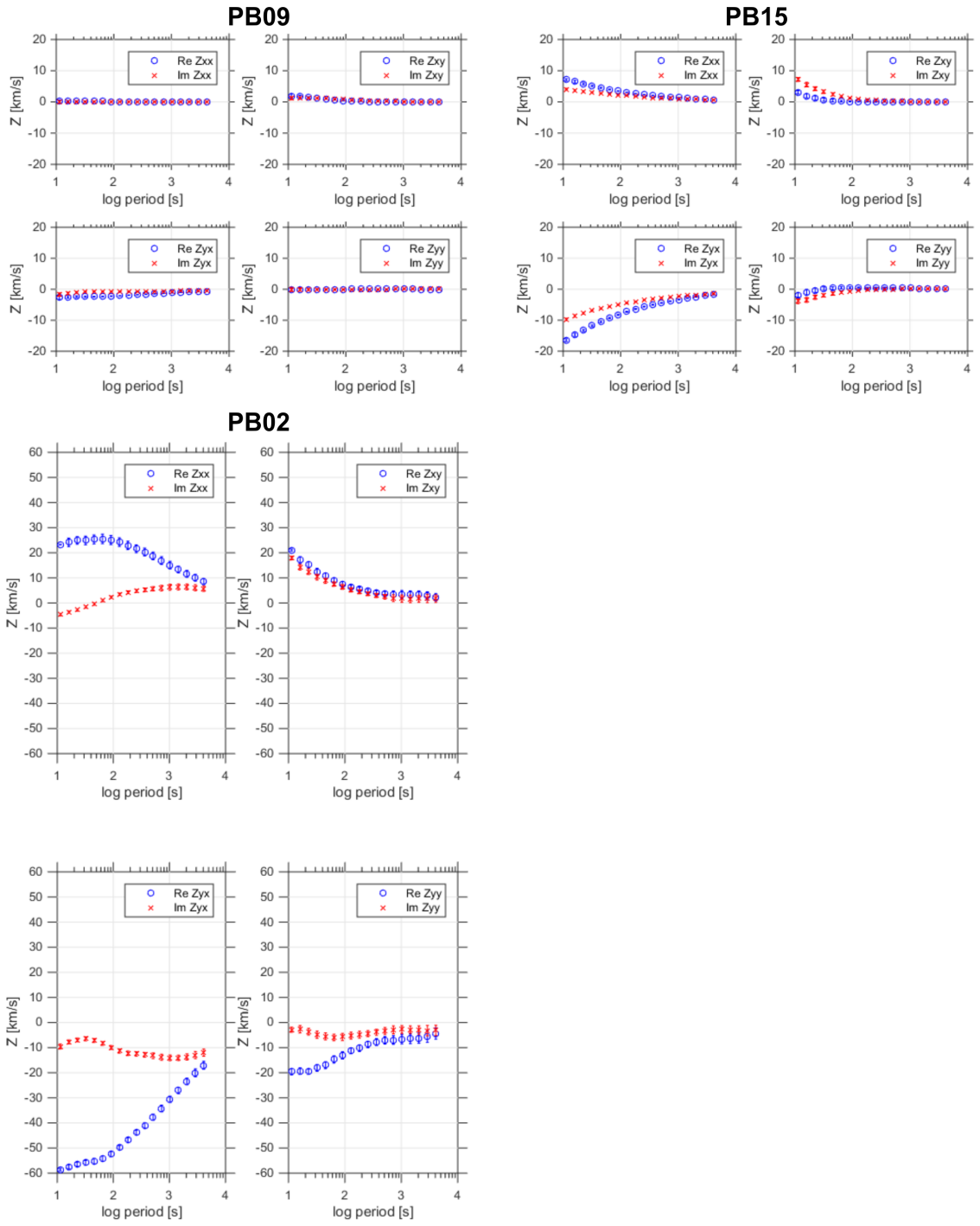

Figure A.7: Same as Figure A.6, but for IPOC sites PB02, PB09 and PB15. Note that sounding curves for site PB02 are displayed using a different Y-axis range.

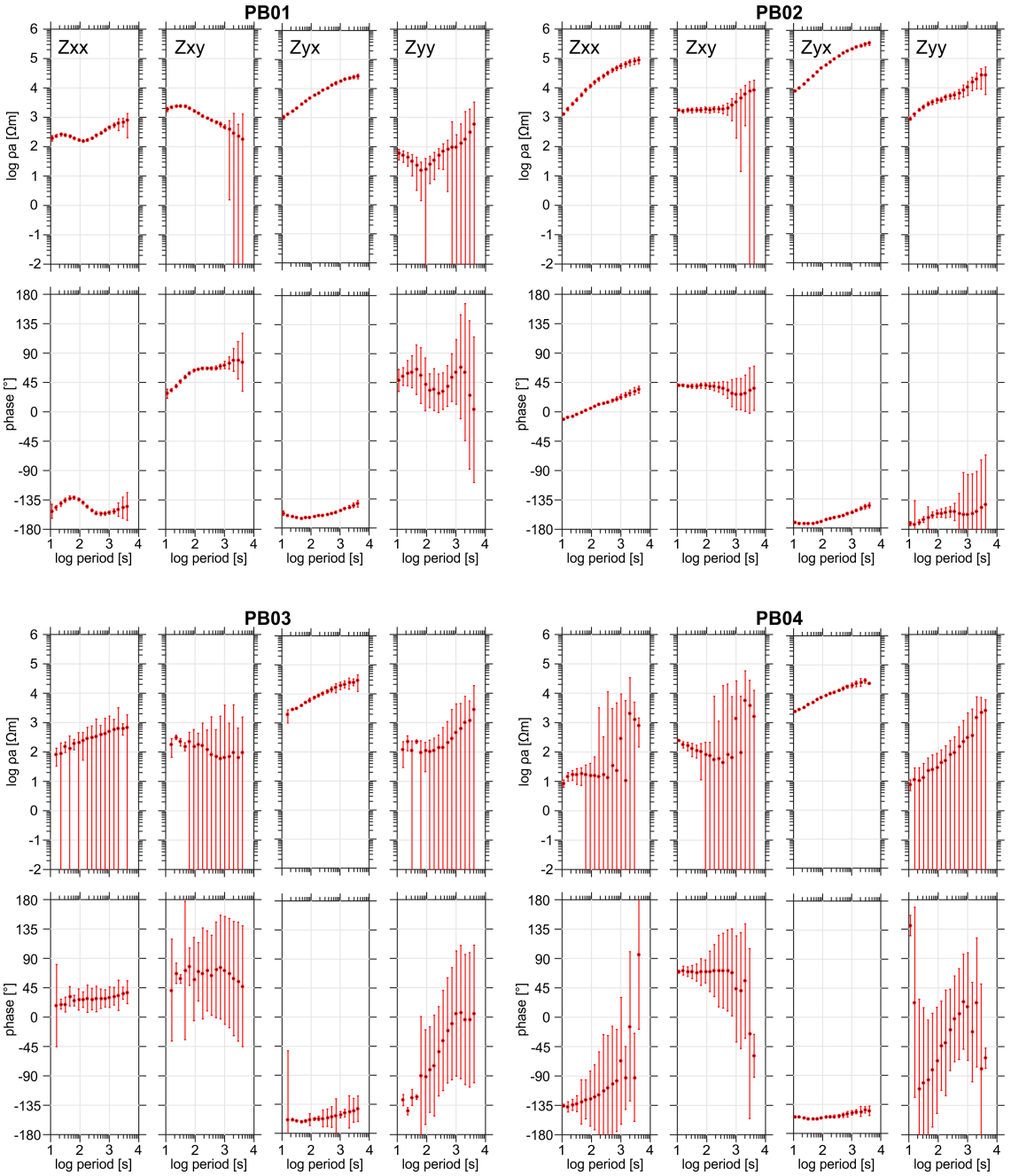

Figure A.8: Long-term average apparent resistivity and phase for IPOC sites PB01 to PB04. For each period, the displayed value is the statistical median of all daily TF estimates obtained from 2011 to 2015, excluding those days which exhibit confidence intervals $\delta Z > 1$ [km/s]. Daily estimates of TFs obtained using the remote reference processing technique (Gamble et al., 1979), employing site PB01 as reference site (when processing PB01 data, the reference site is PB09). Error bars are 1 standard deviation of the population.

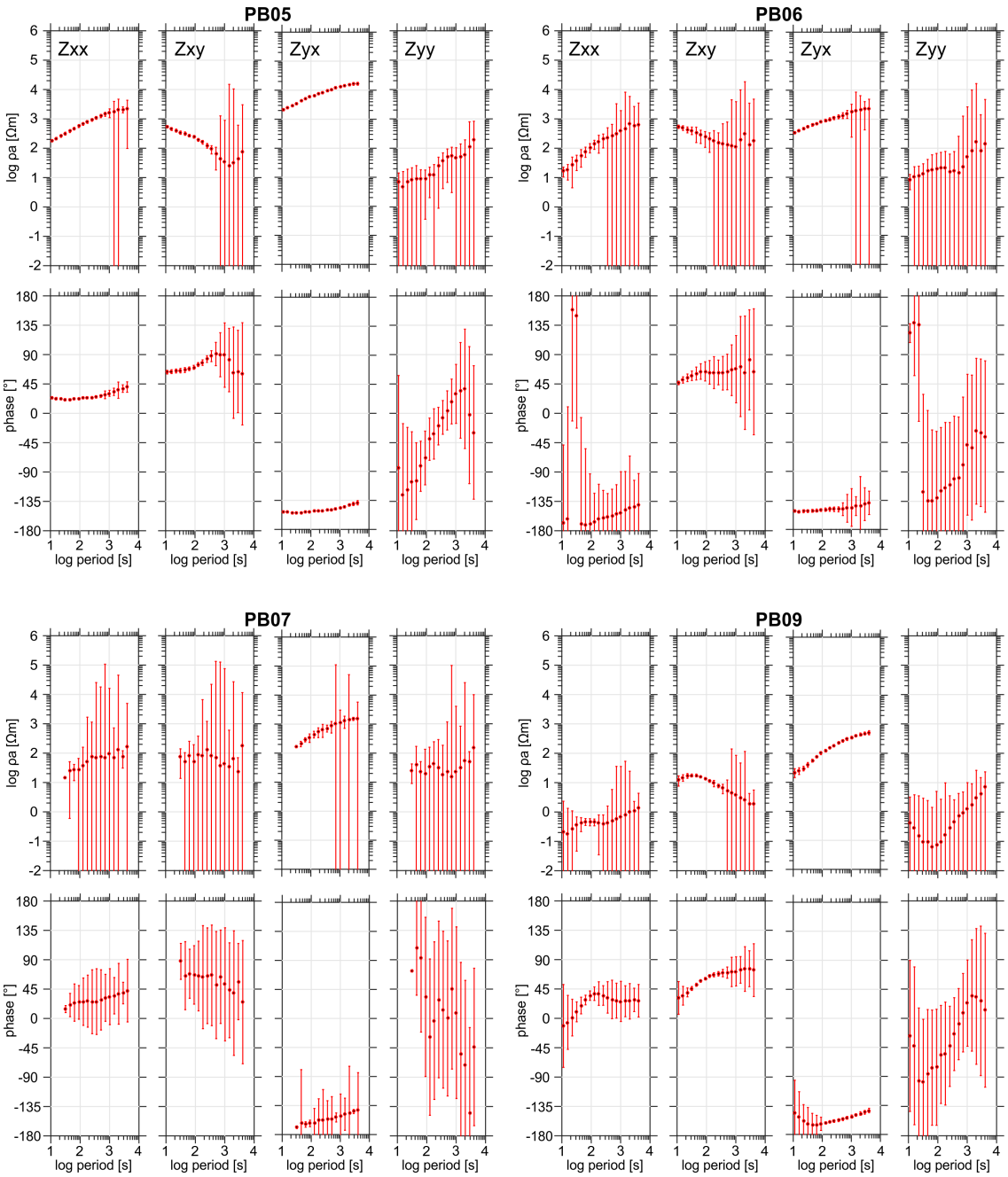

Figure A.9: Same as Figure A.8, but for IPOC sites PB05 to PB09.

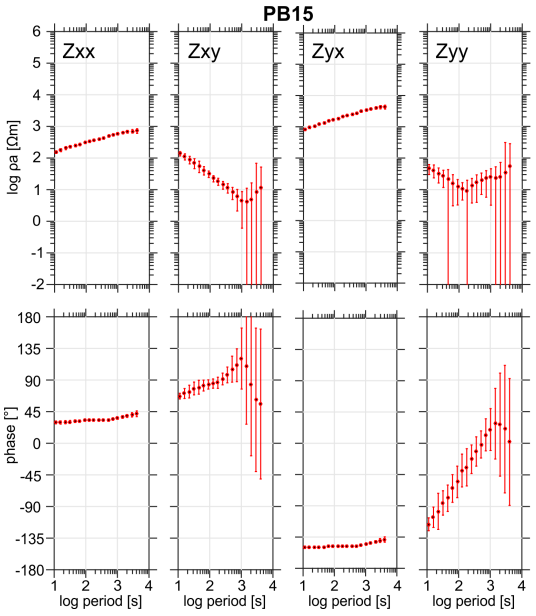

Figure A.10: Same as Figure A.8, but for IPOC site PB15.

Erklärung

Hiermit versichere ich, dass ich die vorliegende Dissertation selbständig ohne Hilfe Dritter verfasst habe. Andere als die angegebenen Quellen und Hilfsmittel wurden nicht verwendet. Die den benutzten Quellen wörtlich oder dem Sinn nach entnommen Abschnitte sind als solche kenntlich gemacht. Dies gilt auch für Zeichnungen, Skizzen, bildliche Darstellungen und dergleichen, sowie für Quellen aus dem Internet. Die Dissertation hat in dieser oder ähnlicher Form weder ganz noch in Teilen einer in- oder ausländischen Hochschule zum Zwecke der Promotion vorgelegen.

Teile von Kapitel 4 wurden bei *Journal of Geophysical Research* eingereicht.

Teile von Kapitel 5 sind veröffentlicht in: Araya Vargas, J., Ritter, O. (2016). Source effects in mid-latitude geomagnetic transfer functions. *Geophysical Journal International*, 204 (1): 606-630, doi:10.1093 /gji/ggv474.

Berlin, _____

Curriculum Vitae

For reasons of data protection, the curriculum vitae is not published in the online version.

Aus Gründen des Datenschutzes erscheint der Lebenslauf nicht in der elektronischen Fassung.